Determination of the Time Profile of Picosecond-Long Electron Bunches through the use of Coherent Smith-Purcell Radiation

Victoria Blackmore
St. Cross College, Oxford

Thesis submitted in fulfillment of the requirements for the degree of Doctor of Philosophy at the University of Oxford

Michaelmas Term, 2008

Determination of the Time Profile of Picosecond-Long Electron Bunches through the use of Coherent Smith-Purcell Radiation

Victoria Blackmore
St. Cross College, Oxford

Thesis submitted in fulfillment of the requirements for the degree of Doctor of Philosophy at the University of Oxford

Michaelmas Term, 2008

Abstract

Coherent Smith-Purcell (SP) radiation was used to determine the longitudinal (time) profile of ps-long bunches during three experiments at intermediate and high energy. Radiation was detected by means of an 11-element array of room temperature pyroelectric detectors. The first experiment was carried out at the FELIX Facility, FOM Institute, Netherlands at an energy of 45MeV. Data from this experiment were re-analysed using the Kramers-Krönig technique. The FELIX bunch was found to have a FWHM of 3.9ps and length of $\sim$ 6.8ps, with a profile similar in a appearance to an asymmetric Gaussian.

Two further experiments were carried out in ESA at SLAC in March and July 2007 at an energy of 28.5GeV. These were the first ever experiments using coherent SP radiation in the multi-GeV regime and they demonstrated that SP radiation was generated in this region with features broadly in line with the 'surface current' theory. The July experiment concluded that the FWHM of the SLAC bunch varied between 2.7 – 3.2ps, with a length between 5 – 6.5ps. All profiles were asymmetric in appearance. These results were consistent with measurements carried out using the LOLA deflecting cavity at SLAC in March 2007.

This thesis also discusses the calibration of pyroelectric detectors in the far-infrared, and the design, manufacture, and commissioning of far-infrared filters and light concentrators. These were all essential components of the above experiments.

Acknowledgements

There are many, many people who deserve acknowledgement here for their help and support during my time as a DPhil student. First amongst these is my supervisor, Dr. George Doucas. He has been a great inspiration to me, and I have always considered myself incredibly lucky to be his student. His endless patience and support have truly made this possible.

I also owe a large debt of gratitude to Prof. Maurice Kimmit. It has been an honour to work with him, and I feel I would have been quickly lost at sea without his book, and advice, on far-infrared techniques to guide me. Similarly, I am grateful to both Dr. Peter Huggard (RAL) and Dr. Michael Johnston (Oxford), for their continued patience and support even after so many transmission and calibration measurements.

Thanks also go to Dr. Colin Perry and Johan Fopma for providing illumination on all things electronic, and to Dr. Michael Woods for making everything run so smoothly at SLAC. I'm glad that I'll never know what could have happened without him in charge.

On a more personal note I must thank my parents, who have supported me through the ups and downs. To all my friends, who have put up with me on the most grumpy of days and listened to my triumphs and failures, I most definitely owe you my gratitude. Finally, last but never least, I am eternally grateful to my husband Pavel, for providing the hugs and chocolate necessary to write this thesis.

Contents

List of Figures

List of Tables

Chapter 1

Introduction

High energy physics experiments are rapidly expanding into the TeV region through accelerators such as the Large Hadron Collider (LHC) and the International Linear Collider (ILC). Diagnostic tools, specifically beam diagnostics, are an essential part of the design, commissioning and running of accelerators. The move to higher energy, intensity and beam quality drives the need for new diagnostics. This thesis describes the development of a novel technique for determining the longitudinal profile of picosecond-long bunches in future accelerators such as the ILC.

1.1 The Motivation to Move to the TeV Scale

The Standard Model (SM) describes virtually all phenomena as observed in current experiments and is capable of making extremely accurate predictions, anticipating the existence of several particles before their discovery (*e.g.*the top quark). However, these predictions rely heavily upon a number of arbitrary parameters and the as-yet unproven hypothesis of the *Higgs Mechanism*.

There are a number of motivations behind the move to TeV scale experiments, which shall be discussed here along with their relevance to the Standard Model:

- The drive to discover the Higgs boson.
- The drive to discover supersymmetric (SUSY) particles.
- The drive to discover extra dimensions.

- The drive to discover dark matter.
- The drive to discover a Grand Unified Theory (GUT) of all the forces.

1.1.1 The Standard Model Higgs Boson

The strong, electromagnetic, and weak gauge theories insist upon the existence of massless gauge bosons (force-carrying particles) of integer spin. However, the $W^{\pm}$ and Z bosons have mass. To solve this problem, it was proposed that they were originally massless and acquired their mass through a symmetry breaking process. Thus, the Higgs mechanism was introduced.

The SM predicts a Higgs field (and associated boson), which permeates all space. The field has 4 components, 3 of which give the $W^{\pm}$ and Z bosons mass, and the 4th creates the Higgs boson. Due to its large expected mass, the Higgs boson has not yet been discovered. Discovering the Higgs boson would prove the Higgs mechanism, solving the problem of massive gauge bosons.

Fortunately, the SM can predict almost exactly what the Higgs should be like; spin, internal quantum numbers, interactions and decays can all be predicted, apart from the Higgs mass. It is possible to constrain the Higgs mass to a particular region based on existing measurements of the $W^{\pm}$, Z, top quark and neutrino scattering. These estimate that the Higgs mass is in the 114–200GeV region, just outside what is achievable today. Hence, the push towards experiments in the TeV region where the Higgs should be easily observable.

However, if other theories that extend the SM are to be believed, there may be multiple Higgs bosons. For example, the Minimal Supersymmetric Model (MSSM) predicts five Higgs bosons, of which the lightest is the Standard Model Higgs. Finding the Higgs boson, and discovering its true nature, provides a strong motivation to move to higher energy accelerators.

It is expected that, if the Higgs boson exists, it will be discovered at the LHC. However, due to the nature of the LHC, experiments will be unable to perform any precision measurements on it. Large numbers of background processes will interfere with measurements regarding the coupling of the Higgs to the quarks, making measurements of its quantum numbers difficult. The ILC, on the other hand, is a much cleaner device, though lower in energy. This would make precision measurements of the Higgs boson much easier. Hence, the ILC is a perfect complement to the LHC, providing all the necessary measurements needed to confirm the properties of the Higgs.

1.1.2 Supersymmetry (SUSY)

Supersymmetry, or SUSY, offers a solution to other weaknesses in the Standard Model. For example:

- *The Hierarchy problem.* This describes the huge differences in energy scale between the Planck scale (at 10^{19}GeV, where gravity and other interactions become equivalent in strength) and the electroweak scale (at a few hundred GeV).
- *The Naturalness problem.* Contributions from the heavy quarks cause corrections to the Higgs mass (through fermion loops). These corrections are proportional to Λ^2/m_f^2, where Λ is associated with the Planck scale, and m_f is the mass of the fermion. Thus, the Higgs mass diverges quadratically with respect to Λ. For the Higgs to remain light, another term similar in magnitude to Λ must be introduced with the Higgs mass arising from the difference between them. This is considered an unnatural tuning of the model.
- *Unification of the forces.* Grand Unified Theories (GUTs) attempt to unify the strong, electromagnetic and weak forces, predicting that they meet at 10^{16}GeV. However, extrapolating to this scale using the SM does not support the unification of the forces. Although the forces appear to converge at first glance, in fact they narrowly miss.

Supersymmetry predicts that there exists a whole new range of particles in the TeV region. These SUSY particles are, in effect, counterparts to existing SM particles with the same properties but different spins. For example, a SM fermion has a SUSY boson partner, and vice versa. These new, massive particles of opposite spin help to solve the Naturalness and Hierarchy problems.

By extending the SM with SUSY, it is possible to ensure that the forces unify, as expected by GUTs, at high energy. Certain SUSY models also provide stable, neutral particles that are ideal dark matter candidates. It also, as previously mentioned, has the side effect of introducing multiple Higgs bosons. However, there are many different SUSY models — the most favoured is known as the Minimal Supersymmetric Model, or MSSM — and it is essential that any TeV experiments can distinguish between the models to see which fits reality. Although SUSY should definitely be visible at the LHC, it lacks the sensitivity needed to pin down the correct model. The ILC, however, is perfectly suited to this task.

1.1.3 Extra Dimensions and Other Alternative Solutions

Another potential solution to the Hierarchy problem is the existence of extra dimensions.Extra dimensional theories, such as String Theory, give rise to the possibility of unifying the Standard Model and gravity by considering all particles and forces as vibrating strings. These theories predict different patterns of phenomena at the TeV scale. If this were the case, a precision accelerator such as the ILC would be able to distinguish between these patterns, and thus determine what manner of extra dimensions exists.

In the case that no Higgs is found, and SUSY is not apparent at the LHC, even more exciting work can be carried out by the LHC and ILC in tandem. If current theories are not satisfactory, there still must be something found in the TeV region that explains the weaknesses of the Standard Model. In this case, it is even more important to couple the high yield of the LHC with the precision measurements offered by the ILC to discover any exciting new physical phenomena in this region.

1.2 The International Linear Collider (ILC)

Historically, as experiments have been performed at greater and greater energy, the trend has been to abandon linear colliders in favour of circular machines. This trend is rooted in the fact it takes an ever increasing distance to accelerate particles to high energy linearly, compared to sending them repeatedly around the same ring of accelerating structures. However, bending charged particles around a ring causes them to emit synchrotron radiation. The power, P, emitted by a relativistic charged particle depends upon the relativistic factor, γ, and the radius of curvature, r,

$$\begin{aligned} P &\propto \frac{\gamma^4}{r} \\ &\propto \left(\frac{E}{m}\right)^4 \frac{1}{r}, \end{aligned}$$

where E is the particle energy and m its mass. This results in a loss of energy, which needs to be replaced by the accelerator.

In the past, this effect has been compensated for by building circular accelerators of increasing radius. Even so, for light particles, such as electrons, circular machines have reached the limits of financial feasibility with energy losses from synchrotron radiation becoming unreasonably large and limiting the achievable energy for experiments. This has fueled the return to linear accelerators as a means of obtaining the ultra-high energies required by future experiments.

It is for these reasons that two new accelerators are being built to aid the expansion of physics into the TeV regime. The Large Hadron Collider (LHC) is a 14TeV centre-of-mass energy, circular pp collider, and the International Linear Collider is a proposed 500GeV e^+e^- linear accelerator, which can be upgraded to 1TeV. Since protons are more massive than electrons, they are not as affected by synchrotron radiation losses, and so it is possible to achieve a much higher energy with them in a circular accelerator. Regardless, since protons are not point particles, collisions between them are not as clean as between electrons. The ILC is, therefore, the perfect partner to the LHC. Although it is of lower energy, colliding point particles will give a much higher precision than that obtainable at the LHC. Thus, the goals of future experiments in the TeV regime can be summarised by the LHC being the vehicle of discovery of new phenomena, and the ILC the precision instrument needed to fully understand them.

1.2.1 Baseline Configuration of the ILC

The baseline configuration covers the basic parameters and layout of the proposed accelerator, such that it can achieve its main physics goals:

- A (variable) centre of mass energy (E_{cm}) of 200 — 500GeV, scalable to 1TeV.
- A peak luminosity (see Section 1.3.1) of $\sim 2 \times 10^{34}\text{cm}^{-2}\text{s}^{-1}$ at 500GeV, and an integrated luminosity of 500fb^{-1} over the first four years of running.
- A minimum of 80% electron polarisation at the interaction point.
- The possibility of 60% positron polarisation.
- The possibility to carry out e^-e^- and $\gamma\gamma$ collisions.
- Energy stability and precision $\leq 0.1\%$.

The basic design parameters for the 500GeV baseline configuration are given in Table 1.1. With parameters such as these the ILC would, for example, be capable of producing large numbers of $t\bar{t}$ pairs, allowing probing of top-quark physics with extremely high precision. Additionally, the proposed energy scale covers the whole region of predicted (SM) Higgs boson masses. A full description of the ILC and its implications for high energy physics can be found in [27].

1.2.1.1 Layout

Figure 1.1 shows an overview of the layout of the current design for $E_{cm} = 500$GeV. This

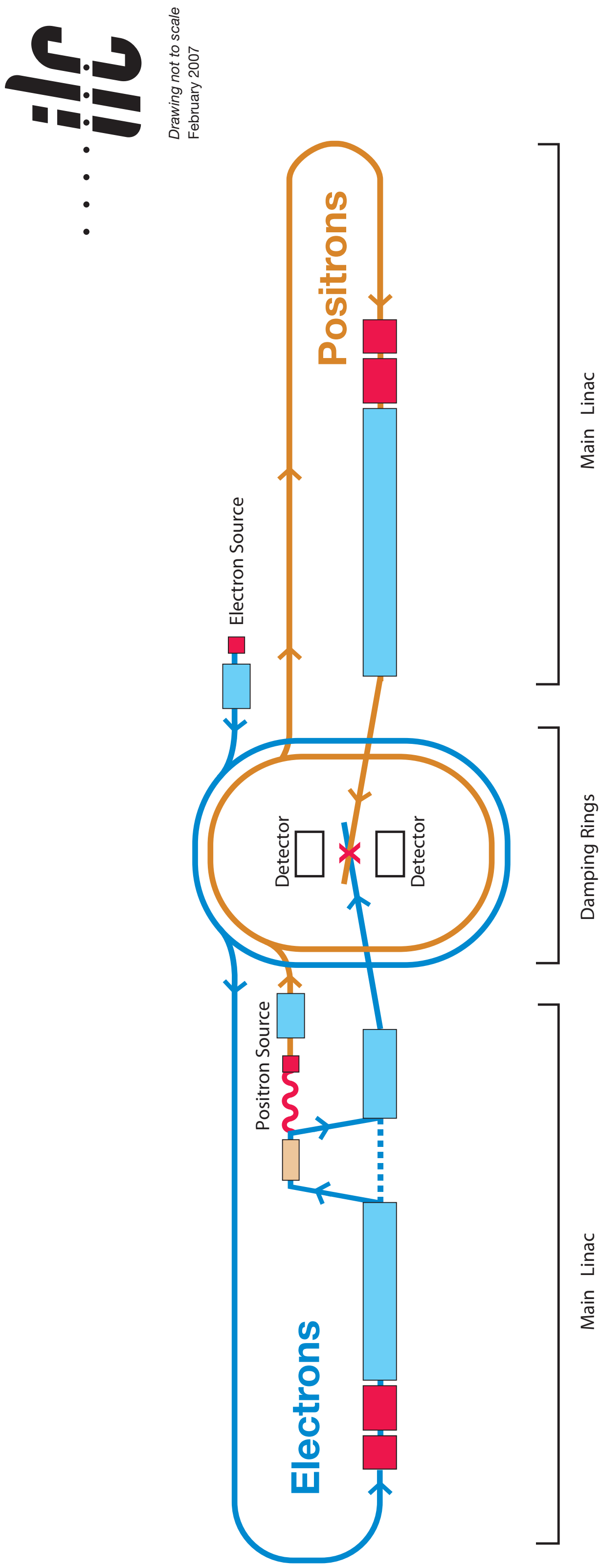

Figure 1.1: Layout of the ILC for 500GeV centre-of-mass energy [28].

Parameter		Unit
Centre-of-mass energy	$200 - 500$	GeV
Peak luminosity	2×10^{34}	$\mathrm{cm}^{-2}\ \mathrm{s}^{-1}$
Average beam current in pulse	9.0	mA
Pulse rate	5.0	Hz
Pulse length (beam)	~ 1	ms
Number of bunches per pulse	$1000 - 5400$	
Bunch charge	$1.6 - 3.2$	nC
Accelerating gradient	31.5	MV/m
RF pulse length	1.6	ms
Beam power (per beam)	10.8	MW
Typical beam size at interaction point	640×5.7	nm
Total AC power consumption	230	MW

Table 1.1: The basic design parameters for the ILC with a centre of mass energy of 500GeV [27].

consists of a polarised electron source, an undulator-based positron source, damping rings, and two 11km main linacs that use superconducting RF cavities to provide a 31.5MV/m accelerating gradient. With the addition of the 4.5km beam delivery line, the ILC has a total length of 31km that can be expanded so as to increase the centre-of-mass energy to 1TeV.

1.2.1.2 Beam Parameters

The parameters set out in Table 1.1 were chosen as a compromise between known accelerator physics challenges and technological limitations (*e.g.*beam current, power, and pulse length limitations in the main linacs). Commonly, high-energy physics accelerators have problems reaching their design luminosity (discussed in Section 1.3.1). To combat this, the design of the ILC requires that each subsystem supports a range of beam parameters so that problems in one area can be compensated for by another. In this way, it is expected that it will be possible to achieve the desired luminosity of $2 \times 10^{34}\mathrm{cm}^{-2}\mathrm{s}^{-1}$. The nominal beam parameters at the interaction point are given in Table 1.2.

1.2.1.3 Beam Delivery System

The Beam Delivery System (or BDS) is used to transport the e^+e^- beams after acceleration to the interaction point, focusing them to the size required by the ILC to meet its luminosity goal. The BDS is also responsible for transporting the beams to the beam dumps after collisions. It must also:

- Focus and steer the beam, matching it into the final focus.
- Protect the beamline and detectors from mis-steered beams.

	Nominal	Supported Range	Unit
Bunch population	2	1 – 2	x10^{10}
Number of bunches	2625	1260 – 5340	
Linac bunch interval	369	180 – 500	ns
RMS bunch length	300	200 – 500	μm
Normalised horizontal emittance	10	10 – 12	mm.mrad
Normalised vertical emittance	0.04	0.02 – 0.08	mm.mrad
Horizontal β function	20	10 – 20	mm
Vertical β function	0.4	0.2 – 0.6	mm
RMS horizontal beam size	640	474 – 640	nm
RMS vertical beam size	5.7	3.5 – 9.9	nm
Vertical disruption parameter	19.4	14 – 26.1	
Fractional RMS energy loss to beamstrahlung	2.4	1.7 – 5.5	%

Table 1.2: Nominal beam parameters at the interaction point of the ILC. [27]

- Remove the beam halo, minimising background in the detectors.
- Measure key beam parameters before and after collisions.

The current design of the ILC has one interaction point with two beams crossing at an angle of 14mrad.

The BDS must be kept stable in order to produce the required luminosity. In the case of the ILC beam with its vertical RMS size of 5.7nm at the interaction point, offsets of even 1nm can reduce the luminosity noticeably. The beam-beam interactions at the interaction point are extremely strong for the ILC parameters, making the luminosity very sensitive to a number of parameters, including variations in the longitudinal shape of the bunch. These are discussed in further detail in the following section.

1.3 Summary of Beam-Beam Effects

The main driving force behind the need for high quality beam diagnostics is the high design luminosity, which in turn is affected by beam-beam effects. These are briefly described in the following sections, with particular emphasis on the processes that are dependent on the longitudinal profile of the bunch. The reader is directed towards [53, 88] for a more complete discussion.

1.3.1 Luminosity

Luminosity is a measure of the rate of collisions. Thus, the higher the luminosity an accelerator can achieve, the higher the number of collisions observed. This increases the likelihood of observing new phenomena.

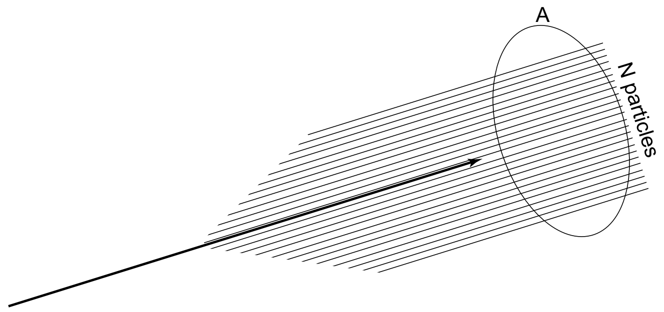

Figure 1.2: A particle in a bunch encounters a colliding bunch of N particles with area A.

For example, consider one particle in a bunch, which sees the oncoming colliding bunch as a cloud of N particles of area A (Figure 1.2). The probability of a physics process of cross section σ occurring is then,

$$\begin{aligned} P &= \frac{N}{A}\sigma \\ &= l\sigma, \end{aligned}$$

where $l = N/A$ is a simplistic measure of luminosity, depending only on the colliding beam's parameters. However, in practice there are many particles in each bunch. In this case, the luminosity (in a head-on collision) is given by [53],

$$\begin{aligned} \mathcal{L} &= \frac{N_1 N_2 f}{A} \\ &= \frac{N_1 N_2 f H_D}{4\pi\sigma_x\sigma_y}, \end{aligned} \tag{1.1}$$

where $N_{1(2)}$ is the number of particles in each bunch, f is the frequency at which bunches collide, $\sigma_{x,y}$ are the transverse dimensions of the beam, and H_D is the luminosity enhancement factor. For round beams H_D is given by [88]

$$H_D = 1 + \frac{2D}{3\sqrt{\pi}}, \tag{1.2}$$

where D is the disruption parameter (see Section 1.3.2), which is a function of σ_z, the longitudinal bunch size. H_D represents the attraction between the Coulomb forces of the opposing bunches, which leads to an increase, or enhancement, in luminosity.

For the case of accelerators with a crossing angle ϕ_c (as is the case for the ILC) Equation 1.1 must be modified. To do this a parameter, $A_{x(y)} = \sigma_z/\beta^*_{x(y)}$, is introduced, where β^* is the beta function at the collision point. The luminosity is then modified as [88]

$$\mathcal{L} = \frac{N_1 N_2 f H_D}{4\pi\sigma_x\sigma_y}\eta\left(\phi_c, A\right), \tag{1.3}$$

where η, in terms of the modified Bessel function K_0, is given by

$$\eta \quad = \quad \frac{1}{\sqrt{\pi}A_{x(y)}}\exp\left[-\frac{1+c_\phi^2/4}{2A_{x(y)}^2}\right]K_0\left(\frac{1+c_\phi^2/4}{2A_{x(y)}^2}\right)$$

and

$$c_\phi = \frac{\phi_c}{\sigma_x/\sigma_z}. \tag{1.4}$$

Thus, the longitudinal bunch length plays an additional role regarding the luminosity in colliders with a crossing angle, ϕ_c.

1.3.2 The Disruption Parameter

Two opposing bunches of oppositely charged particles exhibit attractive Coulomb fields towards each other. The disruption parameter is a measure of this effect. If the focusing effect is considered in terms of that achievable by a thin lens of focal length f, then the disruption parameter is the ratio of the rms bunch length to the focal length, *i.e.*

$$D \quad \sim \quad \frac{\sigma_z}{f}. \tag{1.5}$$

In either the x or y direction, this is [88]

$$D_{x(y)} \equiv \frac{2Nr_e}{\gamma}\frac{\sigma_z}{\sigma_{x(y)}\left(\sigma_x+\sigma_y\right)}, \tag{1.6}$$

where γ is the relativistic factor and r_e is the classical electron radius. Additionally, the ratio of horizontal to vertical beam size, R, is the inverse of the ratio of the disruption parameters [88],

$$R = \frac{\sigma_x}{\sigma_y} = \frac{D_y}{D_x}.$$

This is one of the most important parameters when attempting to characterise the various beam-beam effects that can arise in linear colliders.

1.3.3 The Kink Instability

Deflection can occur during collisions, and the displacement of the bunches can grow with time causing a loss of luminosity. This is known as the kink instability, and all equations describing it in this section follow [88].

Consider a bunch as a sheet of charged particles that are uniform in x and z, but Gaussian in y. For small y, a particle's motion can be approximated by

$$\frac{d^2 y_1}{dt^2} = -\omega_0^2 \left(y_1 - y_2\right),$$

where y_1 and y_2 represent the position of a particle in each bunch and

$$\omega_0^2 = \frac{\sqrt{2\pi}}{6} \frac{D_y}{\sigma_z^2}.$$

The solution to this equation of motion leads to a dispersion relation,

$$\omega^2 = k^2 + \omega_0^2 \pm \sqrt{4\omega_0^2 k^2 + \omega_0^4},$$

which has an unstable solution if $|k| < \sqrt{2}\omega_0$.

The growth rate of this instability contains an exponential function of the disruption parameter. An exponential increase may seem detrimental, but it can also be beneficial since the initial stage of the instability helps to bring the beam centres closer together, giving a luminosity boost.

1.3.4 Disruption Angle

The outgoing, or deflected, angle of a (full energy) particle in a bunch can be characterised by the disruption angle, θ_0, [88]

$$\theta_0 \equiv \frac{2Nr_e}{\gamma\left(\sigma_x + \sigma_y\right)} = \frac{D_x \sigma_x}{\sigma_z} = \frac{D_y \sigma_y}{\sigma_z}. \tag{1.7}$$

This depends upon the disruption parameter and the bunch length. When the disruption parameters are large, the outgoing angle is much larger than the initial angle of the pre-collision particles. In turn, this determines the aperture size of the final quadrupole magnets, so that collided, or 'waste', bunches do not hit the magnet and cause unwanted e^+e^- pair-produced backgrounds.

1.3.5 Centre-of-Mass Deflection and the Multibunch Crossing Instability

Centre-of-mass deflection is a useful tool for observing beam position. It occurs if the bunches are transversely deflected before colliding. In this case, the centre-of-mass of the bunches is deflected by the beam-beam force. The deflection angle, $\Theta_{x,y}$, is used to monitor beam position and is given by [88],

$$\Theta_{x,y} = \frac{1}{2}\theta_0 F\left(\frac{\Delta_{x,y}}{\sigma_{x,y}}\right), \tag{1.8}$$

where θ_0 is the disruption angle, and $\Delta_{x,y}$ is the initial deflection of the centre-of-mass of the bunch.

This effect is more serious when a pulse consisting of several bunches encounters waste bunches prior to their own collision. For example, in the case of a flat beam with a horizontal crossing angle, the second electron bunch before the main collision point will be attracted by the first positron bunch a distance after its collision. This causes the electron bunch to arrive at the collision point with a horizontal displacement. Its opposing positron bunch also undergoes a similar effect and the end result is that the collision takes place at a slightly displaced collision point. However, this is not guaranteed to be the case if there have been any vertical displacement errors upstream of the collision point. Errors such as these can cause the kicks given to incoming bunches to not cancel. In this sense, the effect shares similarities with the kink instability on a smaller scale.

1.3.6 Crossing Angle

The ILC will use a 14mrad crossing angle at the collision point. An angle such as this is thought to be beneficial since it means that used, collided beams will not hit the final quadrupole magnet of the opposing beam and thus not create background radiation. If the crossing angle is made large enough, the used beam will pass outside the magnet.

A crossing angle also introduces an ‘effective’ disruption parameter, since there is an effective reduction in the bunch size. Using c_ϕ from Equation 1.4 this is [88]

$$\begin{aligned} \sigma_{x,y,\mathrm{eff}} &= \sigma_{x,y}\sqrt{1+c_\phi^2/4}, \\ \sigma_{z,\mathrm{eff}} &= \frac{\sigma_z}{\sqrt{1+c_\phi^2/4}}, \\ D_{x,y,\mathrm{eff}} &= \frac{D_{x,y}}{1+c_\phi^2/4}, \end{aligned} \tag{1.9}$$

which in turn leads to a slight decrease in the luminosity enhancement factor, H_D.

1.3.7 Beamstrahlung

Beamstrahlung is a type of synchrotron radiation that is created as the result of the high beam-beam fields associated with multi-GeV colliders. The radiated photons carry energy away from the beam, making beamstrahlung a big contributor to energy losses in high energy colliders. It also provides the dominant source of photons that contribute to pair created backgrounds.

In a head-on collision particles in the centre of the bunch do not feel the beam-beam force, however, they do in the case of collisions with non-zero crossing angle. This would increase beamstrahlung in round beams. For flat beams the average energy lost, δ_E, by beamstrahlung is proportional to [5]

$$\delta_E \propto \frac{1}{\sigma_z \sigma_x^2}.$$

This decouples the energy lost via beamstrahlung from σ_y, negating an increase in beamstrahlung introduced by the crossing angle. In this sense, colliding flat beams is the most practical course of action for linear accelerators.

1.3.8 Flat vs. Round Beams

It may seem more natural to collide round beams in an accelerator, and at first glance round beams would appear to have the advantage with regards to higher luminosity. However, flat beams have some clear advantages:

- Flat beams minimise beamstrahlung losses for collisions at non-zero crossing angles (see Section 1.3.6). This means that the aperture of the final focusing quadrupoles can be smaller, and hence a larger field gradient and stronger focusing can be obtained.
- Using conventional quadrupoles it is easier to focus in one direction when the other is not as important. Stronger focusing can be obtained in this way over attempting to focus symmetrically.
- Damping rings naturally produce asymmetric ($i.e. \sigma_x \neq \sigma_y$) bunches.

Overall, when considering flat beams for the case of a linear collider, there is a net gain in luminosity over that achievable by round beams.

1.4 The Longitudinal Bunch Profile

Beam diagnostics are an essential part of any accelerator system and all accelerator systems have developed the diagnostics that are appropriate to their particular circumstances. However, the beam conditions of the ILC will be vastly more demanding than any previous e^+e^- accelerator, and as such new diagnostic techniques must be developed. In order to reach the desired luminosity goals the beam sizes involved are much smaller and tolerances on measurements of them are also stricter. Due to the high energy of the beams it is preferable to use non-invasive, bunch-by-bunch diagnostics to avoid beam degradation and unnecessary damage to the measuring device.

The longitudinal profile is particularly important in the context of the ILC. By knowing the time profile of the bunch it is possible to quantify and, possibly, counteract the strong beam-beam forces set up at the collision point (as discussed in Section 1.3). A measurement of the longitudinal (time) profile of a bunch determines the distribution of the charges in time compared to a reference particle; for example, it is sometimes assumed that the longitudinal profile might be Gaussian in shape. In addition, such a measurement will also determine the bunch length. The strict definition of bunch length is, in general, a difficult problem. Henceforth, in this thesis, the longitudinal size of the bunch is characterised by its FWHM. However, this may not be appropriate for more complex bunch shapes, *e.g.* those with trailing structure. Hence, the overall *approximate* length of the bunch is used, where appropriate, in this thesis along with the FWHM.

Furthermore, the longitudinal profile plays a part in the commissioning and continual monitoring of components, for example, bunch train compression in the damping rings. Without a bunch length diagnostic, it would be impossible to know whether this section of the accelerator was working effectively and compressing the bunches by the desired amount. However, by involving a longitudinal diagnostic at this point the component can be tuned to reach its optimum parameters. Thus, knowledge of the longitudinal profile is also an essential part of the day-to-day operation of the ILC.

Traditionally, bunch profile monitors have used invasive techniques, whereby the bunch is intercepted or modified in some way (for example, inserting a screen or wire). This would have undesirable consequences — such as the destruction of targets upon collision with high energy bunches — in a linear collider like the ILC, and consequently a noninvasive monitoring method is preferable. Longitudinal bunch profile measurements (using a streak camera) are already being carried out at CLIC [80] as part of the research and commissioning process for the bunch compressor development.

1.4.1 Existing Techniques and Requirements

The ILC has stringent requirements on its longitudinal bunch profile diagnostics. Firstly, since it is a linear machine, each bunch moving down the main linac will only pass each diagnostic once. Thus a diagnostic should be fast enough to respond so as to pick up any changes in the bunch (or bunch train). Secondly, diagnostics should be *non-invasive*, meaning that the beam should not be disrupted or altered in any way by the diagnostic device. These two conditions are made more important by the fact that changes can occur on a bunch-by-bunch basis, so analysing a single bunch destructively, or averaging over a number of bunches, may not be satisfactory.

These requirements rule out several existing techniques for determining the longitudinal profile of a bunch, since, for example, they would not be capable of resolving the proposed ILC bunch length. Techniques that fall into this category include pick-ups and Resistive Wall Current Monitors, which cannot distinguish bunch lengths less than several hundred ps at best. Other methods, such as streak cameras, are still in use [80], with modifications ensuring they are still relevant to the short bunches future experiments aim to achieve. Even so, these could not determine both bunch length and profile.

The streak camera, particularly the *femtosecond streak camera*, has already been mentioned. This has the advantage of being able to directly measure the bunch distribution in the time domain, compared to many alternatives that measure in the frequency domain of coherent radiation emitted by the bunch. By directing Cherenkov radiation emitted by the electrons in the bunch onto the streak camera (which is itself an invasive process), it is possible to obtain a bunch length resolution of about 200fs. However, this is only a bunch length measurement, not a profile measurement.

1.4.2 Developing Techniques

An assortment of new and old approaches are being developed specifically for the detection of ps (or shorter) bunches. They can be categorised as laser based, direct bunch measurement and radiative techniques.

Laser based methods rely upon sampling the bunch with a laser. They are being developed to diagnose both the transverse and longitudinal profile of the bunch.

One of the more promising laser based longitudinal profile diagnostic methods is the *Electro-Optic*(EO) technique as demonstrated by Jamison *et al*[31]. This technique measures the Coulomb field of the bunch directly. Monitoring the change in refractive index of an EO material (*e.g.*a ZnTe crystal) with a linearly polarised laser as it is exposed to the Coulomb field of the passing bunch determines the bunch profile. The emerging laser pulse is elliptically polarised, which is converted into an intensity modulation. In one EO detection regime, the change in intensity is proportional to the Coulomb field, in another it is proportional to the square of the field.

This technique in non-invasive — an essential feature of any potential ILC diagnostic — and can measure bunches down to 50fs in length. However, the simplest form of the EO technique requires the bunch to be sampled repeatedly in order to build up a profile. A more complex EO method exists, known as spatial encoding, which is capable of a single-shot measurement. This, however, has the drawback of having more stringent tolerances on the materials used. A further EO approach called temporal decoding offers another solution, whereby it resolves the intensity modulation of the laser pulse differently. Neither spatial nor temporal decoding manage to approach the multi-sampling method with regards to time resolution; however, the existence of so many different methods within one field of diagnostics shows its robustness as a diagnostic tool.

The cost involved in setting up many EO diagnostics throughout the accelerator complex is one of its main obstacles. Thus, a combination of using EO diagnostics at key points, where the longitudinal profile must be known with greatest accuracy, and other alternative (and cheaper) diagnostic tools throughout the remainder of the accelerator may be a sensible approach.

Direct bunch measurements rely upon flipping (or 'streaking') the bunch itself so that the longitudinal profile is converted into something more easily measured, for example, the transverse profile or energy spread. These methods are destructive, however, since each streaked bunch used in the diagnostic is destroyed. Even so, they are very useful when commissioning components, or investigating specific problems during accelerator development periods, as they are both versatile and sensitive. The most well-known direct bunch technique is the *Transverse Deflection Cavity*, or LOLA [17], where a transverse kick is applied to the bunch, directing it onto a scintillating screen. LOLA is described in further detail in Section 9.6, where it has been used as an independent measurement of the SLAC bunch length.

1.5 Radiative Processes as Diagnostic Tools

Radiative processes are one of three main approaches to longitudinal bunch profile diagnostics and include a wide variety of techniques. Coherent transition, diffraction, Smith-Purcell, synchrotron and Cherenkov radiation, for example, all belong to the radiative process group. Radiative techniques such as these rely upon causing the Coulomb field of the bunch to radiate in a specific way and then interpreting the wavelength distribution of the resulting radiation to infer the longitudinal bunch profile. These diagnostics tend to place a radiation-causing structure close to the beam as the Coulomb field strength drops rapidly with distance from the beam. Hence, some radiative processes are destructive, whilst others are not.

A common feature of radiative processes is that they do not provide any phase information and a straightforward transformation back to the longitudinal profile is not possible. A number of methods can be used, either to find the nearest symmetric bunch, or to attempt to recover the minimal phase information using a Kramers-Krönig analysis (see Chapter 3).

The most well known and widely used radiative phenomena in bunch diagnostics are Coherent Transition Radiation (CTR) and Coherent Diffraction Radiation (CDR). Note that coherence is not a phenomenon exclusive to transition and diffraction radiation, but to all radiative processes. It occurs whenever the emitted wavelengths are longer than the bunch length,giving a significant enhancement to the radiated intensity (see Section 2.3).

1.5.1 Transition and Diffraction Radiation

Transition radiation was first predicted by Frank and Ginzburg in 1945 [18], and was first exploited for beam diagnostics by Wartski [78]. It was considered a very attractive form of beam diagnostics due to the availability of inexpensive position sensitive detectors.

When a charged particle crosses a boundary between two media of different dielectric constants, it emits transition radiatio$n$. This radiation is emitted in two 'cones' in the forward and backward directions, with an opening angle of γ^{-1}. The total intensity emitted by a particle is proportional to the particle's energy (or γ) and the plasma frequency of the material used to cause the transition radiation. Usually a thin sheet of aluminium foil is inserted into the beam at about 45°, but it has also been created using silicon targets or mylar foils. Obviously, since it requires interrupting the beam with a foil, transition radiation is an invasive measurement. If the particles instead pass through an aperture in the foil, the technique is non-invasive and results in diffraction radiation instead. Therefore transition radiation can be considered a limiting case of diffraction radiation, when the aperture becomes vanishingly small.

Coherent optical transition (or diffraction) radiation is most often used for revealing information about the transverse bunch profile, whilst coherent far infrared radiation has been used to reveal the longitudinal profile. Optical transition radiation is particularly suitable for beam diagnostics since it is easy to detect it using CCD cameras, giving a very visual view of the beam size and shape. However, in other regions detection is non-trivial. Performing a bunch length measurement with CTR or CDR relies specifically on the coherence of the emitted radiation, allowing the diagnostic to profit from auto-correlation techniques.

Once the radiation has been extracted from the beamline, auto-correlation techniques (such as using a Michelson Interferometer to measure power as a function of optical pathlength) can be used to derive the longitudinal profile of the bunch.

There is no theoretical limit to the resolution of diagnostics using either transition or diffraction radiation other than the problems associated with detecting far-infrared radiation. Experiments have been carried out using both CTR and CDR down to approximately 200fs [77]. However, a thorough optical alignment of the system must be carried out beforehand to reach these resolutions.

1.5.2 Smith-Purcell Radiation as a Diagnostic Tool

Smith-Purcell (SP) radiation belongs to the same group of processes as transition and diffraction radiation, and like diffraction radiation, it is also non-invasive.It was first observed by Smith and Purcell in 1953 [63], and has gained significant attention as a possible method of obtaining the longitudinal bunch profile. It has also been suggested as a possible source of tunable radiation in the far-infrared part of the spectrum [72]. The basic features of SP radiation and its theoretical formulation are discussed in more detail in Chapter 2.

1.6 Summary

To summarise, this chapter first discussed the move to higher energy experiments requiring new developments in accelerator design, culminating in the LHC and ILC. Following this, a description of the current baseline configuration for the ILC was given and the experimental motivation was stated. The need for new beam diagnostics as an essential part of the ILC was then discussed, with particular attention paid to the longitudinal bunch profile. An outline of the methods of performing longitudinal bunch profile diagnostics was then presented.

Chapter 2

Smith-Purcell Radiation

Smith-Purcell, or SP, radiation is the radiation produced when a charged particle passes close to the surface of a metallic, periodic structure. There are a number of different theories describing the origin of Smith-Purcell radiation, which are discussed in more detail in this chapter.

2.1 Generation of Smith-Purcell Radiation

When a charged particle passes above a metallic, periodic, structure such as an aluminium grating (see Figure 2.1), it emits radiation known as Smith-Purcell radiation. This is characterised by a wide range of wavelengths emitted over a large angular spread. The wavelengths are not emitted in a narrow cone (as in CTR); instead they are dispersed according to observation angle. Thus, observing at one angle with respect to the beam reveals a different wavelength to that seen at another observation angle. In fact, for an observer at infinity, the emitted radiation

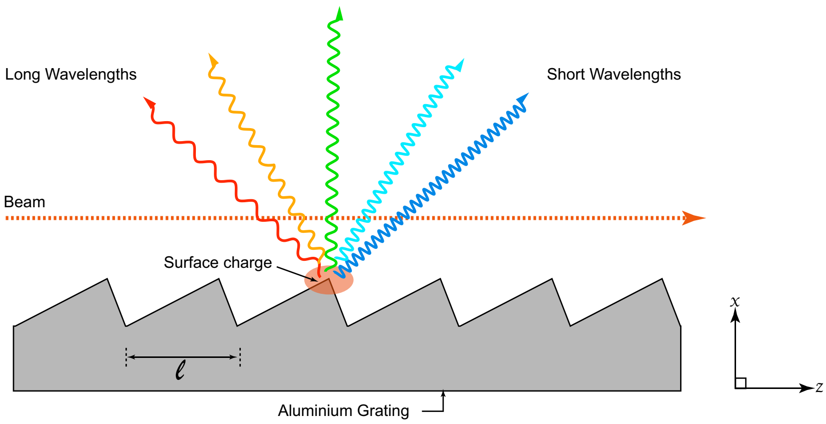

Figure 2.1: Generating Smith-Purcell radiation with a periodic, metallic grating.

satisfies the following condition:

$$\lambda = \frac{l}{n}\left(\frac{1}{\beta} - \cos\theta\right), \tag{2.1}$$

where l is the period of the grating, n is the order of radiation, θ is the angle of observation in the x - z plane according to Figure 2.1, and $\beta = v/c$ is the relativistic velocity of the particle. Since this thesis deals with highly relativistic beams it is assumed that $\beta \simeq 1$.

According the Equation 2.1, the grating period defines the wavelength region covered by SP radiation. As an example, a grating with a period of 1mm will generate far infrared radiation (up to 2mm), whereas a grating with a much shorter period of, say, $\sim$ 700nm will emit in the visible region. Thus an appropriate wavelength region is readily available depending on the desired application. Equation 2.1 also shows that at a given observation angle, higher spectral orders of radiation are also present ($n \neq 1$). Primarily, radiation is emitted in the first order ($n = 1$) but shorter wavelengths can be seen from higher orders if appropriate filtering is applied.

2.2 Theoretical Description

There are several different theoretical descriptions of the physical process that gives rise to Smith-Purcell radiation. The first approach is that suggested by Smith and Purcell after discovering the effect, whereby the radiation is caused by the periodic motion of an induced charge on the surface of the grating, caused by the passage of the electron beam. A related view considered it to be due to the effect of a vibrating electric dipole consisting of the electrons in the beam and their corresponding image charge [29, 60]. In 1960, Toraldo di Francia offered an alternative explanation [69] based on the propagation and excitation of evanescent waves. From this stemmed theories such as those by van den Berg [73, 74] and Haeberlé [22], which in turn have evolved further into the Electric Field Integral Model (EFIE) [33]. The main theories are described here, showing their differences as well as their common ground.

2.2.1 Smith-Purcell Radiation as the Result of Reflected Waves

Toraldo di Francia first introduced the idea that the electromagnetic field of a moving charged particle could be transformed into a set of evanescent waves [69]. These evanescent waves are attenuated in a direction perpendicular to the grating surface and are reflected and refracted in the same way as an ordinary plane wave would be. The (propagating) reflected waves are the SP radiation.

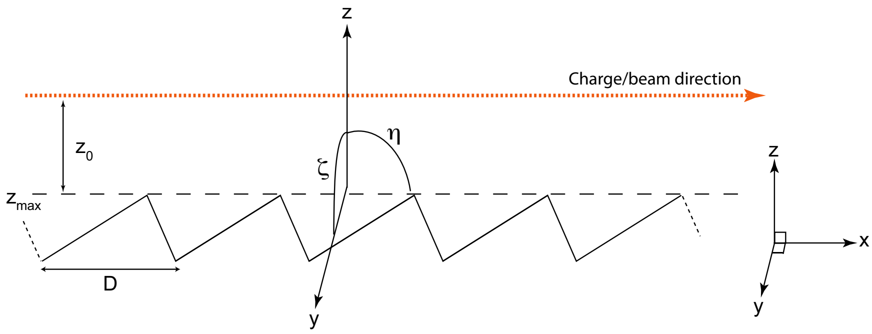

Figure 2.2: Definition of the co-ordinate system used in Section 2.2.1.

The first method used to solve this problem was that of Rayleigh [57], where it is assumed that the discrete set of reflected evanescent and propagating waves are sufficient to describe the total field. However, it is generally accepted that this approach is only a good approximation for gratings with very shallow grooves. Even so, the power (B) per unit solid angle per unit emission surface, as derived by Toraldo di Francia, is [69]

$$B = 2\pi I e \delta_m^2 \frac{m^2}{d^2} \frac{\sin\theta \ \beta^3}{(1-\beta\cos\theta)^3} \exp\left(-4\pi m \frac{a}{d} \frac{\sqrt{1-\beta^2}}{1-\beta\cos\theta}\right), \tag{2.2}$$

where I is the electron current, e is the charge of an electron, δ_m is a number depending on the grating profile, m is the order of emission, d is the grating period, a is the distance between the particle and grating, and θ is the angle of observation.

Van den Berg was the first to consider Smith-Purcell radiation (in two dimensions) arising from gratings of arbitrary profile in a rigorous manner [73, 74]. He considers both a line and point charge moving above an electrically perfectly conducting reflection grating. The grating is periodic in the direction of motion and the charge moves in vacuum. The diffracted SP radiation is then derived by solving Maxwell's equations. The technique used is rather opaque and is most suitable for numerical calculations. For a complete discussion, the reader is directed to [20, 22, 73, 74], from which the equations of this section have been taken.

Gover *et al.*[20] re-worked the van den Berg model and calculated the energy emitted in the η and ζ directions (axes as defined in Figure 2.2). To summarise their results in this case, the energy radiated in a direction (η, ζ) over one grating period, D, is given as [20]

$$
\begin{aligned}
W &= \frac{e^2}{D\varepsilon_0}\sum_n \int_{-\frac{\pi}{2}}^{\frac{\pi}{2}}\int_{-\frac{\pi}{2}}^{\frac{\pi}{2}} \frac{\cos^2\eta\cos^2\zeta}{\left[\frac{1}{\beta}-\sin\eta\right]^3}\left|R_n\left(\eta,\zeta\right)\right|^2 \\
&\quad \times\exp\left[-\frac{z_0-z\mathrm{max}}{h_{\mathrm{int},n}\left(\eta,\zeta\right)}\right]\cos\eta\mathrm{d}\eta\mathrm{d}\zeta
\end{aligned} \tag{2.3}
$$

with

$$
h_{\mathrm{int},n} = \frac{\lambda_n}{4\pi\left(\beta^{-2}-1+\cos^2\eta\sin^2\zeta\right)^{\frac{1}{2}}}. \tag{2.4}
$$

The ‘radiation factor’ $\left|R_n\left(\eta,\zeta\right)\right|^2$ is the classical reflection coefficient of the grating and doesn’t depend upon the distance z_0 between the particle trajectory and the grating surface, whereas $h_{\mathrm{int},n}$ is the ‘effective interaction range’.

In the case of a continuous beam, electrons that pass within $z_0 - z\mathrm{max} < h_{\mathrm{int},n}$ (where $z\mathrm{max}$ is the maximum height of the grating) contribute towards the emitted Smith-Purcell radiation. The total power emitted per unit solid angle is found by multiplying Equation 2.3 by the particle flux density J_0/e (where J_0 is the current density), the beam width b, and the number of grating periods L/D (where L is the grating length), then integrating over z from $z\mathrm{max}$ to ∞.

$$
\begin{aligned}
I_n\left(\eta,\zeta\right) &= \frac{eJ_0bL}{4\pi\varepsilon_0Dn}\left|R_n\left(\eta,\phi\right)\right|^2 \\
&\quad \times\frac{\cos^2\eta\cos^2\zeta}{\left(\beta^{-1}-\sin\eta\right)^2\left(\beta^{-2}-1+\cos^2\eta\sin^2\zeta\right)^{\frac{1}{2}}}
\end{aligned} \tag{2.5}
$$

Haeberlé *et al.* [22] extended van den Berg’s model to high energies (100MeV), providing calculations of the radiation factor R^2 as a function of energy [22]

$$
\begin{aligned}
\left|R_n\left(\beta,\eta,\zeta\right)\right|^2 &= \frac{4}{e^2}\exp\left(2\left|\gamma_0\right|z_0\right)\left\{\frac{\varepsilon_0}{\mu_0}\left|E^r_{y,n}\right|^2+\left|H^r_{y,n}\right|^2\right\} \\
&\quad \times\left(1-\cos^2\eta\sin^2\zeta\right)^{-1},
\end{aligned} \tag{2.6}
$$

where $E^r_{y,n}$ and $H^r_{y,n}$ are the y components of the nth spectral order of the radiated field. Their result indicates a strong decrease in R^2 with increasing energy. This is a crucial point that will be referred to later.

2.2.2 Extension to Finite Grating Lengths (EFIE Model)

Equation 2.5 shows that the emitted energy is proportional to the length of the grating, L. The theory employed by van den Berg (Section 2.2.1) considers only the case of a grating of infinite length. This is not realistically achievable, and so the measured Smith-Purcell output may be different from that predicted by this model. However, there are models that attempt to take the finite length of the grating into account.

The EFIE model was proposed by Kesar *et al.*[33] as a method of calculating Smith-Purcell radiation from a finite length grating, along similar lines to the idea proposed by Toraldo di Francia and refined by van den Berg. It uses a Finite-Difference Time-Domain (FDTD) formula to calculate the diffracted electromagnetic field of a two-dimensional bunch as it passes over a grating, then obtains a frequency-domain Electric-Field Integral Equation (EFIE) model that can describe the emitted radiation.

This model assumes a perfectly conducting metal grating, with zero tangential field component on its edges. It then describes the fields scattered by the grating as [33]

$$E_1(\mathbf{r},\omega) = \frac{q}{2\varepsilon_0\beta c}\exp\left[\left(\frac{k}{\beta\gamma}\right)z - j\left(\frac{k}{\beta}\right)x\right]\left(\frac{j\cos\alpha}{\gamma} - \sin\alpha\right)F(k),$$

where $F(k)$ is the bunch form factor. This affects the couplings of the field to the grating. The EFIE is found by dividing the grating surface into N sections of length Δ_n, and is approximated by N linear equations. The power spectrum is made up of the frequencies seen at observation angles $-\pi/2 < \theta < \pi/2$, [33]

$$P(\theta,\omega) = \left(\frac{\mu_0}{\varepsilon_0}\right)^{\frac{1}{2}} r\left|H_y(r,\theta,\omega)\right|^2, \tag{2.7}$$

where H_y, is the magnetic component of the far field. The angular distribution of radiated energy per groove, per meter of grating is [33]

$$E_{\text{avg}}(\theta) = \frac{1}{N_g\pi}\int_0^\infty P(\omega,\theta)\,d\omega, \tag{2.8}$$

with N_g as the number of grating periods.

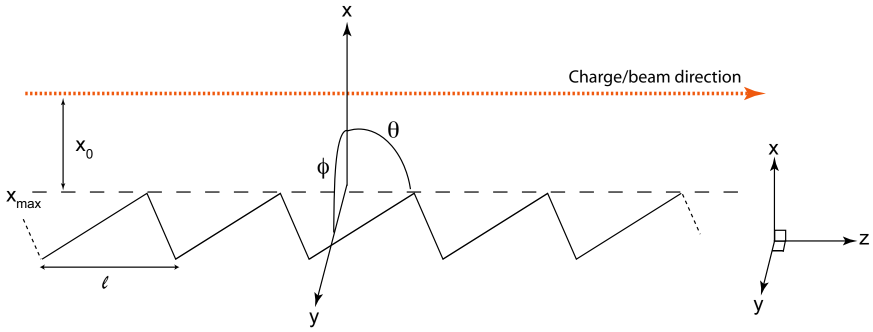

Figure 2.3: Definition of the axis used in Section 2.2.3.

2.2.3 Smith-Purcell Radiation as a Result of Induced Surface Currents

The numerical calculations associated with the van den Berg model can be very time consuming. However, the surface current model [9] provides an excellent alternative approach. A summary of this approach follows, with further details available for the reader in [8, 9, 10, 37, 86].

As before, consider an electron moving at constant velocity v in the z direction at a height x_0 above a metallic grating. The electron induces a surface charge on the grating that is dragged along with the electron. The physical picture now is that the surface charge is accelerated by traversing the grooves in the grating and as a result it emits radiation — Smith-Purcell radiation. The axis convention used here is different to that of Section 2.2.1 and is shown in Figure 2.3 .

According to Equation 14.70 in [30], the energy radiated by a distribution of charge in motion per unit frequency, per unit solid angle is

$$W \equiv \frac{\mathrm{d}^2 I}{\mathrm{d}\omega \mathrm{d}\Omega} = \frac{\omega^2}{4\pi^2 c^3} \left| \int \mathrm{d}t \int \mathrm{d}^3 x \, \hat{\mathbf{n}} \wedge (\hat{\mathbf{n}} \wedge \mathbf{J}(\mathbf{r}, t)) \exp^{i[\omega t - (\mathbf{k} \bullet \mathbf{r})]} \right|^2 \tag{2.9}$$

where $\hat{\mathbf{n}} = \{\hat{\mathbf{x}} \sin\theta \cos\phi + \hat{\mathbf{y}} \sin\theta \sin\phi + \hat{\mathbf{z}} \cos\theta\}$ is the direction radiation is emitted in, ω is the frequency, $\mathbf{k} = \hat{\mathbf{n}}\omega/c$, and $\mathbf{J}$ is the current density induced on the grating surface. Since the grating is periodic, the current density can be expressed as the sum of the currents in each period l over its length L [9].

$$\mathbf{J}(\mathbf{r}, t) = \sum_{m=1}^{L/l} \mathbf{J}_{\mathrm{tooth}} \left(\mathbf{r} - ml\hat{\mathbf{z}}, t - \frac{ml}{v} \right) \tag{2.10}$$

Substituting Equation 2.10 into 2.9, and transforming $\mathbf{r}(x, y, z) - ml\hat{\mathbf{z}} \rightarrow \mathbf{r}(x, y, z)$, $t - ml/v \rightarrow t$ so as to look at a single tooth, [9]

$$\begin{aligned} W &= \frac{\omega^2}{4\pi^2 c^3} \left| \sum_{n=1}^{L/l} \exp\left\{ inl\omega \left(\frac{1}{v} - \frac{\hat{\mathbf{n}} \bullet \hat{\mathbf{z}}}{c} \right) \right\} \right|^2 \\ &\quad \times \left| \int \mathrm{d}t \int \mathrm{d}^3x \, \hat{\mathbf{n}} \wedge \hat{\mathbf{n}} \wedge \mathbf{J}_{tooth}(\mathbf{r}, t) \exp\left\{ i \left(\omega t - \mathbf{k} \bullet \mathbf{r} \right) \right\} \right|^2 \end{aligned} \tag{2.11}$$

The summation over n gives an interference pattern, which for a large number of periods limits the emitted wavelengths to the Smith-Purcell condition (Equation 2.1).

The challenge is to find an expression that describes the surface current itself. Consider one period of the grating made up from two facets (Figure 2.4), where each facet is infinite in y and does not overlap. When a charge passes above at height x_0 with velocity v, a surface charge is induced on the grating surface with density ρ. Thus, the current density over one period, or 'tooth' of the grating, is given by [9]

$$\mathbf{J}_{\text{tooth}}(\mathbf{r}, t) = \sum_{f=1}^{F} \rho(\mathbf{r}, t, s_f) \, \mathbf{v}(\mathbf{r}, t, s_f), \tag{2.12}$$

where s_f represents the facets and F is the total number of facets in one period, *i.e.*two in this case. The total current density over the whole grating is then $\mathbf{J}_{\text{total}} = \sum^{L/l} \mathbf{J}_{\text{tooth}}$, where L/l gives the number of grating periods. The charge density ρ is given by [9]

$$\rho(\mathbf{r}, \mathbf{r}_0, t, s) = -\frac{q\gamma}{2\pi} \frac{\left| (x - x_0)\cos\alpha - (z - z_0 - vt)\sin\alpha \right|}{\left[(x - x_0)^2 + (y - y_0)^2 + \gamma^2 (z - z_0 - vt)^2 \right]^{3/2}} \delta\left[(z - z_1)\sin\alpha - (x - x_1)\cos\alpha \right], \tag{2.13}$$

where q is the charge of the electron, $\mathbf{r}_0 = (x_0, y_0, z_0)$ is its position at $t = 0$, γ is the relativistic factor, and α is the blaze angle of the facet (Figure 2.4).

2.2.3.1 The Single Electron Case

First consider the case of a single relativistic electron, moving with velocity $\mathbf{v} = v\hat{\mathbf{z}} = \hat{\boldsymbol{\beta}}(0, 0, \beta)$. The particle crosses one period of a perfectly conducting grating and induces a charge on the surface. The energy emitted per unit solid angle, $dI/d\Omega$, by one electron is given by [10]

$$\left(\frac{dI}{d\Omega} \right)_1 = 2\pi q^2 \frac{L}{l^2} \frac{n^2 \beta^2}{(1 - \beta\cos\theta)^3} R^2 \exp\left[-\frac{2x_0}{\lambda_e} \right], \tag{2.14}$$

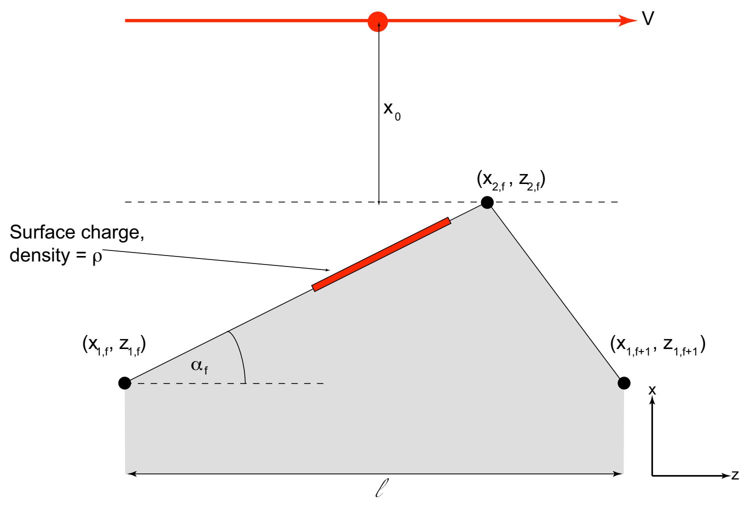

Figure 2.4: Description of the surface current model: A single charged particle crosses one period of a grating, l, at height, x_0, with velocity v.

where λ_e is the evanescent wavelength and R^2 represents the grating efficiency, i.e. the contribution from each period of the grating. R^2 is a complicated parameter that depends upon the blaze angle of the grating, α, and is defined by [10]

$$R^2 = |\mathbf{n} \wedge (\mathbf{n} \wedge \mathbf{G})|^2 ,$$

with $\mathbf{G}$, the vector sum of each facet's contribution, and $\mathbf{n}$, the normal to the grating surface. Thus, R^2 must be determined for each desired grating. Unlike the van den Berg approach, this method cannot be used to determine the Smith-Purcell radiation from an arbitrary grating.

The quantity λ_e in Equation 2.14 is called the evanescent wavelength, and is defined as [10]

$$\lambda_e = \frac{\lambda}{2\pi} \frac{\beta\gamma}{\sqrt{1 + \beta^2\gamma^2 \sin^2\theta \sin^2\phi}} \tag{2.15}$$

and is equivalent to Equation 2.4. The evanescent wavelength plays an important role in the production of SP radiation since it determines the required distance between the beam and the grating to achieve an effective coupling. In the $\phi = 0$ plane, a beam with large γ would appear to imply a large interaction length such that the grating could be several metres (or more) away from the beam and still produce SP radiation. However, as soon as one moves away from this plane, say to $\phi = 5°$, the lower half of Equation 2.15 dominates and the evanescent wavelength becomes much smaller. For a beam energy of $\sim$ 200GeV, as might be initially used at the ILC ($\gamma \sim 391389$), this gives an evanescent wavelength of $\sim$ 3mm with a 1.5mm period grating, observing at $\theta = 90°$ and $\phi = 5°$. As long as the beam is within this distance from the grating, the coupling between beam and grating should be efficient.

2.3 The Multiple Electron Case and Coherence

A bunch of N electrons, each travelling above the grating with velocity $\mathbf{v} = v\hat{\mathbf{z}}$, is treated in exactly the same was as before, except a sum over all electrons is included in Equation 2.12. When $N \gg 1$, the emitted energy is given by [9]

$$\left(\frac{dI}{d\Omega}\right)_N = \left(\frac{dI}{d\Omega}\right)_1\bigg|_{x_0=0} \left[N S_{\text{inc}} + N^2 S_{\text{coh}}\right] \tag{2.16}$$

where $\left(\frac{dI}{d\Omega}\right)_1$ is the contribution from a single electron (Equation 2.14). S_{inc} and S_{coh} are the 'incoherent' and 'coherent' integrals [10]

$$S_{\text{inc}} = \int_0^\infty X(x) \exp\left(-\frac{2(x - x_0)}{\lambda_e}\right) \mathrm{d}x \tag{2.17}$$

and

$$\begin{aligned} S_{\text{coh}} &= \left|\int_0^\infty X \exp\left\{\frac{-(x - x_0)}{\lambda_e}\right\} dx\right|^2 \left|\int_{-\infty}^\infty Y \exp\left\{-ik_y y\right\} dy\right|^2 \\ &\quad \times \left|\int_{-\infty}^\infty T \exp\left\{-i\omega t\right\} dt\right|^2, \end{aligned} \tag{2.18}$$

where X, Y and T are the bunch distributions in x, y and t (or z/v), respectively, *which are assumed to be uncorrelated*, and x_0 is the height of the beam above the grating. For bunch lengths approximately equal to, or smaller than, the emitted wavelength the S_{coh} term dominates and the emitted radiation becomes *coherent*. In the coherent regime, the emission of SP radiation occurs in phase — the radiation emitted by each electron in the bunch adds to the whole. This gives a boost $\propto N^2$ to the total emitted intensity, analogous to coherent transition/diffraction and synchrotron radiation [51].

Equations 2.16 and 2.18 show how the temporal profile of the bunch is 'encoded' in the emitted energy distribution of SP wavelengths when in the coherent regime. The coherent term, S_{coh} includes the Fourier transform of the longitudinal distribution, hence by measuring the emitted energy per solid angle one should be able to retrieve T. However, certain assumptions about the other beam dimensions must first be made, or their properties known. To this end, the bunch distributions in x and y are assumed to be Gaussian. This simplifies the resulting equations and allows the longitudinal profile to be (nominally) extracted.

It is clear from Equation 2.1 that not only does the wavelength vary with observation angle, but it also depends upon the period of the grating used. This offers another benefit to using SP radiation as a diagnostic tool, since the grating used can be 'tuned' to the expected bunch length such that a user can select the *coherent wavelength region*— *i.e.*one where the emitted wavelengths are on the order of the expected bunch length or longer — ensuring coherent radiation is obtained.

Different bunch profiles produce different wavelength distributions (see simulations in Figure 2.5). This shows the differential energy produced by three different bunch profiles of the same length. The solid (black) line arises from a bunch described by a superposition of three Gaussians, the dashed (red) line arises from a simple Gaussian bunch, and the dotted (blue) comes from a bunch with an asymmetric triangular shape. In all cases the differential energy was calculated for a bunch with a FWHM of 2.4ps, assuming $\gamma = 55773$ and $N_e = 1.6 \times 10^{10}$ electrons. Therefore, it is possible to reconstruct the profile by measuring the emitted intensity at each observation angle, *i.e.*wavelength. This reconstruction can be achieved in two ways; by comparison with spectral distributions from known profiles, or by using a Kramers-Krönig analysis to recover minimal phase information. These are discussed in Chapter 3. By detecting radiation simultaneously from multiple observation angles — for example, with an array of detectors — it is entirely possible to use Smith-Purcell radiation as a non-invasive diagnostic tool (with the potential for single-shot operation), without the need for further devices such as spectrometers or interferometers.

2.4 Comparison of Theories

Many Smith-Purcell experiments have been carried out to date and comparisons have been made with several theories since the predicted intensity output varies between them [32]. A definitive description regarding the emitted intensity of radiation has not yet been established, and hence conclusive experimental evidence supporting one approach, or showing a convergence of approaches, is desirable. It must be mentioned, however, that all theories and experimental evidence are in agreement with the fundamental Smith-Purcell equation (Equation 2.1), and are in approximate agreement, as far as radiated intensity is concerned, at low energy (a few MeV).

a)

b)

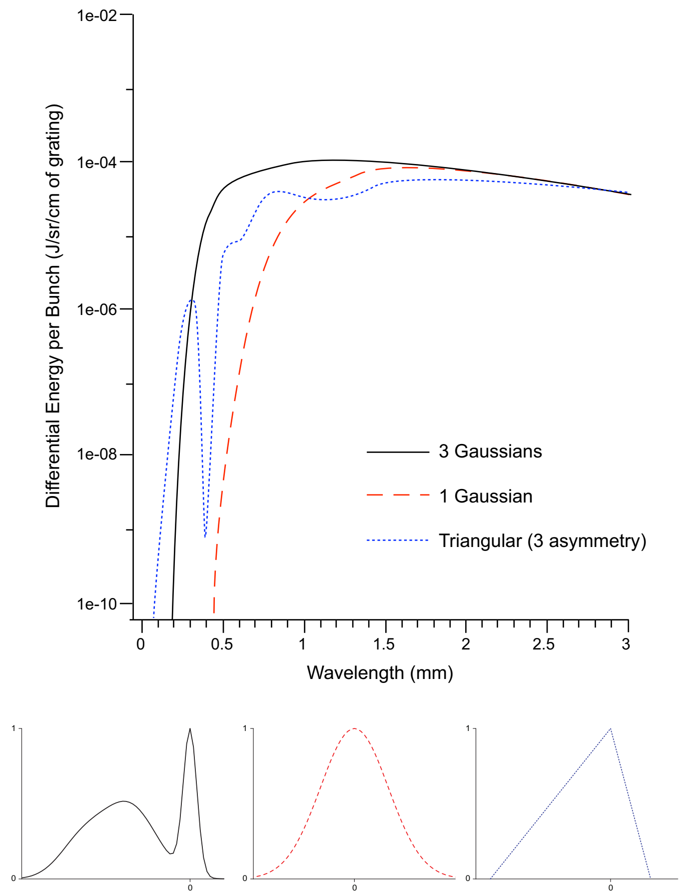

Figure 2.5: a) Simulated wavelength distributions from different bunch profiles; 3 Gaussians (black, solid), a single Gaussian (red, dashed), and an asymmetric triangular shape (blue, dotted). The temporal profiles that gave rise to these distributions are shown in b). See text for further details.

2.4.1 General Comments

Some general comments on the theories discussed here are appropriate. Van den Berg's treatment (Section 2.2.1), for example, may appear advantageous since it can be used to describe an arbitrary grating profile, whereas the surface current model (Section 2.2.3) cannot. However, it is also, by comparison, computationally intensive and as a result is very time consuming.

Contrary to both the surface current and EFIE (Section 2.2.2) approaches, van den Berg's theory also assumes that the grating used is infinitely long. This is obviously unrealistic, and investigations have been carried out comparing the (theoretical) power outputs from a finite and infinite grating using the EFIE model [33]. The results show that the van den Berg model underestimates the power produced from a finite grating by about a factor of 3. The van den Berg model also predicts Woods-Rayleigh anomalies, which are not seen experimentally. Neither EFIE or surface current predict these.

The main deviation between these approaches is in the treatment of R^2, the grating factor. Following the van den Berg approach, Haeberlé *et al.* calculated values of R^2 at relativistic energies ($<$ 100MeV) and found that it depends critically on beam energy. In fact, they predict a strong decrease in R^2 with increasing energy. Thus, the energy output at large beam energy should be small if SP radiation is generated by reflected waves. Contrary to this the surface current model predicts no change in R^2 with increasing energy [10]; instead the energy of emitted SP radiation is expected to increase with increasing beam energy.

2.4.2 Comparisons with Experiment

A wide variety of experiments have been carried out to date in order to test the various Smith-Purcell theories [8, 38, 61, 86]. The majority of the experimental evidence [8, 61, 86] is at relatively low energies and, as such, does not necessarily expose any (theoretical) differences that may occur at higher energy scales. Recent experiments at these lower energies have been in agreement with both surface current and van den Berg's theory.

At higher energies the two theories diverge. Therefore, this is the most interesting region for experiments to be carried out in, since they could potentially verify the correct approach. It is also the region of greatest interest for potential applications.

Prior to the work reported here, the highest energy experiment was that of Kube *et al.* [38], which investigated the SP radiation seen from the 855MeV electron beam of the Mainz Microtron (MAMI). This used a glass (BK7) grating substrate coated with approximately 700nm of aluminium to detect SP radiation in the visible part of the spectrum. The observed SP signal was deemed to be in overall agreement with the van den Berg approach, with the exception of one grating with shallow blaze angle, and the proviso that the deviations seen are due to the theory assuming a perfectly conducting grating surface. The results were also compared to an independently derived surface current model (similar to, but not that described in Section 2.2.3 and [9]), which predicted an intensity a factor of 50 times higher than observed (under the assumption of perfect conductivity). The results of this experiment would, at first glance, seem to support the van den Berg approach.

In order to observe SP radiation in the visible spectrum, the gratings used in the MAMI experiment had very short periods (0.833μm and 9.09μm). Thus the observed wavelengths are orders of magnitude smaller than the MAMI bunch length of 10ns. In this case then, it is reasonable to assume that all of the observed radiation is incoherent. The theoretical comparisons also assumed perfect conductivity, which is only a reasonable approximation as long as the SP frequencies are small compared to the plasma frequency of the metal [36]. This is not the case in the MAMI experiment. Further difficulties acknowledged by this group relate to the finite thickness of aluminium substrate, resulting in possible image charges beneath the surface cancelling the surface charge.

Since the Smith-Purcell effect is similar in principle to transition and diffraction radiation — neither of which show any decrease in efficiency at higher energy — there is no logical reason for the energy emitted by SP radiation to decrease at increasing beam energies. This is discussed in further detail in [10].

2.5 Summary

Using Smith-Purcell radiation as a diagnostic method has a number of advantages over transition and diffraction radiation, especially in the context of the ILC. It is an entirely non-destructive, non-intercepting method, causing minimal disruption to the beam itself and satisfying all of the conditions mentioned in Section 1.4.1. Contrary to CTR/CDR, the radiation is not emitted in a narrow cone, but is in fact dispersed over a wide range of angles according to wavelength. The emitted intensity is proportional to the number of grating periods, and so it is also strong compared to CDR from a single aperture. By a suitable choice of the grating period, it allows the selection of the wavelength region of the emitted radiation in order to take advantage of the coherent regime.

The experimental setup itself is relatively simple, compared to other techniques, requiring a few small metallic gratings and an array of detectors arranged over several observation angles. The array itself can be very compact (<0.5m), and would easily fit between components. Depending also on the detectors used, the equipment is relatively inexpensive — especially if room temperature detectors are employed as in this thesis. Diagnostics are also easily performed at the touch of a button, with minimal expertise required once software is in place to swiftly analyse data. Also, with some consideration over the detectors and electronics used, it is even feasible to create a single-shot diagnostic using Smith-Purcell radiation.

Section 2.1 has discussed the creation and use of Smith-Purcell radiation experimentally, showing that different longitudinal bunch profiles create different intensity distributions that can then be measured. With this knowledge it is possible to return to the incident longitudinal profile, either by fitting 'template' profiles to the measured data points, or by using a Kramers-Krönig analysis (Chapter 3).

The two main approaches to describing Smith-Purcell radiation have also been discussed here. Section 2.2.1 describes a theory whereby the radiation is emitted as a result of the diffraction of the original electromagnetic field of the electron by a grating, and Section 2.2.3 uses a model based on the acceleration of surface charges induced by the electron on the grating. Both of these approaches have their advantages and disadvantages. For example, the models based on the van den Berg theory are computationally intensive (on the order of days), and the calculation can give rise to spurious Wood-Rayleigh anomalies – resonances that occur when an evanescent wave becomes a radiating wave. On the other hand, the calculations can be carried out for any arbitrary grating profile.

The surface current model results in a smooth output, with no evidence of Wood-Rayleigh anomalies and is much faster to compute (on the order of seconds), but it is non-trivial to extend to arbitrary profiles. However, special cases of grating profile (such as the 'sawtooth' profile used experimentally) can be calculated more easily.

The crucial difference between these theories is at highly relativistic energies ($i.e. E >$ 100MeV) and the expected behaviour of the grating factor, R^2. In this region the van den Berg model predicts that the emitted energy should decrease (since R^2 is thought to decrease with increasing energy), whereas the surface current model predicts the opposite.

The ***surface current***approach is the model of choice throughout this thesis. Not only is it less computationally intensive, but it also presents a more physical picture. SP radiation can also be considered as a limited case of diffraction radiation, with each 'peak' of the grating acting as part of a diffraction aperture. Both transition and diffraction radiation have been used as diagnostic tools for many years at highly relativistic energies and no drop in emitted energy has been observed. By analogy, it seems more sensible to follow the theoretical approach which predicts a similar effect on the output of SP radiation.

Chapter 3

Reconstruction of the Longitudinal Bunch Profile

As with other radiative processes, SP provides only the square of the magnitude of the form factor. The lack of phase information means that the profile cannot be immediately recovered via the inverse Fourier transform of the measured distribution.

There are two ways of retrieving the profile indirectly, however, after some data processing. The first approach is to compare the data with ‘templates’ generated from known bunch profiles. Alternatively, a Kramers-Krönig analysis can be carried out to recover the minimal phase information. Both of these approaches are described here in detail.

3.1 ‘Template’ Fitting

This approach uses template energy distributions based on known bunch profiles combined with the surface current model. They are compared to the measured data points and a weighted least square fit is carried out. The template with lowest χ^2 is then the closest approximation to the bunch.

The program BUNCH2 was derived from, and expands upon, an original C program (BUNCH) by G. Doucas. This can generate a SP spectrum from a number of pre-defined profiles, given appropriate beam (and grating) parameters, and can iterate through a given range of variables to find the lowest χ^2 fit to the experimental data. The following bunch profiles are currently supported:

- Asymmetric Gaussian.
- Multi-Gaussian — a superposition of up to 6 symmetric Gaussians.
- Asymmetric triangular.
- Asymmetric double exponential.
- Asymmetric parabolic.
- Cosine.
- Asymmetric Lorentz.

The term 'asymmetric' means that these profiles need not be symmetric about a central axis. The amount of skew around this axis is controlled by an 'asymmetry factor', ϵ. A symmetric bunch profile has a value of $\epsilon = 1$. The analysis procedure is as follows.

3.1.1 Data and Corrections

The first stage of the analysis method is to obtain a suitable data set and correct for the various losses in the experimental system. For example, the signal is decreased as it passes through the quartz window and optical system. Such decreases must be taken into account before a proper comparison can be carried out with a template distribution. All known losses, and the corrections associated with them, are described in more detail in Chapters 8 – 10. Data are also arranged according to the grating used.

3.1.2 Analytical Profiles

An analytical profile and bunch length must be assumed before generating a template. BUNCH2 allows any of the previously noted profiles to be considered over a range of bunch lengths and asymmetry values (where applicable). For example, the program can be instructed to assume a symmetric Gaussian profile (or multiple profiles) and to iterate through bunch lengths of 1 – 6ps in 0.1ps steps.

In addition to the assumed longitudinal profile, the following assumptions were made about the bunch:

- The distributions that make up the bunch, $X(x), Y(y)$ and $T(t)$, are uncorrelated.
- The distributions in x and y are Gaussian.
- The transverse bunch size, and other beam parameters, are known.

3.1.3 Calculation of the Differential Energy, dE

Equations 2.16 – 2.18 are used to generate the initial template distribution. This depends on a theoretical prediction for the energy emitted by one electron, combined with the Fourier transform of the chosen analytic bunch profile. The result is a template distribution in terms of energy per solid angle per unit grating length, dE. This calculation is carried out for each grating used to obtain the data in Section 3.1.1.

3.1.4 Calculation of the Expected Energy Accepted by Each Detector

The differential energy is not the final energy seen by each detector. Therefore, the next step is to calculate the effect of the optical system on the observed energy. There are four parts to this process:

1. The entire grating length, L, is visible to all detectors (see Section 7.3.1).
2. Each detector subtends a solid angle of $\Omega \approx 6.5$msr (see Section 7.3.2).
3. Due to mechanical restrictions, each detector can accept a maximum of $\phi = \pm 5°$.
4. Due to the optical system, each detector accepts a number of angles and therefore wavelengths.

Therefore, the energy received by each detector is actually the average energy collected over a narrow range of observation angles.

BUNCH2 gives the differential energy, dE, in terms of Joules per solid angle, per cm of grating length. To get the actual energy, E, it then averages over all angles observed by each detector, multiplied by the solid angle and grating length. For example, consider the detector at $\theta_0 = 90°$ with respect to the beam direction. The optical system collects all angles within the range $\theta_0 \pm 6.3°$. This translates to the detector accepting a wavelength range of 0.89 – 1.1mm with a 1mm period grating. The actual energy seen is

$$E\left(\theta_0\right) = \Omega L \frac{1}{N_\theta} \sum_{i=\theta_0-6.3}^{\theta_0+6.3} \frac{1}{N_\phi} \sum_{j=-5}^{5} dE_{i,j}\left(\theta, \phi\right), \tag{3.1}$$

where $N_{\theta,\phi}$ is the number of θ or ϕ angles seen. These values make up the template distribution used in the next step.

3.1.5 Calculation of χ^2

There are now two distributions; the template points, and the measured data points. Both distributions should express energy as seen by a detector in nJ (performed automatically by BUNCH2). The template can then be compared with the measurements, detector to detector. For example, a detector at $\theta_0 = 90°$ with respect to the beam direction would be compared with the equivalent simulated template 'detector'.

The comparison between template and measured distributions is performed by a Weighted Least Squares (WLS) fit. In this case, the template with the lowest χ^2 value represents the closest approximation to the actual bunch shape. The χ^2 is given by [85]

$$\chi^2 = \sum_{i \text{ points}} (d_i - t_i)^2 \frac{1}{w_i^2},$$

where d is a measured point, t is the equivalent template point, and w is the error associated with that point. BUNCH2 compares the template for each grating used experimentally in turn, storing the final value for the next step.

The above steps are then repeated for a variety of bunch profiles and lengths until the minimum χ^2 is found. This is then the closest analytical profile to the actual profile. Since this process can be time consuming if done by hand, BUNCH2 accepts a range of profiles to compare against and iterates through all associated values. The χ^2 for each template is stored and, once the process has been completed, the top five minimum χ^2 profiles (and their parameters) are presented to the user.

3.1.6 Limitations

There are certain disadvantages to retrieving the profile in this way. Templates can only be made for simple profiles that can be expressed analytically, for example, a Gaussian or cosine distribution. Obviously, this limits the number of WLS fits that can be performed, reducing the accuracy of this method. It also means that a template profile with minimum χ^2 is not necessarily the best fit to the data. There is always the possibility of an as yet unthought of distribution performing better. This is especially true if the actual bunch profile is not a simple shape.

Distributions can also have many variables to iterate through, such as varying the asymmetry of a Gaussian or changing the spacing between the peaks of a multi-Gaussian. The more variables a distribution has, the longer it takes to iterate through the possibilities and find the best fit to the bunch profile. This can make fitting especially slow. Nevertheless, this method is adequate in providing an approximation to the bunch profile when there is some prior knowledge about the bunch length.

3.2 Kramers-Krönig Relations

The Kramers-Krönig (KK) equations relate the real and imaginary parts of an analytic function. They were originally developed to recover either the real or imaginary part of the complex refractive index of crystals. In this case, knowledge of one part of the refractive index allows the other to be calculated. More recently, Lai and Sievers [39] have applied this technique to the coherent far infrared radiation produced by a bunch in order to recover its longitudinal profile.

3.2.1 Derivation of the Kramers-Krönig Relations for Retrieving the Longitudinal Bunch Profile

The KK relations connect the real and imaginary parts of a linear, causal system. The question then arises as to if this is satisfied by the SP process. SP satisfies the condition of linearity, since the total field, $\bar{\mathcal{E}}_{\text{total}}$, is proportional to the number of particles in the bunch, *i.e.* $\bar{\mathcal{E}}_{total} = N\bar{\mathcal{E}}_1$, where $\bar{\mathcal{E}}_1$ is the field from a single electron, and N is the number of particles in the bunch. The process is also causal as the response of the system cannot occur prior to the stimulus — radiation is not emitted before the bunch has passed over the grating. KK is difficult to apply to the case of SP radiation, as only the magnitude of the bunch form factor is known. Nevertheless, the possibility of its application to retrieving the longitudinal bunch profile, and the derivation of all relevant equations, has been well documented by Lai and Sievers [39, 40, 41, 42, 43]. For completeness sake their approach (and notation) is used here and the reader is directed to [21] for a more mathematically rigorous derivation.

First, consider the general equation for the radiated intensity spectrum produced by a bunch of N particles, ignoring the transverse shape of the bunch (this is included in the following section) [42],

$$I_{\text{tot}}(\nu) = I(\nu)\left[N + N(N-1)F(\nu)\right], \tag{3.2}$$

where $F(\nu)$ is the *square of the magnitude of the longitudinal bunch form factor*, given by [42]

$$F(\nu) = \left|\int_{-\infty}^{\infty} S(z)\exp\left[i\frac{2\pi\nu}{c}z\right]dz\right|^2,$$

and $S(z)$ is the normalised longitudinal distribution of particles in the bunch. The first term in Equation 3.2 is the intensity expected from N sources emitting independently (incoherent emission), whilst the second term takes into account the phase relations between the different particles (coherent emission). Thus, measuring the coherent emission spectrum gives the square of the longitudinal form factor, which in turn can provide information about the longitudinal profile.

Now define a complex form factor amplitude $\hat{S}(\nu)$ in terms of magnitude, $\rho(\nu)$, and phase, $\psi(\nu)$, such that [39]

$$\hat{S}(\nu) \equiv \int_0^\infty S(z) \exp\left[i\frac{2\pi\nu}{c}z\right] dz \equiv \rho(\nu) \exp\left[i\psi(\nu)\right]. \tag{3.3}$$

Hence,

$$F(\nu) = \hat{S}(\nu)\,\hat{S}^*(\nu) = \rho^2(\nu).$$

Thus a measurement of $F(\nu)$ over the entire frequency range gives the magnitude of the form factor, $\rho(\nu)$. Causality requires that Equation 3.3 is only integrated over positive frequencies since the effective total electric field cannot reach the detector before the field of the reference particle at $z = 0$. Choosing a different reference particle introduces a time shift in the bunch resulting in an overall phase factor that can be ignored as long as the bunch length is finite. This gives rise to the first two conditions that must be met before applying this technique:

- The radiative process must obey causality.
- The bunch length must be finite.

Writing Equation 3.3 as

$$\ln \hat{S}(\nu) = \ln \rho(\nu) + i\psi(\nu)$$

leads, eventually, to [42, 67]

$$\psi_m(\nu) + \psi_B(\nu) = -\frac{2\nu}{\pi}\mathcal{P}\int_0^\infty \frac{\ln \rho(x)}{x^2 - \nu^2}dx + \sum_j \arg\left(\frac{\nu - \hat{\nu}_j}{\nu - \hat{\nu}_j^*}\right), \tag{3.4}$$

where $\psi_m(\nu)$ is the minimal phase, $\psi_B(\nu)$ is the Blaschke phase and ν_j identifies zeros in the complex form factor, $\hat{S}(\nu)$. $\mathcal{P}$ denotes the principal value integral. Therefore, if $\hat{S}(\nu)$ has no zeros, $\psi_B(\nu) = 0$, and only the minimal phase is required. This leads to the third condition on the application of this method to real bunches:

- The bunch form factor must be a well-behaved, smoothly varying function with no δ-like features and nearby zeros.

When this condition is not met, the minimal phase alone may not be enough to accurately reconstruct the bunch profile. In this case, knowledge of the Blaschke phase is also required. However, the Blaschke contribution is not available experimentally, and hence KK cannot return a unique profile. This is most important when the bunch form factor possesses zeros that lie near to the region the spectrum is measured over [42].

When the above condition is satisfied, Lai and Sievers found the minimal phase to be a good approximation to the actual phase [43]. In this case, the minimal phase can be calculated as [21]

$$\psi_m(\nu) = \frac{2\nu}{\pi}\int_0^\infty \frac{\ln\left[\rho(x)/\rho(\nu)\right]}{\nu^2 - x^2}dx, \tag{3.5}$$

and the bunch profile distribution, $S(t)$, as [21]

$$S(t) = 2\int_0^\infty \rho(\nu)\cos\left(2\pi\nu t + \psi_m(\nu)\right)dt. \tag{3.6}$$

The KK relations were applied to the case of SP radiation (via the program BUNCH2) according to the following procedure. Note that the following steps follow a different notation from that of Lai and Sievers, that is more appropriate to the specific case of coherent SP radiation.

3.2.2 Corrections to Data and Recovery of $\rho(\nu)$

As in Section 3.1.1, the first stage is to obtain a suitable data set with all experimental losses accounted for. However, in this case data is ordered by increasing wavelength before applying the KK relations with BUNCH2.

Equation 2.16 can be re-written in terms of the transverse and longitudinal form factors, $F_T(\nu)$ and $F_L(\nu)$ respectively, as

$$\begin{aligned} dE &= dE_1\left[NS_{\text{inc}} + N^2 S_{\text{coh}}\right] \\ &= dE_1\left[NS_{\text{inc}} + N^2\left|F_T(\nu)\right|^2\left|F_L(\nu)\right|^2\right], \end{aligned} \tag{3.7}$$

where $F_L(\nu) = \rho(\nu)\exp\left[i\psi(\nu)\right]$ as in Equation 3.3. Here dE is the differential energy per solid angle per unit grating length, dE_1 is the one-electron differential energy, S_{inc} is the incoherent contribution and N is the number of particles in the bunch. Therefore, the first step is to extract $F_L(\nu)$ from the measured data points and then recover $\rho(\nu)$.

The transverse form factor $F_T(\nu)$ must be calculated before extracting $F_L(\nu)$. This requires the assumption that $X(x)$, $Y(y)$ and $T(t)$ are uncorrelated, and that the beam is Gaussian in x and y. BUNCH2 calculates $F_T(\nu)$ automatically given the transverse size of the bunch. Equations 2.14 and 2.17 can then be used to calculate dE_1 and S_{inc} respectively — note that the calculation of dE_1 is theory-dependent.

As discussed in Section 3.1.4, each detector sees a range of wavelengths. The average differential energy, $\overline{dE}$, on the detector is given by

$$\overline{dE} = \frac{E}{\Omega L},$$

where Ω is the detected solid angle, L is the length of grating, and E is the measured energy (in J). Substituting this into Equation 3.7 and rearranging gives

$$\left|\overline{F}_L(\nu)\right|^2 = \frac{\overline{dE} - N dE_1 S_{inc}}{dE_1 N^2 \left|F_T(\nu)\right|^2} = \rho^2(\nu). \tag{3.8}$$

BUNCH2 calculates $\rho(\nu)$ for each given data point, ordered by increasing frequency.

3.2.3 Extrapolation and Interpolation

A data set consists of a number of discrete points measured at specific frequencies over a limited range. Equation 3.5, however, requires knowledge of $\rho(\nu)$ over all frequencies. Therefore, some interpolation between the data points, and extrapolation beyond them to high and low frequencies, must take place. Errors in the reconstructed profile may potentially arise here as a result of this.

Lai and Sievers suggest a *high*frequency extrapolation of the form [43] $\rho(\nu) \rightarrow (\nu_H/\nu)^n$, where ν_H is the highest frequency available from the data, and n is typically between 4 and 6. Therefore, a function of the form

$$\rho(\nu) = \rho_H \left(\frac{\nu_H}{\nu}\right)^4, \tag{3.9}$$

was used when extrapolating to high frequencies, where ρ_H is the $\rho(\nu)$ point corresponding to the highest frequency in the data table. The 4th power was used after it was established that the reconstruction was not particularly sensitive to this value.

Grimm and Schmüser suggest a *low*frequency extrapolation of the form [21] $\rho(\nu) \propto \exp\left[-\alpha\nu^2\right]$, where α is chosen to smoothly join the low frequency data. The low frequency extrapolation should also satisfy the following conditions:

1. $\rho \to 1$ as $\nu \to 0$.
2. The extrapolating function should match the data at the lowest frequency point obtained from the data, ν_L.
3. The slope of the extrapolating function should match the slope of the data at the lowest frequency point.

This requires three variables, a, b and c, and an extrapolating function of the form

$$\rho(\nu) = \rho_L \exp\left(-a\nu^2 + b\nu + c\right) \tag{3.10}$$

with

$$\begin{aligned} a &= \left(\ln \rho_L - \nu_L \frac{s}{\rho_L}\right) \frac{1}{\nu_L^2} \\ b &= \frac{s}{\rho_L} + 2a\nu_L \\ c &= -\ln \rho_L \end{aligned}$$

where ρ_L is the lowest frequency ρ point and s is the slope derived from the existing ρ values,

$$s = \frac{\rho_i - \rho_L}{\nu_i - \nu_L}.$$

The slope used in BUNCH2 uses $i = 8$, *i.e.*it is the slope between the 1st and 8th recovered ρ points. This slope was chosen after examining the recovered ρ values from simulated data. The effect of different slopes on the KK reconstruction was found to be small, and so the slope between the 1st and 8th points was chosen to maximise the matching ability of the extrapolating function over the whole set of recovered ρ values. Equation 3.10 satisfies all of the above conditions and joins the extrapolated $\rho(\nu)$ smoothly onto the recovered $\rho(\nu)$ values. This function is used in BUNCH2 to extrapolate to low frequencies.

Interpolation between data points is also of particular importance. Unlike theoretical data points, where a simple interpolator suffices, real data points require a more robust solution. Interpolating over real data can introduce wild oscillations if the interpolator is not chosen wisely. The most robust interpolator found for the data presented here is a Monotone Cubic Hermite spline [47].

Overall BUNCH2 extrapolates (and interpolates) 2000 equally spaced $\rho(\nu)$ points over the range $0.001 \leq \nu \leq 10$THz. These values are then passed on to the next step to recover the minimal phase.

3.2.4 Recovery of the Minimal Phase, $\psi_m(\nu)$

For each value of $\rho(\nu)$, the minimal phase can be calculated from Equation 3.5. Therefore, BUNCH2 calculates 2000 corresponding points of the minimal phase, $\psi_m(\nu)$.

The time profile can then be calculated using Equation 3.6. BUNCH2 calculates this from -10 to 10ps in 0.2ps steps by default, which can be changed if necessary. Finally, the time profile must be normalised. This is done by identifying the maximum, $S(t)_{\text{max}}$, and minimum, $S(t)_{\text{min}}$, extremes of the profile (from Equation 3.6) and normalising according to

$$S(t)_{\text{normalised}} = \frac{S(t) - S(t)_{\text{min}}}{S(t)_{\text{max}} - S(t)_{\text{min}}}.$$

This returns the longitudinal bunch profile that is most consistent with the minimal phase recovered from the data.

3.2.5 Accuracy of Reconstruction

The accuracy of reconstructing the bunch profile using KK depends critically on the measured wavelength range. Long wavelengths, in particular, play a large role in how accurate the minimal recovered phase is with respect to the actual phase. When these wavelengths are missing, the minimal phase deviates from the actual phase. Thus extrapolation (Section 3.2.3) is very important in this region. Short wavelengths (high frequencies) have a lesser impact, but do help to identify fine structure.

Smith-Purcell radiation is in a unique position as the wavelengths produced can be tuned,by changing the grating period, to give an appropriate range of wavelengths. Multiple gratings can then be used to extend this wavelength range even further. The challenge then is in deciding on an appropriate range to take data over for an expected bunch length.

It is helpful to define a dimensionless parameter Γ, which is a function of grating period l and overall *approximate* bunch length σ_z.

$$\Gamma = \frac{l}{\sigma_z}. \tag{3.11}$$

The overall approximate bunch length removes the possibility of underestimating the wavelength region required. Now the accuracy of the KK reconstruction can be investigated in a more general fashion given different overall approximate bunch lengths. For demonstration purposes, overall bunch lengths within $\sim 2 - 8$ps have been chosen. The selected values of Γ were 0.5, 1.0 and 2.0. Data were simulated by BUNCH2 for these values assuming a beam such as at SLAC (see Section 9) and reconstructed using the KK method described in Sections 3.2.2 – 3.2.4.

First consider a simple Gaussian profile. The Fourier transform — or bunch form factor — of a Gaussian profile has no nearby zeros, and so the minimal phase should be all that is necessary to reconstruct it. Figures 3.1 and 3.2 show the reconstruction of a ~ 2 and 8ps Gaussian profile respectively. The reconstruction is very good for short bunches and only suffers slightly with increasing bunch length. This is probably due to inadequacies in the low frequency extrapolation function. Reconstruction with the gratings used experimentally (Figures 3.1e and 3.2e) is also very good. This behaviour confirms that the minimal phase is sufficient when there are no nearby zeros in the bunch form factor.

A more complicated bunch can be simulated by a superposition of three Gaussians. The width, amplitude, and displacement of the three peaks then define the total bunch shape. However, there is no guarantee that the form factor for this shape has no nearby zeros. Lai and Sievers suggest that the minimal phase is only sufficient when the largest component comes first in the bunch [41] — *i.e.*the bunch has a large leading peak. To test this hypothesis, Figures 3.3 – 3.6 show the reconstruction of $\sim 2 - 8$ps profiles, which have a large leading peak and Figure 3.7 shows the reconstruction of a bunch where the middle Gaussian is the largest component.

Consider first Figures 3.3 – 3.6. The reconstruction is very good, when combining data from multiple gratings, up to $\sim$ 6ps and begins to suffer at around 8ps when it begins to underestimate the bunch shape and length. Also, a lack of long wavelength data with the experimental gratings causes the reconstruction to suffer with long bunches (*e.g.*Figure 3.6e).

The KK reconstruction does not work as well when the middle Gaussian is the largest, as in Figure 3.7. However, the dominant peak is still identified with roughly the correct FWHM — although it misses the details at the start of the bunch — and the overall bunch length is approximately correct. This is in line with what Lai & Sievers observed in [41].

Further to this, Figure 3.8 shows the reconstruction of a $\sim$ 3ps symmetric Lorentz profile. The form factor for this profile also has nearby zeros and so should not be reconstructed very well. As expected, the reconstruction is poor. However, as in the case of Figure 3.7, the major peak is identified and the approximate FWHM and bunch length is correct.

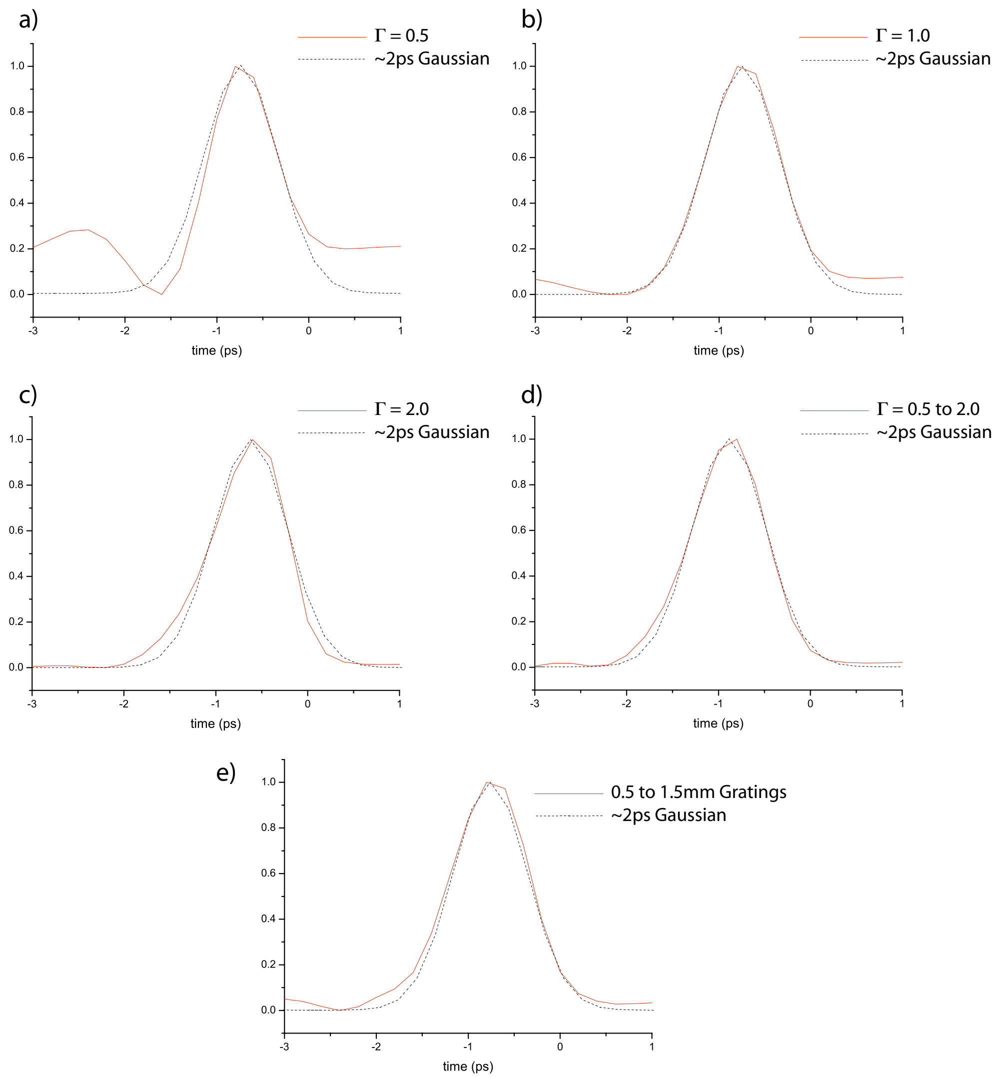

Figure 3.1: Reconstruction of a $\sim$ 2ps Gaussian profile using a grating with: a) $\Gamma = 0.5$, b) $\Gamma = 1.0$, c) $\Gamma = 2.0$, d) $\Gamma = 0.5$ to 2.0 combined (33 points), and e) the three grating periods used experimentally; 0.5, 1.0 and 1.5mm combined (33 points). The KK relations were used to reconstruct the original bunch profile. The KK fit is marked with a red (solid) line.

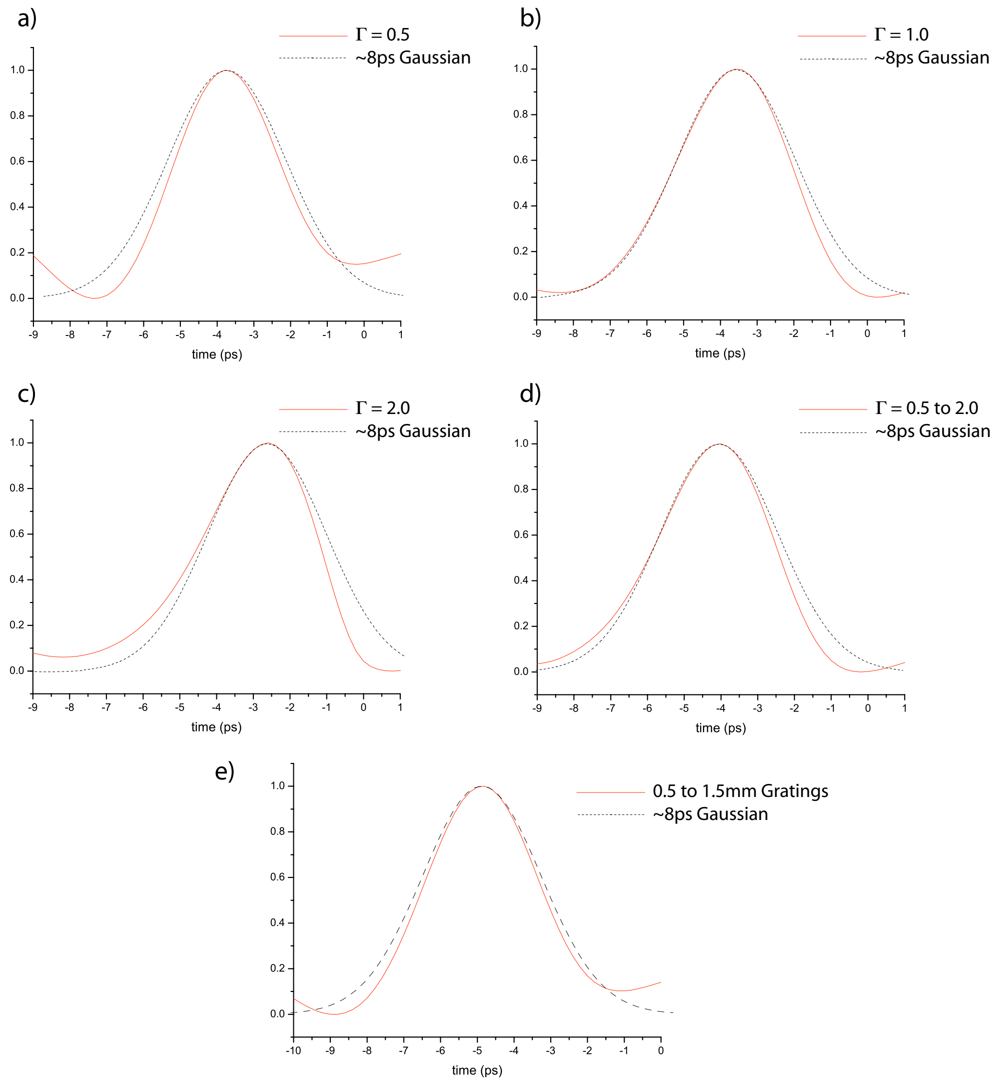

Figure 3.2: Reconstruction of a $\sim$ 8ps Gaussian profile using a grating with: a) $\Gamma = 0.5$, b) $\Gamma = 1.0$, c) $\Gamma = 2.0$, d) $\Gamma = 0.5$ to 2.0 combined (33 points), and e) the three grating periods used experimentally; 0.5, 1.0 and 1.5mm combined (33 points). The KK relations were used to reconstruct the original bunch profile. The KK fit is marked with a red (solid) line.

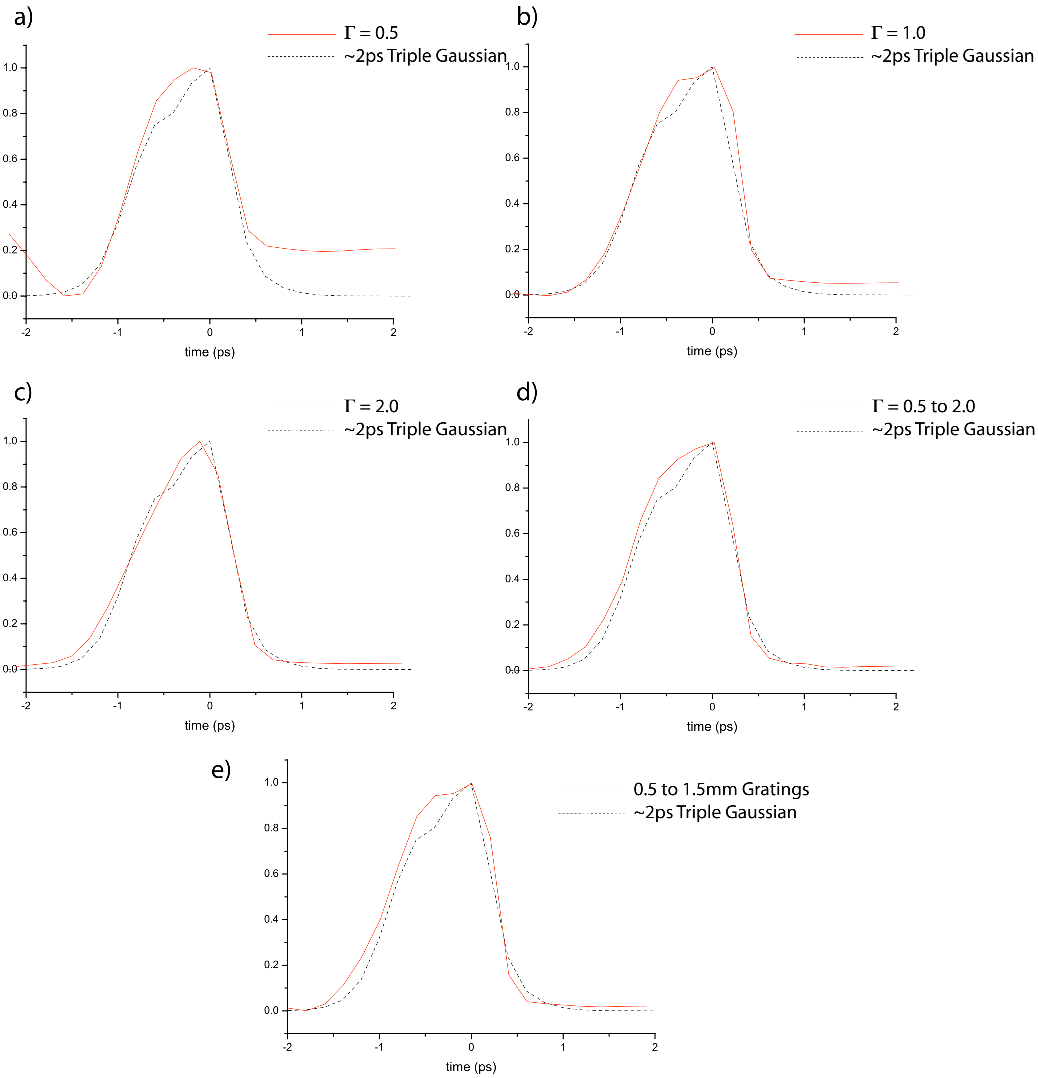

Figure 3.3: Reconstruction of a $\sim$ 2ps triple Gaussian profile using a grating with: a) $\Gamma = 0.5$, b) $\Gamma = 1.0$, c) $\Gamma = 2.0$, d) $\Gamma = 0.5$ to 2.0 combined (33 points), and e) the three grating periods used experimentally; 0.5, 1.0 and 1.5mm combined (33 points). The KK relations were used to reconstruct the original bunch profile. The bunch parameters are: $\sigma_1 = 0.2$ps, amplitude $a_1 = 3$, displacement along the t axis $t_1 = 0$ps; $\sigma_2 = 0.5$ps, $a_2 = 2$, $t_2 = -0.3$ps; $\sigma_3 = 0.3$ps, $a_3 = 2$, $t_3 = -0.6$ps. The KK fit is marked with a red (solid) line.

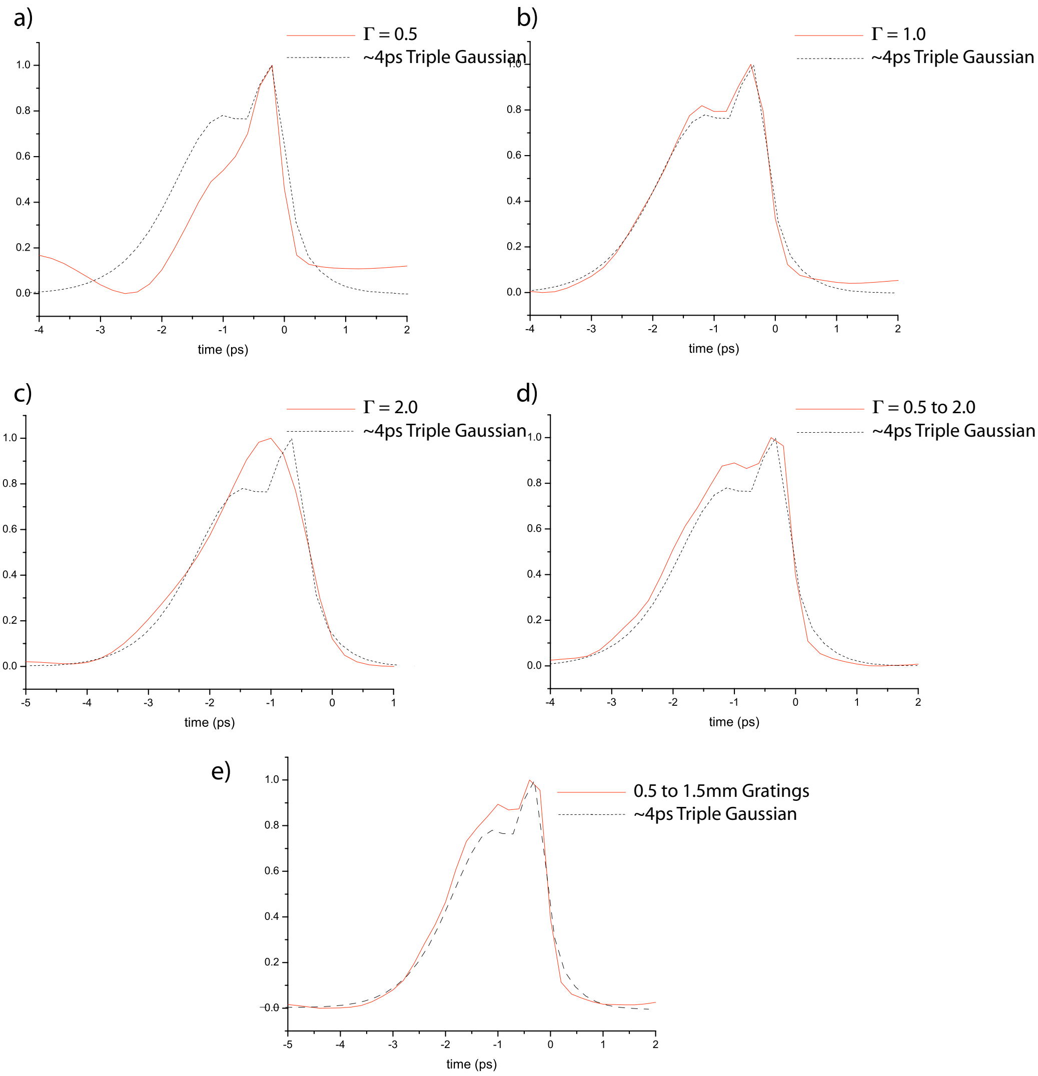

Figure 3.4: Reconstruction of a $\sim$ 4ps triple Gaussian profile using a grating with: a) $\Gamma = 0.5$, b) $\Gamma = 1.0$, c) $\Gamma = 2.0$, d) $\Gamma = 0.5$ to 2.0 combined (33 points), and e) the three grating periods used experimentally; 0.5, 1.0 and 1.5mm combined (33 points). The KK relations were used to reconstruct the original bunch profile. The bunch parameters are: $\sigma_1 = 0.2$ps, amplitude $a_1 = 1$, displacement along the t axis $t_1 = 0$ps; $\sigma_2 = 0.7$ps, $a_2 = 1$, $t_2 = -0.7$ps; $\sigma_3 = 1.0$ps, $a_3 = 0.5$, $t_3 = -1.1$ps. The KK fit is marked with a red (solid) line.

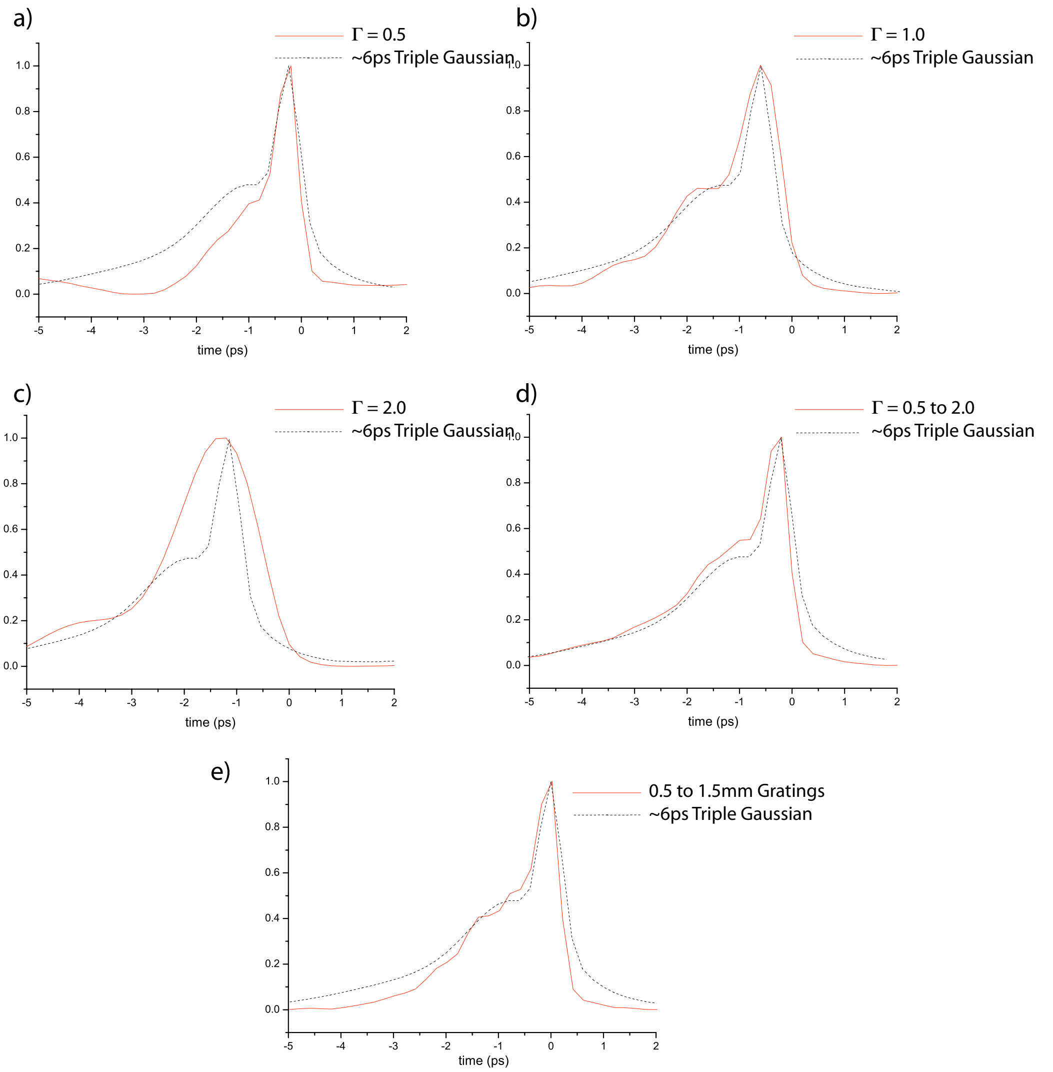

Figure 3.5: Reconstruction of a $\sim$ 6ps triple Gaussian profile using a grating with: a) $\Gamma = 0.5$, b) Γ =1 .0, c) Γ =2 .0, d) Γ =0 .5 to 2.0 combined (33 points), and e) the three grating periods used experimentally; 0.5, 1.0 and 1.5mm combined (33 points). The KK relations were used to reconstruct the original bunch profile. The bunch parameters are: $\sigma_1 = 0.2$ps, amplitude $a_1 = 2$, displacement along the t axis $t_1 = 0$ps; $\sigma_2 = 0.8$ps, $a_2 = 1$, $t_2 = -0.7$ps; $\sigma_3 = 1.9$ps, $a_3 = 0.5$, $t_3 = -1.6$ps. The KK fit is marked with a red (solid) line.

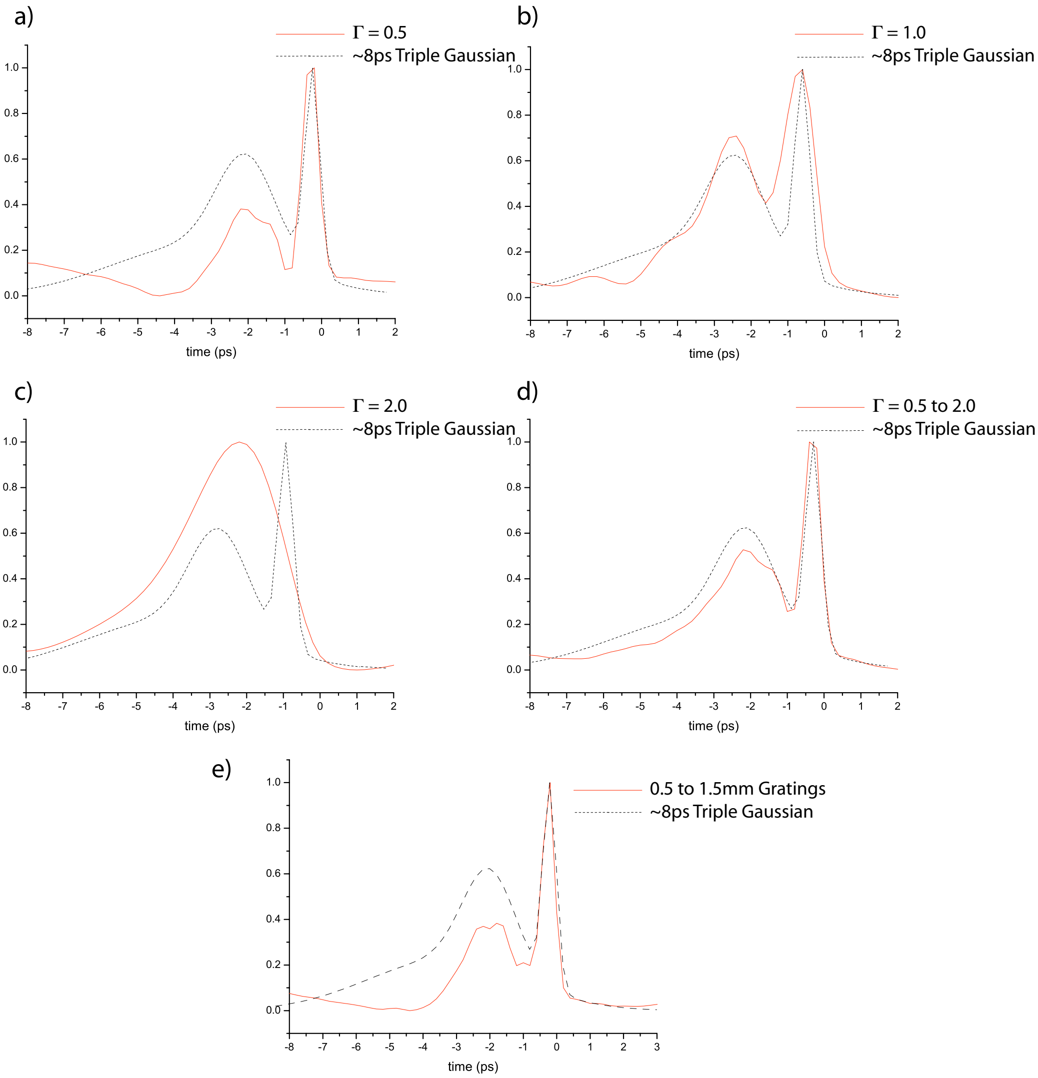

Figure 3.6: Reconstruction of a $\sim$ 8ps triple Gaussian profile using a grating with: a) $\Gamma = 0.5$, b) $\Gamma =1 .0$, c) $\Gamma =2 .0$, d) $\Gamma =0 .5$ to 2.0 combined (33 points), and e) the three grating periods used experimentally; 0.5, 1.0 and 1.5mm combined (33 points). The KK relations were used to reconstruct the original bunch profile. The bunch parameters are: $\sigma_1 = 0.2$ps, amplitude $a_1 = 2$, displacement along the t axis $t_1 = 0$ps; $\sigma_2 = 0.8$ps, $a_2 = 1$, $t_2 = -1.8$ps; $\sigma_3 = 2.3$ps, $a_3 = 0.5$, $t_3 = -3.2$ps. The KK fit is marked with a red (solid) line.

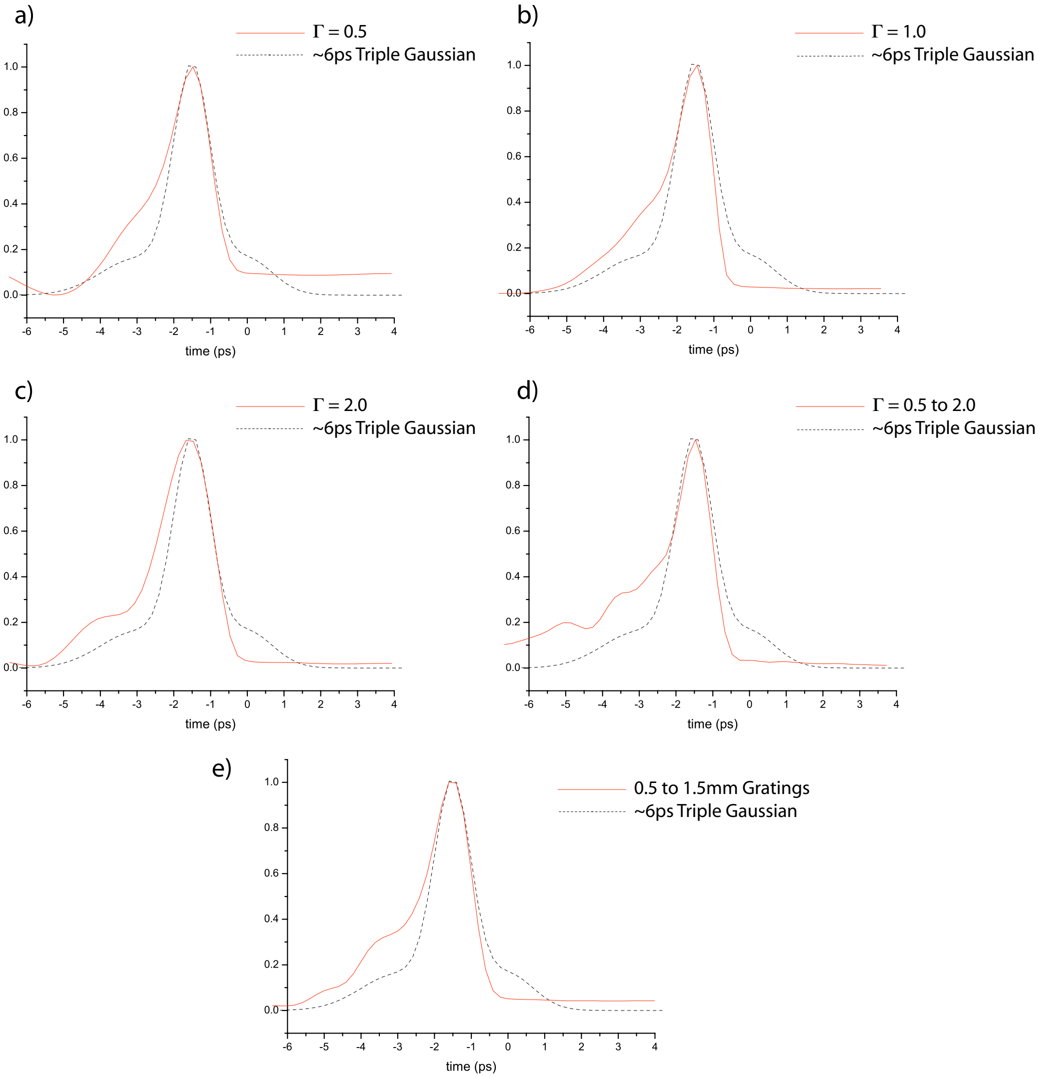

Figure 3.7: Reconstruction of a $\sim$ 6ps triple Gaussian profile using a grating with: a) $\Gamma = 0.5$, b) $\Gamma =1 .0$, c) $\Gamma =2 .0$, d) $\Gamma =0 .5$ to 2.0 combined (33 points), and e) the three grating periods used experimentally; 0.5, 1.0 and 1.5mm combined (33 points). The KK relations were used to reconstruct the original bunch profile. The bunch parameters are: $\sigma_1 = 0.7$ps, amplitude $a_1 = 0.5$, displacement along the t axis $t_1 = 0$ps; $\sigma_2 = 0.5$ps, $a_2 = 3$, $t_2 = -1.5$ps; $\sigma_3 = 1$ps, $a_3 = 0.5$, $t_3 = -3$ps. The KK fit is marked with a red (solid) line.

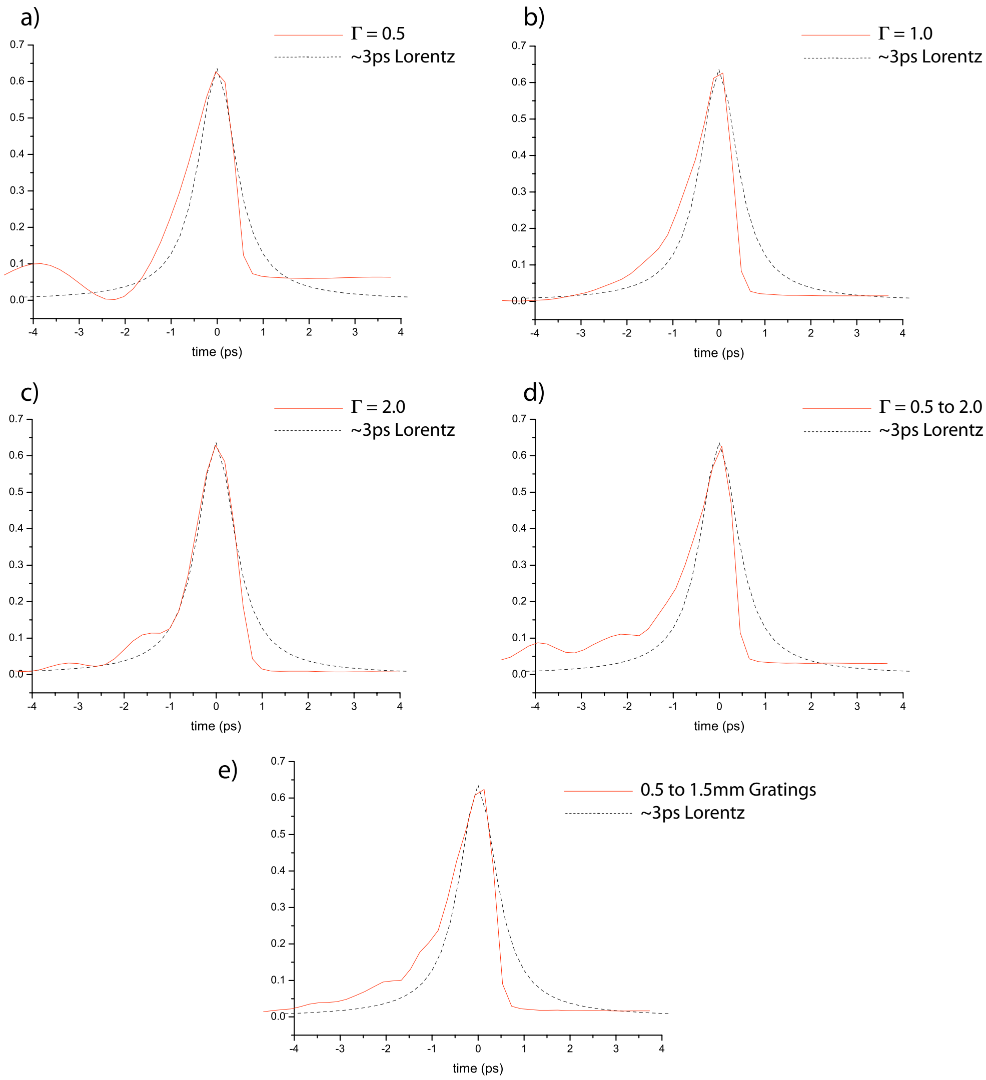

Figure 3.8: Reconstruction of a $\sim$ 3ps Lorentz profile using a grating with: a) $\Gamma = 0.5$, b) $\Gamma = 1.0$, c) $\Gamma = 2.0$, d) $\Gamma = 0.5$ to 2.0 combined (33 points), and d) the three grating periods used experimentally; 0.5, 1.0 and 1.5mm combined (33 points). The KK relations were used to reconstruct the original bunch profile. The KK fit is marked with a red (solid) line.

There are several general comments to note that apply to the above reconstructions:

1. A short period grating ($\Gamma = 0.5$) almost always results in an underestimate of the bunch length, and a contraction of the bunch profile. However, it is useful in identifying any sharp leading peaks and always shows the presence of fine structure.

2. $\Gamma = 1.0$ provides the closest match to the actual bunch shape when considering one grating, *i.e.*11 data points. Fine structure in the bunch can be seen and additional peaks are well represented. However, the sharpness of these peaks relative to the actual profile is not as defined as with $\Gamma = 0.5$.

3. $\Gamma = 2.0$ tends to simplify the bunch into an asymmetric Gaussian. Whilst on its own it would appear to only be useful for retrieving the bunch length, it also provides essential long wavelength information. The effect of this becomes very clear when examining Figures 3.1 – 3.6d. In this case, 33 points are combined from $\Gamma = 0.5$ to 2.0, and in all cases the KK reconstruction is greatly improved by the addition of the longer period grating.

4. The more data points available, the more reliable the fit. A good balance of long and short wavelengths is necessary. Where long wavelengths are missing, the bunch length can be underestimated. When short wavelengths are missing, fine structure in the profile is lost.

5. The gratings used experimentally (0.5, 1.0 and 1.5mm) provide good reconstruction for *simple*profiles up to 8ps, and adequate reconstruction of complex profiles up to 6ps. Above 6ps the information they provide would tend to underestimate the bunch length, since there is insufficient long wavelength data. Care must therefore be taken when considering reconstructed profiles in this region when using these particular gratings

Compared to the template method of Section 3.1.6, there are notable advantages to using the KK technique to recover the bunch profile. It does not require any knowledge, or guess, of the bunch length or longitudinal profile. Hence, it is much more flexible than the template method as it can also deal with non-analytical shapes. This also makes the KK method much faster.

However, like all procedures based on a radiative process, it cannot return a *guaranteed unique profile*. Instead it gives a profile consistent with the minimal phase. When long wavelength data are included, and the bunch form factor contains no nearby zeros, the minimal phase tends to the actual phase and the bunch profile returned is close to the true profile (Section 3.2.5). The accuracy of the KK process depends upon the overall approximate bunch length, and not only on the FWHM. Therefore, if only an estimate of the FWHM of the bunch is known when selecting grating periods, it is advisable to assume a safe margin about this value to account for any trailing structure that may lengthen the overall approximate bunch length, without affecting its FWHM. It is also assumed that the distributions in x, y and t are uncorrelated in order to extract ρ from the data points. Despite these problems, the KK method is still advantageous over fitting the data with templates.

3.2.6 Bunch Profile Reconstruction and Experimental Uncertainty

It is important to determine the effect of experimental uncertainties on the KK technique itself. First, a set of data points is simulated as in Section 3.2.5. Each data point, d, is associated an an assumed uncertainty of $\pm U$. Two further data sets are generated based on this uncertainty; a maximum data set consisting of points $d_{\text{max}} = d + U$, and a minimum data set consisting of points $d_{\text{min}} = d - U$. The bunch profile is then recovered from each new data set, as in Sections 3.2.1 – 3.2.4. Thus, two new bunch profile distributions are obtained that can be compared to the original reconstructed profile (*i.e.*from the original simulated data points, ignoring any possible uncertainty). The overall effect of this method is to shift the original simulated data points up (or down) by a set amount of energy. Hence, this approach does not account for *random* fluctuations in the uncertainty, which may result in a different pattern of data points.

To account for this, a further method is used based on a Monte Carlo [2] approach. New data sets are generated randomly within the assumed uncertainty. For example, each data point, d, has a maximum, d_{max}, and minimum, d_{min}, as stated above. A new data point is independently generated within the range $d_{\text{min}} \leq d \leq d_{\text{max}}$ for each wavelength. This produces a new data set whose values fluctuate within the boundaries of the uncertainty estimate. The bunch profile is then recovered from the randomly generated data, producing a profile consistent with both the minimum recovered phase and the uncertainty estimate. When repeated multiple times, this demonstrates the full range of reconstructed profiles produced by KK.

The above approaches were first applied to the reconstruction of a $\sim$ 2ps Gaussian profile, as previously shown in Figure 3.1d. An uncertainty of $U = \pm 50\%$ was applied to the simulated data, and the resulting KK reconstructions are shown in Figure 3.9 . The original reconstructed bunch profile is shown in black, and the reconstructions of the ‘maximum’ and ‘minimum’ data sets are shown in orange and green respectively. Both reconstructions are consistent with the original reconstructed shape. However, the maximum reconstruction tends to overestimate

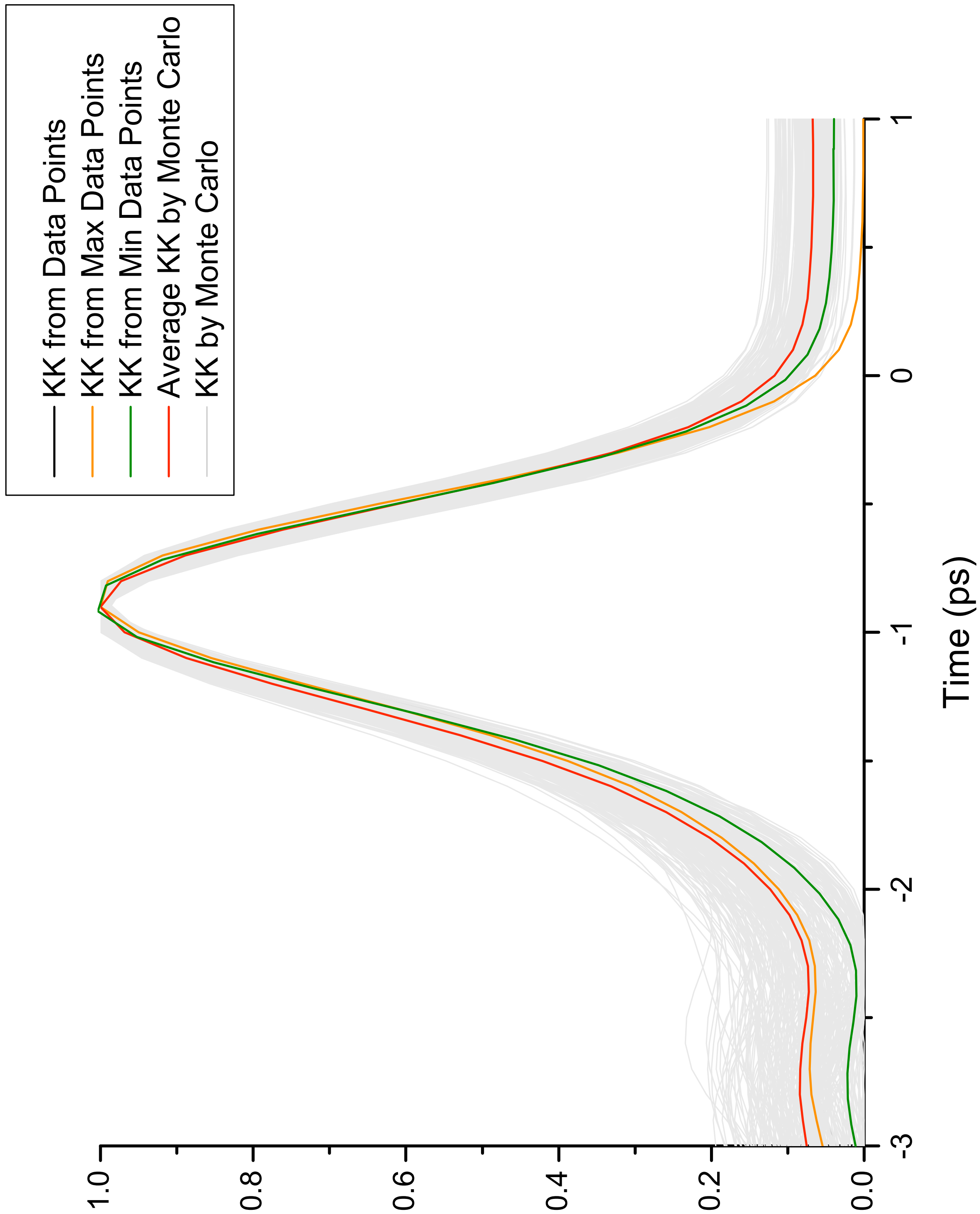

Figure 3.9: KK reconstruction using the data of Figure 3.1d, assuming an uncertainty of ±50%.

the trailing edge of the profile, whereas the minimum reconstruction slightly overestimates the leading edge. The similarity of the reconstructed profiles is to be expected as the overall shape of the simulated SP spectrum that they are derived from has not been altered.

Fluctuations within the uncertainty estimate gives rise to the grey lines of Figure 3.9. These show 250 reconstructed bunch profiles from randomly generated data sets (within the uncertainty). The average of these reconstructed bunch profiles is shown in red. Therefore, the introduction of a large uncertainty in the simulated data points results in a band of reconstructed profiles approximating that of the original reconstruction. This band is wider on the trailing edge of the bunch, and it introduces an uncertainty in the FWHM of the reconstructed profile. For this case, the reconstructed FWHM is $0.95^{+0.22}_{-0.13}$ps as determined by the maximum and minimum width of the grey band in Figure 3.9 relative to the original reconstruction. It should be noted that, although the FWHM is recovered quite accurately, the uncertainty band introduced by the experimental uncertainty makes it more difficult to derive a reasonable approximation of the "overall" bunch length.

The KK technique was further tested by reconstructing a $\sim$ 4ps triple Gaussian profile, previously shown in Figure 3.4d, assuming an uncertainty of $U = \pm 20\%$ and $\pm 50\%$. Figures 3.10 and 3.11 show the result of these investigations respectively. As previously discussed, the maximum and minimum reconstructed profiles are in line with the original reconstruction. The maximum reconstruction overestimates the trailing edge of the profile and the minimum reconstruction overestimates the leading edge, irrespective of the size of the uncertainty.

The uncertainty estimate does have an affect on the size of the band of profiles reconstructed by the Monte Carlo approach. The larger the uncertainty, the larger the spread of profiles. Hence, the larger the uncertainty on the recovered FWHM. The average reconstructed profile from this technique also tends towards the original profile as the uncertainty in the data points is decreased. The FWHM of the profile after assuming an uncertainty of $\pm 20\%$ is $2.05^{+0.15}_{-0.10}$ps, whereas after assuming an uncertainty of $\pm 50\%$ it is $2.05^{+0.36}_{-0.25}$ps.

The uncertainty band about the bunch profile does not tend to zero in either direction. A similar effect has also been observed, in the previous section, where insufficient wavelengths were available. Therefore, the effect of increasing the experimental uncertainty on the data has similar consequences to lack wavelength information. Hence, the most accurate KK reconstruction is for measurements with sufficient wavelength information *and* small experimental uncertainty.

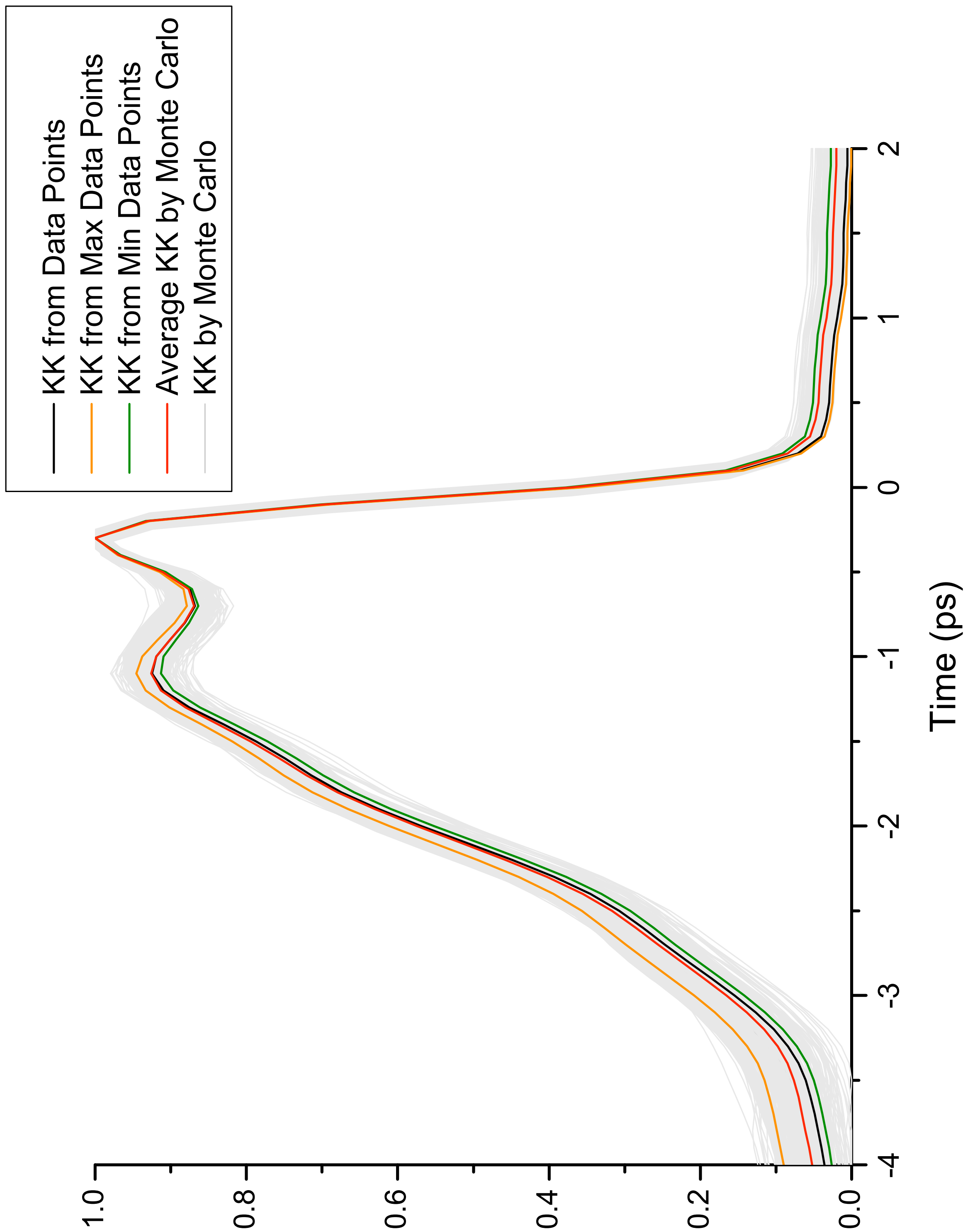

Figure 3.10: KK reconstruction using the data of Figure 3.4d, assuming an 'experimental uncertainty' of ±20%.

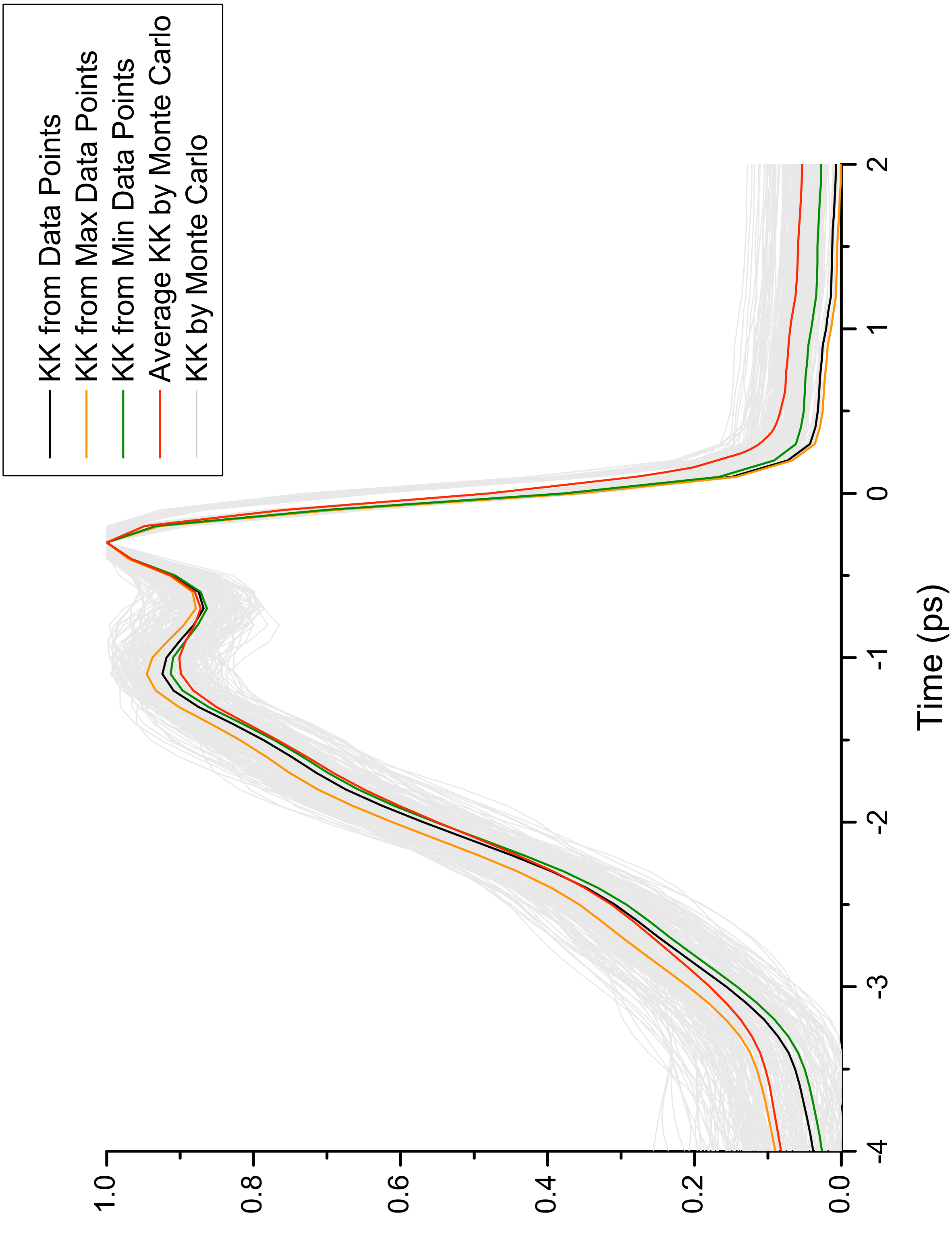

Figure 3.11: KK reconstruction using the data of Figure 3.4d, assuming an 'experimental uncertainty' of ±50%.

3.3 Summary

This chapter discussed two main methods that can be used to recover the longitudinal bunch profile from the measured spectral distribution of coherent SP radiation. Section 3.1 covers the first of these where data is fitted with templates generated from known, simple bunch profiles. Whilst this method is suitable for simple shapes, it is not practical for complicated bunch profiles as there is no guarantee that the template shape used is the best one.

Section 3.2 describes a more attractive alternative. This uses the Kramers-Krönig relations to recover the minimal phase consistent with the data. This can then be used to recover the bunch profile and does not rely upon it being a simple analytical shape. However, the accuracy of the reconstruction depends upon the available wavelength range, the number of data points (Section 3.2.5), and the experimental uncertainty (Section 3.2.6). In this respect, SP is particularly useful as both the wavelength range and number of data points can be expanded upon by using multiple gratings.

Experimentally, the data were limited to three gratings with periods of 0.5, 1.0 and 1.5mm. The accuracy of reconstruction using these specific gratings is also considered in Section 3.2.5. They provide sufficient wavelength range for good reconstruction of simple profiles with an overall approximate bunch length of up to 8ps long, and adequate data for complex, multi-peak, bunch shapes up to 6ps long.

Chapter 4

Experimental: General

The three main experiments discussed in Chapters 8 – 10 used slightly different experimental setups. To avoid confusion in later chapters, the basic apparatus is described first. Additions to each experiment are then described in chronological order.

A schematic of the apparatus is shown in Figure 4.1. It consists of a vacuum chamber, housing the gratings, and an optical detection system on the atmospheric side.

4.1 Vacuum Chamber

The vacuum chamber contained the gratings that generated SP radiation and a crystalline quartz window, which let radiation exit the chamber. The chamber was a cylinder approximately 510×200mm in size, exclusive of the grating motor.

Figure 4.2 shows the vacuum chamber used. The beam travelled from right to left and passed over a grating. The grating was moved closer to (or further away from) the beam using a motor at the rear. The SP radiation produced passed through the quartz window at the front where it was measured by an array of detectors.

4.1.1 Gratings

Each grating was made from a 40×20mm piece of aluminium with a sawtooth profile machined on its surface. Three different periods were used to extend the measured wavelength region: 0.5, 1.0 and 1.5mm. These had a blaze angle, α, of 40, 35 and 30°, respectively. A blank 'grating' was also used to quantify the amount of background radiation caused by the grating structure inside the beampipe. This was the same size as the gratings, but without the periodic surface.

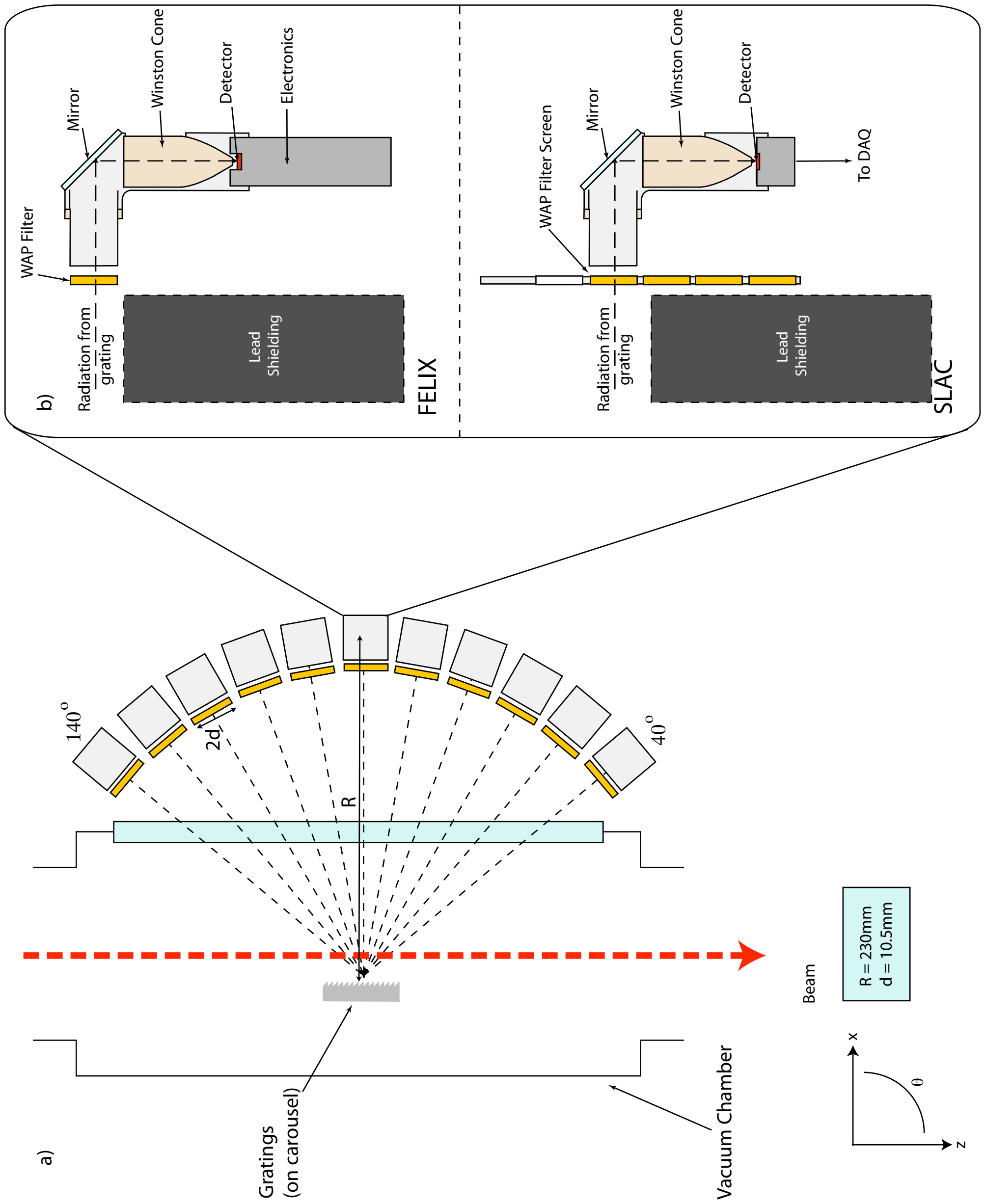

Figure 4.1: Schematic of a) the experimental arrangement and, b) a close-up of the optical system.

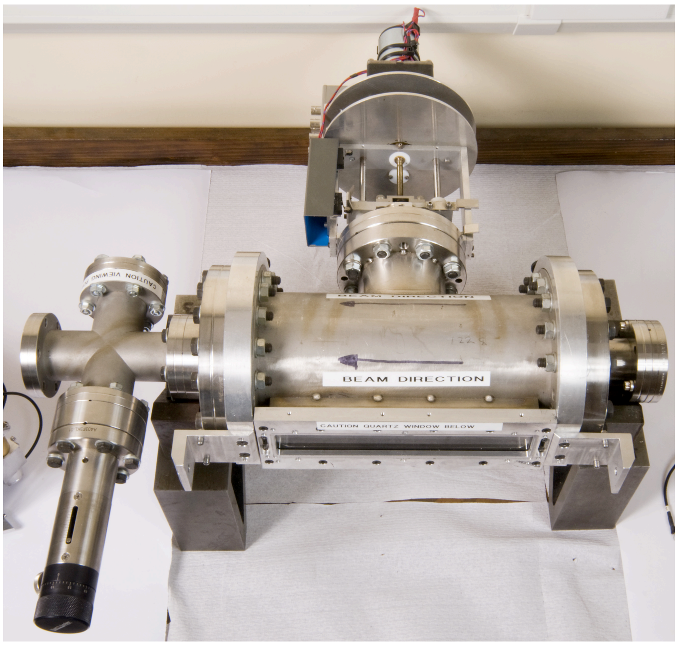

Figure 4.2: The vacuum chamber contained three gratings and a quartz window. The grating motor is behind the chamber.

The accuracy of the reconstructed bunch profile depends on the wavelength range covered by the measurements and, hence, on the number of gratings used and their respective periods (see Chapter 3). However, measurements with multiple gratings must be taken in quick succession (ideally simultaneously) to minimise the effect of any changes in the beam.

This issue was solved by mounting three gratings and a blank on a ‘carousel’-like structure. The carousel was rotated by a ‘ratchet and pawl’ mechanism so that different gratings were brought towards the beam without having to physically remove and insert new ones. Figure 4.3 shows the carousel inside the vacuum chamber with the 0.5mm grating clearly visible.

A major consideration was the existence of non-SP background radiation. This can arise from:

- Diffraction radiation from the edge of the grating or carousel structure.
- Diffraction radiation from the vacuum chamber apertures.
- Similar, long wavelength radiation produced by components upstream.

Therefore, it was important to quantify this radiation and subtract it from the SP signal seen.

The primary method of discriminating against this radiation was by taking a measurement with the blank. All radiation seen with the blank in the same position as a grating should account for the above points. Subtracting this measurement from that seen with a grating

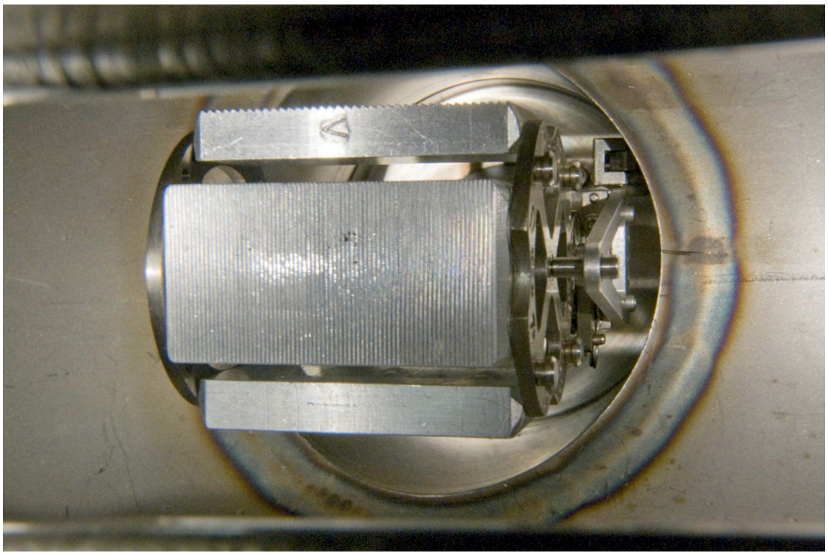

Figure 4.3: The ‘carousel’ of gratings inside the vacuum chamber.

leaves only the radiation arising from the periodic structure itself. Therefore, all data presented in this thesis represents the difference in signal seen with a grating and with a blank (unless stated otherwise).

4.1.2 Quartz Window

A z-cut crystalline quartz window allowed SP radiation to exit the vacuum chamber and enter the optical system. The window was approximately $210 \times 50 \times 6$mm in size. Crystalline quartz is useful as it has a high transmission in the far infrared. It also does not buckle under pressure and keeps a satisfactory vacuum.

Quartz has been used in far infrared experiments for many years, and so its transmission is well defined [34]. In this region the window has a refractive index of 2.1 and a constant transmission of $\sim 75\%$ for $\lambda \geq 150\mu$m.

4.2 Optical System

Eleven pyroelectric detectors were placed around the vacuum chamber at angles from $40 - 140^\circ$ with respect to the beam direction. The detectors were positioned at the end of a Winston cone, after a 90° bend (see Figure 4.1). Using a cone maximised the amount of light collected by the system. A high pass filter was used at the entrance to the optical system. The exact filter used depended upon the expected SP wavelength seen at each observation angle. These three components are discussed in more detail in Chapters $5 - 7$.

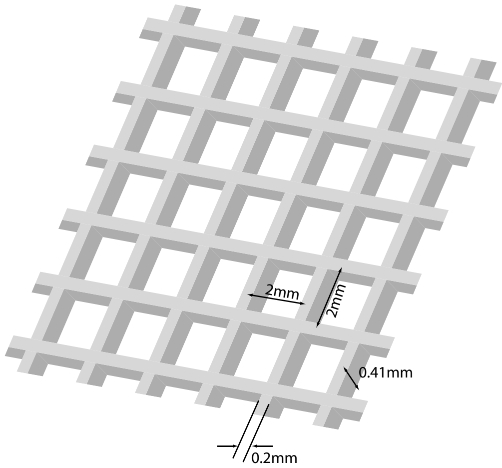

Figure 4.4: Diagram of the copper wire mesh screen with overall dimensions 200×35mm, perforated with 2mm square holes.

4.2.1 The 90° Bend

In the early experiments a 90° bend was not used. This meant that the electronics were unshielded, and hence exposed to X-rays. Unfortunately, they were particularly sensitive to X-rays, and so this caused a lot of interference and lead to unreliable data.

The solution was to introduce a 90° bend in the optical system. This brought the electronics out of the line of sight of the beamline and meant that they could be shielded from X-rays. A schematic is shown in Figure 4.1b. Radiation that entered the 90° bend was then reflected from a mirror towards a detector, passing through the Winston cone.

4.2.2 Additional Filters

In the early stages of the experiments there was some concern that very long wavelength radiation — *e.g.*from higher machine harmonics — might leak into the detection system. To prevent this, two types of filter were placed against the quartz window in addition to the filters described in Chapter 5.

The first of these was a wire grid screen. The screen consisted of 2mm square holes in a 200×35×0.41mm copper sheet. The holes were arranged in a regular grid as in Figure 4.4. The screen was expected to behave like an inductive grid. These have low transmission for wavelengths longer than the mesh period, and good transmission otherwise.

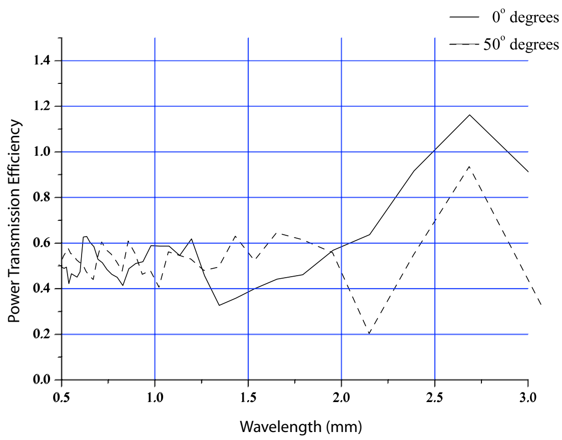

Figure 4.5: Measured power transmission efficiency through an inductive wire grid at 0° and 50° angle of incidence.

A measurement of the screen's transmission in the 0.5 – 2mm region, at various angles of incidence, was carried out using THz Time Domain Spectroscopy in the Clarendon Laboratory, Oxford [66]. Figure 4.5 shows the result of this measurement, which approaches the limit of the spectrometer at $\lambda \sim 1.8$mm. Regardless of the angle of incidence and wavelength, the grid had a transmission of $\sim 50\%$. The source power was too weak beyond 1.8mm to determine the transmission at longer wavelengths.

In retrospect this mesh was an unnecessary complication and should not have been used. However, since it was present in all three experiments discussed here, a correction of $50\% \pm 10\%$ must be made to all data to account for it. A more complete measurement should ideally be made in the future using a stronger source. It would also be helpful if the transmission was measured with the screen and quartz window in contact. This would allow reflections between the two to be taken into account.

The second stage was to use a sheet of black polyethylene, which is a basic absorber of visible and near infrared radiation. It has good transmission in the far infrared on the order of 90%. This was put on top of the window since it scatters light as well as absorbing it. Thus is needed to be located as far away from the optical system as possible. This avoided the risk of detecting scattered background radiation.

4.3 FELIX

This is the first of the experiments described in this thesis. It was carried out in November 2005 at the FELIX Facility, Netherlands. Many aspects of the basic apparatus described in the above

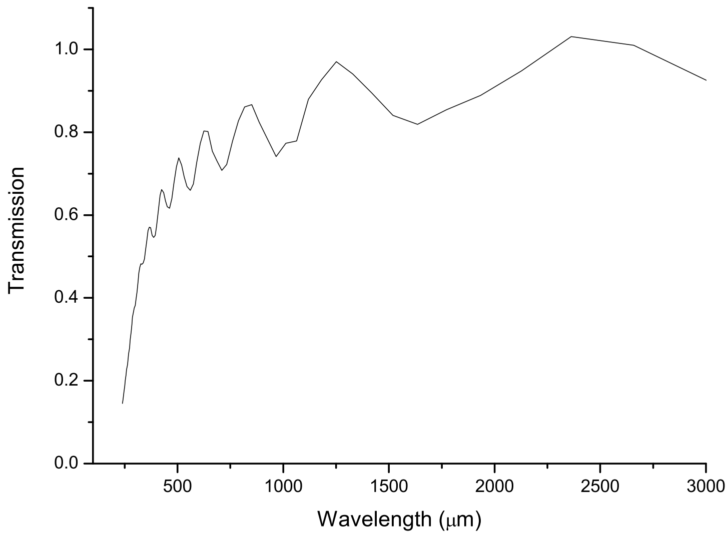

Figure 4.6: Measured power transmission efficiency of flurogold.

sections were developed for, and tested during, this experiment. The main difference between this and later experiments is in the electronics and filters used.

4.3.1 Flurogold

A piece of flurogold was placed against the quartz window as well as the wire screen and black polyethylene (Section 4.2.2). This is a well-known infrared absorber whose transmission characteristics were measured using THz Time Domain Spectroscopy (Figure 4.6). It effectively removes the near and mid-infrared, whilst leaving $\lambda > 1$mm largely untouched. However, it still removes a portion of the short wavelength spectrum that SP radiation is emitted in. Due to this effect it was not used in later experiments. Whenever used, its measured power transmission efficiency was accounted for.

4.3.2 WAP Filters and Aluminium 'Plugs'

This experiment only had a complete set of filters available for the 0.5 and 1.0mm gratings. These two sets of filters also covered the $40 - 110°$ observation angles with the 1.5mm grating. The last three angles were then used either without a filter, or with an aluminium 'plug', when this grating was in position.

The plugs were a solid piece of aluminium designed to fit over, and inside, the entrance to the 90° bend. They stopped all far infrared (SP) and other radiation from being detected.

Thus, when the plugs were used, any signal seen was the irreducible background due to X-rays or electronic noise.

Due to easy access to the beamline, filters and plugs were changed by hand and were placed directly over the entrance to the 90° bend. This had the additional advantage of being able to change filters on-the-fly. By doing this, it was possible to confirm that an inappropriate filter could remove the SP signal.

4.3.3 Electronics

The detector electronics used a low noise JFET (2SK117) input. This had a rise time of 500ns and its output was proportional to the incident power. The electronics were found to be very sensitive to X-ray radiation, which lead to the development of the 90° bend described in Section 4.2.1. Lead shielding had a large impact, reducing the amount of X-ray radiation, though it did not resolve the issue completely.

Both the detector and electronics were housed inside an 85×25mm aluminium cylinder using a SMA coaxial bulkhead connector. The housing connected onto the end of the Winston cone so that its exit was 0.5mm away from the detector. A coaxial cable ran from this to a common power and load box in the control room. Signals were recorded on four digital oscilloscopes (a total of 16 channels), triggered by the accelerator timing system. Each measurement was then averaged over a minimum of 64 triggers [54].

4.4 SLAC

Experiments were carried out at SLAC in March and July 2007 with slightly different equipment. The changes were prompted by inadequacies in the FELIX setup. For example, it would have been particularly cumbersome to carry out the experiment at SLAC using four oscilloscopes, and so a data acquisition (DAQ) system was designed and installed. This had the added bonus of housing all of the electronics for the experiment and further addressing the X-ray interference problem experienced at FELIX.

4.4.1 Filters

A complete set of filters for all gratings was available for this experiment. An optimum filter was chosen for each angle based on the measurements described in Chapter 5. In March these

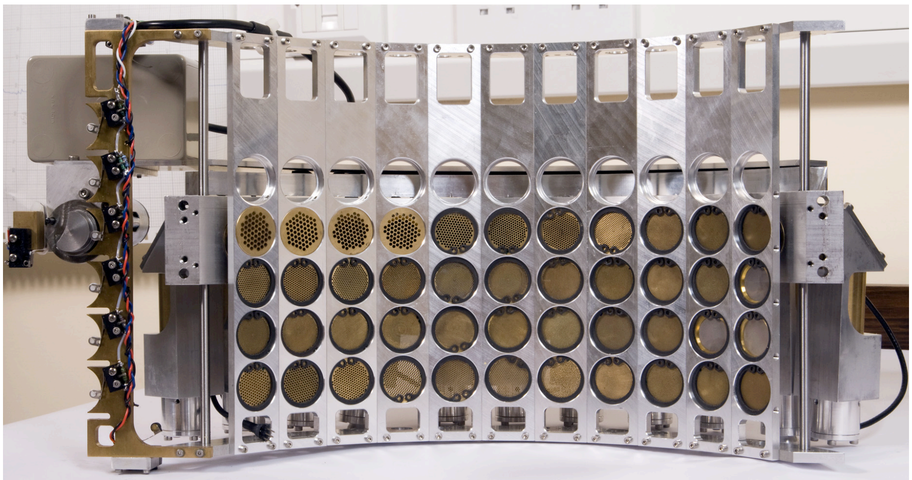

Figure 4.7: The filter changing mechanism used at SLAC in July 2007. From top to bottom the filters correspond to: a solid piece of aluminium, no filters, 1.5mm first order, 1.5mm second order, 0.5mm first order, and 1mm first order radiation.

filters were changed by hand. This presented a significant obstacle to taking data since, unlike at FELIX, the turnaround for changing filters was in excess of 45 minutes.

A mechanism was introduced in July that could change filters remotely (Figure 4.7), and held four complete sets of filters. Each row of the mechanism corresponded to (from top to bottom):

- A piece of solid aluminium for a measurements of the irreducible background.
- An empty space for the study of unfiltered radiation.
- Filters for radiation from the 1.5mm grating, 1st order.
- Filters for radiation from the 1.5mm grating, 2nd order.
- Filters for radiation from the 0.5mm grating, 1st order.
- Filters for radiation from the 1.0mm grating, 1st order.

Note that according to Equation 2.1, filters for the 0.5mm grating, 1st order, also correspond to radiation from the 1mm grating, 2nd order, and 1.5mm grating, 3rd order. The screen was moved to bring the correct filters in front of the entrance to the optical system corresponding to the grating used at the time.

In both March and July it was possible to take a measurement of the irreducible background. However, whereas at FELIX this was done with aluminium plugs, at SLAC it was measured either with an aluminium screen covering the quartz window (March) or by blocking the entrance

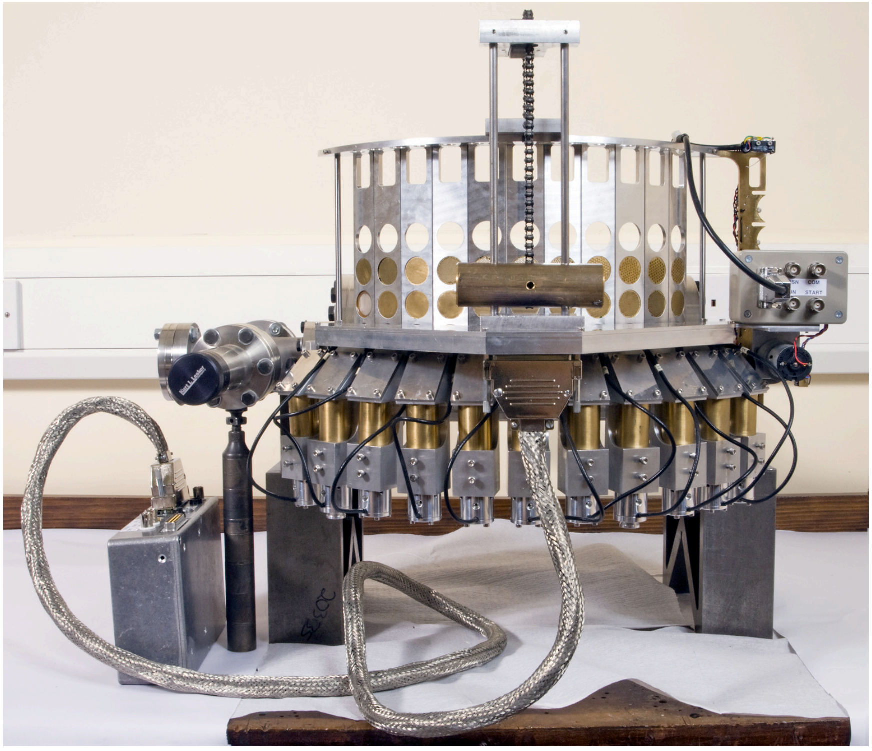

Figure 4.8: View of the experimental arrangement used at SLAC in July 2007 with the DAQ box on the left. The beam travelled from right to left.

to the elbow bends (July). This had the same effect, eliminating all far infrared radiation, and was carried out remotely. Once the aluminium screen was in place, all signal seen on the detectors corresponded to the irreducible background measurement caused by X-rays, leaked radiation, or electronic noise. The final setup used in July can be seen in Figure 4.8.

4.4.2 Electronics

Different electronics were required for SLAC since the beam consisted of single bunches rather than a bunch train. At the same time, since the electronics are ~ 3 times more sensitive to X-rays than the pyroelectric detectors, they were separated from the optical system to minimise this interference. This meant that the detector housing itself could be much smaller (Figure 4.9).

The electronics for the SLAC experiments took the form of a data acquisition system (DAQ) box. Signals were taken from the pyroelectric detectors, via a bundle of shielded coaxial cables, to the DAQ box. This was situated on the tunnel floor and was completely surrounded by lead, greatly reducing the amount of X-ray interference compared to the FELIX experiments.

Figure 4.9: The difference in size between the detector casing used at SLAC (left) and FELIX due to the separation of the detector and electronics.

The DAQ had a total of 14 data channels; eleven for the pyroelectric detectors arranged from 40 to 140° with respect to the beam direction, two for background radiation detectors, and one for a PIN diode that was used to monitor X-rays. The two background radiation detectors were attached underneath the 50 and 130° detectors and provided an additional measure of the background radiation. Each channel had a charge sensitive preamp with JFET input, driving 14bit ADC sampling at 400kSa/s [54].

The DAQ box also included signal digitisation with control and readout over a slow serial link. The grating carousel and the aluminium screen, used in the March experiment, could both be controlled via the DAQ box. However, the filter changing mechanism was introduced later and was connected to a separate control box. The DAQ box was connected to a laptop computer via a RS-232 link. A terminal emulator program enabled the unit to be controlled from the laptop computer, controlling the movement of the grating *etc.* whilst also logging all data acquired during the experiment. Figure 4.10 shows a schematic diagram of this arrangement.

4.5 Summary

Slightly different experimental arrangements were used for the experiments described in Chapters 8 – 10. The apparatus can be roughly divided into two sections; the vacuum chamber (Section 4.1) and the optical system (Section 4.2). The vacuum chamber contained three different period gratings and a blank that was used for background measurements. The optical system consisted of 11 pyroelectric detectors positioned at 40 – 140° with respect to the beam

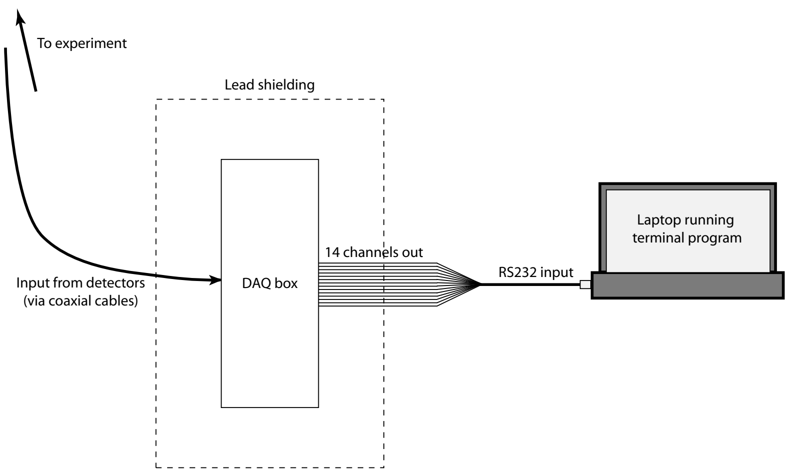

Figure 4.10: Schematic of the DAQ box.

direction. Each of these was housed inside a 90° bend. at the end of a Winston cone. This meant that the optical system was brought out of the line of sight of the beamline.

The additions made to the FELIX and SLAC experiments are described in Sections 4.3 and 4.4 respectively. Both of these experiments used waveguide array plate filters (see Chapter 5), albeit in different configurations. They also both had a method of measuring the irreducible background noise. This is the amount of signal seen when SP radiation is stopped from entering the optical system. FELIX used a set of aluminium plugs for this purpose, whilst an aluminium screen was used at SLAC.

Due to the different natures of the beams, the experiments at FELIX and SLAC also had different electronics. These were attached directly to the detector at FELIX, but were separated at SLAC. This separation greatly simplified data acquisition at SLAC and also meant that the electronics could be placed away from the beamline where it was properly shielded. This significantly improved the signal-to-noise ratio.

Chapter 5

Filters

Equation 2.1 states that SP wavelengths are dispersed according to the angle of observation. Each detector observes a specific range of wavelengths and so, in principle, no external spectrometer is required. However, non-SP wavelengths can also enter the detector. Thus, filters play an important role in the experimental arrangement. The ideal shape of the filter transmission curve resembles a narrow top hat distribution with maximum transmission around the SP wavelength and zero transmission for all other wavelengths. This would provide the following benefits for an SP experiment:

1. Removal of unwanted background radiation.
2. Verify the correct SP wavelengths are seen according to Equation 2.1 without the use of an external spectrometer.

Two types of filters have been used as part of the optical system in the past; wire mesh and waveguide array plate filters. Their properties are discussed in this chapter, along with measurements of their transmission characteristics.

5.1 Transmission Measurement Techniques

Two techniques were used to measure the transmission through each filter, which are described here. The experimental procedure for measuring the transmitted power through each filter is described in Sections 5.2.1 and 5.3.2.

5.1.1 Tera-Hertz Time Domain Spectroscopy (THz-TDS)

THz Time Domain Spectroscopy (THz-TDS) is a spectroscopic method that uses short pulses of THz radiation to probe a sample. It can measure the sample's effect on both the amplitude and phase of the THz radiation [11].

THz radiation is generated by using an ultra-short (< 100fs) optical laser pulse to create electron-hole pairs in a semiconductor (*e.g.*GaAs). This causes the semiconductor to change from an insulating to conducting state, which generates a current across its surface. The result is the creation of THz radiation, which is focused onto a sample. The radiation passes through the sample and is detected by a polarisation sensitive detector. The ratio of the spectrum recorded with and without a sample in place gives the transmission spectrum of the sample itself. All THz-TDS measurements described in this thesis were carried out with the THz Photonics Group, Clarendon Laboratory, University of Oxford [66].

5.1.2 Fourier Transform Spectroscopy (FTS)

Fourier Transform Spectroscopy (FTS) uses a Martin-Pupplet interferometer. This is similar to a Michelson interferometer and works by splitting an infrared source beam into two orthogonal polarisations via a beam splitter (polariser). This transmits half of the radiation and reflects the rest. The two beams are then reflected from a pair of mirrors (one fixed, one movable) and recombined. The path difference between the two beams is controlled by the moveable mirror. As the mirror is moved, the intensity of the recombined beam varies. When this is recorded as a function of the mirror's position it gives an interferogram that can be Fourier transformed to give a frequency spectrum.

Various samples, *e.g.*filters, can be placed at the end of the interferometer in front of a detector. The passage of the radiation through the sample, or its effect on the radiation, can then be measured. Note that it is the ratio of measurements with and without the sample that gives the final frequency spectrum for the sample itself. All FTS measurements described in this thesis were carried out with the Space Science and Technology Group, Rutherford Appleton Laboratory [64]. Further details on the FTS technique can be found in [46, 52].

5.2 Electroformed Wire Mesh Filters

Interference filters and Fabry-Perot interferometers have been available for wavelengths up to 20μm, and longer than 6mm, for many years. However, there was nothing available in the far infrared until Renk and Genzel [58] demonstrated the use of metal mesh grids in 1962. They measured the transmission of wire mesh filters designed for $100 - 800\mu$m, achieving a peak transmission of $\sim 90\%$. Since then they have been a staple far-infrared filter.

They are often used in conjunction with other filters to make up a bandpass filter. This approach was investigated by Ressler and Möller [59] who found that a combination of electroformed and wirecloth mesh filters, when chosen carefully, performed well. Rawcliffe and Randal [56] then investigated the use of these filters as part of a Fabry-Perot interferometer. They measured the (individual) transmission of meshes with 5 – 2000 lines per inch made from different metals, with nickel performing best.

Electroformed wire mesh filters were used prior to the experiments described in this thesis. Nevertheless, they are of some relevance since their properties prompted the search for more suitable filters.

5.2.1 Transmission Characteristics

Each filter set used consisted of 11 filters — one for each observation angle. Three sets of these, with 110, 200 and 500 lines/inch, were used prior to the experiments reported in this thesis. Up to two filters were used at once separated by $\sim$ 10mm, *i.e.* combinations of 110/200, 110/500 and 200/500 filters were used as well as single filters. The transmission characteristics of these filters were measured using THz-TDS (Section 5.1.1) as follows:

1. Filters were mounted in a holder that mimicked the experimental arrangement and minimised reflections in the system. This was a 21mm diameter short tube of aluminium, with two slots for holding filters. The holder was mounted in the THz beam path.

2. The background spectrum, *i.e.*without a filter in the holder, was first recorded and averaged over three measurements.

3. The sample spectrum through a filter was then recorded and averaged over three measurements.

4. The ratio of sample to background spectrum was taken. The square of this gives the transmitted power through the filter.

5. Note that all measurements were taken under vacuum to eliminate water absorption lines.

These steps were repeated for each filter (or combination of filters) required. A schematic of the experimental arrangement can be seen in Figure 5.1.

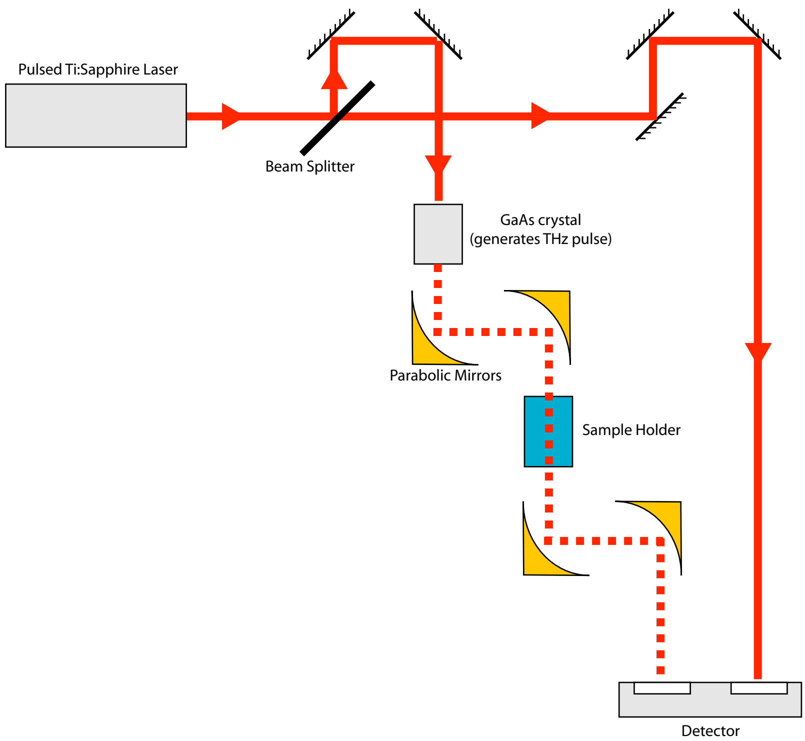

Figure 5.1: A schematic of the experimental arrangement used to measure the transmitted power through electroformed wire mesh filters with THz-TDS.

First, comparisons were made between three nominally identical filters chosen at random. These displayed no significant deviations from each other, and were all in line with the theoretical prediction. When the transmission characteristics of a combination of filters was investigated, for example combining the 110 lines/inch filter and the 200 lines/inch filter, the order filters were placed in was investigated and found to be irrelevant.

The transmission through each individual filter is shown in Figure 5.2. The higher the number of lines/inch a filter has, the steeper the drop in transmission through the filter. The THz-TDS signal is strongest in the region $100 \leq \lambda \leq 1800\mu$m, and within this region the transmitted power is in line with Renk and Genzel's original findings for filters of this type [58]. Peak transmissions of $\sim 90\%$ are achieved at short wavelengths, with the transmitted power dropping rapidly beyond this point.

The transmission characteristics of combinations of filters are shown in Figure 5.3. Peak transmission is reduced to $\sim 10\%$ and the reduction in transmitted power is even more marked beyond this point. Any signal is effectively removed by combining filters with the 500 lines/inch filter.

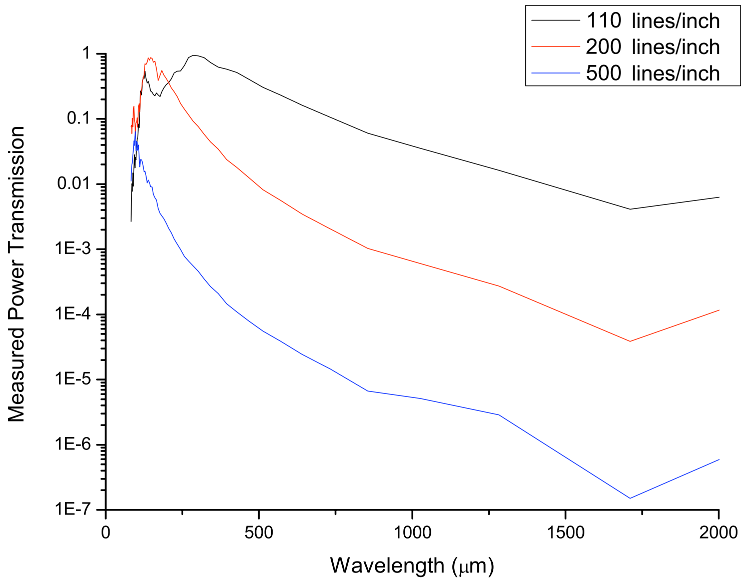

Figure 5.2: The average measured transmission through different wire mesh filters with 110, 200 and 500 lines/inch.

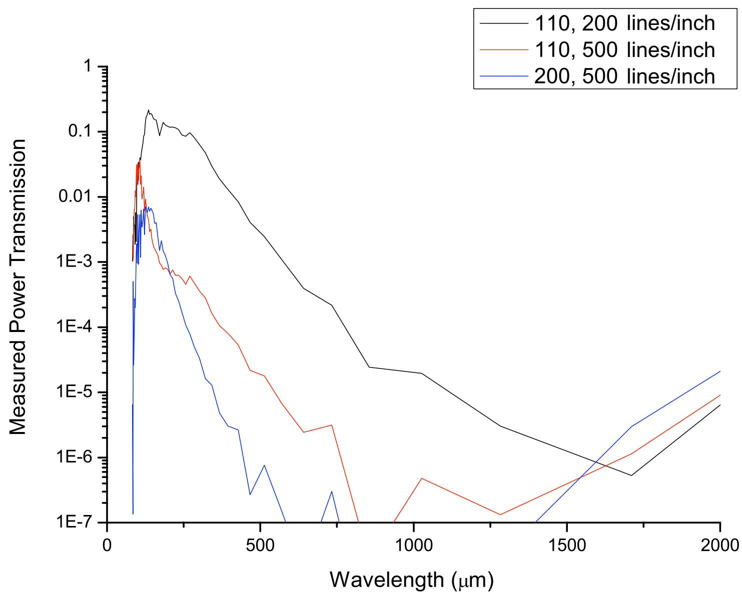

Figure 5.3: The average measured transmission through the following combinations of wire mesh filter: 110/200, 110/500 and 200/500 lines/inch.

5.2.2 Conclusions

These filters were not designed for a specific SP wavelength and so the same filtering is applied to all observation angles. Consider a filter with a smooth, slow drop in transmission towards long wavelengths. In this scenario long wavelengths are subject to increasingly harsh filtering and it becomes difficult to discriminate between SP wavelengths and background radiation. In turn, this has a detrimental affect on the bunch profile reconstruction, which relies on an accurate measurement of all wavelengths. Wire mesh filters do not possess the desired 'top hat' transmission characteristics, and so new filters were investigated to replace them.

5.3 Waveguide Array Plate Filters

Waveguide Array Plate (WAP) filters consist of a metal plate perforated with a periodic arrangement of holes. They were developed, alongside other far-infrared filters, by Ulrich [71], who considered the 2-dimensional pattern of holes as the optical equivalent of the iris in a waveguide. WAP filters have a cut-off frequency and are similar to the coupled waveguide filters used in the microwave region [76].

WAP filters are widely used in the microwave to far infrared and have a number of applications (filters, frequency multipliers, Fabry-Perot interferometers). The shape, size and arrangement of the holes determines the filter's properties. Only filters with circular holes are considered here, since these are the simplest to manufacture. However, there are other filters of this type available — such as cross-shaped bandpass filters — that were discounted due to the difficulties (and costs) associated with making them. Henceforth, a 'WAP' filter refers to a metal disc with a periodic, hexagonal array of circular holes (waveguides) in it.

5.3.1 Design and Manufacture

The design, manufacture, and transmission characteristics of these and other similar filters has been investigated by Winnewisser *et al.*[7, 81, 82, 83]. Although the numerical models describing WAP filters are beyond the scope of this thesis, it should be noted that Winnewisser *et al.* found very good agreement between the model used and the manufactured filter's transmission [7]. The most common models used (and tested in [7]) employ the Finite-Difference Time-Domain (FDTD) or Finite-Element Method (FEM) techniques.

WAP filters were acquired in two stages:

1. 17 filters were designed by the Rutherford Appleton Laboratory (RAL), and four of each design were then manufactured in Oxford. These correspond to first order SP wavelengths from the 0.5 and 1.0mm gratings, along with the $40-110°$ observation angles of the 1.5mm grating. This set of filters was used during the FELIX experiment (Chapter 8).

2. A further 11 filters were later designed and manufactured in Oxford, using the same criteria as the RAL designs. These additional filters correspond to first order radiation from the $120-140°$ observation angles of the 1.5mm grating, as well as completing a set of filters (all angles) for second order radiation from the 1.5mm grating. These were used during the SLAC experiments (Chapters 9 and 10).

Each filter was a 21mm diameter brass disc with a hexagonally close-packed array of holes drilled in it. Therefore, the design was limited by the available drill size, d. This determined the final design of the second (Oxford) set of filters, according to the following ratios obtained from the original RAL filters

$$
\begin{aligned}
\lambda_c &= \frac{cd}{1.758\times10^5}, \\
\lambda_{\mathrm{peak}} &= \frac{1}{1.2}\lambda_c, \\
s &= \frac{d}{0.7433}, \\
w_{\mathrm{min}} &= \frac{d}{2.8856}, \\
t &= \frac{d}{0.4005}, \\
a &= 6\left(1\times10^{-12}\frac{\sin 30}{\sin 60}\right)\left(\frac{s}{2}\right)^2, \\
A &= \pi r^2, \\
N &= \frac{A}{a},
\end{aligned}
$$

where λ_c is the cut-off wavelength for a filter of finite length, λ_{peak} is the wavelength at which peak transmission occurs, s is the separation between adjacent holes (in μm), w_{min} is the minimum wall distance (in μm), between two adjacent holes, t is the thickness of the filter, a is unit area of one hexagon surrounding each hole, A is the total area of the filter, and N is the number of holes (see Figure 5.4). Table 5.1 gives the design parameters of the original filters designed by RAL, and Table 5.2 gives the design parameters of each filter from the Oxford set.

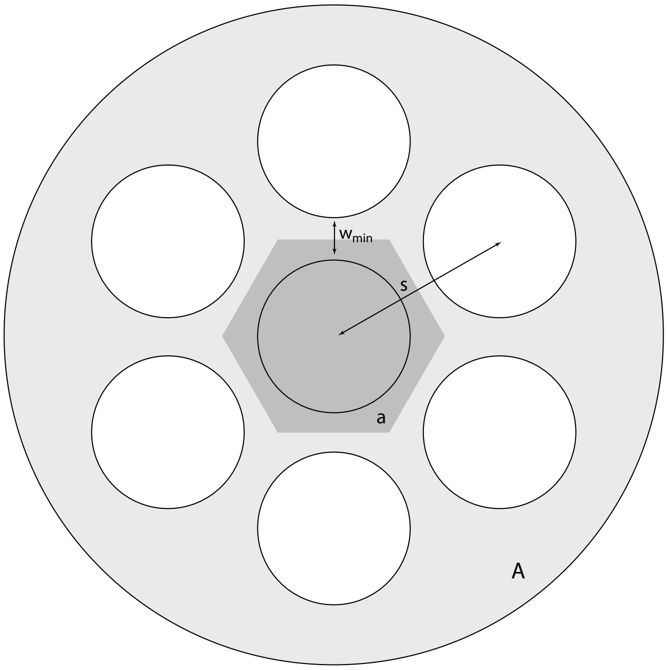

Figure 5.4: Diagram of a WAP filter and the variables used to design one (see text for details).

5.3.2 Transmission Characteristics

A detailed study of all the filters made and used experimentally was necessary to fully account for transmission losses in the optical system. The measurements were carried out with THz-TDS and FTS (see Sections 5.1.1 and 5.1.2), and measurements of the same filter were consistent between the two approaches. The THz-TDS measurements were primarily used for the short wavelength WAP filters, and were carried out as in Section 5.2.1, with the filter instead held in a lens holder.

FTS measurements were carried out for the longer wavelength filters using a mercury arc lamp in the arrangement shown in Figure 5.5. The radiation was chopped at 524Hz before passing through the interferometer, after which it was focused onto the filter and the liquid helium cooled InSb detector. All of these measurements were carried out, in air, as follows:

1. A block holding a filter was positioned in front of the InSb detector. This had an aperture slightly smaller than the filter itself. The block had a magnetic base that ensured it was returned to the same position each time.

λ_{SP} (mm)	λ_c (mm)	d (μm)	s (μm)	w_{min} (μm)	t (μm)	N
0.2340	0.2896	170	229	59	425	7628
0.3289	0.3984	230	310	80	575	4167
0.3571	0.4392	260	350	90	650	3261
0.4076	0.4894	290	391	101	725	2621
0.5	0.5758	340	458	118	850	1907
0.5871	0.6593	390	525	135	975	1449
0.6579	0.7979	470	633	163	1175	998
0.6711	0.7335	430	579	149	1075	1192
0.8219	0.8547	500	674	174	1250	882
0.8264	0.9772	570	768	198	1425	679
0.8824	0.9063	530	714	184	1325	785
1.0	1.1494	670	902	232	1675	491
1.1719	1.3216	770	1037	267	1925	372
1.3393	1.4706	860	1158	298	2150	298
1.5	1.5957	940	1266	326	2350	249
1.6393	1.7143	1000	1347	347	2500	220
1.7647	1.8072	1060	1428	368	2650	196

Table 5.1: Design parameters of the original 17 WAP filters designed by RAL.

λ_{SP} (mm)	λ_c (mm)	d (μm)	s (μm)	w_{min} (μm)	t (μm)	N
0.2679	0.3242	190	256	66	474	6121
0.375	0.4607	270	363	94	674	3031
0.6197	0.7509	440	592	152	1099	1141
0.75	0.9044	530	713	184	1312	787
0.8802	1.058	620	834	235	1548	575
1.0065	1.2116	710	955	246	1773	438
1.125	1.3652	800	1076	277	1998	345
1.2321	1.4846	870	1170	302	2172	292
2.25	2.4824	1600	2159	556	4007	86
2.4642	2.4874	1750	2361	608	4381	72
2.6491	3.1993	1870	2522	650	4681	63

Table 5.2: Design parameters of the remaining 11 WAP filters designed at Oxford (see text for details).

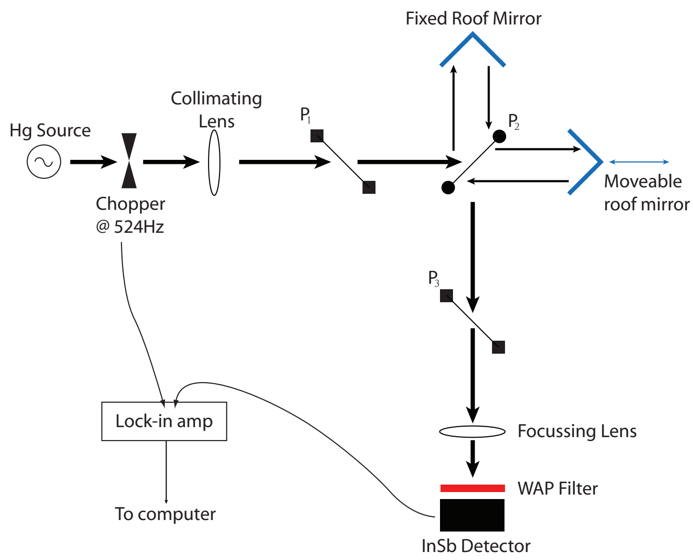

Figure 5.5: The Fourier Transform Spectrometer, as used to measure the transmission characteristics of a Waveguide Array Plate filter. $P_{1,3}$ are vertically aligned polarisers, and P_2 is a polariser aligned at 45°, which acts as a beam splitter.

2. The interferometer scanned over 1024 points up to a maximum frequency of 2THz (with 2GHz frequency resolution), waiting 100ms between each point.

3. The Fourier transform of the interferogram was recorded.

4. The filter block was replaced with a nominally identical block without a filter. This gives a reference spectrum after repeating the previous steps.

5. Three measurements of each filter were taken, interspersed by reference measurements.

6. The ratio of the average filter measurement to average reference measurement then gives the power transmitted through the filter.

7. These above steps were repeated for all measured filters.

Figure 5.6 shows the transmitted power through three different, individual filters. These transmission curves are typical of the vast majority of the filters. Of particular note is the fact that the designed SP wavelength occurs very close to the cut-off wavelength in all cases. Beyond this point the transmission drops rapidly. However, the design cut-off wavelengths are an underestimate compared to the measured values — the actual position of the cut-off wavelength is consistently longer than the design value. Even so, the SP wavelength occurs at, or very close to, the measured peak transmission point.

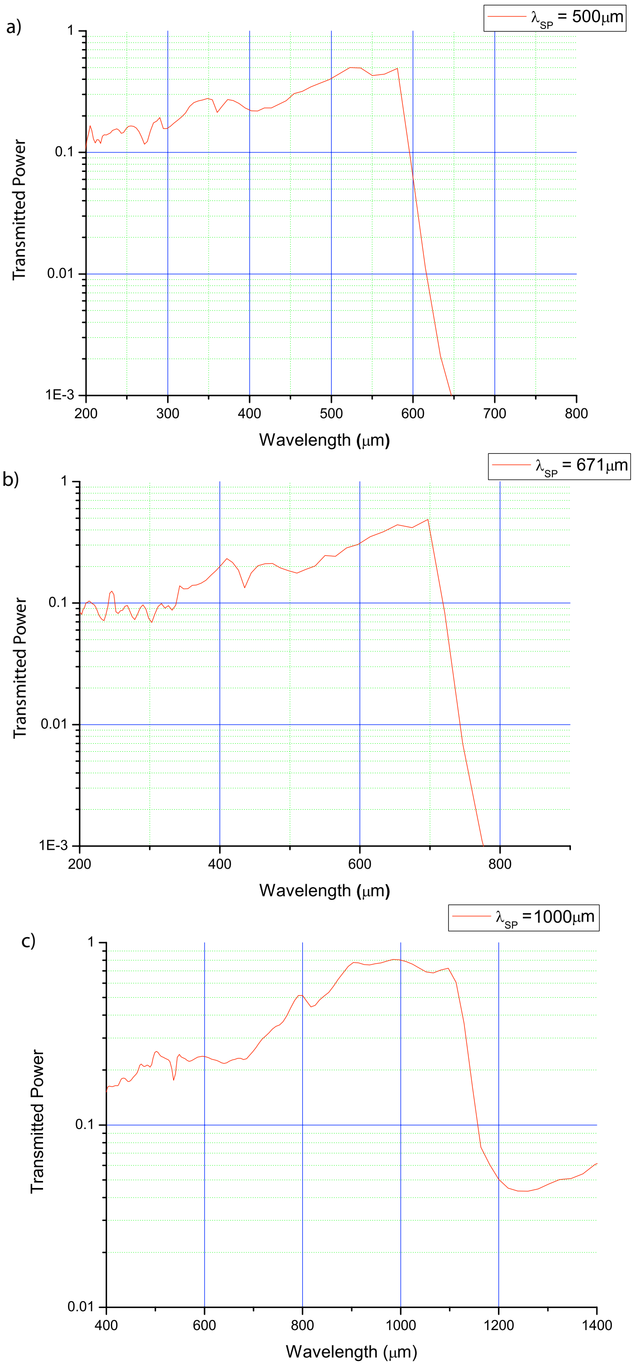

Figure 5.6: Measured transmitted power from three different WAP filters: a) $\lambda_{\text{SP}} = 500\mu\text{m}$, b) $\lambda_{\text{SP}} = 671\mu\text{m}$ and c) $\lambda_{\text{SP}} = 1000\mu\text{m}$.

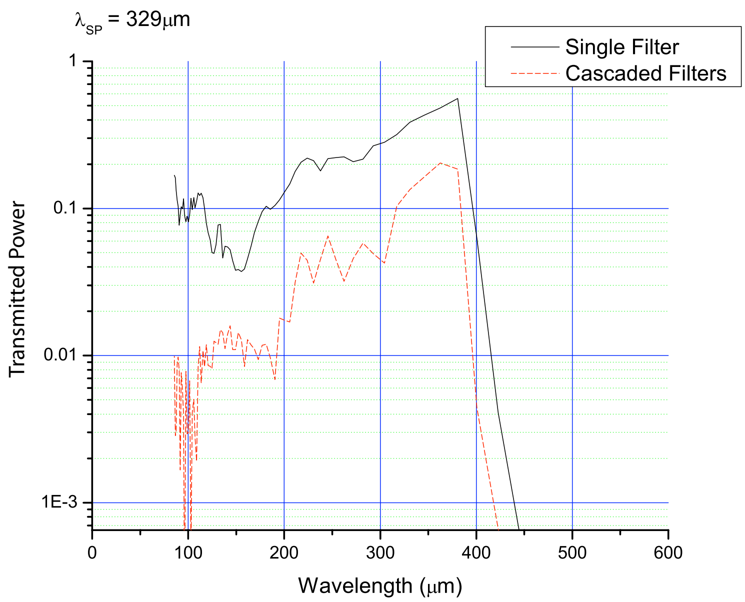

Figure 5.7: Measured transmitted power for a single and cascaded WAP filter.

Using two filters together (cascading), separated by $\sim 1-2$mm, results in a steeper cut-off wavelength transition. Figure 5.7 shows the transmission through a single filter (black, solid) and two cascaded, nominally identical, filters (red, dashed). The drop in transmission beyond the cut-off wavelength is steeper in the cascaded arrangement, however, there is also a drop in the overall transmitted power. Therefore, the benefits of sharper discrimination versus long wavelength background radiation are balanced by a much lower overall transmission. Only single filters were used experimentally as a result of these measurements.

Measurements with two filters were also carried out to test their polarisation dependence. The transmission was measured first through two filters, and then again through the same filters where one had been rotated through 90°. No difference was observed in the transmitted power, and therefore WAP filters are polarisation independent.

The manufacturing tolerances were also of interest since WAP filters are non-trivial to manufacture. For example, a filter for $\lambda_{\mathrm{SP}} = 0.23$mm requires a drill size of 170μm diameter making 7628 holes in a precise hexagonal array. This requires great precision, since it is the size and arrangement of the holes that determine the filter properties. Thus, two nominally identical filters were first compared (Figure 5.8). These filters had no obvious defects visible by eye, and indeed their transmission curves coincide as expected.

Figure 5.9, however, shows a filter whose defects are visible by eye. This was a particularly interesting measurement to make, comparing the transmission through this filter to a good

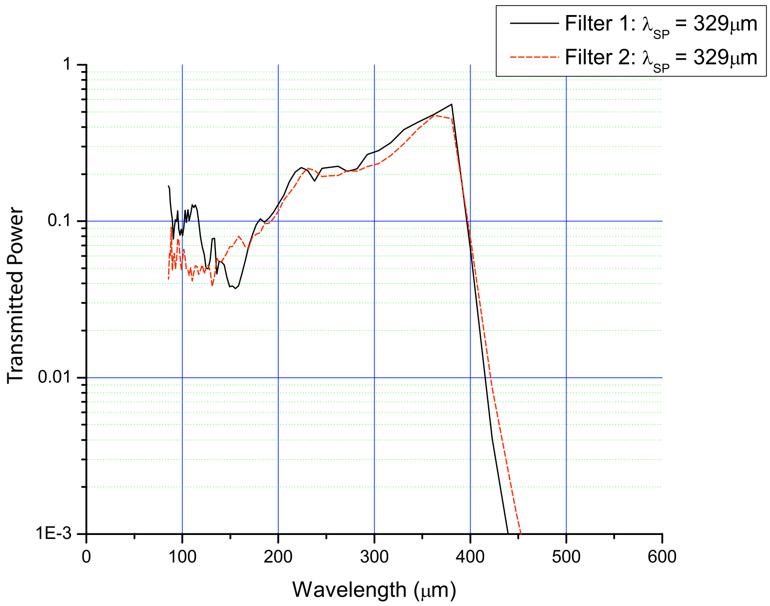

Figure 5.8: Measured transmitted power for two nominally identical WAP filters.

filter of the same wavelength (λ_{SP} = 1mm). The transmitted power through each filter is shown in Figure 5.10. It is obvious that the misplacement of the holes had a drastic effect on the quality of the filter. This reinforces the fact that it is the size, shape and *arrangement*of the holes that determines the filter properties. Therefore, it is essential that filters possess minimal manufacturing errors. Conversely, measuring the filter's transmission properties can easily reveal manufacturing errors that may be too small to be seen by the naked eye. As a result of this measurement, all filters were checked both visibly and by transmission measurement. Thus, sub-standard filters were discarded before they could be used experimentally. The actual transmission efficiency of each filter is given in the appropriate chapter where that filter was used experimentally (Chapters 8 – 10).

5.3.3 Conclusions

It becomes much more difficult to manufacture WAP filters for short wavelengths due to the small hole sizes, and hence, small drill sizes required. Errors whilst making these filters can have a large impact on their quality. However, it is easy to determine the filter's quality by either a transmission measurement or examining the filter carefully by eye.

Overall, these filters are excellent at removing wavelengths longer than a desired wavelength. However, the cut-off wavelength is consistently longer than the design wavelength. Even so,

a)

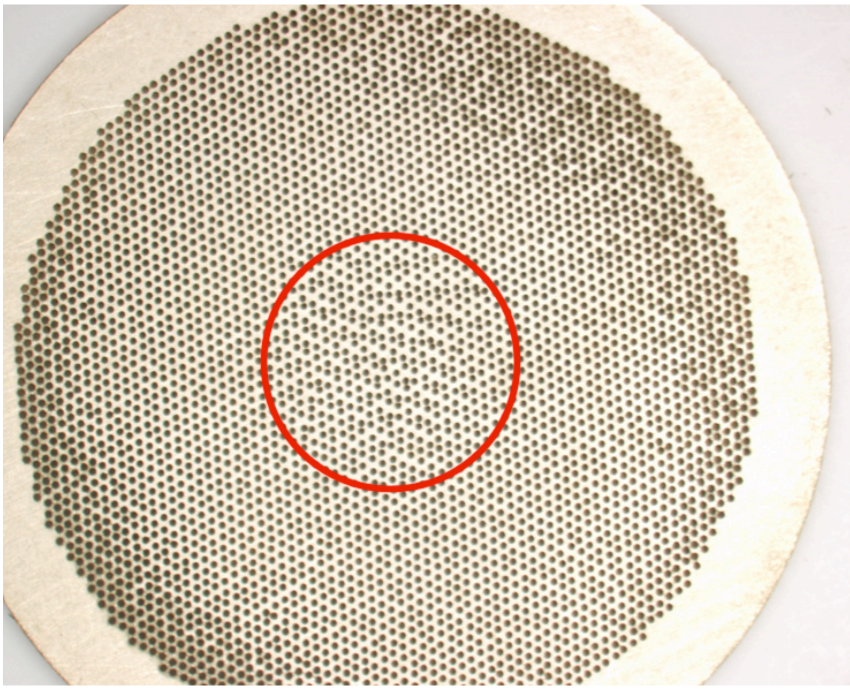

b)

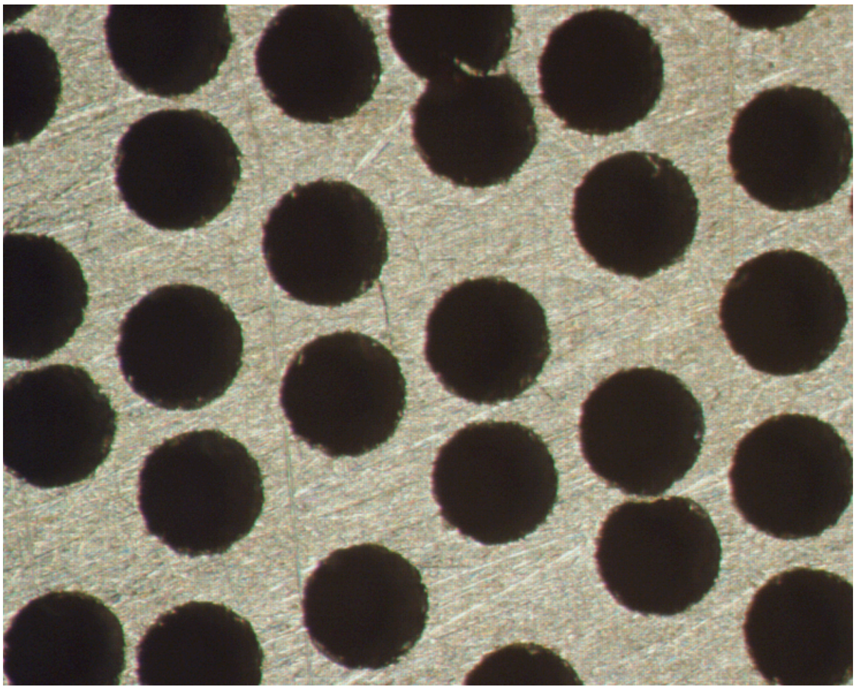

Figure 5.9: Manufacturing errors in a WAP filter: a) $\lambda = 1$mm filter with obvious deviations from the hexagonal close-packed structure, the clearest example of which is within the circled area b) a close-up of these deviations.

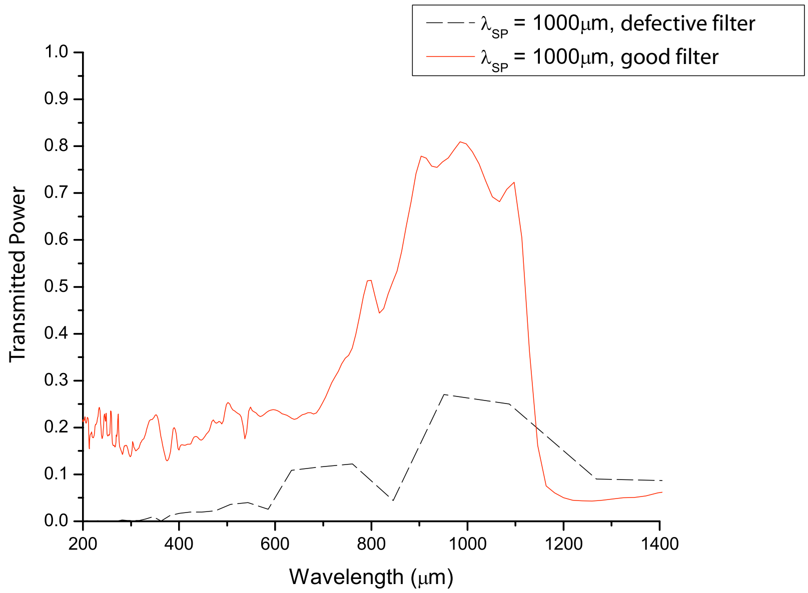

Figure 5.10: The measured transmitted power for a $\lambda = 1$mm WAP filter with and without obvious manufacturing errors.

peak transmission occurs at approximately the SP wavelength. It is also worth noting that the Oxford designed filters were of similar quality to those from RAL.

5.4 Comparison of Filters

For this particular application, WAP filters are a definite improvement over wire mesh filters. Figure 5.11 shows how the transmitted power through a WAP filter for $\lambda_{SP} = 329\mu$m compares to the three wire mesh filters discussed in Section 5.2.1. The WAP filter has a high transmission at $\lambda = 329\mu$m, compared to the wire mesh filters, and drops sharply beyond $\sim 350\mu$m. This sharp drop in transmission makes them much more desirable, since background wavelengths beyond this point are almost completely removed, whilst the SP wavelengths are left relatively untouched.

Overall, WAP filters transmit more power at the desired wavelength, and remove unwanted long wavelengths efficiently. They also provide a small measure of short wavelength discrimination. As such, they satisfy both of the conditions laid down at the start of this chapter — *i.e.*filters must be able to remove unwanted background radiation while efficiently transmitting the SP wavelengths.

Unlike wire mesh filters, however, WAP filters require an individual filter for each observation angle and grating used. Although some wavelengths (from different gratings) overlap, reducing

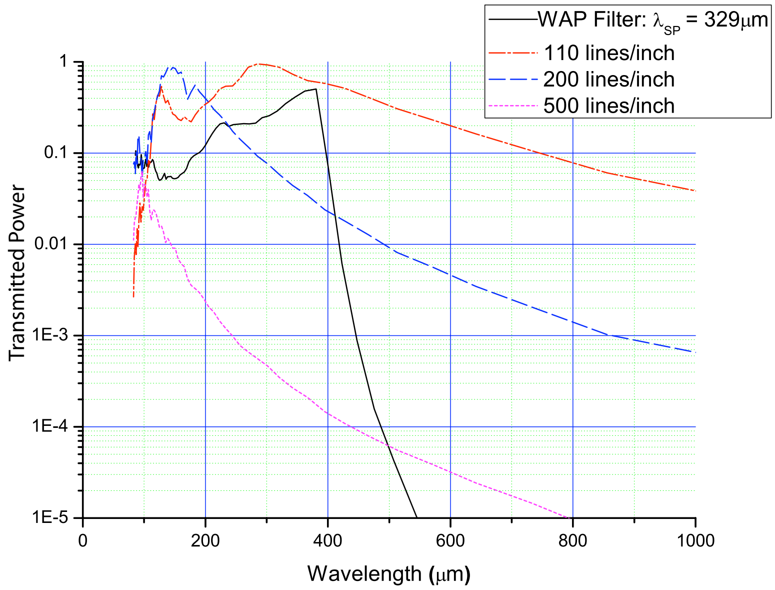

Figure 5.11: Comparison of $\lambda_{\rm SP} = 329\mu$m WAP filter and three wire mesh filters with 110, 200 and 500 lines/inch.

the total number of filters made, 11 filters must be used for each grating. This introduces some complications, for example, the need for a mechanism to change filters according to the grating used. As such, WAP filters are: i) Not as easy to make and use as wire mesh filters, ii) are more expensive, since more filters must be made, and iii) are time consuming as transmission measurements must be made for each individual filter.

5.5 Summary

The SP experimental setup required filters to: (a) Remove background radiation, and (b) verify that the observed wavelengths are the expected SP wavelengths. Two different types of filters have been considered in this chapter. The first of these, electroformed wire mesh filters, is discussed in Section 5.2. These filters were used prior to the experiments described in this thesis, but they were quickly found to be unsatisfactory for this purpose.

Waveguide Array Plate, or WAP, filters were used throughout the experiments described here. They are described in detail in Section 5.3. The transmission properties of single and multiple filters, along with the effect of manufacturing errors, is discussed in Section 5.3.2.

Section 5.4 compares the two filter types used. WAP filters give far better discrimination against non-SP wavelengths, and can be used to verify the wavelength seen. They have a high transmission around the desired SP wavelength, with a sharp cut-off on the long wavelength side. This makes them a far more suitable filter than wire mesh filters. However, they are also more difficult (and expensive) to make, and incur some complications for the experimental setup.

Chapter 6

Pyroelectric Detectors

The experiments described in Chapters 8 – 10 used 11 pyroelectric detectors viewing at 40 – 140° with respect to the beam direction. Each detector observed a restricted set of angles, and thus a set range of wavelengths.

Each SP measurement consisted of recording 11 individual detector signals. It was important to judge how one detector responded compared to another and, hence, to relate these signals to each other. For example, the naive approach of treating all signals equally is unsatisfactory if one detector is more or less sensitive than others. It has been suggested in the literature [89] that the response of pyroelectric detectors can oscillate with respect to each other as well as with wavelength. Thus, it was necessary to calibrate all of the detectors used experimentally in two ways:

- Relative calibration: allowed a proper comparison of all measured signals.
- Absolute calibration: allowed the signal detected by the detectors to be converted to Joules and ensures all detectors are within the manufacturer's specifications.

Comprehensive calibration measurements in the far infrared — including the experimental range considered here ($0.12 \leq \lambda \leq 2.64$mm) — with this type of detector are few and far between. Therefore, it is very important to measure the response of each detector carefully at all expected SP wavelengths.

6.1 The Pyroelectric Detector

Far infrared detectors are usually one of two types: Photoconductive, or thermal. Pyroelectric detectors belong to the latter group. Thermal detectors typically work by 'heating' an absorber;

the detector surface, or volume, absorbs the radiation. A change in temperature then generally results in a measurable, physical change that is converted to an electrical signal via a sensor or transducer. Thermal detectors are typically slow to respond and their wavelength response depends on the characteristics of the absorbing material.

Pyroelectric detectors use a material that has a permanent electric dipole moment. For example, ferroelectric crystals possess this property. When the temperature of the material is changed its dipole moment also changes. If this happens quickly, charges on the surface do not redistribute themselves quickly enough, which results in an electric potential difference. The magnitude of this signal depends upon the change in temperature and the efficiency of the material used. This is known as the *pyroelectric effect*.

Note, however, that it is a change in temperature that generates the signal. Therefore, the radiation being detected must either be naturally pulsed, or mechanically chopped, for example, with a rotating blade. SP radiation is an example of the former effect since the emission of radiation depends upon the repetition rate of the beam. In the case of the calibration measurements, the radiation must be chopped mechanically since a source of constant radiation was being used.

Pyroelectric detectors have been used in the infrared for many years and have been extensively studied [3, 13, 45]. The model used during the SP experiments was the Eltec 400 [16] with no window covering the detector housing. The pyroelectric element was a lithium tantalate ($LiTaO_3$) crystal, 2mm in diameter. The detector absorbs radiation at angles of incidence up to 60°, although the absorption efficiency is not constant with increasing angle. This, in turn, affected the design of the Winston cone (see Section 7.3).

6.2 Calibration in the Far Infrared

Calibration measurements are particularly difficult in the far infrared as sources are limited. The most suitable source types would be bright and tunable (or bright and broadband with an interferometer) yet these are not readily available in this region. For example, thermal sources only produce a small amount of their power in the far infrared, especially at long wavelengths. Sources that cover the entire range of wavelengths required to calibrate SP detectors (*i.e.* in the region $\lambda = 0.12 - 2.64$mm) are not generally available. Therefore, different sources had to be used and the results pieced together, which is not optimal. Where a tunable source was not available, filters were used to isolate a specific range of wavelengths from a broadband source.

Absolute calibration is also complicated as it is non-trivial to measure the power emitted by the source at various wavelengths. Therefore, measurements here are restricted to confirming that the detectors used conform to the manufacturer's specifications. Anything further than this becomes difficult in this wavelength region.

There are many sources of noise in this wavelength region that can affect the accuracy of the calibration. In order of decreasing contribution these are:

- *Environmental Noise*. The signal generated by the detector fluctuates due to variations in the emitted blackbody radiation of the surroundings. This is typically the largest contribution to errors when calibrating room temperature detectors.

- *Amplifier noise*. The amplifier used during calibration was different (slower) from that used at SLAC. The amplifier was optimised for noise performance with the pyroelectric detectors for frequencies in the range of 10 to 50Hz [54]. It was also particularly sensitive to drifts in temperature, for example, when handling/installing the detector, or walking around the setup during measurements.

- *Electrical fluctuations*in the detector.

- *Fluctuations in the source*. This is typically small compared to background radiation.

All of these contribute to the difficulty of taking accurate calibration measurements in the far infrared.

The primary goal of these measurements was to define the response of each detector relative to a reference (pyroelectric) detector's response at a specific wavelength. As with other calibrations, the detectors are also compared to the response of a Golay cell (Section 6.3). The reference detector was chosen to be the one that observes at 90° with respect to the beamline when used experimentally. Therefore, all measurements are related to the signal seen by this detector at $\lambda = 1.5$mm. Note that this wavelength was chosen as it was easily available from sources and coincides with the wavelength produced at 90° from the longest period grating used. Calibration relative to what the 90° detector sees at $\lambda = 0.5$ and $\lambda = 1.0$mm (the other grating periods used) was not possible, since these wavelengths were not easily available from calibration sources.

The relative response of each detector was found as follows:

1. Let $S_P(\lambda)$ and $S_G(\lambda)$ be the signals from the pyroelectric detector and Golay cell respectively, for the same power level, at wavelength λ.

2. Let $R_P(\lambda = 1.5)$ and $R_G(\lambda = 1.5)$ be the signals from the 'reference' pyroelectric detector and Golay cell, respectively, at $\lambda = 1.5$mm.

3. The response of each detector relative to the Golay cell can then be found:

$$S(\lambda) = \frac{S_P}{S_G}, \tag{6.1}$$

while the response of the reference detector, at the "reference" wavelength ($\lambda = 1.5$mm), is given by

$$R(\lambda = 1.5) = \frac{R_P}{R_G}. \tag{6.2}$$

4. The relative responsivity of the pyroelectric detector used in step 1 at wavelength λ is then defined as

$$D(\lambda) = \frac{S}{R}. \tag{6.3}$$

This must be repeated over all measurable wavelengths, resulting in the relative calibration of all detectors to the reference detector at $\lambda = 1.5$mm.

6.3 The Golay Detector

This detector was invented by Golay in 1947 [19], and has been a staple far infrared detector ever since. Golay cells are typically used when calibrating other detectors in the far infrared since they have a well-known, relatively flat response across this part of the spectrum. They consist of a chamber of xenon gas, which has low thermal conductivity, and a window at one end that is transparent to infrared radiation (*e.g.*diamond or crystalline quartz). At the other end of the chamber is a flexible mirror. In between there is a thin absorbing film, usually made from aluminium, which has an impedance approximately the same as that of free space. Golay cells typically have an active area of 6mm diameter.

When radiation enters the chamber it is absorbed by the film, which in turn heats the gas. The increase in pressure deforms the flexible mirror and causes it to move slightly. The deformation is converted into an electrical signal by light that passes through a double-lens system onto the back of the mirror and thence back towards a photocell.

There are a number of environmental conditions required to maximise the Golay's performance:

- Draughts, that can cause rapid changes in temperature that can affect the Golay, must be minimised.
- The temperature of the room must be kept as steady as possible throughout the experiment.
- Vibrations must be minimised.
- For maximal signal to noise, the signal should be chopped between 10 – 20Hz.

6.4 Relative Calibration: Long Wavelengths

As a single tunable source covering the entire SP wavelength range of $\lambda = 0.12 - 2.64$mm was not available, the calibration measurements had to be split over available sources. Tunable sources were available in the $\lambda = 1.2 - 2.4$mm region, however, in the form of photomixers. Photomixers use two temperature tuned lasers ($\lambda = 1.55\mu$m) and far-infrared radiation is generated by altering the frequency difference between the two. The lasers then interfere in a photodiode, generating a beat signal. The photodiode output is coupled to a hollow waveguide. When the laser frequency separation is above the cut-off frequency of the waveguide, 60GHz, the difference frequency signal can propagate [24]. Therefore, the power output varies with wavelength; giving maximum power in a narrow band of wavelengths and tailing off to either side. Since the source power is wavelength-dependent, the Golay cell is critical for characterising the spectrum as it has a relatively flat response across all wavelengths in this region.

A chopping frequency of 14Hz was chosen to complement the slow amplifier used during these measurements. This was kept constant throughout all of the calibration experiments described in this chapter so as to keep the detector gain constant. The chopping blade was placed at an angle of $\sim 45°$ w.r.t. the incident radiation. This meant that it could be used as a reflector itself, reflecting $\sim 50\%$ of the source power towards the Golay cell. Reflected radiation was focused onto the Golay cell by a parabolic mirror and lens arrangement, whilst transmitted radiation

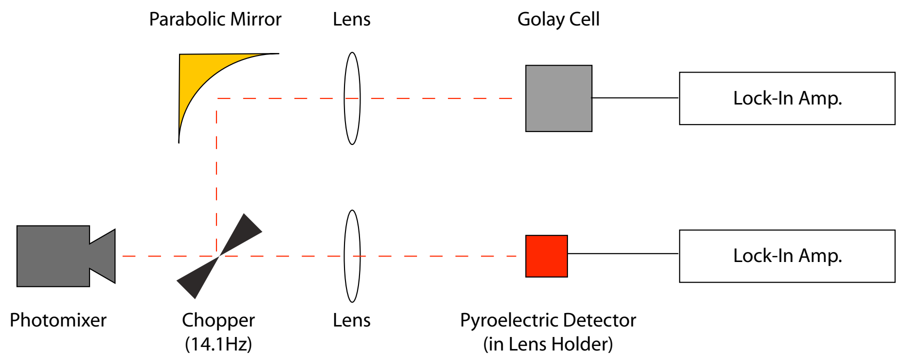

Figure 6.1: Experimental arrangement for the long wavelength calibration of a set of pyroelectric detectors.

was focused onto the pyroelectric detector via a lens. Both pyroelectric detector and Golay positions were optimised to receive maximum power, ensuring that they were both at the focal points of their respective lenses.

The pyroelectric detector was held in a lens holder on a translation stage, and care was taken to ensure that the detectors could be removed and returned to the same position each time. Rotation of the detector within the lens holder had no bearing on the signal seen. The pyroelectric detector and Golay cell were connected to separate lock-in amplifiers with a time constant of 3 seconds. Readings were taken simultaneously after allowing ~ 30 seconds per measurement for the signal to settle. Figure 6.1 shows a schematic of the experimental arrangement used.

Two photomixers were used in total, one spanning the range $\lambda = 1.03 - 1.58$mm, and the other $\lambda = 1.24 - 2.68$mm. These sources differed slightly in their use, and the procedure for each measurement is given below.

6.4.1 1.03 – 1.58mm Photomixer Procedure

This source differs from the following photomixer source in that it was tuned to maximise its power output at each wavelength. Therefore, a 'tuning detector' was randomly chosen at the start of these measurements. Prior to each measurement, this detector was inserted and the signal seen by it maximised by tuning the photomixer source.

Wavelengths were chosen by keeping one laser temperature constant and varying the temperature of the second laser, thus changing the frequency difference between them and producing different output wavelengths. Measurements were made as follows:

1. The source was tuned to provide maximal power using the tuning detector and Golay cell.

2. A pyroelectric detector was placed in the lens holder, ensuring that the rear of the detector was flush with the rear of the lens holder.

3. After approximately 30 seconds, the readings from the pyroelectric detector and Golay lock-in amplifiers were recorded.

4. Another detector was put in the same position in the lens holder and the above was repeated for each consecutive detector.

5. Once all detectors had been measured, another wavelength was chosen and the photomixer re-tuned. Measurements were taken at $d\lambda \sim 0.04$mm intervals.

6.4.2 1.24 – 2.68mm Photomixer Procedure

This photomixer source could not be tuned. Therefore, the order of measurements differs slightly from before. Nevertheless, the setup remains the same.

1. A pyroelectric detector was put in the lens holder, ensuring that the rear of the detector was flush with the rear of the lens holder.

2. One laser's temperature was kept constant, whilst the other was varied to produce different wavelengths.

3. A reading was taken from both the pyroelectric detector and Golay lock-in amps after waiting approximately 30 seconds for the signal to stabilise.

4. This was repeated over the whole range of the photomixer at 0.04mm intervals.

5. Steps 1 – 4 were repeated for all pyroelectric detectors used experimentally.

6.4.3 Calibration Results

The relative calibration of each detector was calculated according to Equations 6.2 and 6.3. The average relative response value was taken when measurements exist from multiple sources at the same wavelength. Eleven detectors were calibrated in this fashion, all of which were used at known positions during the SLAC experiments (Chapters 9 and 10). At the time, each detector was numbered from 1 – 16 (the total number of available detectors), and their positions in the experimental arrangement recorded. The reference detector is detector number 13.

Figure 6.2 shows the variation in response of two detectors relative to the reference detector. The SP wavelength that would be detected by these detectors is marked by a circle. Although the

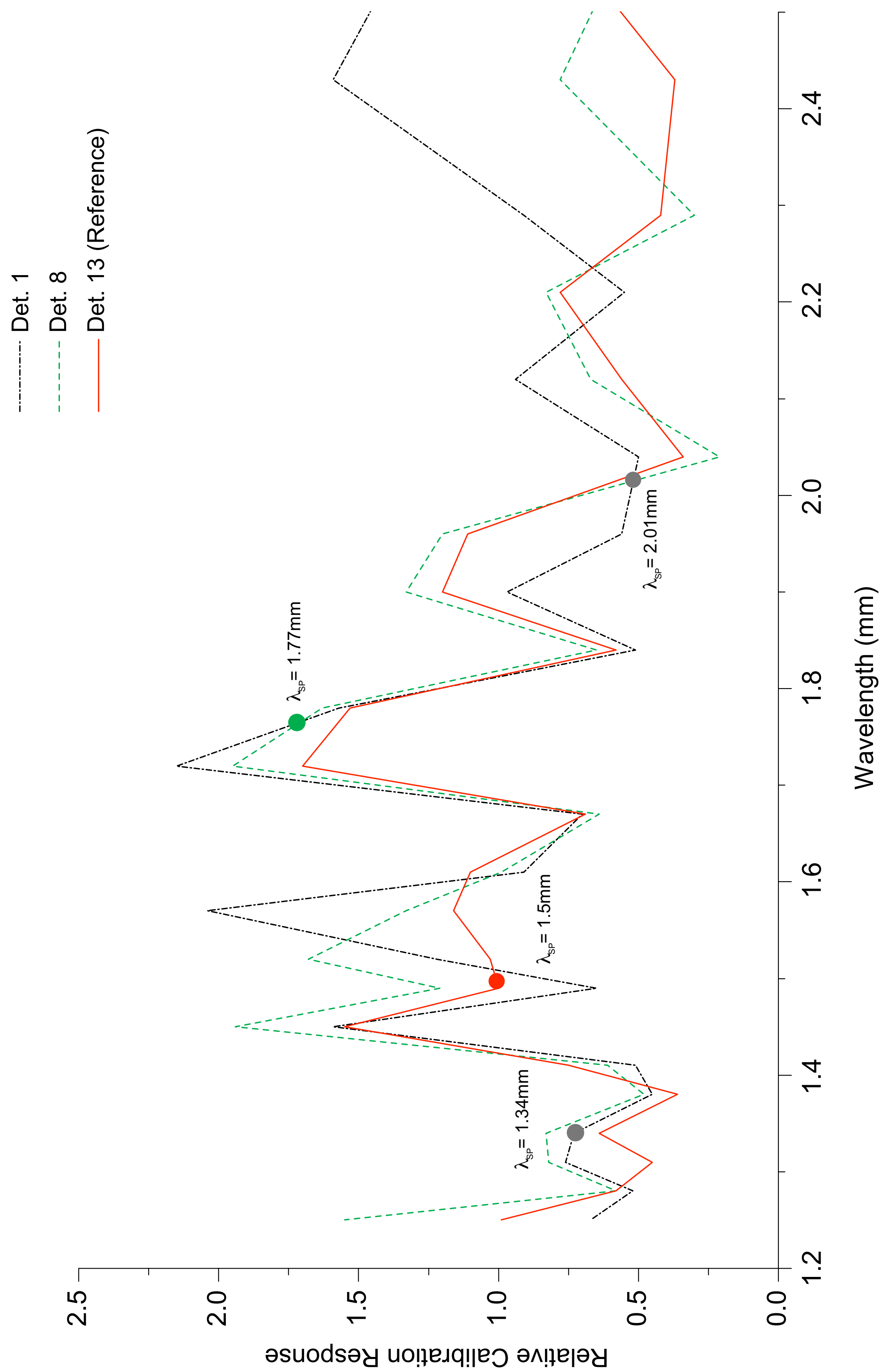

Figure 6.2: The measured response of two detectors (numbers 1 and 8) relative to the reference detector (13) from the $1.24 \leq \lambda \leq 2.68$mm photomixer source. The circles correspond to the SP wavelengths expected to be detected by each detector.

Wavelength (mm)	Detector Used	Relative Response
1mm Grating:		
1.17	11	1.56±0.47
1.34	1	0.86±0.26
1.5	7	1.20±0.36
1.64	16	0.77±0.23
1.77	8	1.69±0.51
1.5mm Grating:		
1.24	6	1.53±0.46
1.5	**13 (reference)**	**1.00**±0.3
1.76	11	1.24±0.37
2.01	1	0.52±0.16
2.25	7	0.59±0.18
2.46	16	1.26±0.38
2.65 (extrapolated)	8	0.50±1.8

Table 6.1: The measured relative response of each detector used at SLAC, and the Smith-Purcell wavelength they observe.

response is not flat, they follow the same general trend. This is contrary to what was suggested in [89], where the responses consistently oscillated with respect to each other – *e.g.*when one detector response was high, the other was low and *vice versa*. The results observed in [89] are possibly due to standing waves within the pyroelectric material itself — *i.e.*the detector response depends on its thickness. If this is true, the detectors calibrated here have been manufactured to a higher tolerance so that their thicknesses are more closely matched. Hence their responsivity does not change as dramatically with respect to each other.

The relative response from the 1.03 – 1.58mm source is shown in Figure 6.3 for all detectors. Again, the detectors all follow the same general trend. Note that the source output becomes very weak beyond 1.15 and 1.55mm and, therefore, points in this region are not significant. The majority of the detector responses are within a factor of 2 of the reference detector.

The relative response of each detector to the (first order) SP wavelengths it observes is given in Table 6.1. Within the experimental uncertainty (±30%) the relative response of the majority of detectors was similar to the reference detector at the reference wavelength. Note that this table shows only SP wavelengths for which an equivalent source could be used. Therefore, it is still important to calibrate these detectors at wavelengths less than 1mm.

6.5 Relative Calibration: Short Wavelengths (< 1mm)

Unfortunately, there were no tunable sources available with $\lambda < 1$mm. Therefore, the only solution was to perform a broadband calibration with a black body source, using an approximate

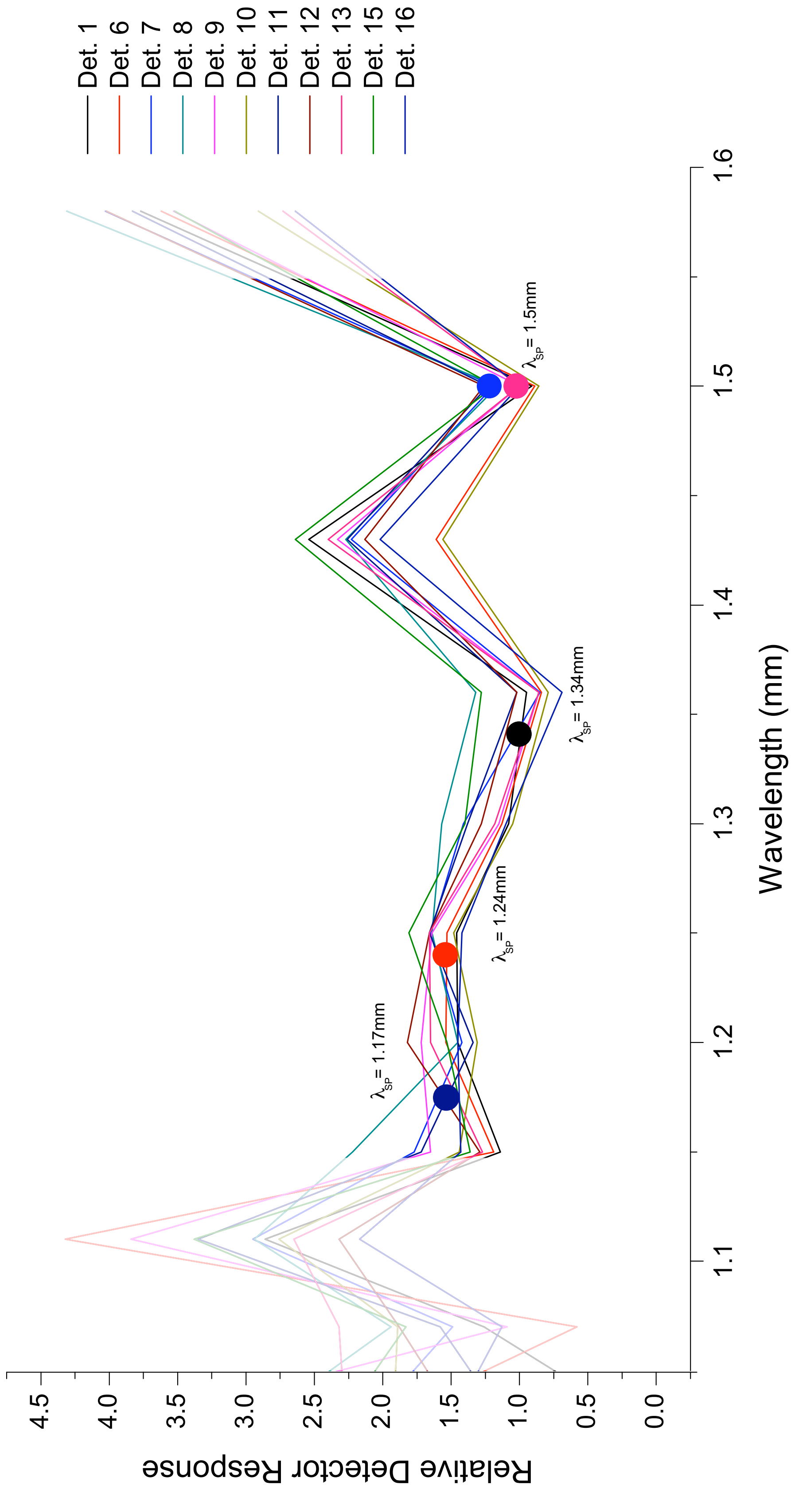

Figure 6.3: Thirteen detectors and their measured response relative to the reference detector (13) at $\lambda = 1.5$mm from the $1.03 \leq \lambda \leq 1.58$mm photomixer source. The circles correspond to the SP wavelengths expected to be detected by each detector.

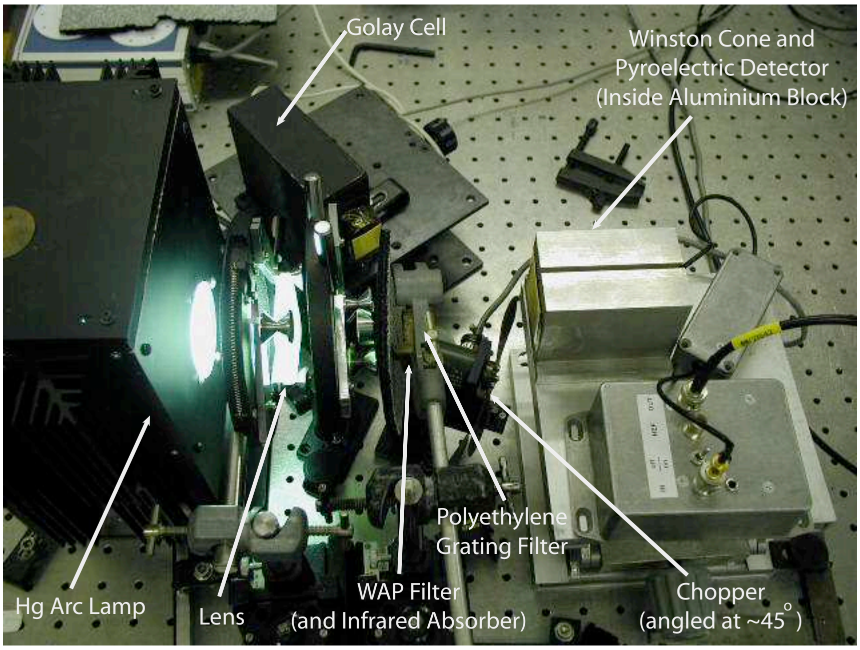

Figure 6.4: The experimental arrangement used whilst calibrating pyroelectric detectors at wavelengths < 1mm.

bandpass filter to isolate the necessary wavelengths. The 'bandpass' filter was made up of two filters: a WAP filter (see Section 5.3) and a polyethylene grating filter. As before, all measurements made at these wavelengths are considered relative to the reference detector measurement at $\lambda = 1.5$mm from Section 6.4.

The experimental setup is shown in Figure 6.4. This compact arrangement used a mercury arc lamp source focused by a lens through a WAP filter whose cut-off wavelength occurred at $\sim$ 1mm. The WAP filter was surrounded by 'Eccosorb' — an infrared and far infrared absorber — to eliminate any radiation leakage around the filter. Immediately after the WAP filter was a 400μm polyethylene grating filter, which scattered short wavelengths and transmitted beyond $\sim$ 200μm [35]. This arrangement restricted the detected wavelengths to approximately 0.5 – 1mm. The transmission curves for the individual and composite filter arrangement are given in Figure 6.5. Although the composite transmission appears to be dominated by the WAP filter, the polyethylene filter was necessary to remove short wavelengths. This was particularly important as the source power increases with decreasing wavelength. The radiation was then incident upon the chopping blades, which, as before, were angled to allow approximately 50% of the radiation to be reflected onto a Golay cell.

The pyroelectric detector was contained inside an aluminium block (see Figure 6.4) and mounted at the end of a Winston cone (Chapter 7) to maximise the amount of power reaching

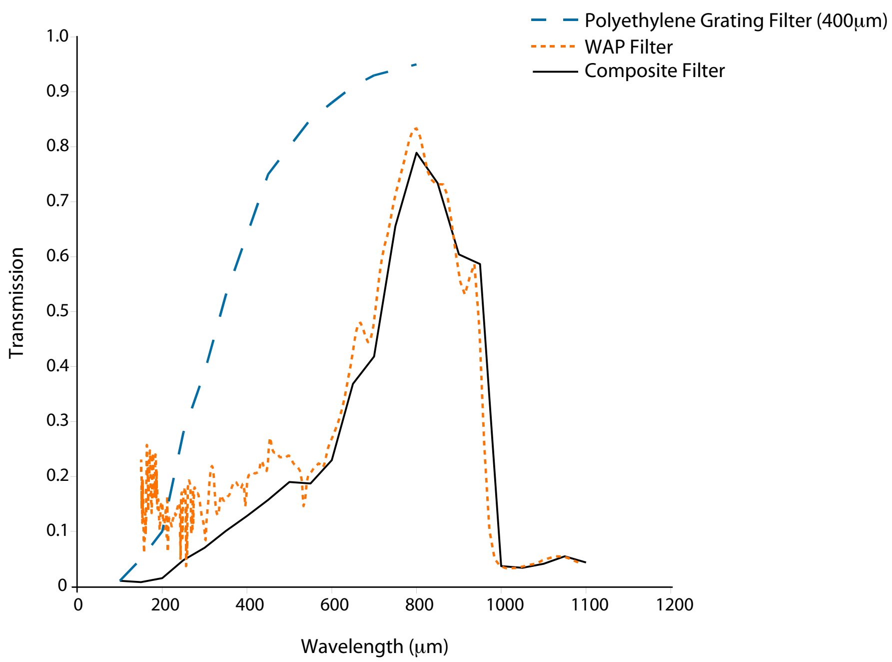

Figure 6.5: Transmission spectra for the 400μm polyethylene grating filter, WAP filter and composite filter.

the detector . Each cone-detector assembly was placed inside the block, with the front of the cone flush with the front of the block. This ensured that detectors were returned to the same position each time. The position of the pyroelectric detector and Golay cell was then optimised so as to receive maximal power.

As in the previous section, the response of each detector was measured in turn along with the Golay's response. However, these measurements required the use of a Winston cone to maximise the power incident on the pyroelectric detector, whereas the previous measurements did not. The Golay cell measurements did not require the use of a cone. Therefore, the effect of the Winston cone must first be taken into account before comparing them to the previous measurements. The Winston cone provides an increase of approximately 26 times the signal detected without one (see Chapter 7). Thus, dividing all of the short wavelength calibration measurements through by this factor gives measurements that can be compared with those of with the previous section.

Therefore, the relative response of each detector in the 0.5 – 1mm region can be found using Equations 6.2 and 6.3, replacing S with

$$S = \frac{S_P}{S_G}\frac{1}{26}.$$

Detector	Relative Calibration
1	1.47±0.44
3	1.49±0.45
6	1.36±0.41
7	1.49±0.45
8	1.34±0.40
9	1.19±0.36
10	1.32±0.40
11	1.28±0.38
12	1.65 ±0.50
13	1.38±0.41
14	1.40±0.42
15	1.61±0.48
16	1.34±0.4

Table 6.2: Measured short-wavelength ($\lambda = 0.5 - 1$mm) relative detector responses.

Table 6.2 gives the measured relative calibration results for this wavelength region. Variations between detectors are small. However, this is a *broadband*calibration covering many wavelengths. Therefore, these measurements are equivalent to the *average*relative calibration of each detector between 0.5 and 1mm. For comparison, treating the previous calibration measurements as a broadband calibration and averaging over all measured wavelengths gives relative responses in the range of 1.2 – 1.5.

6.6 Absolute Calibration

An absolute calibration of the reference detector was carried out at wavelengths of 1.5, 1.8 and 1.82mm using the photomixer sources used in Section 6.4. This was done to determine whether or not the pyroelectric detectors were operating within the manufacturer's specifications. This experiment was carried out directly after those in Section 6.4, and so uses the same experimental arrangement as in Figure 6.1.

The pyroelectric detector holder was mounted on a translation stage. Thus, it could be 'scanned' across the far infrared beam to give an indication of the beam size and the proportion of radiation falling onto the detector itself. A Thomas Keating absolute power meter [65] was used to determine the power output of the photomixer. This has a known response of 0.5μV/μW when the radiation is *chopped at 19Hz*. Therefore, all measurements in this section use a chopping frequency of 19Hz, which must then be scaled to match the previous measurements carried out at 14Hz.

The procedure for each wavelength measured was as follows:

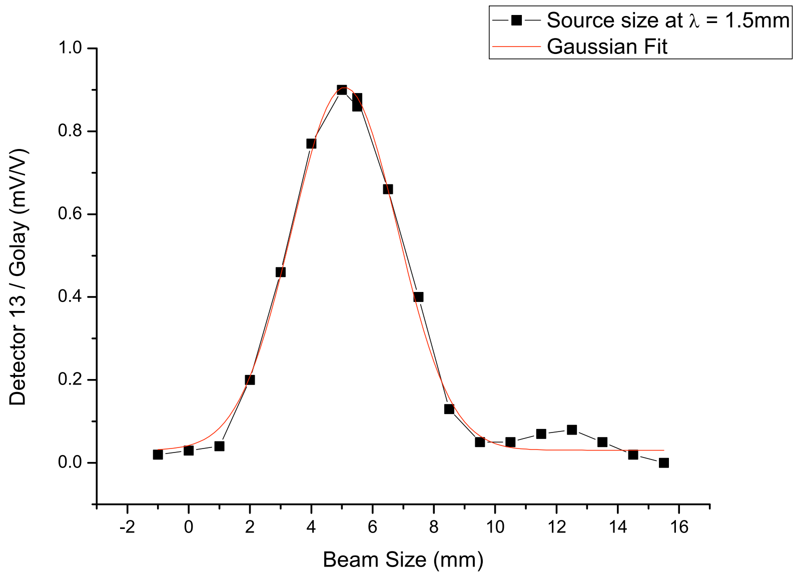

Figure 6.6: Beam size of a photomixer source operating at 1.5mm, as determined by scanning the reference pyroelectric detector across it.

1. The photomixer was set to output wavelengths at either 1.5, 1.8 or 1.82mm.

2. The pyroelectric detector was scanned over the width of the photomixer beam in x, taking measurements every 1mm. This gave the shape of the beam, and allowed the proportion of radiation falling upon the detector to be calculated. The beam spot was assumed to be symmetric in x and y.

3. The absolute power meter was placed in the same position as the pyroelectric detector, angled at the Brewster angle with respect to the photomixer beam. Its output was recorded.

4. The above steps were repeated for the remaining wavelengths.

The absolute power meter's window was large enough to accept the whole of the photomixer beam. Therefore, the output of the absolute power meter represents the total power output of the source. The absolute response of the reference pyroelectric detector can then be calculated as follows.

First, calculate the fraction of the beam, F_B, falling on the pyroelectric detector. Figure 6.6 shows the result of scanning the pyroelectric detector across the photomixer beam ($\lambda = 1.5$mm). The beam can be approximated by a Gaussian in x and y, and the σ of the beam can determined from a Gaussian fit to the data. Given that the detector element had a radius of 1mm, the

Wavelength (mm)	$P_{\text{APM, 19Hz}}$ (μW)	F_B	$P_{\text{Pyro, 19Hz}}$ (μW)	R, Response (μA/W, μC/J)
1.5	2.2	0.19	0.42	1.1±0.3
1.8	5.0	0.11	0.55	1.3±0.4
1.82	4.8	0.13	0.62	1.1±0.3

Table 6.3: Measured absolute calibration of the reference pyroelectric detector.

fraction of beam incident on the detector element is

$$\begin{aligned} F_B &= \left(\frac{1}{\sigma\sqrt{2\pi}}\right)^2 \int_{-1}^{+1}\int_{-1}^{+1} \exp\left(\frac{-x^2}{2\sigma}\right)\exp\left(\frac{-y^2}{2\sigma}\right) \mathrm{d}x\ \mathrm{d}y \\ &= \left(\frac{1}{\sigma\sqrt{2\pi}}\right)^2 \mathrm{Erf}\left(\frac{1}{\sqrt{2}\sigma}\right)^2. \end{aligned} \tag{6.4}$$

The values of F_B are given in Table 6.3.

Calling $P_{\text{APM, 19Hz}}$ the power measured by the absolute power meter, and $P_{\text{Pyro, 19Hz}}$ the power falling on the pyroelectric detector at 19Hz, then

$$P_{\text{Pyro, 19Hz}} = P_{\text{APM, 19Hz}} F_B.$$

The amplifier's response at 19Hz is 120pA/V [54], and so calling S the signal (in Volts) measured by the pyroelectric detectors at 19Hz, the response of the detector, R, is

$$R = \frac{S}{P_{\text{Pyro, 19Hz}}} \times 120$$

in μA/W.

Table 6.3 shows the result of these calculations for measurements taken at $\lambda = 1.5$, 1.8 and 1.82mm. The detector responsivity is in line with the manufacturer's specifications of 0.8 – 1.4μA/W, given the uncertainty estimate of ±30%. Therefore, the average manufacturer's value of 1.1μA/W (or 1.1μC/J) is assumed in all subsequent analysis throughout this thesis.

6.7 Summary

The SP experiments described in Chapters 8 – 10 rely upon measurements taken from 11 individual pyroelectric detectors. One important factor to consider when analysing the data is how the responses of the detectors vary with respect to each other, given that there were suggestions in the literature [89] that the response of these detectors can vary significantly with respect to each other.

Pyroelectric detectors were calibrated by comparing them with the signal measured by a Golay cell (Section 6.3). Two experiments were carried out to determine the relative response of these detectors compared to a reference detector. These were carried out at wavelengths greater than 1mm (Section 6.4) and less than 1mm (Section 6.5).

An absolute calibration measurement was carried out with the reference detector at three different wavelengths: 1.5, 1.8 and 1.82mm. This, and the calculations to derive the absolute response of the detectors, is described in Section 6.6. The response of the reference detector was found to be within the manufacturer's specifications and a value of 1.1μA/W, or 1.1μC/J, has been used in the analysis of the experimental data.

Chapter 7

Winston Cones

Winston cones, otherwise known as light concentrators, are widely used for many applications in physics as they can substantially increase the amount of radiation collected. The SP experiments described in this thesis required a very efficient light collection system as they used small, relatively insensitive detectors to detect radiation emitted over a large angular spread. Special Winston cones were designed and built for the experiment and were tailored to its requirements. This chapter details the design, fabrication and characterisation of these cones.

7.1 Non-Imaging Light Concentrators

Consider the problem of boiling water by concentrating energy from the Sun. The radiated power density, S, received at the Earth's surface is approximately 1kW/m^2 [79]. If this were absorbed by a 'perfect' blackbody absorber its temperature, upon reaching equilibrium, would be $\sim 364°\text{K}$ — just beneath the boiling point of water. In order to increase this temperature, the power density, S, on the absorber must be increased by a factor C.

This is the essence of a concentrator: The ability to increase the power density of incident radiation.The principles of this have been known for centuries, for example, Archimedes used a lens system to focus the image of the sun, producing his 'burning glass'. The problems, therefore, lie in finding (i) the largest value of C that is theoretically possible, and (ii) determining if this is achievable in practice.

The most obvious approach to the problem is to design an image-forming lens system; however, there exists another group of concentrators that would make poor image-forming systems. These are known as *non-imaging concentrators*and the Winston cones designed for the SP ex-

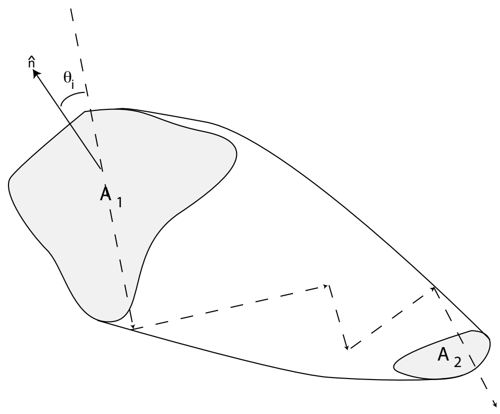

Figure 7.1: A basic conceptual model of a non-imaging light concentrator with entrance aperture area A_1 and exit aperture area A_2.

periments belong to this group. Non-imaging concentrators are unlike other optical systems, possessing some of the properties of light pipes as well as some of the image-forming properties of lenses (albeit with very large aberrations). They are especially useful for situations involving the concentration of multiple wavelengths as their concentration depends only on the reflectivity of the material used and not on its refractive index (as is the case for a lens system). When only concentration is required, non-imaging concentrators can vastly outperform other concentration methods by a factor of four or more. A detailed discussion of the origin, design and use of these concentrators can be found in [79]. A similar approach is adopted here.

7.1.1 The Concentration Factor

The most important parameter of a concentrator is known as its 'concentration factor'. This is a measure of the increase in power density of incident radiation on a surface, which depends on its distance from the exit of the concentrator. The maximum possible increase in power density is achieved in the limiting case where the surface is exactly at the exit of the concentrator. In this case the increase is given by the ratio of the concentrator entrance area to its exit area. This ratio is known as the concentration factor and is typically denoted by C.

Consider an arbitrary 3-dimensional concentrator such as in Figure 7.1 with entrance aperture area A_1 and exit area A_2. The concentration factor is then given by [79]

$$C = \frac{A_1}{A_2}. \tag{7.1}$$

Three assumptions must be made before the theoretical maximum concentration factor can be found: i) The source is spherical, at infinity, and emits rays over a half-angle θ_i, ii) all rays that enter within an angle θ_i pass through the concentrator, and iii) there are no radiative losses within the concentrator. With these in mind, the maximum concentration factor is governed by Liouville's theorem. This states that the particle density in phase space is conserved provided that the particles move in a conservative field. Therefore, the area of the phase space contour enclosing the position and momenta of particles in an accelerator beam, its emittance, is constant. The optical equivalent of phase space is étendue, which is the product of area and solid angle, $A\Omega$, therefore,

$$A_1\Omega_1 = A_2\Omega_2.$$

Since the source is spherical with half-angle θ_i, $\Omega_1 = 4\pi \sin^2\theta_i$ and $\Omega_2 = 4\pi \sin^2\theta_2$, where θ_2 is the exit's half-angle,

$$\begin{aligned} 4\pi A_1 \sin^2\theta_i &= 4\pi A_2 \sin^2\theta_2 \\ \therefore C = \frac{A_1}{A_2} &= \frac{\sin^2\theta_2}{\sin^2\theta_i}. \end{aligned}$$

For maximum concentration, radiation can exit the concentrator with angles up to $\theta_2 = 90°$ and so the above equation becomes [79],

$$C_{\text{max}} = \frac{1}{\sin^2\theta_i}. \tag{7.2}$$

Equivalently, the maximum concentration for the 2-dimensional case is $C_{\text{max}} = 1/\sin\theta_i$ [79]. Note that although it is possible to construct a 2-dimensional concentrator with the maximum concentration factor (under the three assumptions stated earlier), it is not possible to make a 3-dimensional concentrator to this standard. However, certain types of 3-dimensional concentrator do approach the theoretical limit.

7.1.2 The Basic Design of a Light Concentrator

The simplest concentrator is the light cone. This is a cone that has an opening angle, γ, relative to the axis of symmetry and a maximum input angle θ_i for the incoming radiation. The maximum input angle is set such that $2\gamma = \frac{\pi}{2} - \theta_i$, and as long as this is satisfied any rays that enter with angle $\theta < \theta_i$ will be reflected once before exiting the light cone. Rays that enter at angles larger than the maximum input angle are reflected out of the light cone, and

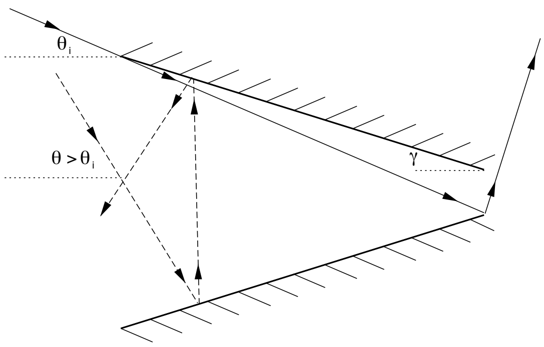

Figure 7.2: A basic model of a non-imaging concentrator as a cone with semi-angle γ, and maximum input angle θ_i.

do not pass through it. This is illustrated in Figure 7.2, where the solid line represents a ray entering at $\theta = \theta_i$ and the dashed line one entering with $\theta > \theta_i$. Although the light cone is not an optimum concentrator, it is an extremely simple arrangement compared to alternative image-forming systems. It is possible to improve upon the concentrating abilities of the light cone, whilst keeping the simple arrangement, by employing the *edge-ray principle*.

For an image-forming concentrator it is important that all rays entering at the maximum input angle θ_i (*i.e.* extreme rays) should form a sharp image at the exit of the concentrator. Then it can be assumed that all rays entering at angle $\theta < \theta_i$ pass through the concentrator. However, for a non-imaging concentrator these extreme rays do not have to form a sharp image. This further relaxes the requirements, and all that is required is that extreme rays strike the edge of the exit aperture of the concentrator [84]. This is known as the edge-ray principle, which leads to non-imaging concentrators with high concentration factors. Applying the edge-ray principle to the light cone gives rise to the Compact Parabolic Concentrator, or CPC, which has been widely described in the literature [55, 79, 84] and is briefly summarised here.

Consider first the simpler case of a 2-dimensional concentrator, which can then be rotated about its symmetry axis to form a 3-dimensional concentrator. By the edge ray principle, all rays that enter at the maximum input angle θ_i should exit at a point P at the rim of the concentrator. A well known shape capable of focusing rays in this fashion is a parabola *whose axis is parallel to* θ_i. Note that this profile has negligible slope at the concentrator's entrance. This process is illustrated in Figure 7.3, which shows a parabola that satisfies this condition, with extreme rays reflecting on to point P. The length of the concentrator is defined by the requirement that all extreme rays that enter the concentrator must pass through point P.

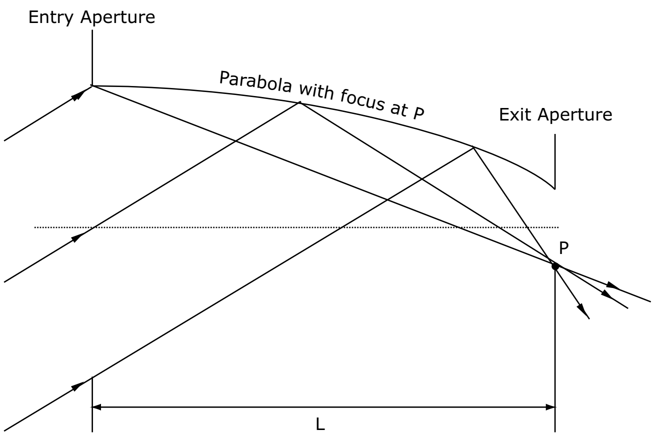

Figure 7.3: The basic design of a Compact Parabolic Concentrator. All edge rays must exit through point P.

Rotating this 2-dimensional shape about the concentrator (symmetry) axis — not the parabola axis — gives the 3-dimensional concentrator. Both of these shapes are known as 'CPCs', however, the length of the 3-dimensional concentrator is defined by its rotational symmetry and must be long enough to pass the extreme rays through the edge of its exit aperture. The CPC is completely defined by the radius of its exit aperture, a', and its maximum input angle θ_i such that [79]

$$\begin{aligned} f &= a'\,(1+\sin\theta_i)\,, \\ a &= \frac{a'}{\sin\theta_i}. \\ L &= (a+a')\cot\theta_i, \end{aligned}$$

where f is the focal length of the parabola, a is the radius of the concentrator's entrance aperture, and L is its total length.

Assuming that all rays entering with $\theta < \theta_i$ exit the concentrator, the 2-dimensional CPC has a concentration factor equal to the theoretical maximum, [79]

$$\frac{a}{a'} = \frac{1}{\sin\theta_i} = C_{\mathrm{max}}.$$

However, this is not the case for the 3-dimensional concentrator. Since it has many more degrees of freedom, it is impossible to ensure that all rays exit the concentrator. Therefore, although it can approach the theoretical maximum concentration, there is no guarantee that multiple reflections in the cone do not turn back rays that enter with $\theta < \theta_i$. Even so, this effect is small and generally 3-dimensional CPCs come very close to the concept of an 'ideal' concentrator.

Non-imaging concentrators have a number of advantages over imaging equivalents. They are practical, robust devices that are much simpler to manufacture and integrate into existing experimental systems. However, they are not necessarily the most compact solution and are relatively long compared to their diameter. Therefore, concentrators may need to be truncated so as to fit into the experimental arrangement, which in turn decreases their concentration efficiency (Section 7.3).

7.2 Winston Cones and Truncated Winston Cones

The angle at which rays exit a concentrator is not a concern with the CPC, and as such rays can emerge at angles up to 90° with respect to the concentrator axis. However, it is not always possible to use all of these rays. For example, the pyroelectric detectors used during the SP experiments (described in Chapter 6) can only detect radiation that is incident on them at up to a 60° w.r.t. the normal to their surface. This is equivalent to wasting all radiation exiting the concentrator with angles greater than 60°.

One solution to this problem is the $\theta_1 - \theta_2$ converter, otherwise known as a Winston cone, first described by Rabi and Winston in 1976 [55]. This restricts the exit angles of the concentrator to a specific range and is therefore ideal for these purposes. Calling the maximum input angle θ_i and the maximum output angle θ_o, the maximum concentration for this type of concentrator is given by [55]

$$\begin{aligned} C_{\text{max; 2D}} &= \frac{\sin\theta_o}{\sin\theta_i} \\ C_{\text{max; 3D}} &= \left(\frac{\sin\theta_o}{\sin\theta_i}\right)^2, \end{aligned} \tag{7.3}$$

assuming the refractive index of the input and output media is 1.

The Winston cone is a modification of the CPC described in the previous section. It includes a straight section in its design along with the parabolic section common to the CPC. Consider first the 2-dimensional case where exit angles must be restricted to $\theta < \theta_o$. Contrary to the design of the CPC, rays are traced in *reverse*from the exit of the concentrator to the entrance insisting that they make one reflection on the way (see Figure 7.4). Rays then fall into two categories, corresponding to the two sections that make up the Winston cone:

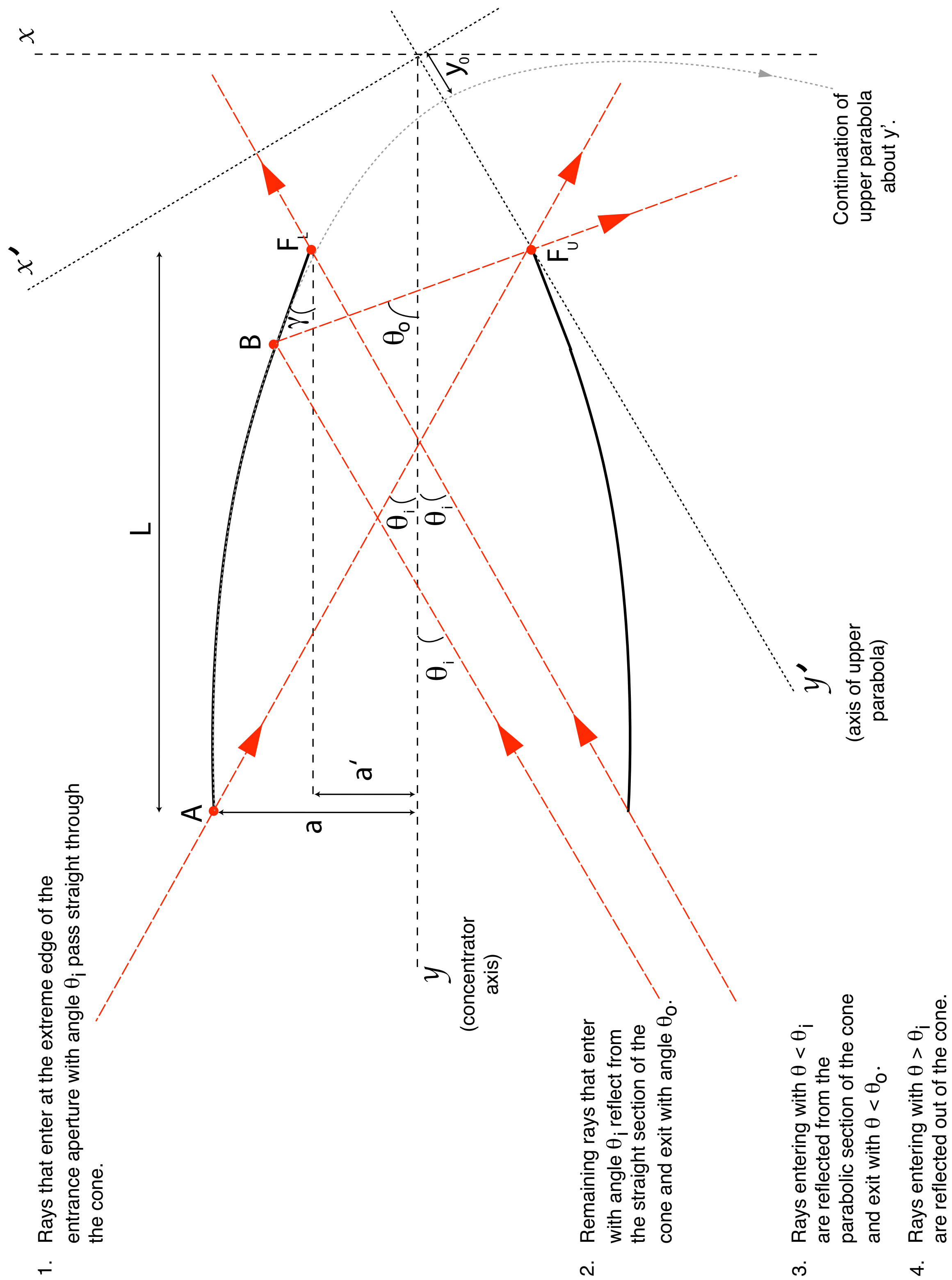

Figure 7.4: Designing a $\theta_1 - \theta_2$ converter (note that the axis of the lower parabola is not shown).

1. Those that exit with $\theta = \theta_o$.

2. Those that exit with $\theta < \theta_o$.

The first of these strike the straight section of the reflecting surface (section $B - F_L$ in Figure 7.4), which has a slope [55]

$$\gamma = \frac{1}{2}\left(\theta_o - \theta_i\right) \tag{7.4}$$

w.r.t. the concentrator axis. The latter group of rays are reflected from the parabolic section of the reflecting surface (section $A - B$ in Figure 7.4), whose focus is at point F_U and whose axis is parallel to θ_i — as in the case of the CPC.

The two co-ordinate systems of Figure 7.4 — where (x, y) denote the concentrator axes and (x', y') denote the parabola axes — are related by [55]

$$\begin{aligned} x &= x' \cos\theta_i - y' \sin\theta_i \\ y &= x' \sin\theta_i + y' \cos\theta_i. \end{aligned} \tag{7.5}$$

Then, the parabolic section of the Winston cone is defined by

$$y' = \frac{x'^2}{4f} + y'_0, \tag{7.6}$$

with

$$\begin{aligned} f &= a' \left(\sin\theta_i + \sin\theta_o\right) \\ y'_0 &= a' \left(\frac{1}{\sin\theta_i} - \sin\theta_i - \sin\theta_o\right), \end{aligned}$$

where a' is the radius of the exit aperture. The (upper) parabola's focal point has coordinates [55]

$$\begin{aligned} x_{F_U} &= -a' \\ y_{F_U} &= a' \cot\theta_i. \end{aligned} \tag{7.7}$$

The straight section of the Winston cone, with slope γ, then joins the parabolic section at point B. This is located at [55]

$$\begin{aligned} x_B &= a' \frac{\tan\theta_o + \tan\gamma}{\tan\theta_o - \tan\gamma} \\ y_B &= a' \cos\theta_i + \frac{2a'}{\tan\theta_o - \tan\gamma}. \end{aligned} \tag{7.8}$$

The entrance to the cone is located at the end of the parabolic section at A [55]

$$\begin{aligned} x_A &= a' \frac{\sin\theta_o}{\sin\theta_i} \\ y_A &= a' \left(2 + \frac{\sin\theta_o}{\sin\theta_i}\right) \cot\theta_i, \end{aligned} \tag{7.9}$$

and so the length of the cone is

$$\begin{aligned} L &= y_A - y_{F_U} \\ &= a' \left(1 + \frac{\sin\theta_o}{\sin\theta_i}\right) \cot\theta_i. \end{aligned} \tag{7.10}$$

The whole shape can then be rotated about the y-axis to make the 3-dimensional concentrator known as the Winston cone.

7.3 Design of the Winston Cone for the SP Experiments

There were a number of design constraints placed on the cone required for these experiments. Whilst it is usually the exit aperture radius, a', that defines the cone parameters, in this case it was the entrance aperture radius. In order for the cone to integrate smoothly into the existing experimental arrangement, the entrance aperture had to have a fixed radius of $a = 10.5$mm. Also, since the pyroelectric detectors have a radius of 1mm, and the longest SP wavelength is 2.6mm, it was very important that diffraction effects at the cone exit were minimised whilst also minimising ‘wasted’ radiation. This was made more difficult as it was not possible to place the detector at the exit of the cone in order to avoid potential damage to the detector element. The maximum output angle, θ_o, was restricted to 60° in line with the manufacturer’s specification for the pyroelectric detector.

With this in mind, a series of Winston cones were designed based upon Equations 7.3 – 7.10. These covered a variety of maximum input angles and hence also exit aperture radii, lengths, and concentration factors. One further consideration was the length of the cone. Although a larger acceptance angle improves the solid angle observed by the cone, it also greatly increases its length. Since the cone had to work within the existing space limitations of the FELIX experimental setup this was an important issue.

The Winston cone was ‘truncated’ to address the issue of length. Truncating a cone decreases its length, but also decreases its concentration factor. For example, consider a cone with maximum acceptance angle $\theta_i = 6.8°$, entrance aperture radius $a = 11$mm, and exit aperture

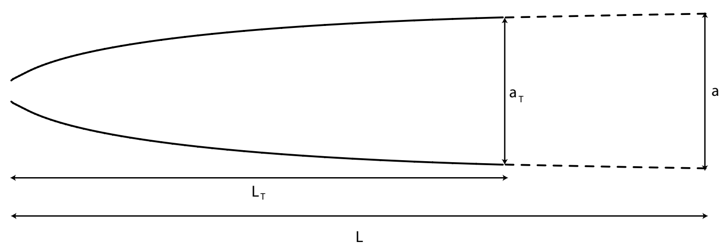

Figure 7.5: Truncating a CPC or Winston cone.

radius $a' = 1.5$mm. A cone with these parameters would have a length of $L = 104.9$mm and concentration of $C = 53.5$. Next, finding the point where the 'truncated' cone would begin with entrance aperture radius $a_T = 10.5$mm gives rise to a much shorter cone with length $L_T = 66.9$mm and concentration $C = 48.8$. This decrease in length is illustrated schematically in Figure 7.5. A large decrease in length is possible as the reflecting surface has negligible slope at the entrance aperture. Reducing the length of the cone at this point does not have a large effect on the concentration factor of the cone ($\sim 10\%$ reduction in this case), and is therefore preferable to reducing θ_i and in turn reducing the observed solid angle.

The final design parameters of the (truncated) Winston cone used in these experiments were

$$\begin{aligned}
\theta_i &= 6.3^\circ \\
\theta_o &= 60^\circ \\
a_T &= 10.5\text{mm} \\
a' &= 1.4\text{mm} \\
f &= 1.36\text{mm} \\
L_T &= 71.5\text{mm} \\
C_{T,\,\max} &= 56.8,
\end{aligned}$$

where $C_{T,\,\max}$ is the maximum theoretical concentration factor for the *truncated*cone. For comparison, the original non-truncated cone has the following parameters,

$$\begin{aligned}
a &= 11\text{mm} \\
L &= 112.26\text{mm} \\
C_{\max} &= 62.28.
\end{aligned}$$

Figure 7.6: The final manufactured Winston cones.

Since all metals have nearly perfect conductivity in the far infrared, it was decided to fabricate eleven of these cones from brass, with the exterior of the end of the cone shaped so that it could be inserted inside the detector canister. This gave a distance of $d = 0.5$mm between the cone and detector. The detector (and associated electronics) could then be attached to the cone via grub screws such that the exit of the cone was centered over the pyroelectric detector element. Figure 7.6 shows a photograph of the Winston cones used during the SP experiments.

7.3.1 The Effective Grating Length

Since the detectors were not located at infinity relative to the grating, it was important to know how much of the grating was visible to each detector whilst a Winston cone was used. Consider a detector at 90° with respect to the beam direction. This detector should detect radiation from the *minimum*length of grating, assuming that all radiation that enters the elbow bend (see Figure 4.1) is passed on to the Winston cone.

The distance between the grating and Winston cone entrance is 230mm, and the cone has a maximum acceptance angle of ±6.3° w.r.t. the normal. Thus the effective grating length, L_{eff} is (Figure 7.7)

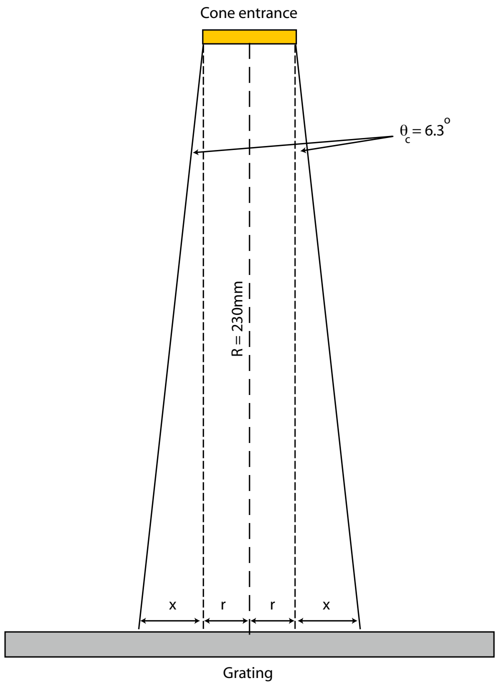

Figure 7.7: Calculation of the effective grating length for a detector at 90° (not to scale).

$$L_{\text{eff}} = 2x + 2r,$$

with

$$x = 230 \tan 6.3 = 25.4\text{mm}$$

and $r = 10.5$mm. Therefore the effective grating length at 90° is $L_{\text{eff}} = 72$mm. This is longer than the actual length of the grating (40mm) and so the whole grating is visible at all angles.

7.3.2 The Solid Angle

Having specified the properties of the Winston cone, the next step is the calculation of the solid angle defined by the grating-cone system. First examine the case of the grating considered as an extended source a distance $R = 230$mm away from the entrance of the Winston cone, which has a radius of $r = 10.5$mm (Figure 7.8). Consider the total solid angle seen by a detector, Ω_T, as the average of the N individual solid angles, Ω_i, for each observation angle detected,

$$\Omega_T = \frac{1}{N} \sum_{\theta_i=\theta_0-6.3}^{\theta_0+6.3} \Omega_i$$

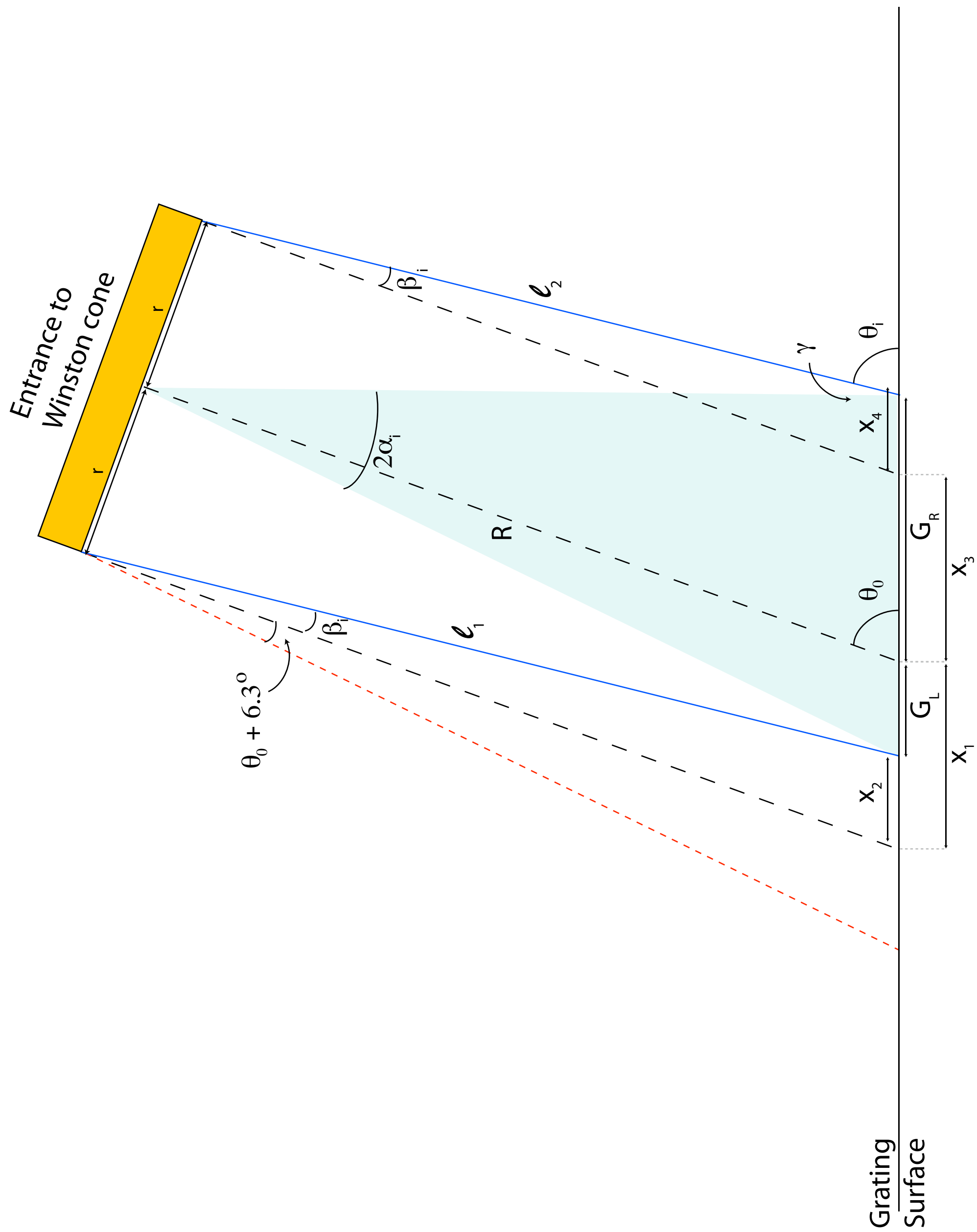

Figure 7.8: The solid angle (shaded area) for one observation angle seen by the detector at angle θ_0 to the beam direction.

with

$$\Omega_i = 2\pi\left(1 - \cos\alpha_i\right)$$

and $2\alpha_i$ is the apex angle. Defining

$$\begin{aligned}
\beta_i &= \theta_i - \theta_0 \\
\gamma_i &= \pi - \theta_0 \\
l_1 &= \frac{R\sin\theta_0 + r\cos\theta_0}{\sin\theta_i} \\
l_2 &= \frac{R\sin\theta_0 - r\cos\theta_0}{\sin\theta_i} \\
x_1 &= \frac{r}{\sin\theta_0} \\
x_2 &= \frac{l_1\sin\beta_i}{\sin\theta_0} \\
x_3 &= \frac{r}{\sin\theta_0} \\
x_4 &= \frac{l_2\sin\beta_i}{\sin\theta_0},
\end{aligned}$$

and

$$\begin{aligned}
G_L &= x_1 - x_2 \\
G_R &= x_3 + x_4,
\end{aligned}$$

the left and rightmost extent of the grating surface covered, allows α_i to be calculated as

$$\begin{aligned}
\alpha_i &= \frac{\sin^{-1}\left[G_R\left(\frac{\sin\theta_0}{\sqrt{R^2+G_R^2-2RG_R\cos\theta_0}}\right)\right]}{2} \\
&+ \frac{\sin^{-1}\left[G_L\left(\frac{\sin\theta_0}{\sqrt{R^2+G_L^2-2RG_L\cos\gamma_i}}\right)\right]}{2}.
\end{aligned} \tag{7.11}$$

Note that G_L and G_R must be constrained such that

$$\begin{aligned}
G_L &\leq \frac{L}{2} \\
G_R &\leq \frac{L}{2},
\end{aligned}$$

where L is the length of the grating. Calculating the total solid angle for a detector at $\theta_0 = 90^\circ$ gives $\Omega_T = 6.538$msr, and for a detector at $\theta_0 = 40^\circ$ gives $\Omega_T = 6.578$msr.

Now consider the case of the grating as a point source in the centre of a sphere the same distance, R, away from the entrance to the Winston cone. In this case, all observation angles are equivalent to the 90° case, where the solid angle, Ω, is given by

$$\begin{aligned}\Omega &= \frac{\pi r^2}{R^2} \\ &= \frac{\pi 10.5^2}{230^2} \\ &\approx 6.5\text{msr}.\end{aligned}$$

Therefore, treating the grating as a point object yields simpler equations, and the same result, as the extended source calculations. The value of Ω =6 .5msr is used throughout this thesis.

7.4 The Efficiency of the Cone-Detector System

It is important to emphasise that the previously derived concentration factor of 56.8 represents a theoretical upper limit that cannot be achieved in practice for three reasons: a) it was not possible to position the detector directly at the exit of the cone, b) zero losses would require an exit radius equal to, or smaller than, the pyroelectric detector radius (1mm), which would introduce detrimental diffraction effects (see Section 7.5) , and c) radiation can exit the cone at angles up to 60°, the maximum angle the pyroelectric detector can detect (with decreasing efficiency), so radiation is emitted beyond the radius of the detector itself.

Figure 7.9 shows a schematic of the exit of the cones used. Geometrically, the detector should only be able to observe $\sim$ 20% of the radiation emitted by the cone assuming a uniform spread of radiation over the exit aperture area and all exit angles. This would reduce the efficiency of the cone-detector assembly to around 20% of the theoretical concentration of the cone itself. In other words, the ratio of signal seen with a cone and without a cone would be approximately 11 if the cone is 100% efficient and emits radiation uniformly over all angles. There is no guarantee that this is the case, however. Therefore, it is important to determine what increase in observable signal the Winston cone brings over measurements without one, *i.e.the efficiency of the cone-detector assembly.*Also, by investigating the decrease in efficiency with increasing cone-detector separation, d, it may be possible to determine if radiation is uniformly emitted by the Winston cone.

A photomixer source emitting in the 1.24 – 2.68mm region (as in Section 6.4) was used in broadband mode as the source for a series of FTS measurements at the Rutherford Appleton

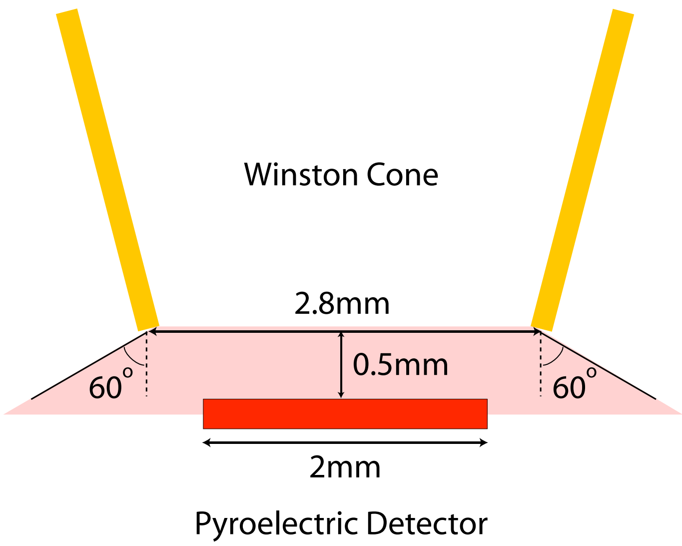

Figure 7.9: Schematic diagram of the exit aperture of the cone and its distance to the pyroelectric detector. Radiation can exit the cone at angles up to 60°.

Laboratory. The reference detector used during the calibration measurements in the previous chapter was again used here. A schematic of the experimental setup is shown in Figure 7.10. This setup is very similar to the one used when measuring the WAP filter transmissions in Chapter 5.

Radiation from the photomixer source was chopped at 14Hz and then focused with a lens towards the interferometer. The Winston cone and detector are situated at the end of this arrangement, securely held inside the aluminium block used in Section 6.5. The front of the Winston cone, or the front of the detector, was placed flush with the front of this block, ensuring that it was returned to the same location each time. A Golay cell was also used in this position to characterise the source. Note that no lens was used before the Winston cone so that the incident radiation was as parallel as possible. This most closely matches the radiation seen during the SP experiments. The procedure was then as follows:

1. The Winston cone was attached directly to the detector housing; the cone detector separation was equal to 0.5mm.

2. An interferogram was generated over 130 points over the full range of the photomixer with a step size of 4GHz.

3. This was repeated after inserting a 0.27mm shim between the cone and detector (d = 0.77mm), a 0.27 and 0.49mm shim (d = 1.26)mm, and two 0.27 with two 0.49mm shims (d = 2.02mm).

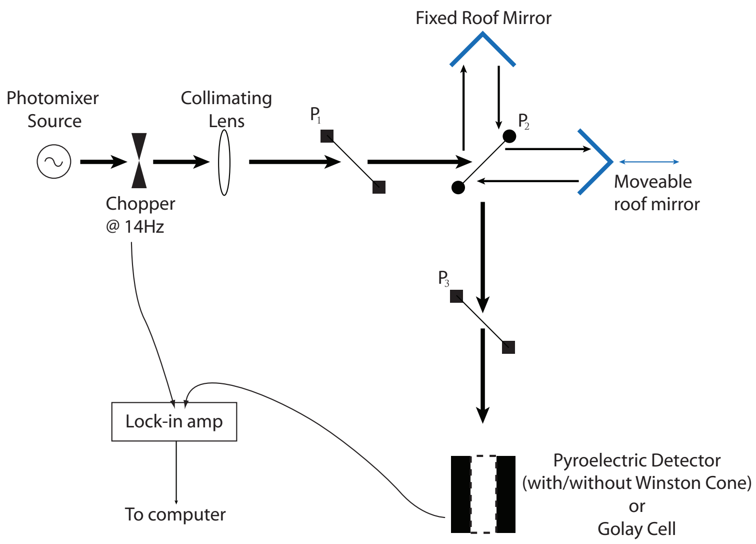

Figure 7.10: Schematic of the experimental setup used when investigated radiation losses between the Winston cone and pyroelectric detector.

4. A measurement was then taken with the reference detector *without* a Winston cone, and with the Golay cell in the same position.

The Fourier transform of each of these interferograms was then taken, giving the signal observed on the pyroelectric detector (or Golay cell) as a function of frequency.

Calling the signal on the pyroelectric detector without a cone S_{nc}, and the pyroelectric with a Winston cone S_c, then the efficiency of the system is

$$\varepsilon = \frac{S_c}{56.8 S_{nc}}. \tag{7.12}$$

Using a Golay cell, a relatively flat portion of the spectrum — with maximal output — was selected away from any possible diffraction effects that may occur at the cone's exit. Figure 7.11 shows the average efficiency of the cone-detector assembly between λ = 1.6 to 1.9mm with different distances between the cone and detector. These results can be extrapolated back to zero distance, and so discover what the increase in signal would be if the detector was located *exactly*at the exit of the cone. The measured efficiencies follow an approximate straight line, contrary to the inverse square law decrease that might be expected. This suggests that radiation is not being emitted uniformly from the cone, or alternatively, that all exit angles are not absorbed equally by the detector.

Table 7.1 shows these results compared to a purely geometrical calculation assuming that the cone emits uniformly over all exit angles. In this case, at zero separation the detector

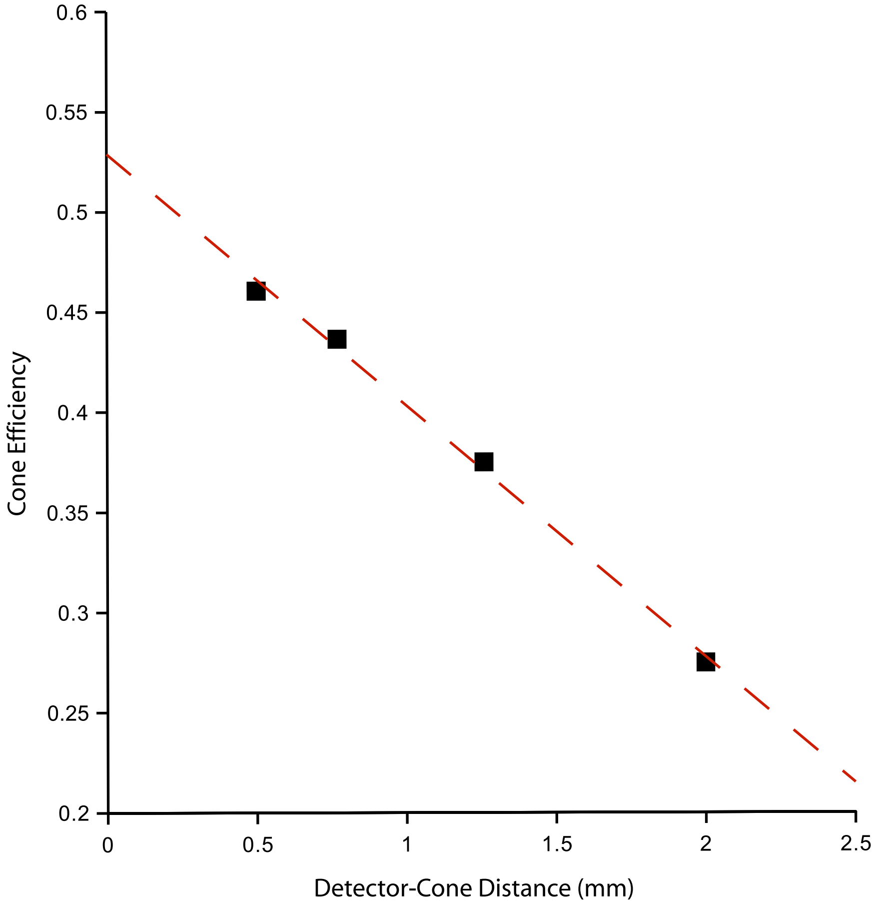

Figure 7.11: Variation of the average efficiency of the cone-detector assembly with increasing distance between the exit aperture and detector in the region $\lambda = 1.6$ to 1.9mm. The efficiency seen when the cone-detector distance is extrapolated back to 0mm is 53%.

Cone-Detector Distance (mm)	Theoretical Efficiency $(\theta \leq 60°)$	$(\theta \lesssim 10°)$	Measured Efficiency
0 (extrapolated)	51%	$\sim$ 51%	52.8%
0.5	19.5%	$\sim$ 45%	46.6%
0.77	13.4%	$\sim$ 42%	43.7%
1.26	7.8%	$\sim$ 38%	37.5%
2.02	4.2%	$\sim$ 32%	27.5%

Table 7.1: The average measured efficiency with increasing cone-detector distance compared with the theoretical expectation assuming a uniform distribution of light from the exit aperture.

should detect approximately 51% of the radiation emerging from the cone exit aperture. As the distance between the two increases to 0.5mm, the efficiency decreases to ∼20%. Experimentally, it was found that the efficiency at zero distance was approximately 53%, which is in line with the geometric calculation. However, the efficiency was much higher than expected at increasing distance. For example, the cone-detector assembly has an efficiency of ∼47% compared to the expected 20% with a separation of 0.5mm.

For comparison, consider a cone that emits light uniformly up to a maximum exit angle of 10°. The calculations for this case are also presented in Table 7.1. These calculations are much more in line with the experimental observation, suggesting that a large proportion of the light is emitted with exit angles up to 10°. However, it should also be noted that the response of the pyroelectric detector itself decreases with increasing angle of incidence. Therefore, larger exit angles may not be detected as easily as smaller ones. Alternatively, in the setup at RAL, the majority of the radiation may have been incident on the cone at angles $\leq 6.3°$, causing most of the radiation to exit with much smaller exit angles. As the experiment used radiation that was approximately parallel, this is the most likely explanation for the effect.

In summary, this experiment has shown that the Winston cone is an important addition to the SP experiments. It collects a solid angle of $\Omega = 6.5$msr, of which 46.6% is detected by a pyroelectric detector when it is positioned 0.5mm away from the cone exit. An alternative way of expressing this would be to state that a detector detects 26 times more radiation when used with a cone than without one. When extrapolated back to zero separation between the cone exit and detector it has an efficiency in agreement with the theoretical maximum efficiency, verifying that the cone works as designed.

7.5 Diffraction Effects

Diffraction effects at the exit of the Winston cone are a concern as the longest SP wavelength and the diameter of the exit aperture are very close in size; 2.6mm compared to 2.8mm. Any reduction in signal with increasing wavelength must therefore be accounted for prior to any analysis of SP data. As such, it was important to measure any decrease in observed signal with increasing wavelength.

This experiment was carried out in a similar fashion to that of Section 7.4, using a source that emits most strongly in the 2 – 3mm region. This source was used in the same FTS arrangement as in Figure 7.10 and followed the same procedure. Measurements were taken with three different detectors (the reference detector from Chapter 6 and two others) with an attached Winston cone, and then compared to the signal observed without the use of the cone. The cone-detector assembly was held firmly in place inside an aluminium block, with the front of the cone flush with the front of the block. When the pyroelectric detector was used alone, the front of the detector canister was placed so that it was also flush with the front of the block, ensuring repeatability between measurements.

Contrary to the previous measurements, a lens was used during *part*of this experiment. This was due to the fact that the source did not produce sufficient output to be detected by the pyroelectric detector without being at the focal point of a lens. In this case measurements were first taken with the Golay cell, with and without a lens, and the decrease in signal from the lens to the no-lens case was found. The pyroelectric detector measurements were then taken with a lens, and decreased by the same amount as observed by the Golay cell.

The procedure was then as follows:

1. A lens was positioned in front of a pyroelectric detector. The detector was held in an aluminium block, which was positioned in the focal point of the lens. An interferometer measurement was then taken as in the previous section, to obtain the signal $S_1(\lambda)$.

2. A Golay cell was then put in the same position as the detector, and an interferometer measurement was taken, to obtain the signal $S_2(\lambda)$.

3. The lens was removed from the lens holder, and another Golay cell measurement was taken, $S_3(\lambda)$.

4. A Winston cone was attached to a pyroelectric detector and placed inside the aluminium block in the same position as steps $1-3$. Another interferometer measurement was taken, $S_4(\lambda)$.

5. These steps were repeated for three different detectors, and the average of the Fourier transform of their interferogram was taken.

6. The ratio of signal measured by the Golay with a lens, S_2 to that seen without a lens, S_3 then gives the decrease in signal caused by removing the lens: $D = S_2/S_3$.

7. The signal expected from the pyroelectric detector without the use of a lens and cone, can be estimated by dividing S_1 by D.

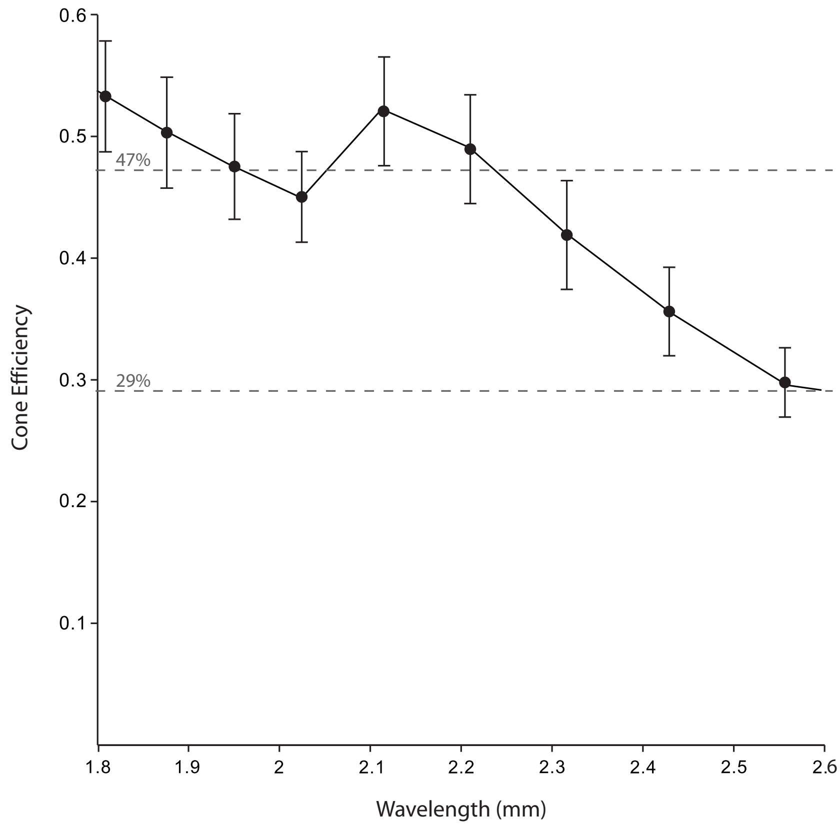

Figure 7.12: Diffraction effects at the exit of the Winston cone, averaged over three detectors, cause a loss in efficiency (see text for details)

8. The efficiency, ε, of the cone-detector assembly was then calculated as in as in Equation 7.12, as

$$\varepsilon = \frac{S_4}{S_1}\frac{D}{56.8}.$$

Figure 7.12 shows the reduction in efficiency as a function of wavelength. From the previous section, the cone-detector assembly has a typical efficiency of approximately 47%. This is consistent with these measurements, where the efficiency is approximately this value up to 2.2mm. Beyond this wavelength the efficiency decreases, due to diffraction effects at the exit of the cone, to $\sim$ 29%. This decrease was taken into account when analysing the data.

7.6 Summary

Winston cones were designed to improve the light collection efficiency of the SP experiments. The design of the cone required by the SP experiments is discussed in Section 7.2. This details the differences between the Winston cone and other non-imaging concentrators such as the Compact Parabolic Concentrator and gives the equations necessary for its design. The chosen design is given in Section 7.3.

The theoretical concentration factor of the cone is not achievable in practice for the cone-detector assembly. The actual increase in signal due to using the Winston cone was therefore investigated in Section 7.4. This revealed that a detector receives 26 times more radiation when attached to a cone than without one, which is equivalent to an efficiency of $\sim 47\%$ for the cone-detector assembly. Section 7.5 investigates the decrease in signal observed at long wavelengths due to diffraction at the exit of the cone. Diffraction begins to play a role beyond $\lambda = 2.2$mm and must be taken into account before any analysis of SP data. However, an added benefit of diffraction at the cone's exit is that it also enables to Winston cone to act as a very long wavelength filter.

The final cones used throughout the SP experiments described in this thesis had a maximum theoretical concentration factor of 56.8. When attached to the detector housing, its efficiency is 47% of its theoretical maximum at short wavelengths and drops approximately linearly to 29% at long wavelengths. These figures are used throughout the analysis carried out in Chapters 8 – 10.

Chapter 8

FELIX — November 2005

Coherent SP radiation was used to determine the longitudinal profile of electron bunches at the FELIX Facility, FOM Institute, Netherlands. These experiments were carried out in January and November 2005. The primary goals of the experiments were threefold:

1. FELIX provides an intermediate energy beam with very short bunch lengths. Thus, it was the next step towards developing a longitudinal bunch diagnostic tool for GeV and TeV beams with ps-long bunches.

2. To verify that SP bunch length measurements can be carried out with room temperature pyroelectric detectors. November's experiment also entailed commissioning the WAP filters described in Chapter 5, and the Winston cones described in Chapter 7.

3. To verify that the measured SP signal is in line with predictions from the surface current model (Section 2.2.3).

The first experiment carried out in January 2005 was a pilot study, and as such all significant data were obtained from the subsequent experiment in November. Hence, only this data set is considered in this chapter.

Data from the FELIX experiments have been previously analysed by the Smith-Purcell group at Oxford and reported in [15]. However, there are a number of issues that were not known, or considered, at the time that contribute towards the analysis. For example, diffraction effects from the exit of the Winston cone (Section 7.5) were ignored, the transmission through some experimental components was not known, and assumptions made about the visible solid angle were later found to be incorrect. In addition to this, data were only analysed through a variant of the 'template' method described in Section 3.1. Instead of using a weighted least squares method, template distributions were judged by eye. Therefore, this chapter is dedicated to the reanalysis of this data, in the light of what has since been learnt.

8.1 Beam Parameters

The FELIX beam operates in two different modes: Low frequency and high frequency. In both operational modes the accelerator produces electron bunch trains that are $\sim 5\mu s$ long, at a repetition rate of 10Hz. The normalised emittance of the beam was 100πmm.mrad. The beam was brought to a waist at approximately the centre of the grating with a measured FWHM of $\sim$ 2mm in x ($\sigma_x \approx 0.85$mm) and $\sim$ 4mm in y ($\sigma_y \approx 1.70$mm). The other beam parameters are:

- Low frequency mode:
  - Operating frequency: 25MHz.
  - Bunch spacing: 40ns.
  - Number of electrons per bunch, N_e : 1.5×10^9.
  - Maximum energy, $E_{\max}$: 50MeV, or $\gamma \approx 97.8$.
- High frequency mode:
  - Operating frequency: 1GHz.
  - Bunch spacing: 1ns.
  - N_e: 1×10^9.
  - $E_{\max}$: 45MeV, or $\gamma \approx 88.1$.

Although data were taken using both modes, all data considered in this chapter were taken from experiments using the high frequency mode of the FELIX beam

The beam was positioned and focused by adjusting an upstream quadrupole magnet and observing the beam shape and position on a retractable scintillating screen, which was located approximately 20cm downstream from the grating. Once the adjustments were made, the screen was pulled out of the beamline. The beam current was measured at the beam dump, which was located approximately 2m downstream of the experiment.

8.2 Experimental Issues

The experiment described in this chapter was carried out before those at SLAC (Chapters 9 and 10), and hence, the apparatus was slightly different from that used at SLAC. Apparatus specific to the FELIX experiments has been described in Section 4.3, however, the primary features of the experimental setup can be summarised as follows.

A vacuum chamber containing a carousel of three different period gratings (0.5, 1.0 and 1.5mm) and a blank 'grating' with no period (henceforth referred to as the 'blank') was inserted into the FELIX beamline. Radiation could exit the chamber through a crystalline quartz window. It then passed through three separate broadband filters; a wire mesh grid placed against the quartz and which was, at the time, thought to remove long wavelength background radiation, a sheet of black polyethylene, and a sheet of flurogold to remove short wavelength background radiation. These are described more fully in Section 4.2.2.

Radiation was detected by 11 detectors, placed at the end of the optical system, which were arranged from $40 - 140°$ w.r.t. the beam direction. The optical system was composed of a $90°$ bend with a WAP filter, for first order SP radiation, and a Winston cone. The WAP filters were changed by hand, depending on the grating used. The final arrangement used during the experiment is shown in Figure 8.1, where the beam travels from right to left. Lead shielding surrounds the electronics (and attached detectors) to minimise the effect of X-rays from the beampipe, upstream, and downstream. Downstream shielding was especially important as the beam dump was only a short distance away ($\sim$ 2m).

Measurements were taken with all three gratings, and the blank, under different filtering conditions. Each measurement was repeated several times. However, only two complete sets of WAP filters existed throughout this experiment. These covered all first order wavelengths from the 0.5 and 1.0mm gratings, but not for the 1.5mm grating. Fortunately, many of the wavelengths from the 1.5mm grating overlap with those from the other gratings, and therefore only three observation angles remained without suitable filters: 120, 130 and $140°$. Since filters did not exist for these wavelengths at the time, either no filters were used or an aluminium plug was inserted at these angles to suppress all radiation, when it was deemed necessary, for calibration purposes.

The signal measured at each observation angle was recorded as a trace on one of four oscilloscopes (Figure 8.2). Each trace was recorded as a running average over a minimum of 64 accelerator trigger signals. In order to obtain the 'true' SP signal — *i.e.*that which arises only from the periodic surface of a grating — background radiation measurements were taken by in-

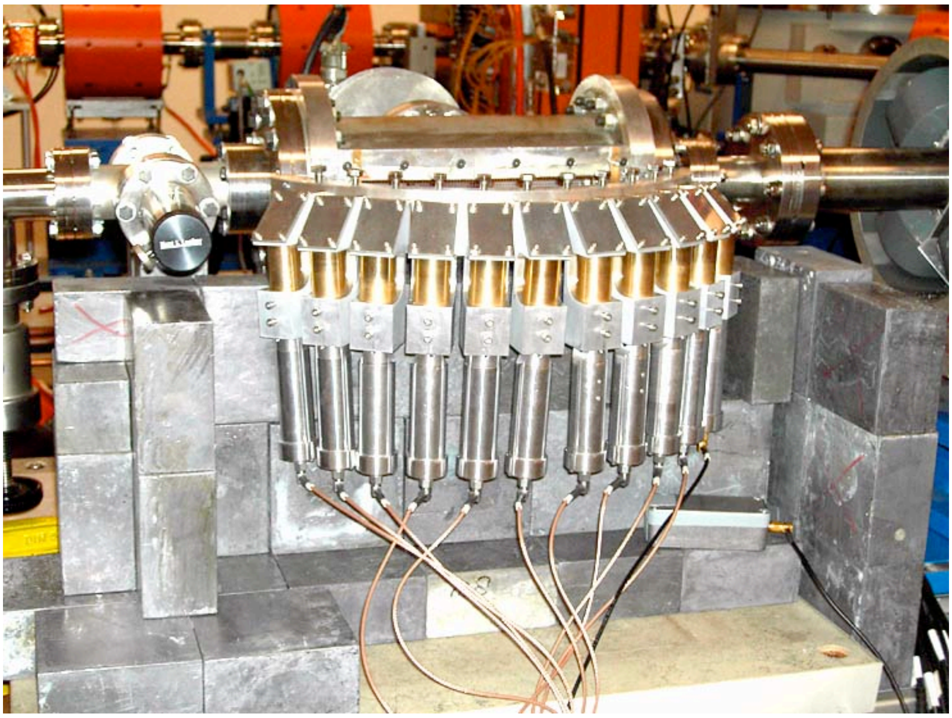

Figure 8.1: The experimental arrangement at FELIX in November 2005.

Figure 8.2: Data acquisition at FELIX using four oscilloscopes.

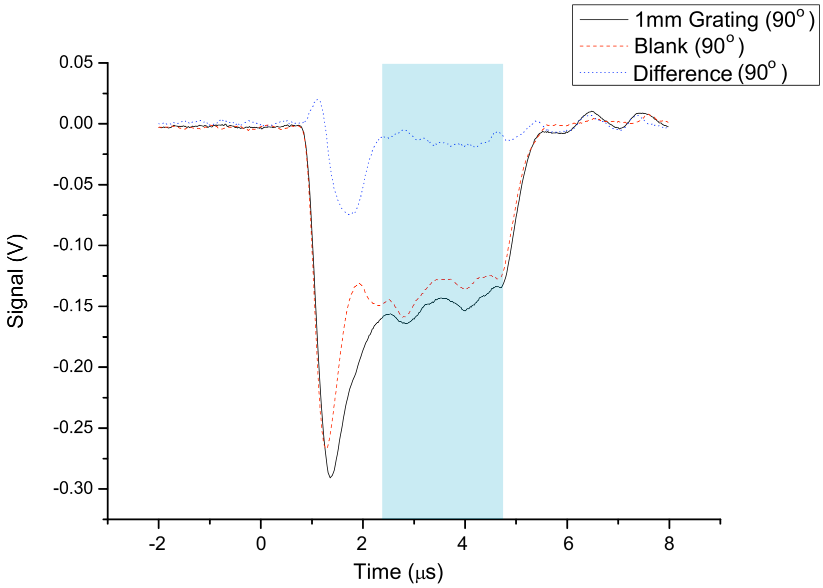

Figure 8.3: Measured raw signal at 90° from the 1mm grating, with appropriate WAP filters, the blank with the same filters and, the difference between them. The shaded area denotes the time period the signal is averaged over.

serting the blank to the same position relative to the beam, and observing the signal under the same filtering conditions as for the grating. Subtracting the signal detected from the blank, from that detected with a grating, then leaves only radiation that arises from the periodic surface itself. Henceforth the 'true' SP signal, in the context of this thesis, is defined as *the difference between the signals detected from a grating and the blank under the same filtering conditions*.

Figure 8.3 shows an example of the raw signal detected during the experiment. The black (solid) line shows the measured signal from a 1mm grating, with appropriate WAP filters for the expected first order SP wavelengths, the red (dashed) line shows the equivalent measured background signal from the blank, and the blue (dotted) line shows the SP signal. The leading spike on each trace is due to X-ray radiation from i) the beam halo impinging on the grating (the initial bunches in the bunch train are displaced with respect to those that follow them [75]), ii) produced elsewhere in the accelerator, or iii) from the nearby beam dump. This was a persistent problem throughout the experiment and is the primary reason why the optical system was arranged so that the emitted radiation was reflected through a 90° bend, in an effort to (partially) shield the detector and the sensitive electronics from X-rays. To minimise the effect of the spike, all data analysed within this chapter is the average SP signal recorded after the X-ray spike (*i.e.*in the period denoted by the shaded area of Figure 8.3).

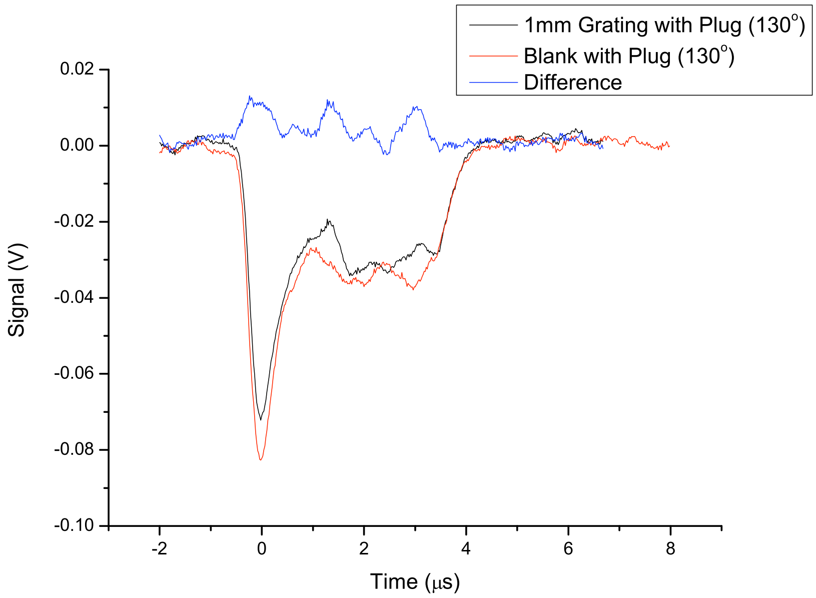

Figure 8.4: Measured raw background signal from (black, solid) the 1.5mm grating, (red, dashed) the blank, and (blue, dotted) the difference between the two, using an aluminium plug at 130°.

Further measurements were carried out in order to quantify the X-ray spike. For example, the blue (dotted) line in Figure 8.3, representing the difference, still possesses a partial X-ray spike. This means that the X-rays detected whilst using a grating and a blank were not equal. Aluminium plugs were introduced into the experiment to measure this effect. These were thick caps that covered the entrance to the optical system, replacing the filters. Far infrared radiation cannot pass through the aluminium plugs, and so all 'signal' measured with them present is entirely due to X-ray radiation. This is demonstrated in Figure 8.4, which shows the signal detected when using an aluminium plug in the 130° observation angle. The black (solid) line represents the signal seen from a grating, and the red (dashed) line that from a blank. Note that the blue (dotted) line represents the difference between the two, which under ideal circumstances should be zero. The fact that the two plots do not coincide, and that the signal from the blank is larger, suggests either: (i) the blank is misaligned relative to the gratings on the carousel and may extend further in towards the beam, (ii) the beam has drifted between measurements, or (iii) both of these. The first of these possibilities is discussed further in Section 8.3.

Beam drift was an important consideration during the FELIX experiments as filters were changed by hand. This introduced a turnaround time between measurements, where a change of filters was necessary, of up to 15 minutes. To this end, two nominally 'identical' measurements

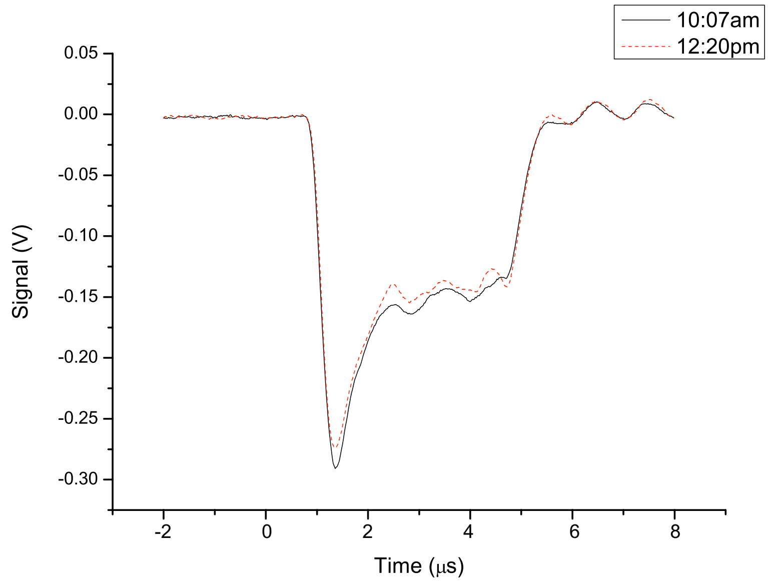

Figure 8.5: The raw signal observed from two nominally identical runs separated by 2 hours. Both measurements were observed at 90° with the 1mm grating and appropriate WAP filters.

were made after 10 and 60 minutes respectively. These were then compared, and the observed output was found to vary by ±5mV, which was taken as the irreducible noise level of the beam. This was still the case even after several hours (Figure 8.5). Therefore, all SP signal values that fall beneath this level were ignored during the analysis presented here.

8.3 Corrections to Data

A variety of corrections must be made to the data points before the analysis can proceed. These corrections account for losses as the radiation propagates from the beampipe to the detector. For example, a filter may only transmit 80% of the incident radiation, whilst another may transmit 70%. All of the measured data points must therefore be processed so that all possible losses in the system have been accounted for. Each correction factor that was applied to the measured data points is considered here in turn, working out from the vacuum chamber towards the detectors.

The first correction is due to the misalignment of the blank with respect to the other gratings on the carousel inside the vacuum chamber. This was briefly touched upon in the previous section (Figure 8.4), where it was suggested that the blank grating was consistently closer to the beam. Measurements made at Oxford after the experiment determined that the blank protruded 0.22mm further towards the beam than the gratings. During the FELIX experiment, measurements were made by gradually retracting both a grating and the blank away from the beamline and recording the signal seen. Therefore, a correction factor, C_{blank}, was determined from the ratio of the signal measured with the blank in its nominal position and that measured with the blank retracted by a further 0.22mm. The scaling factor is

$$C_{\text{blank}} = \frac{0.0504}{0.0471} = 1.07.$$

Therefore, all blank measurements were divided through by this value before subtracting them from the grating measurements to find the SP signal.

The next set of corrections arise from the quartz window. Transmission through the window is affected by both absorption and reflection losses. First, consider losses due to absorption. The absorption coefficient, α, of crystalline quartz has been measured in the far infrared by Loewenstein *et. al*[44]. However, the SP measurements carried out in this thesis were at shorter wavelengths than those of [44]. Therefore, the absorption coefficient $\alpha = 0.3 \pm 0.2\text{cm}^{-1}$ [44], measured at the lowest wavelength, was considered appropriate for these circumstances. The absorption loss depends upon the angle of incidence, θ_i, of the emitted radiation (w.r.t. the window surface), the refractive index of the window, $n = 2.1$, and its thickness, $d = 6$mm. The amount of radiation transmitted through the window after absorption is then given by [6]

$$T = \exp\left(-\alpha x\right),$$

where $x = d/\cos\theta_r$ and

$$\theta_r = \sin^{-1}\left[\frac{\sin\theta_i}{n}\right],$$

is the angle of refraction as given by Snell's law. Corrections arising from this absorption are given in Table 8.1. It can be seen that the aborption loss, for this experimental arrangement, has only a small dependence on the angle of incidence.

In addition to absorption losses, radiation may be lost by multiple reflections from the window surfaces. The following wavelength-dependent equations were used to calculate the amount of radiation transmitted through the window for a given wavelength λ. Consider first the $x - y$ polarisation of incident SP radiation [6],

$$\begin{aligned} r_{12} &= \frac{\cos\theta_r - n\cos\theta_i}{\cos\theta_r + n\cos\theta_i}, \\ r_{21} &= \frac{n\cos\theta_i - \cos\theta_r}{n\cos\theta_i + \cos\theta_r}, \end{aligned}$$

Observation Angle (°)	Transmission
40	0.82±0.05
50	0.83±0.05
60	0.83±0.05
70	0.83±0.05
80	0.83±0.05
90	0.84±0.05
100	0.83±0.05
110	0.83±0.05
120	0.83±0.05
130	0.83±0.05
140	0.82±0.05

Table 8.1: Power transmission efficiency through the crystalline quartz window after absorption losses.

$$\begin{aligned} t_{12} &= \frac{2\cos\theta_i}{\cos\theta_r + n\cos\theta_i}, \\ t_{21} &= \frac{2n\cos\theta_r}{n\cos\theta_i + \cos\theta_r}, \\ T_1 &= \frac{t_{12}^2 t_{21}^2}{1 + r_{12}^2 r_{21}^2 + 2r_{12}r_{21}\cos(2\beta)}, \end{aligned}$$

and then the $x - z$ polarisation [6],

$$\begin{aligned} r_{12} &= \frac{\cos\theta_i - n\cos\theta_r}{\cos\theta_i + n\cos\theta_r} \\ r_{21} &= \frac{n\cos\theta_r - \cos\theta_i}{n\cos\theta_r + \cos\theta_i} \\ t_{12} &= \frac{2\cos\theta_i}{\cos\theta_i + n\cos\theta_r} \\ t_{21} &= \frac{2n\cos\theta_r}{n\cos\theta_r + \cos\theta_i} \\ T_2 &= \frac{t_{12}^2 t_{21}^2}{1 + r_{12}^2 r_{21}^2 + 2r_{12}r_{21}\cos(2\beta)}, \end{aligned}$$

where

$$\beta = \frac{2\pi n d\cos\theta_r}{\lambda}.$$

The fraction of radiation transmitted through the quartz window, after multiple reflections, is

$$C_{\text{quartz}} = AT_1 + BT_2. \tag{8.1}$$

This depends on the theoretically expected polarisation, as calculated from the surface current model assuming an *infinitely wide grating*. The details of this calculation are shown in Appendix

Observation Angle	0.5mm Grating		1mm Grating		1.5mm Grating	
	λ(mm)	C_{quartz}	λ(mm)	C_{quartz}	λ(mm)	C_{quartz}
40	0.12	0.58	0.23	0.65	0.35	0.84
50	0.18	0.65	0.36	0.84	0.53	0.75
60	0.25	0.94	0.50	0.98	0.75	0.63
70	0.33	0.61	0.66	0.79	0.99	0.82
80	0.41	0.79	0.83	0.63	1.24	0.74
90	0.50	0.63	1.00	0.81	1.50	0.81
100	0.59	0.81	1.17	0.63	1.76	0.73
110	0.67	0.98	1.34	0.6	2.01	0.65
120	0.75	0.63	1.50	0.67	2.25	0.91
130	0.821	0.78	1.64	0.60	2.46	0.70
140	0.88	0.58	1.77	0.65	2.65	0.84

Table 8.2: Power transmission efficiency through the crystalline quartz window after multiple reflections (first order SP radiation only).

A. SP radiation is 100% polarised in the $x-z$ plane at $\phi = 0$. However, the degree of polarisation decreases with increasing azimuthal angle, ϕ, until the radiation is effectively unpolarised. Based upon the calculations of Appendix A, for the case of FELIX, $A = 0.411$ and $B = 0.589$. The values for C_{quartz}, for first order SP radiation from each grating used, is given in Table 8.2 and are shown in Figure 8.6.

SP radiation then passes through a wire mesh grid, a sheet of blank polyethylene and sheet of flurogold, all of which covered the quartz window. The wire mesh grid was made from copper wire, with 2mm square holes (Figure 4.4), and its transmission was measured using THz-TDS up to a wavelength of 1.8mm. At wavelengths less than 1.8mm the measured transmission was 0.5 ± 0.05, however, further measurements are necessary to determine its transmission at longer wavelengths. The black polyethylene sheet had a transmission of 0.9 ± 0.05 [35], and the flurogold contributed a wavelength dependent correction factor. The transmission through the sheet of flurogold, as determined by a THz-TDS measurement, is given in Table 8.3 and shown in Figure 8.7. No correction was made to account for water vapour absorption as the path length between the vacuum chamber and the detector was short, and no SP wavelengths were expected to occur near sharp absorption lines.

Two different types of filters were used during the FELIX experiments, both of which were described in detail in Chapter 5. However, only WAP filters were used during the November experiment considered in this chapter. As mentioned in the previous section, no filters were available for the $120-140°$ observation angles with the 1.5mm grating.The effect of observing at these angles without filters is shown in Figure 8.8. The black (square) points denote the average raw signal detected from the 1.5mm grating with no filters in place.These can be compared with

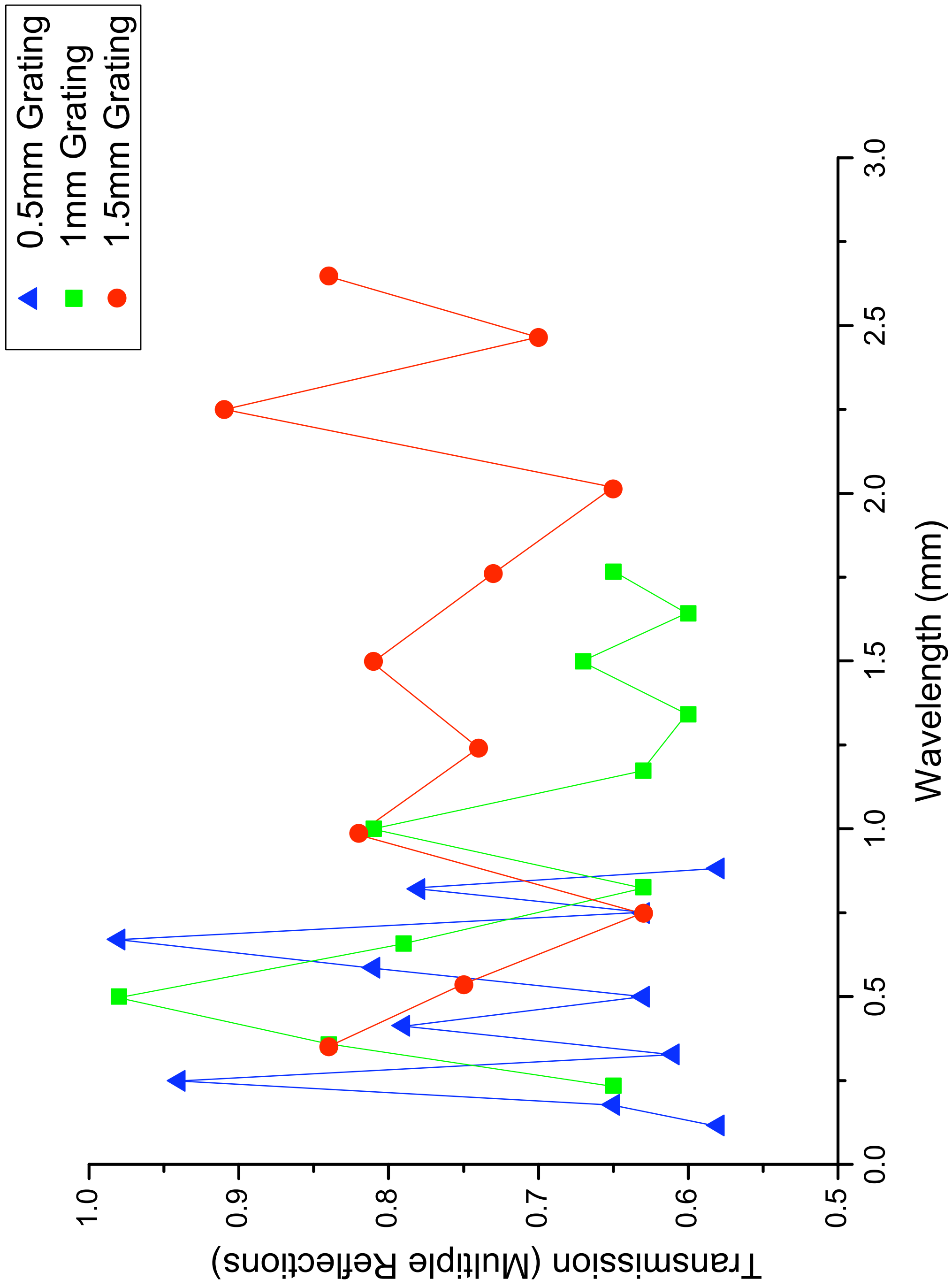

Figure 8.6: Power transmission efficiency through the crystalline quartz window after multiple reflections for first order SP radiation only (from Table 8.2). The lines connecting the points are to guide the eye only.

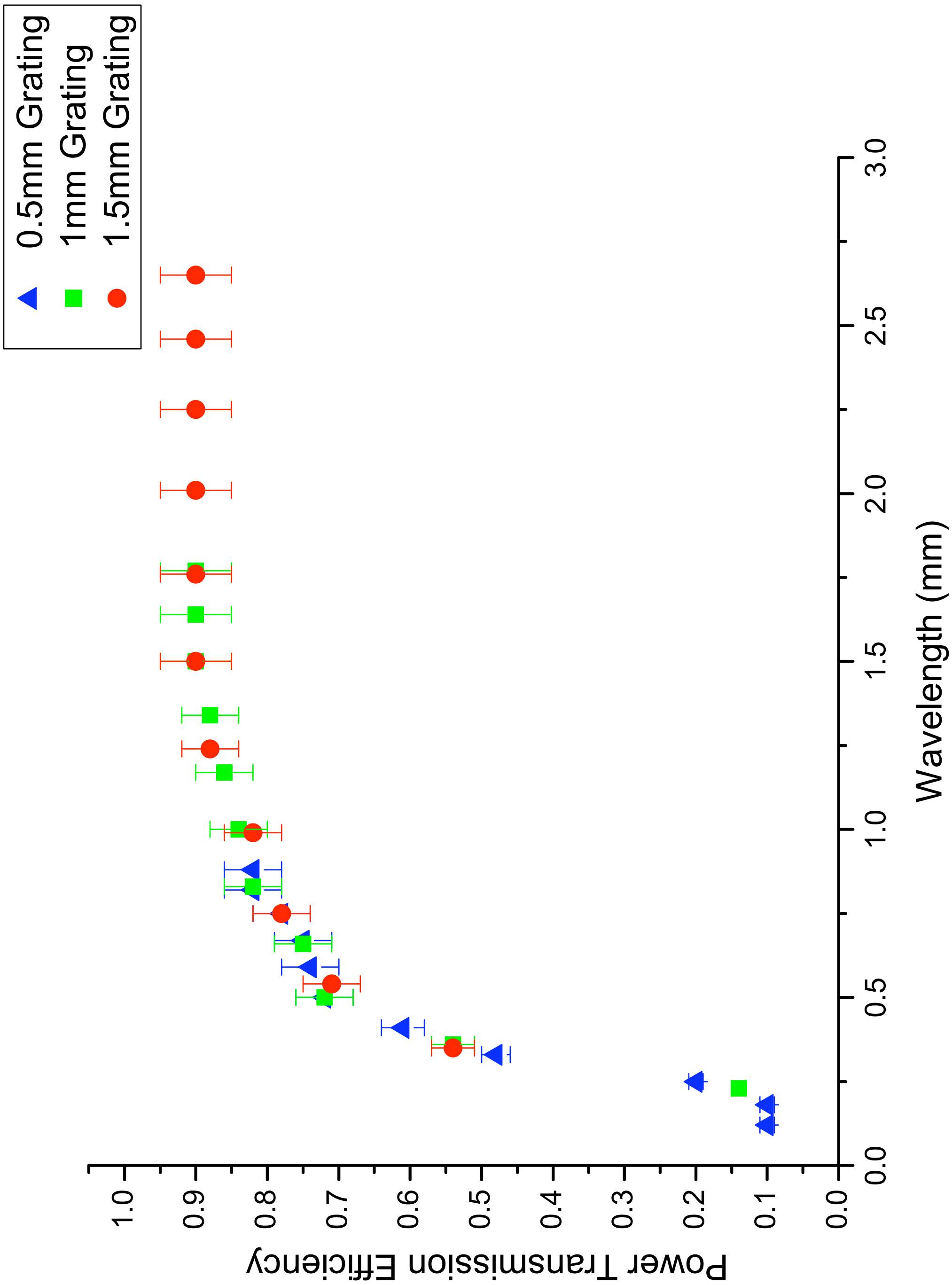

Figure 8.7: Measured power transmission efficiency through flurogold (from Table 8.3).

Observation Angle (°)	0.5mm Grating		1.0mm Grating		1.5mm Grating	
	λ(mm)	T(% ± 5%)	λ(mm)	T (% ± 5%)	λ(mm)	T (% ± 5%)
40	0.12	0.10 ± 0.01	0.23	0.14 ± 0.01	0.35	0.54 ± 0.03
50	0.18	0.10 ± 0.01	0.36	0.54 ± 0.03	0.53	0.71 ± 0.04
60	0.25	0.20 ± 0.01	0.50	0.72 ± 0.04	0.75	0.78 ± 0.04
70	0.33	0.48 ± 0.02	0.66	0.75 ± 0.04	0.99	0.82 ± 0.04
80	0.41	0.61 ± 0.03	0.83	0.82 ± 0.04	1.24	0.88 ± 0.04
90	0.50	0.72 ± 0.04	1.00	0.84 ± 0.04	1.50	0.90 ± 0.05
100	0.59	0.74 ± 0.04	1.17	0.86 ± 0.04	1.76	0.90 ± 0.05
110	0.67	0.75 ± 0.04	1.34	0.88 ± 0.04	2.01	0.90 ± 0.05
120	0.75	0.78 ± 0.04	1.50	0.90 ± 0.05	2.25	0.90 ± 0.05
130	0.821	0.82 ± 0.04	1.64	0.90 ± 0.05	2.46	0.90 ± 0.05
140	0.88	0.82 ± 0.04	1.77	0.90 ± 0.05	2.65	0.90 ± 0.05

Table 8.3: Measured power transmission efficiency through flurogold. The uncertainty in the quoted values is estimated at ±5%.

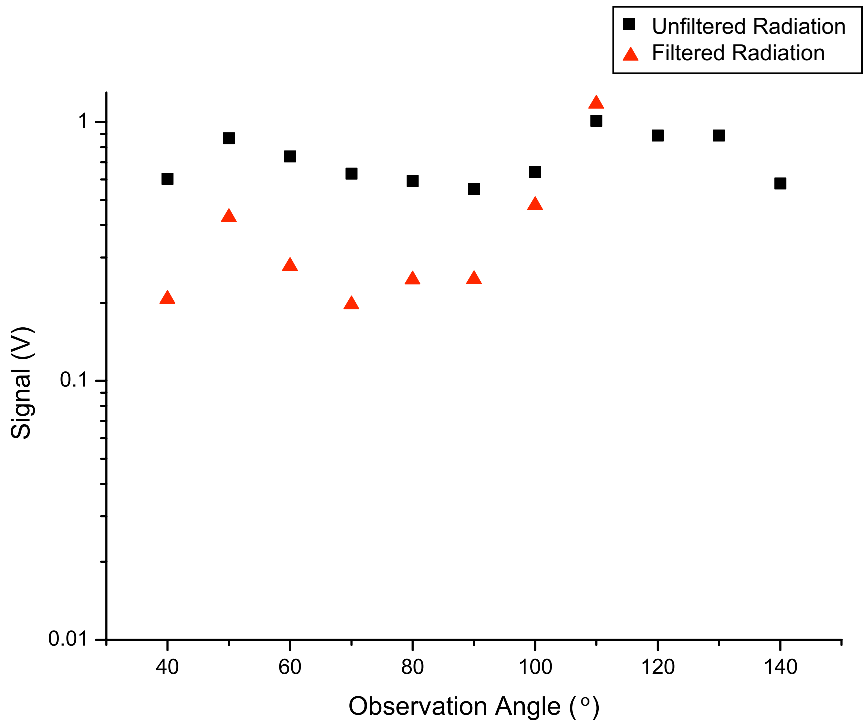

Figure 8.8: Comparison between the measured average raw signal from the 1.5mm grating without filters, and with WAP filters (with filter transmission corrections applied).

Observation Angle (°)	0.5mm Grating		1.0mm Grating		1.5mm Grating	
	λ(mm)	T	λ(mm)	T	λ(mm)	T
40	0.12	0.181 ± 0.009	0.23	0.448 ± 0.022	0.35	0.340 ± 0.017
50	0.18	0.127 ± 0.006	0.36	0.352 ± 0.018	0.53	0.492 ± 0.025
60	0.25	0.143 ± 0.007	0.50	0.415 ± 0.021	0.75	0.793 ± 0.040
70	0.33	0.090 ± 0.004	0.66	0.296 ± 0.015	0.99	0.810 ± 0.041
80	0.41	0.204 ± 0.010	0.83	0.789 ± 0.039	1.24	0.720 ± 0.036
90	0.50	0.254 ± 0.013	1.00	0.802 ± 0.040	1.50	0.804 ± 0.040
100	0.59	0.240 ± 0.012	1.17	0.859 ± 0.043	1.76	0.536 ± 0.027
110	0.67	0.231 ± 0.012	1.34	0.929 ± 0.046	2.01	0.101 ± 0.005
120	0.75	0.268 ± 0.013	1.50	0.803 ± 0.040	2.25	$1.0\pm^{0.0}_{0.1}$
130	0.821	0.308 ± 0.015	1.64	0.426 ± 0.021	2.46	$1.0\pm^{0.0}_{0.1}$
140	0.88	0.269 ± 0.013	1.77	0.528 ± 0.026	2.65	$1.0\pm^{0.0}_{0.1}$

Table 8.4: Filter transmission efficiencies for first order radiation from the 0.5, 1.0 and 1.5mm gratings. Filters did not exist for the 120 – 140° observation angles of the 1.5mm grating (see text for further details).

the red (triangular) points, which are the values obtained when the appropriate set of filters was used; the filter transmission has been taken into account. At shorter wavelengths there is a large difference between the unfiltered data points and the filtered points, suggesting that there is a lot of background radiation in this region that is longer than the expected SP wavelength. However, at long wavelengths the unfiltered and filtered data points begin to converge. This suggests that the majority of the radiation in the backwards direction is SP radiation. Therefore, although filters were not available at these wavelengths it was considered acceptable to treat all (unfiltered) radiation as SP radiation. This introduces an additional small error for these observation angles, with the 1.5mm grating only, of $\sim 10\%$. Table 8.4 (and Figure 8.9) gives the transmission of each WAP filter for 1st order radiation. Due to limited experimental time, the 0.5mm grating measurements were taken with filters designed for first order radiation from the 1mm grating. Hence, the transmissions listed for the 0.5mm grating are lower than expected.

After passing through the appropriate filter, SP radiation was reflected through the 90° bend in the optical system, which has a measured transmission efficiency of 0.80 ± 0.05, into the Winston cones. As examined in Chapter 7, this collected a solid angle of ≈ 6.5msr of which $\sim 47\%$ was detected by the pyroelectric detector. This decreases to $\sim 29\%$ at long wavelengths due to diffraction effects at the exit of the cone. The transmission factor applied to the data, depending on wavelength, is given in Table 8.5.

Following these corrections, an additional uncertainty of $\pm 50\%$ was added to the data to account for differences in the relative calibration of the pyroelectric detectors. No record exists of which detector was used at each observation angle, so a more accurate correction for this is not possible. However, Chapter 6 suggests that the majority of detectors are within a factor of

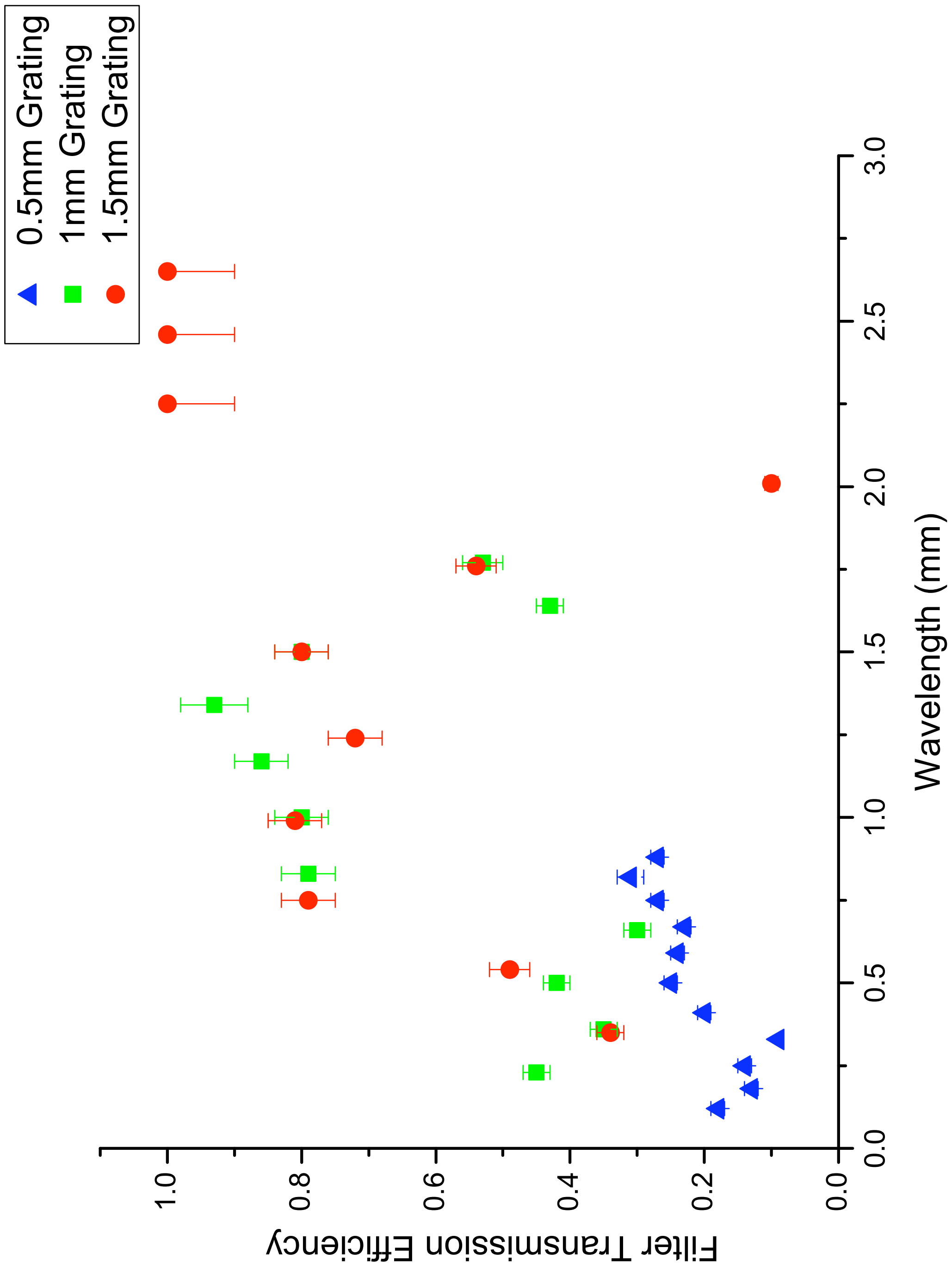

Figure 8.9: Filter transmission efficiencies for first order radiation from the 0.5, 1.0 and 1.5mm gratings. Filters did not exist for the 120 – 140° observation angles of the 1.5mm grating (from Table 8.4).

λ (mm)	T
$\lambda \leq 2.21$	0.47 ± 0.05
$2.22 \leq \lambda \leq 2.32$	0.44 ± 0.04
$2.33 \leq \lambda \leq 2.43$	0.37 ± 0.04
$2.44 \leq \lambda \leq 2.56$	0.31 ± 0.03
$\lambda > 2.56$	0.29 ± 0.03

Table 8.5: Correction factors due to diffraction effects at the exit of the Winston cone.

two of each other at each SP wavelength. This is represented by the additional uncertainty of $\pm 50\%$.

Finally, the viewing angles at 40 and 140° are partially obstructed by the edge of the window in the vacuum chamber. This introduced an additional correction factor, for the two extreme detectors, of 0.674 and 0.431 respectively. The signal was then converted into watts per bunch train, using a value of 1V = 5.3W [75]. Table 8.6 shows the complete set of correction factors that were applied to the data, many of which are also valid for the subsequent experiments of Chapters 9 and 10.

8.4 Analysis

For all gratings, the signal detected from observation angles less than 80° was $\leq$ 5mV, and therefore less than the error arising from the uncertainty in the beam position. These data points were excluded from the analysis. This was also the case for the majority of data from the 0.5mm grating for which only one measurement exists, taken with the 1mm grating filters. As a result, this analysis concentrates on data from the 1.0 and 1.5mm gratings only.

Equation 2.1, which states that the grating period and angle of observation determine the SP wavelength, is well tested. Hence, there was no need to use a spectrometer for the purpose of verifying this equation. However, several WAP filters were rearranged to check that the detected wavelengths were those expected. For example, consider the wavelength observed at 130° from the 1mm grating, $\lambda = 1.64$mm. The WAP filter for this wavelength was designed with a cut-off wavelength slightly longer than the expected SP wavelength. With this filter in place, SP radiation was detected. However, replacing it with another WAP filter, for example, one designed for $\lambda = 0.36$mm (50°) suppressed the signal. This is shown in Figure 8.10, which compares two measurements (note the negative y-axis). The black (crossed) points represent the SP signal detected from the 1mm grating at each observation angle with optimal WAP filters.

Observation Angle:	40°	50°	60°	70°	80°	90°	100°	110°	120°	130°	140°
Blank Distance	1.07										
Quartz Absorption	see Table 8.1										
Quartz Reflection	see Table 8.2										
Wire Grid	0.5 ± 0.05										
Black Polyethylene	0.90 ± 0.05										
Flurogold	see Table 8.3										
Filter Transmission	see Table 8.4										
90° Bend in Optical System	0.80 ± 0.05										
Diffraction	see Table 8.5										
Obstructed View	0.674	1.0									0.431
Converting V to W	5.30 ± 0.05										
Pyroelectric Detector Calibration (error only)	$\pm 50\%$										

Table 8.6: Complete transmission factors and corrections that were applied to the FELIX data before analysis (see text for details).

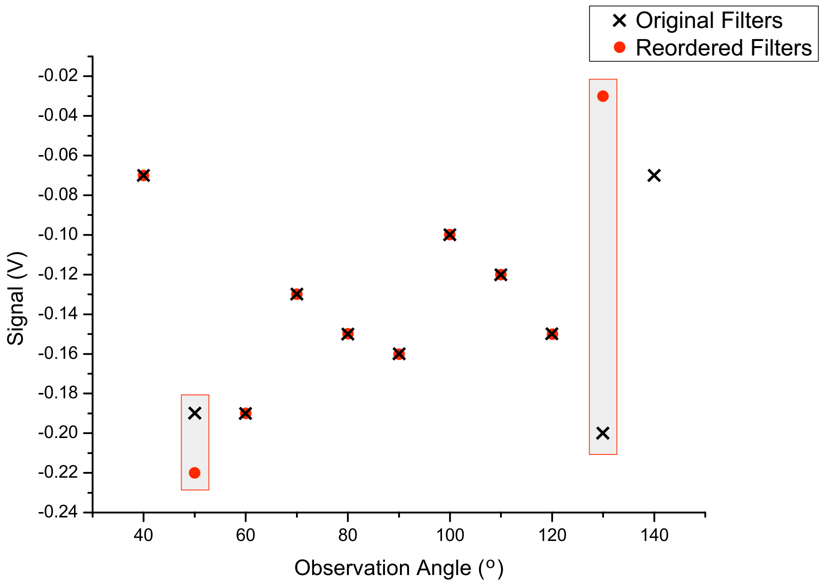

Figure 8.10: Confirming SP wavelengths by reordering WAP filters (see text for details). Note the negative y-axis.

The red (circular) points show a measurement taken under the same conditions, except with the following changes:

- 50° uses the filter for 130° and *vice versa*.
- All other observation angles retained their optimum filters.

The detector at 130° detects significantly less radiation when the shorter WAP filter is used and the 50° detector detects slightly more radiation with the longer wavelength WAP filter in place. This is due to the 130° filter's much longer cut-off wavelength compared to the wavelength of SP radiation expected at 50°. Therefore, more (background) radiation was accepted whilst this filter was used at 50° resulting in the observed increase. This observation confirms that the general pattern of the wavelength distribution is consistent with that of SP radiation.

A Kramers-Krönig analysis was carried out on the average data from the 1.0 and 1.5mm gratings. This followed the procedure of Sections 3.2.2 to 3.2.4, with an additional step prior to Equation 3.7. This converts the measured power per bunch train, P (in watts) to energy per bunch, E (in Joules).

$$E = P\tau_s,$$

where τ_s is the bunch spacing in the bunch train. As the high frequency beam operated at 1GHz, $\tau_s = 1 \times 10^{-9}$. The remainder of the procedure then continues from Equation 3.7.

a)

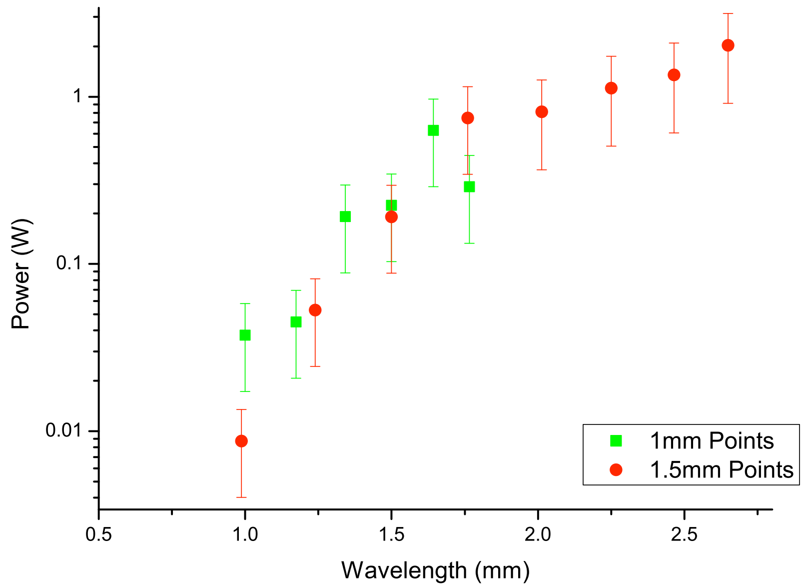

b)

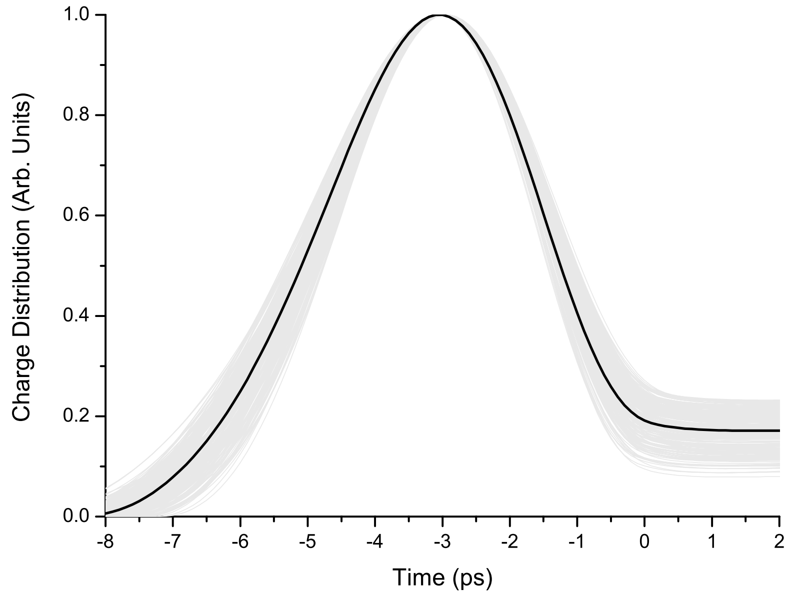

Figure 8.11: a) The average SP signal measured from the 1.0 and 1.5mm gratings, and b) a Kramers-Krönig reconstruction of the FELIX bunch using this data. The reconstruction can be approximated by the sum of three Gaussians (dotted lines).

The average measured SP signal from the 1.0 and 1.5mm gratings is shown in Figure 8.11a. The measurements are consistent with each other within the experimental uncertainty, however, this is large (±54%). The KK reconstruction is shown in Figure 8.11b. The reconstructed bunch has a FWHM of $3.9^{+0.5}_{-0.5}$ps. However, the reconstruction does not tend to zero in the positive time direction, which suggests that it requires more long wavelength data points to accurately reconstruct the bunch profile.

The reconstructed profile shows no fine structure and tends towards an asymmetric ($\varepsilon \approx 1.4$) Gaussian. This could be an accurate representation of the profile, or it could be due to the fact that insufficient short wavelength data were collected to define any fine structure in the bunch profile, *i.e.*the KK reconstruction presented here may be equivalent to the $\Gamma = 2$ case from Section 3.2.5. If this is the case, the reconstructed FWHM is still a reasonably accurate estimate of the actual FWHM. More data points, over a larger range of wavelengths, would clarify the issue.

8.5 Conclusions

The above re-analysis of the FELIX data was compared with the previously published values. The original data set combined data from all three gratings (0.5, 1.0 and 1.5mm) and in general has a lower output than the re-analysed data. Both the original and re-analysed data sets are presented in Figure 8.12, which also includes two potential distributions describing the original data set (a Gaussian and asymmetric triangular profile). These profiles were chosen via a variation of the template method described in Section 3.1; instead of fitting templates to the measured power distribution using a weighted least squares (WLS) analysis, they were instead judged by eye. The addition of data from the 0.5mm grating appears to discriminate between the two potential profiles and, hence, lead to the published conclusion that the FELIX beam was 5.5ps long with an approximately asymmetric triangular appearance. However, it should be noted that the published bunch length of 5.5ps was based upon a different definition of 'length' to that used in this thesis. The definition used in [15] was that the bunch length is the length of time containing 90% of the particles in the bunch. This thesis uses the FWHM to characterise the bunch length. Therefore, the previously published result of 5.5ps is equivalent to a FWHM of 3.8ps.

The original analysis was based on a number of incorrect assumptions and on details that were not accurately known at the time, including:

a)

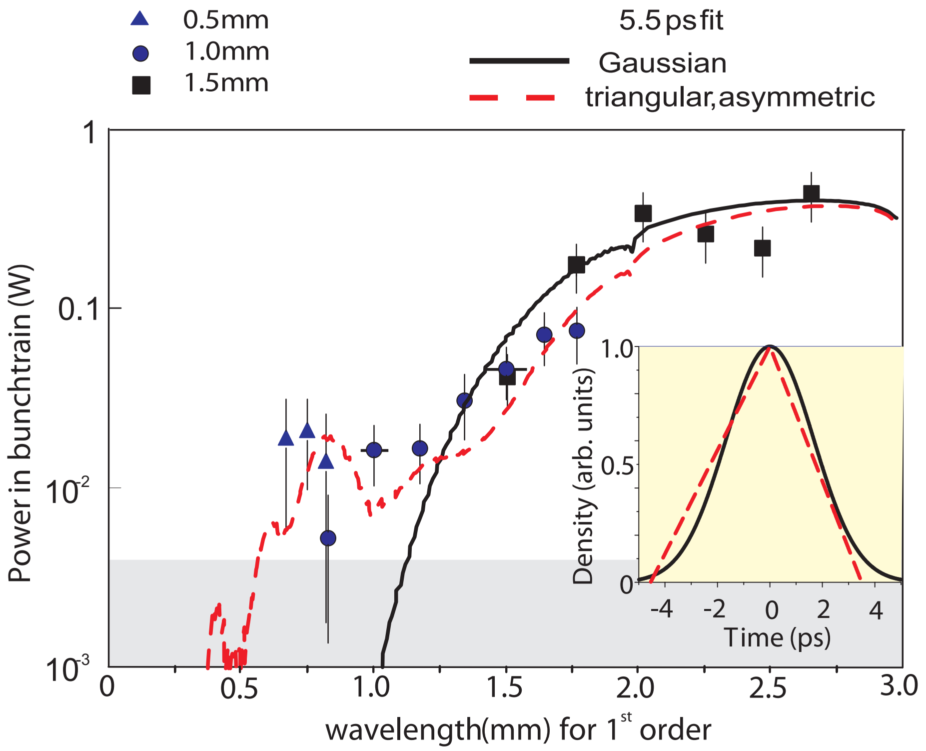

b)

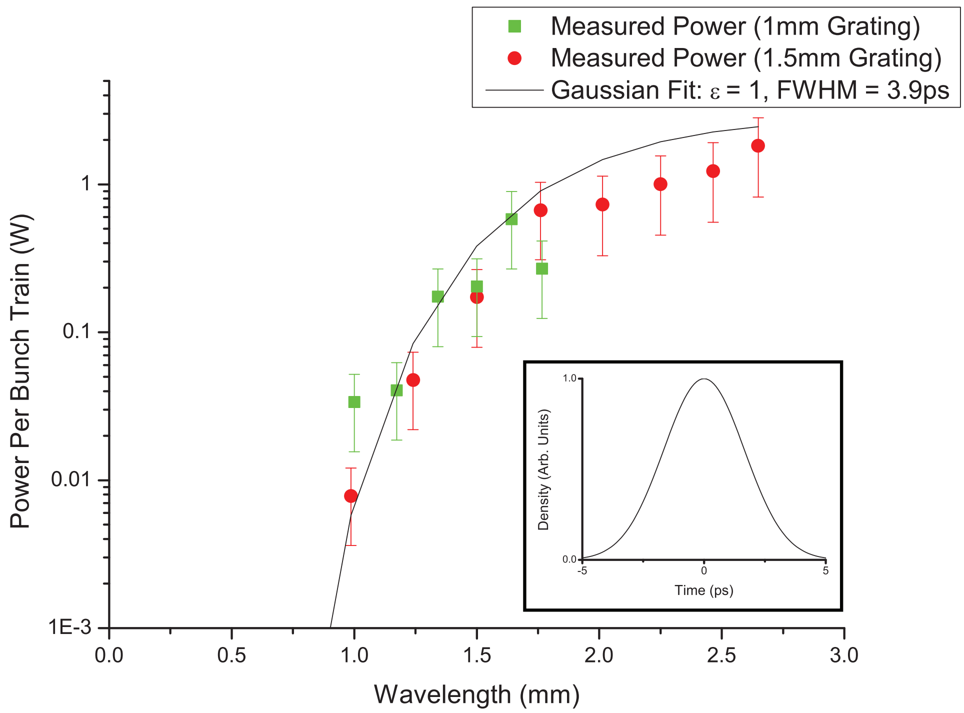

Figure 8.12: a) Data previously published in [15], b) the re-analysed data, excluding the 0.5mm grating, with a WLS fit (see text for details). The inset shows the bunch profile chosen by the WLS fit.

- The quartz window was assumed to transmit 100% of the incident radiation.
- Reflection from the surfaces of the quartz window were calculated using wavelength-independent equations.
- No correction was made to account for the transmission of the wire grid screen, or the transmission of radiation through the 90° bend of the optical system.
- The assumed power transmission efficiency of the filters used for radiation from the 0.5mm grating were incorrect.
- The values for the solid angle, and for the visible grating length, were low.
- Diffraction of long wavelengths through the Winston cone were ignored.
- The value used to correct for the partial obstruction of the 40 and 140° observation angles was incorrect.

The above were all more accurately accounted for in the re-analysis presented in this chapter, hence the overall signal levels reported in Figure 8.12b are higher than those of 8.12a. The overall shape of the power distribution is also different from the original, particularly at long wavelengths were diffraction effects were accounted for. The KK reconstruction of the re-analysed data has already been presented in the previous section. This returned a profile that tended towards an asymmetric Gaussian ($\varepsilon \approx 1.4$) with a FWHM of 3.9ps.

A WLS analysis was carried out on the re-analysed data, based on the KK result. This searched for the closest Gaussian profile to the measured power distribution, using templates simulated by BUNCH2, with FWHM between 2.6 − 4ps and asymmetry factor $\varepsilon = 1 - 5$. The lowest χ^2 result is shown as a solid line in Figure 8.12b. This was a symmetric (*i.e.*$\varepsilon = 1$) Gaussian with a FWHM of 3.9ps. However, this had a χ^2 of 6.7, which is not particularly good. The poor χ^2 demonstrates the unsuitability of this approach to analysing SP data, especially the approach of judging the suitability of a profile by eye. Although the χ^2 is poor, when plotted alongside the data it appears to follow the approximately correct trend — as did the proposed profiles of Figure 8.12a — which can be misleading. Both the old and new WLS analysis produce similar FWHMs. However, the Gaussian derived from the new analysis has a higher energy output because the correct values of solid angle, grating length, *etc.* have been used for its calculation.

The FWHM obtained from a KK and WLS analysis are in agreement, but the recovered profiles are not. The KK analysis gives an asymmetric profile, whilst the WLS gives a symmetric Gaussian. However, the χ^2 of the WLS fit was not good. As KK has been shown to reliably recover both the overall approximate length and the FWHM of the bunch when there is insufficient wavelength information (see Chapter 3), the KK result is more likely to approach the true distribution. As the FWHM of the original and reanalysed data coincide, it is likely that the the bunch length proposed in [15] is correct. However, the profile proposed in [15] may not be accurate. More data are necessary to draw further conclusions about the bunch profile itself with a KK analysis.

8.6 Summary

SP radiation was used to determine the longitudinal bunch profile of the 45MeV FELIX beam in November 2005. The results from this experiment have already been published [15], however, there were a number of issues that were not known at the time that could affect the outcome of the analysis. To this end, this chapter detailed the re-analysis of the same data. The experimental layout, and the procedure for obtaining and preparing the data for analysis, is described in Sections 8.2 and 8.3.

The re-analysis of the FELIX data, using the Kramers-Krönig technique is dealt with in Section 8.4. Considering only data from the 1.0 and 1.5mm gratings gives a reconstructed bunch profile with a FWHM of 3.9ps. The reconstructed profile is an asymmetric Gaussian, though there are concerns over whether this is the actual profile or insufficient short wavelength data were collected to define any finer structure in the bunch.

The re-analysed bunch profile is compared to the previously published results in Section 8.5. The FELIX bunch was previously analysed under incorrect assumptions about the correction factors that were applied to the data. However, analysing the data using more accurate correction factors using a WLS approach returns similar results to those published in [15], *i.e.*a Gaussian profile with a FWHM of 3.9ps. Note that this is equivalent to the previously reported bunch length of 5.5ps in [15] due to a difference in the definition of bunch length. The old and new analyses of the data are in agreement over the FWHM of the FELIX bunch (3.8ps and 3.9ps respectively). However, more data is required to clarify the bunch profile.

Chapter 9

SLAC — March 2007

Coherent SP radiation was used at SLAC in March 2007 to determine the longitudinal bunch profile of its 28.5GeV electron beam. This experiment had two primary goals. The first of these was to prove that it was possible to observe SP radiation in the highly relativistic regime.

Recalling Chapter 2, there are two main theoretical treatments that can be applied to the generation of SP radiation. One of these, pioneered by van den Berg, examines SP radiation as the result of the diffraction of the beam's electromagnetic field by a grating (Section 2.2.1), and the other treats it as the result of a current induced on the surface of the grating by a passing charged particle beam, the surface current model (Section 2.2.3).

When the van den Berg theory was extended to the highly relativistic regime by Haeberlé *et al.*[22], the predicted emitted energy was thought to decrease with increasing beam energy. The surface current model, on the other hand, predicts no such decrease. SP can also be compared to other similar radiative processes, such as transition or diffraction radiation, which have been used in the highly relativistic regime for many years with no observed decrease in emitted energy. Hence, it was necessary to prove that SP radiation could also be generated in the highly relativistic regime.

Continuing from this, the second goal of the experiment was to show that coherent SP radiation, and the experimental arrangement used, was a viable diagnostic tool for determining the longitudinal profile of the bunch. The transverse deflecting cavity, LOLA, was also used at this time to determine the bunch length of the SLAC beam. This is a well-known and trusted technique, albeit invasive, whose results are ideal to compare with those of the SP experiment.

9.1 SLAC Beam Parameters

The beam consisted of a single electron bunch at 10Hz repetition. Consequently, the measurements reported here give the average bunch shape detected during the time observed. The beam had an energy of 28.5GeV ($\gamma \simeq 55773$), with between 0.9 and 1.6×10^{10} electrons per bunch (as measured $\sim$ 20m upstream of the SP experiment). The transverse size of the beam was measured by two wire scanners, one before and one after the experiment, approximately 10m away. These gave an average beam size of $\sigma_x = 0.49$mm and $\sigma_y = 0.14$mm. The emittance of the beam was 310mm.mrad in x, and 13mm.mrad in y.

9.2 Experimental Issues

This was the first SP experiment at SLAC and as such it lacked some of the necessary additions of the subsequent experiment (Chapter 10). The apparatus was located in End Station A (ESA), as indicated in Figure 9.1, and is somewhat similar to that used at FELIX (Chapter 8). For example, it used the same gratings (0.5, 1.0 and 1.5mm period gratings and a blank) except that the discrepancy between the blank and grating positions on the carousel (see Section 8.2) had been addressed.

A complete set of WAP filters were also available for the following gratings and radiation orders:

- 0.5mm grating, 1st order.
- 1mm grating, 1st and 2nd order.
- 1.5mm grating, 1st, 2nd and 3rd order.

The filters were changed by hand, and were selected in order to achieve the highest transmission for each expected SP wavelength. The transmission of each WAP filter is given in the following section. A moveable aluminium screen was also added to the experiment to take the place of the aluminium plugs from FELIX. This could be moved up and down in front of the window of the vacuum chamber and provided a measurement of the irreducible background.

The main difference between the experiment at SLAC and the preceding experiment at FELIX, however, is in the design of the data acquisition system. This was redesigned to improve and simplify data acquisition. The electronics were separated from the pyroelectric detectors and were housed in a separate DAQ system on the tunnel floor that was completely surrounded

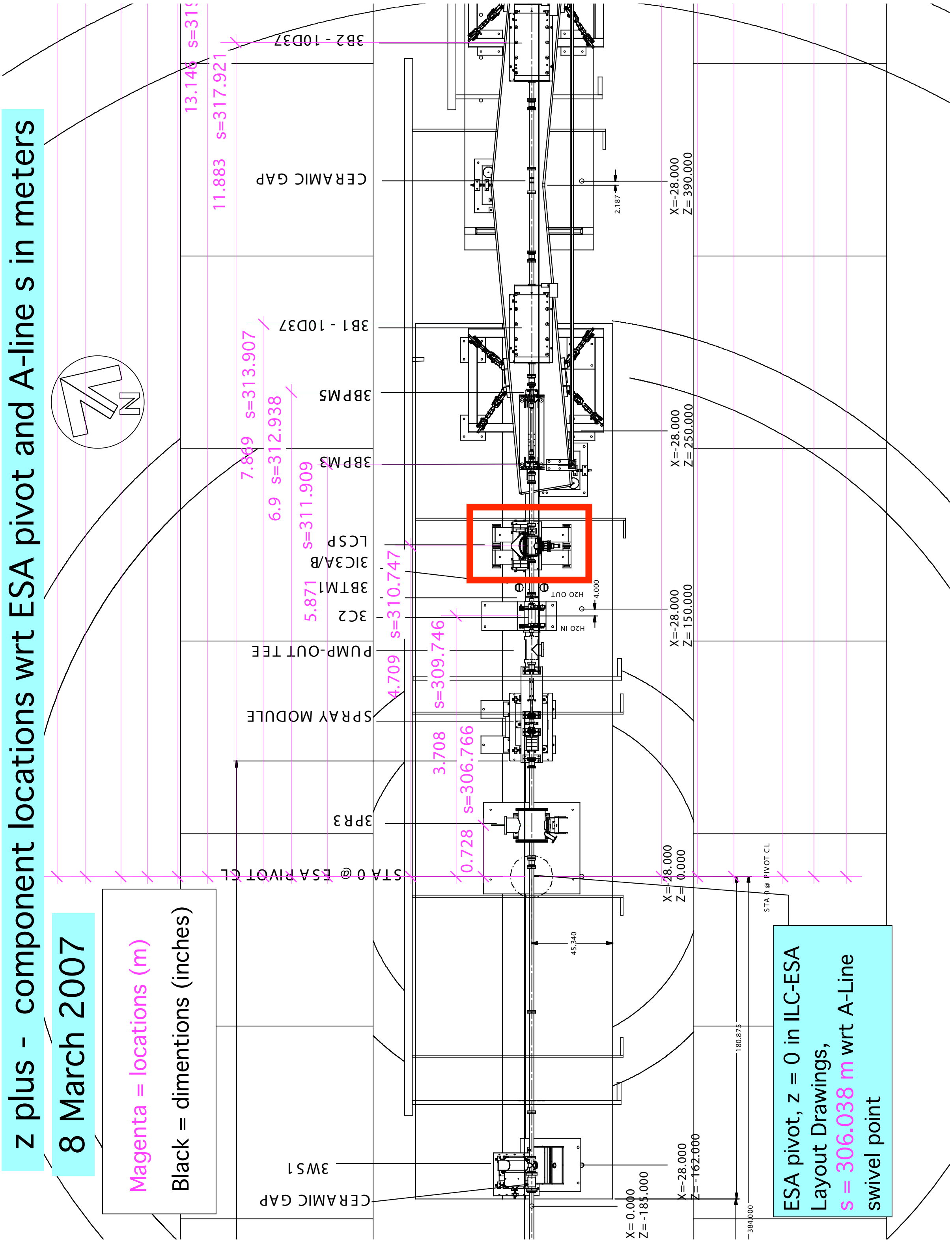

Figure 9.1: Schematic of the first section of ESA. The location of the SP experiment is highlighted [62].

by lead shielding. An additional benefit of this arrangement was that it also shortened the detector system (Figure 4.9). The details of the DAQ system and experimental arrangement can be found in Section 4.4.2. Figure 9.2 shows the apparatus set up in the SLAC beamline.

Prior to the start of the experiment, the grating was moved towards the beam until evidence was observed that it was impinging upon the beam halo. The grating was then retracted slightly, and its position was recorded. The gratings (and blank) were then moved into this position for each measurement, approximately 2.5mm away from the beam centre. At the time, the DAQ system could only provide data taken at 1Hz (triggered by the accelerator system). Hence, data were taken over a ~ 2 minute period (~ 120 bunches) for each grating in turn.

The largest obstacle faced by this experiment was due to the method of changing filters. Since this had to be done by hand, and the time taken to gain access to the beamline was relatively long, it introduced a turn-around time of about 45 minutes between measurements with different gratings and filter combinations. This raised concerns about the possibility of beam drift, and consequently, measurements spanning several hours cannot be reliably compared.

9.3 Processing SLAC Data

The data were processed in a series of steps, which are described below. Although the process is similar to that described in Section 8.3, there are some differences.

9.3.1 Conversion to Joules and Calculation of the SP Signal

The DAQ system returned data in terms of ADC values, which were converted into Joules. Starting with a data file, the signal detected at each observation angle was first converted to Joules as follows.

Let the average ADC value for each detector be A. The DAQ system was calibrated after the experiment, providing 3.5×10^{-17} C/ADC count [54]. The absolute calibration of the pyroelectric detectors performed in Chapter 6 yielded a value of 1.1μC/J. Therefore, the conversion factor between ADC counts and Joules, C_{adc} is

$$C_{\text{adc}} = \frac{3.5 \times 10^{-17}}{1.1 \times 10^{-6}} \approx 32\text{pJ/ADC count.} \tag{9.1}$$

The DAQ recorded 14 readings before the bunch had passed the grating, and 14 readings afterwards. These two sets of readings were summed, and the difference between them was

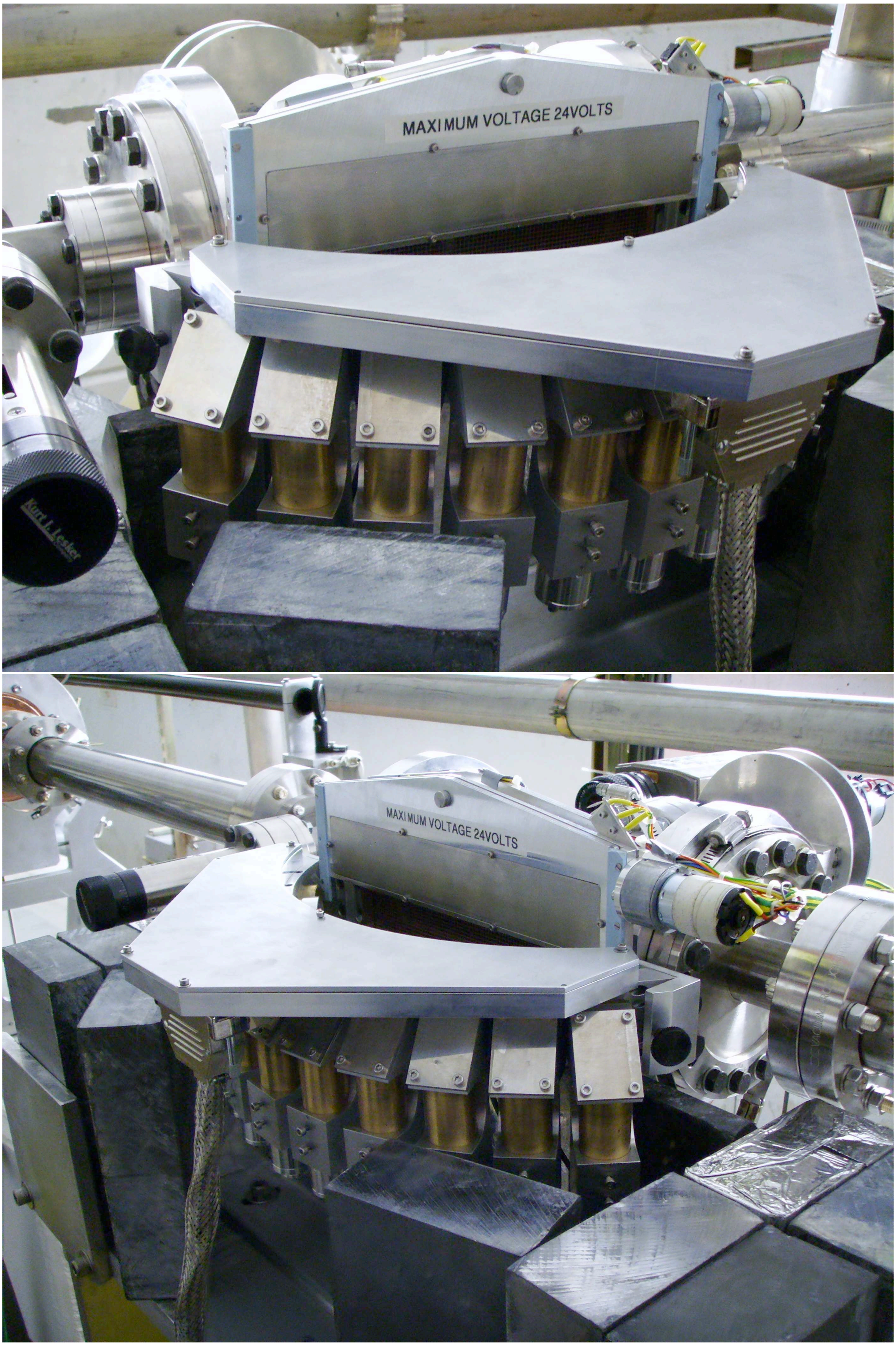

Figure 9.2: The SP apparatus in ESA (March 2007) with the aluminium screen in the raised position. The DAQ box is not pictured. The beam direction is from right to left.

found. The ADC gain meant that the output was also divided by 16. Hence, the average ADC value was found by multiplying by 16/14, or 8/7, and the average signal detected at each observation angle, R, in Joules is

$$R = \frac{8}{7} \times 32 \times A\,(\mathrm{pJ}).$$

Let the average uncorrected signal at each observation angle, in Joules, from a grating be R_G, and the blank, R_B. The difference in signal between that seen with a grating and a blank, under the same filtering conditions, was then due to radiation that arises from the periodic structure of the grating, *i.e.*it was the 'true' SP radiation. Hence, the uncorrected SP signal, S_U, is

$$S_U = R_G - R_B. \tag{9.2}$$

9.3.2 Corrections

Once the uncorrected SP signal, S_U, was determined there were a number of corrections that were applied to the data to account for losses within the experimental system (as in Section 8.3). Although some of these corrections have been mentioned with respect to the FELIX experiment, they are listed here again to avoid potential confusion.

First, all corrections related to the transmission of radiation out of the vacuum chamber were applied. This included i) transmission due to absorption through the quartz window, ii) transmission through the wire grid screen, and iii) transmission through the black polyethylene sheet. Flurogold was not used during any of the SLAC experiments and does not need to be considered. These correction factors are the same as for FELIX. The transmission loss through the quartz window due to multiple reflections is slightly different from that of FELIX. On *average*, the theoretically expected polarisation at SLAC is described by $A = 0.494$ and $B = 0.506$ (see Equation 8.1). The reflection loss corrections for SLAC are given in Table 9.1 and are also shown in Figure 9.3.

Secondly, corrections to account for transmission losses through the WAP filters and optical system were applied. The WAP filters used during this experiment were different from those used at FELIX and their transmission is given in Table 9.2 and Figure 9.4. At short wavelengths it is very difficult to manufacture WAP filters. Therefore, so-called 'hi-mesh' [23] filters were

Observation Angle	0.5mm Grating		1mm Grating		1.5mm Grating ($n = 1$)		1.5mm Grating ($n = 2$)	
	λ(mm)	C_{quartz}	λ(mm)	C_{quartz}	λ(mm)	C_{quartz}	λ(mm)	C_{quartz}
40	0.12	0.62	0.23	0.69	0.35	0.86	0.18	0.70
50	0.18	0.67	0.36	0.85	0.53	0.77	0.27	0.61
60	0.25	0.94	0.50	0.98	0.75	0.64	0.38	0.73
70	0.33	0.62	0.66	0.8	0.99	0.82	0.49	0.63
80	0.41	0.79	0.83	0.63	1.24	0.74	0.62	0.60
90	0.50	0.63	1.00	0.81	1.50	0.81	0.75	0.63
100	0.59	0.81	1.17	0.63	1.76	0.73	0.88	0.60
110	0.67	0.98	1.34	0.60	2.01	0.66	1.01	0.70
120	0.75	0.64	1.50	0.68	2.25	0.91	1.13	0.76
130	0.821	0.79	1.64	0.63	2.46	0.73	1.23	0.61
140	0.88	0.62	1.77	0.69	2.65	0.86	1.32	0.69

Table 9.1: Power transmission efficiency through the crystalline quartz window after multiple reflections.

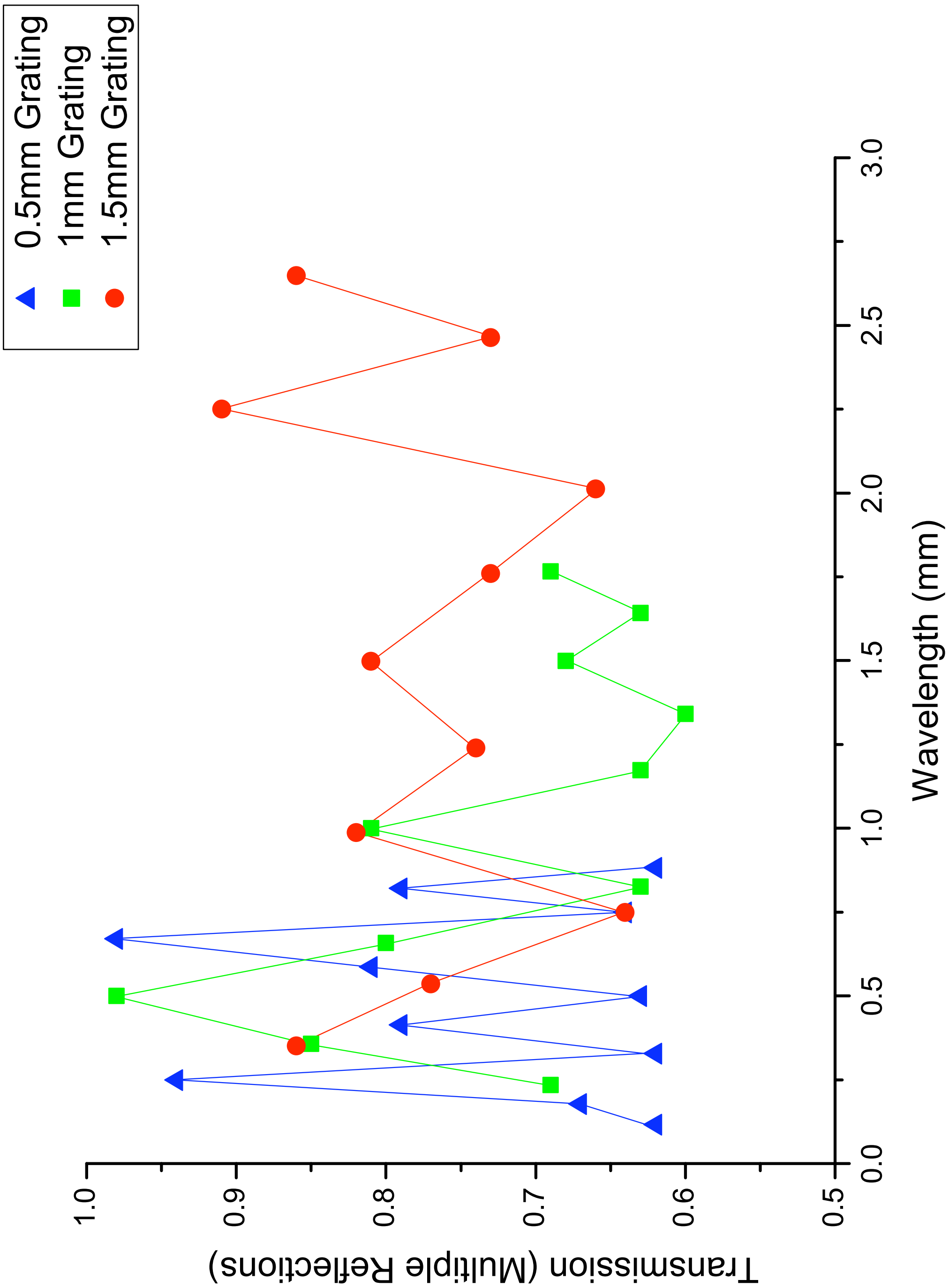

Figure 9.3: Power transmission efficiency through the crystalline quartz window after multiple reflections (from Table 9.1). The lines connecting the points are to guide the eye only.

Observation Angle (°)	0.5mm Grating, $n = 1$		1mm Grating, $n = 1$		1.5mm Grating, $n = 1$		1.5mm Grating, $n = 2$	
	λ(mm)	T	λ(mm)	T	λ(mm)	T	λ(mm)	T
40	0.12	1.0	0.23	0.75 ± 0.04	0.35	0.34 ± 0.02	0.18	1.0
50	0.18	1.0	0.36	0.36 ± 0.02	0.53	0.48 ± 0.02	0.27	0.99 ± 0.05
60	0.25	0.52±0.03	0.50	0.42 ± 0.02	0.75	0.90 ± 0.05	0.38	0.91 ± 0.05
70	0.33	0.65±0.03	0.66	0.86 ± 0.04	0.99	0.92 ± 0.05	0.49	0.39 ± 0.02
80	0.41	0.38±0.02	0.83	0.78 ± 0.04	1.24	0.97 ± 0.05	0.62	0.94 ± 0.05
90	0.50	0.42±0.02	1.00	0.90 ± 0.05	1.50	0.80 ± 0.04	0.75	0.90 ± 0.05
100	0.59	0.43±0.02	1.17	0.85 ± 0.04	1.76	0.52 ± 0.03	0.88	0.89 ± 0.04
110	0.67	0.90±0.05	1.34	0.91 ± 0.05	2.01	0.72 ± 0.04	1.01	0.89 ± 0.04
120	0.75	0.90±0.05	1.50	0.80 ± 0.04	2.25	0.75 ± 0.04	1.13	0.94 ± 0.05
130	0.821	0.80±0.04	1.64	0.77 ± 0.04	2.46	0.65 ± 0.03	1.23	0.97 ± 0.05
140	0.88	0.90±0.05	1.77	0.52 ± 0.03	2.65	0.77 ± 0.04	1.32	0.98 ± 0.05

Table 9.2: Power transmission efficiency through WAP filters for all measured SP wavelengths. Filters for radiation arising from the 0.5mm grating, $n = 1$, are also suitable for radiation arising from the 1mm grating, $n = 2$, and 1.5mm grating, $n = 3$.

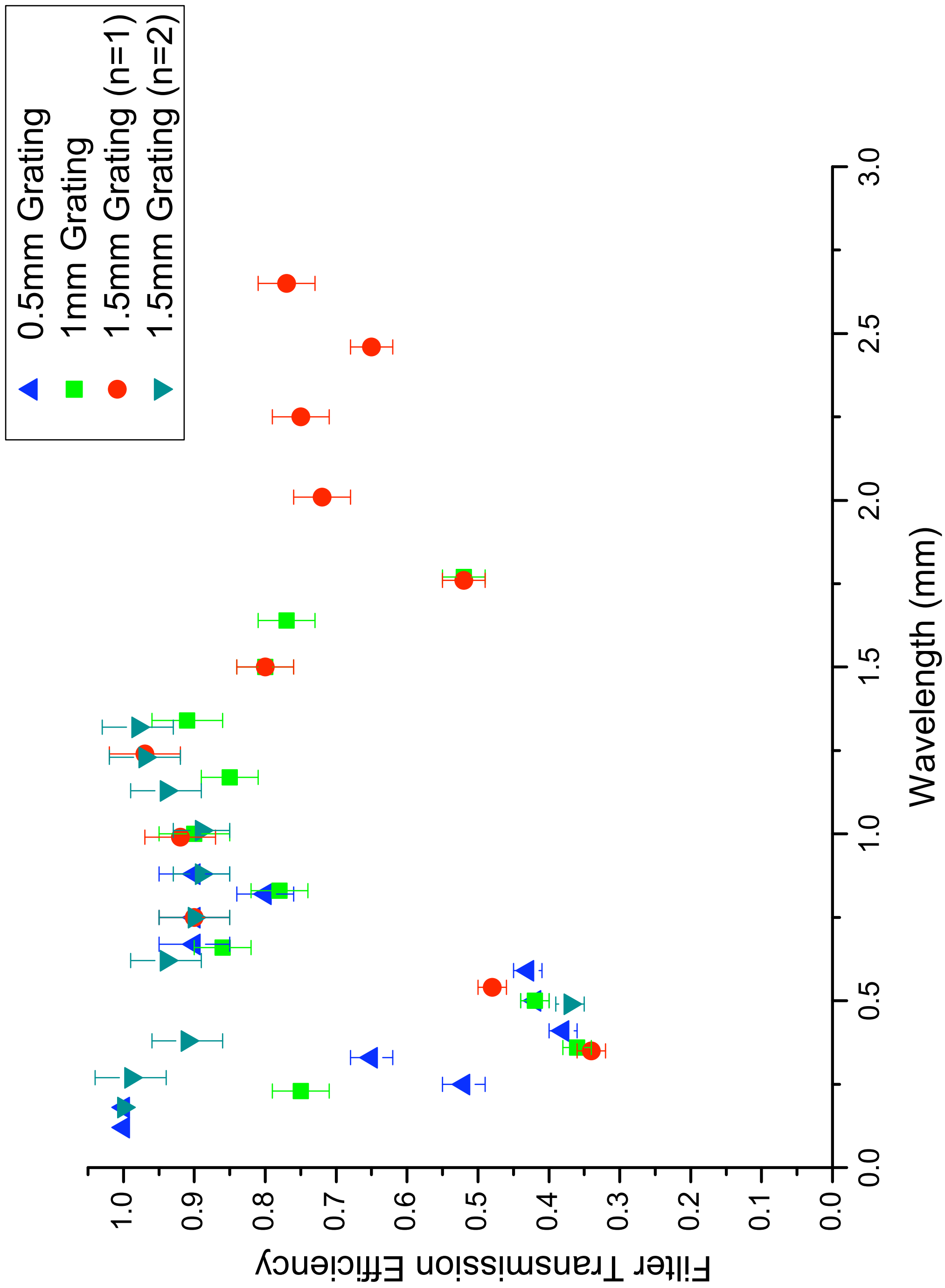

Figure 9.4: Power transmission efficiency through WAP filters for all measured SP wavelengths (from Table 9.2).

used at 40 and 50° for first order radiation from the 0.5mm grating. These filters remove all radiation above a cut-off wavelength, λ_c, where $\lambda_c > \lambda_{\text{SP}}$, and were assumed to have a transmission approximately equal to 1 for $\lambda \leq \lambda_{\text{SP}}$ [25]. Filters suitable for radiation from the 0.5mm grating, first order, were also suitable for radiation from the 1mm grating, 2nd order, and 1.5mm grating, 3rd order. All remaining corrections related to the optical system are the same as for FELIX, for example, losses within the optical system, and losses at the exit of the Winston cone due to diffraction effects.

Finally, corrections were made to account for the responsivity of each pyroelectric detector relative to the reference detector at $\lambda = 1.5$mm (see Section 6.4 and 6.5). These values are given in Table 9.3 and Figure 9.5. The total correction applied to the uncorrected SP signal was the product of all the factors listed in Table 9.4, C_{all}. The fully corrected SP signal is then

$$S = S_U/C_{\text{all}}.$$

It is interesting to note that, approximately, only 7% of the emitted radiation is detected.

9.4 Uncertainty Estimate for the SLAC Data Sets

The only experimental difference between this data set and the following chapter lies in the filter transmissions and the rate of data acquisition. The uncertainty in the transmission efficiency of each filter is the same, regardless of the filter used. Therefore, this section is also applicable to Chapter 10.

The largest contributions to the experimental uncertainty lie in systematic effects, for example, the relative calibration of the pyroelectric detectors and the transmission of the wire grid screen. A best estimate of the uncertainty in the detector calibration is ±30%, and it would be difficult to improve upon this in the far-infrared. The wire grid screen measurement carries an uncertainty of ±10%, which could potentially be improved upon with further measurements. Measurements of the wire grid screen were not available for wavelengths greater than 1.8mm, and an assumption was made that its transmission remains at 0.50 ± 0.05. Improvements would require taking measurements of the wire grid screen and quartz window together, over a wider range of angles and wavelengths. The total systematic uncertainty associated with these measurements is ±35%.

The statistical error of each measurement is typically small. However, it does depend on the grating used and the angle of observation. Therefore, the combined statistical and systematic

Observation Angle (°)	Detector Used	0.5mm Grating, $n = 1$		1mm Grating, $n = 1$		1.5mm Grating, $n = 1$		1.5mm Grating, $n = 2$	
		λ(mm)	R	λ(mm)	R	λ(mm)	R	λ(mm)	R
40	12	0.12	1.65 ± 0.50	0.23	1.65 ± 0.50	0.35	1.65 ± 0.50	0.18	1.65 ± 0.50
50	15	0.18	1.61 ± 0.48	0.36	1.61 ± 0.48	0.53	1.61 ± 0.48	0.27	1.61 ± 0.48
60	10	0.25	1.32 ± 0.40	0.50	1.32 ± 0.40	0.75	1.32 ± 0.40	0.38	1.32 ± 0.40
70	9	0.33	1.19 ± 0.36	0.66	1.19 ± 0.36	0.99	1.19 ± 0.36	0.49	1.19 ± 0.36
80	6	0.41	1.36 ± 0.41	0.83	1.36 ± 0.41	1.24	1.53 ± 0.46	0.62	1.36 ± 0.41
90	13	0.50	1.38 ± 0.41	1.00	1.38 ± 0.41	1.50	1.0	0.75	1.38 ± 0.41
100	11	0.59	1.28 ± 0.38	1.17	1.56 ± 0.47	1.76	1.24 ± 0.37	0.88	1.28 ± 0.38
110	1	0.67	1.47 ± 0.44	1.34	0.86 ± 0.26	2.01	0.52 ± 0.16	1.01	1.47 ± 0.44
120	7	0.75	1.49 ± 0.45	1.50	1.25 ± 0.38	2.25	0.59 ± 0.18	1.13	1.49 ± 0.45
130	16	0.821	1.34 ± 0.40	1.64	0.77 ± 0.23	2.46	1.26 ± 0.28	1.23	1.19 ± 0.36
140	8	0.88	1.34 ± 0.40	1.77	1.69 ± 0.51	2.65	0.5 ± 0.15	1.32	1.16 ± 0.35

Table 9.3: The relative response, R, of each detector for the SP wavelength detected relative to detector 13 detecting at $\lambda = 1.5$mm.

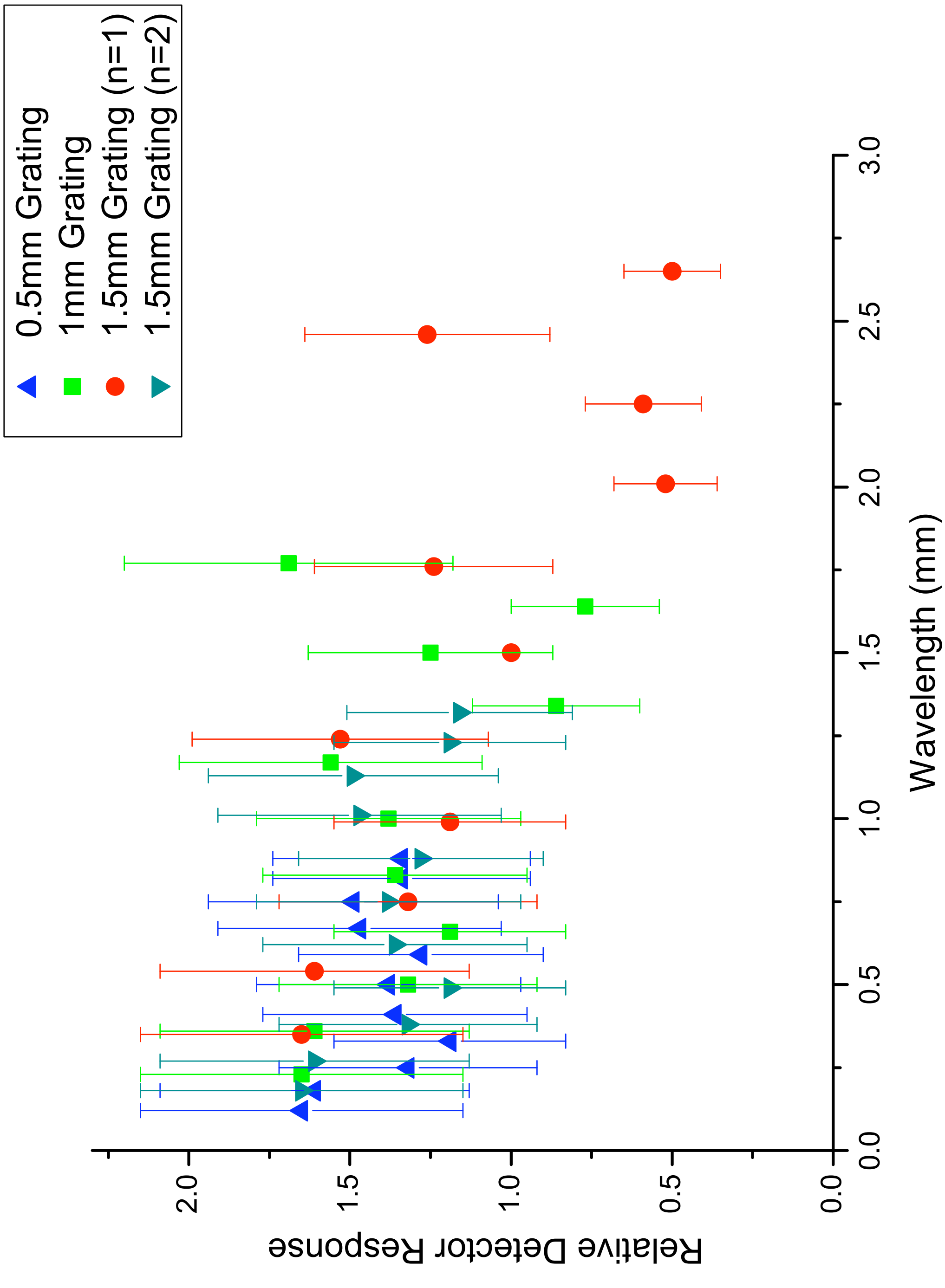

Figure 9.5: Relative response of each detector for the SP wavelength detected relative to detector 13 detecting at $\lambda = 1.5$mm (from Table 9.3).

Observation Angle:	40°	50°	60°	70°	80°	90°	100°	110°	120°	130°	140°
Convert ADC Counts to Joules	see Equation 9.1										
Quartz Absorption	see Table 8.1										
Quartz Reflection	see Table 9.1										
Wire Grid	0.5 ± 0.05										
Black Polyethylene	0.90 ± 0.05										
Filter Transmission	see Table 9.2										
90° Bend in Optical System	0.80 ± 0.05										
Diffraction	see Table 8.5										
Obstructed View	0.674	1.0									0.431
Pyroelectric Detector Relative Response	see Table 9.3										

Table 9.4: Complete list of all corrections that were applied to the data from this experimental run.

uncertainty varies from the region of ±40% to ±60% depending upon the angle of observation and grating used. The uncertainty in each reported measurement is calculated individually. Even so, the average total uncertainty in the data sets reported here (and in Chapter 10) is about ±50%, which could be reduced to $\sim 35\%$ in a future experiment after investigating the considerations highlighted in this section.

9.5 Analysis of SP Data

As previously mentioned, the largest obstacle faced by this experiment was due to the time delay between measurements, caused by changing filters. Measurements from different gratings were often separated by several hours, which raised concerns over possible fluctuations in the beam over this time. Hence, the majority of data sets considered here belong to individual gratings taken in isolation. This limits the amount of information that can be gained from the data, and therefore the analysis concentrates mostly on confirming that the SP process works in the highly relativistic regime.

9.5.1 Confirmation of SP Signal

If the radiation detected is SP radiation there should be a difference in the signal size detected when using a grating and when using a blank, due to the periodic surface of the grating; by definition, radiation arising from this periodic surface must be SP radiation.

Figure 9.6 shows the signal detected from the 1.5mm grating and the blank, with WAP filters corresponding to first order radiation from this grating, and an equivalent plot for radiation from the 1mm grating and blank. The corrections listed in the previous section have been applied to the individual grating (or blank) data. There is a large difference in signal size between the 1.5mm grating and blank measurements. Radiation detected from the blank could be due to diffraction radiation from; i) the edge of the blank itself, ii) the discontinuity in the beam pipe around the experiment, or iii) radiation propagated from accelerator components upstream. There is also clear evidence of SP radiation originating from the 1mm grating (Figure 9.6b), although to a lesser extent. Additional supporting evidence can be found in the fact that more radiation was detected from the 1.5mm grating than the 1mm grating. It is worth noting that the increase in signal from a grating is not by a constant amount, and depends upon the angle of observation, *i.e.*wavelength. This is most obvious in Figure 9.6b, where there is a much larger increase in signal at 90 and 100° than at other angles.

a)

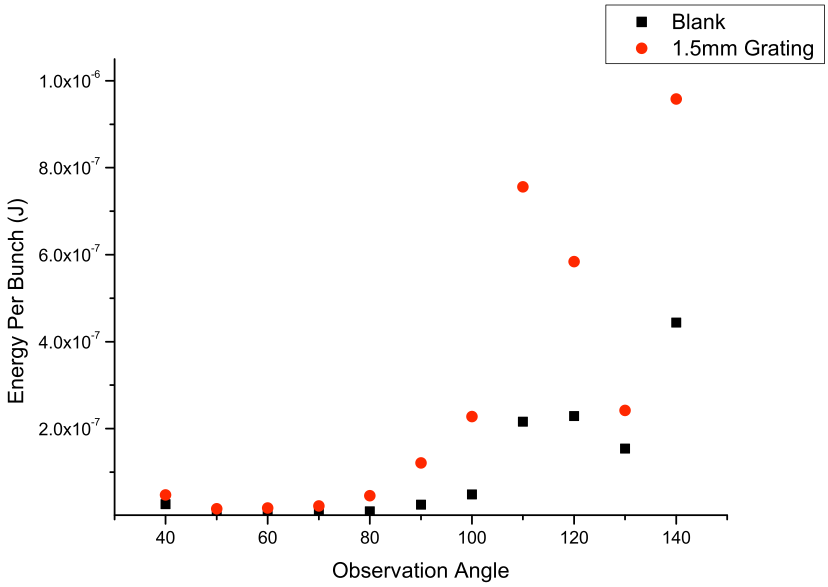

b)

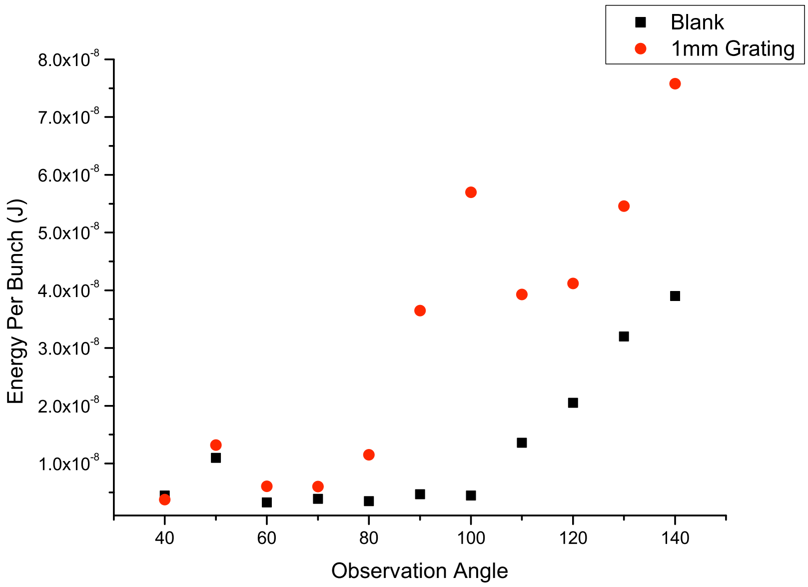

Figure 9.6: The measured signal from a) the 1.5mm grating and blank, and b) the 1.0mm grating and blank, both with first-order radiation filters. The corrections for all losses have been applied.

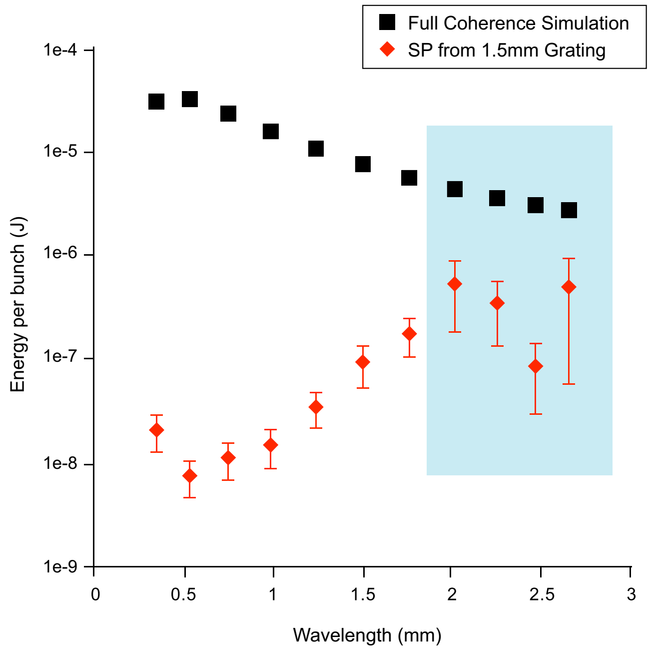

Figure 9.7: Comparison of SP signal from the 1.5mm grating and the theoretical fully coherent case ($N_e = 1.6 \times 10^{10}$) from the same grating.

A further useful test would be to compare the measured energy levels to those expected from an ultra-short bunch. The energy emitted per bunch depends on the single electron formula modified by the bunch form factor (Equation 2.16). Coherence occurs when the bunch length is approximately equal to, or is shorter than, the emitted wavelengths (see Section 2.3). The shorter the bunch is, with respect to the emitted wavelengths (or alternatively, the grating period), the more coherent it becomes and the higher the energy output. Therefore, decreasing the bunch length, whilst keeping the grating period constant, allows the bunch to be treated as a single 'lump' of charge, *i.e.*the emitted radiation becomes fully coherent. Maximum energy is emitted in this regime, but all information about the bunch profile is lost.

The code BUNCH2 was used to calculate the expected maximum energy levels from an ultra-short (0.01ps) bunch passing over the 1.5mm grating. In this case the emitted radiation is fully coherent. Figure 9.7 shows the simulated energy levels as would be detected by the apparatus at SLAC. The measured energies from the 1.5mm grating are also shown. The measured energy rises steadily and saturates at long wavelengths (the point at 2.5mm is addressed in Section 9.5.3), tending towards the expected energy from the fully coherent case (shaded area of Figure 9.7). Therefore, the measured energy levels, at long wavelengths, are consistent with what might be expected from SP radiation tending towards full coherence.

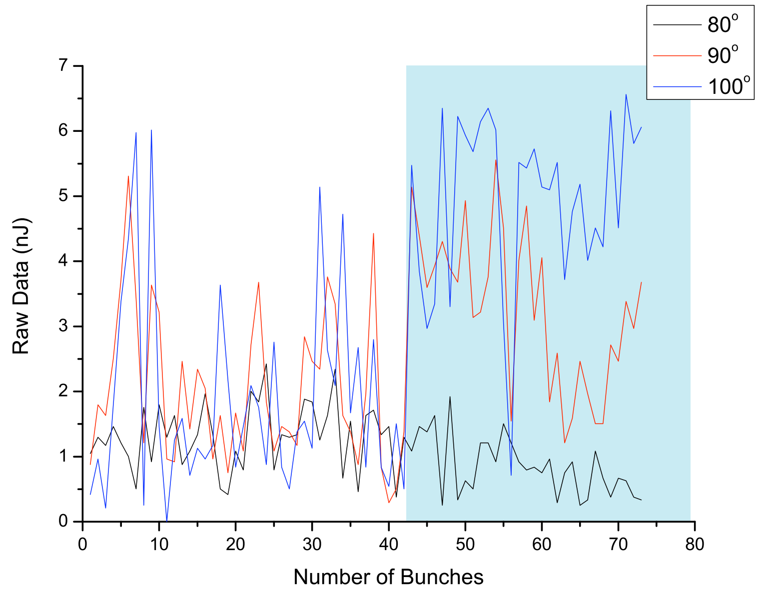

Figure 9.8: Indication of changes in the bunch profile (see text for details).

9.5.2 Evidence of Bunch Profile Changes

If the bunch profile remains constant there should be no change in the spectral distribution of the radiated energy. However, if the profile does change this will be reflected in the relative levels of energy output at each SP wavelength. For example, a change in bunch profile may be indicated by the signal detected at some wavelengths increasing, whilst decreasing at others. The most sensitive region of the emitted distribution to bunch profile changes is at the onset of coherent emission. For this experiment, this is between 80 and 100°. This is to be distinguished from an overall change in energy output that is uniform over all detected wavelengths, which would be due to a change in bunch charge.

The raw data, in ADC values, from 80 − 100° of the 1mm grating with first order filters is shown in Figure 9.8. This data set was taken at 06:22am on the 22nd of March with a bunch charge of 1.6×10^{10}. The figure shows the measured energy from this grating as each bunch passes it. After $\sim$ 40 bunches the energy detected from each bunch increases at 90 and 100°, whilst decreasing slightly at 80°. The energy output at other angles (not shown, for clarity) remains approximately constant. As the change in signal is not the same across all observation angles, and therefore SP wavelengths, it is most likely due to a change in bunch profile. Unfortunately, the experimental arrangement is not single-shot, and so this can not be compared with an equivalent set of simultaneous data from the blank grating. However, these fluctuations were not observed whilst using the blank, only appearing (infrequently) when a grating was used.

Similar evidence of bunch profile changes were observed in the July experiment. These are explored in Section 10.2.2.

9.5.3 Anomalous Data Points

This, and the following sections, concern only data from the 1.5mm grating as this provided the only data set suitable for analysis from this experiment. However, similar observations were made in the following experiment in July 2007 (see Chapter 10). The points specific to the July data set are discussed in Section 10.2.

It was observed that at certain observation angles, the signal appeared to be anomalously low (or high), even after all the corrections had been applied. For example, the signal detected at 40° ($\lambda = 0.35$mm) showed large fluctuations and the 130° ($\lambda = 2.46$mm) signal was always low. Figure 9.7 shows these points clearly. Upon examination, the grating signal was found to always be lower at 130° than expected. Therefore, the resultant SP signal is consistently lower than expected at this angle.

There are two possible explanations for these points. The first relates to the wire grid screen used throughout these experiments (Section 4.2.2). This 2mm diameter mesh covered the quartz window of the vacuum chamber and was later found to have a transmission of $\sim 50\%$ up to $\lambda = 1.8$mm. Its transmission at long wavelengths could not be measured due to a lack of source power. Thus, there is the possibility that its transmission is lower at these wavelengths. This view is supported by examining Figure 9.6a, which shows that the signal decreases at 130° for both the grating and blank, suggesting some wavelength dependence.

The second possibility lies in the fact that the edges of the grating and the blank are not exactly identical. Although the blank was the same size as the grating, its leading edge was different. This is shown schematically in Figure 9.9. As the emitted diffraction radiation pattern depends upon the orientation of the diffracting surface, the difference between the edge of the grating and the blank would be equivalent to a rotation of the diffracting surface and a change in the angular distribution of the emitted diffraction radiation. Hence, the diffraction radiation pattern from the edge of the blank may not be the same as the pattern from the edge of the grating. The issue is complicated by the fact that diffraction radiation may be entering the optical system from the beam pipe after many (unknowable) reflections. The magnitude of the amount of diffraction radiation entering the system is quantified by the blank grating measurements (*e.g.* Figure 9.6), and it is already clear that there is a large increase in background signal with increasing observation angle. In general, all sources of diffraction

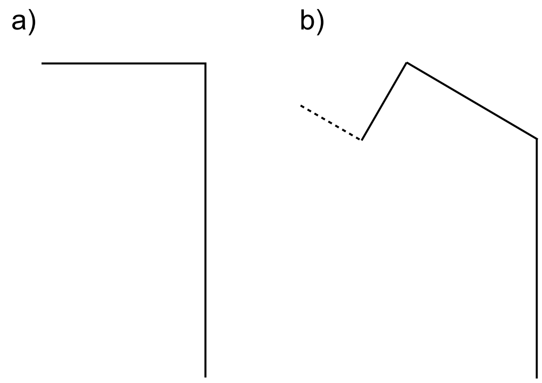

Figure 9.9: Schematic diagram of the difference between the edges of a) the blank and b) a grating.

radiation (*e.g.*the increase/decrease in beam pipe diameter around the experiment) should be the same for grating and blank and should cancel. The edge of the grating/blank is the only source of diffraction radiation that may not cancel, and so lends itself as a possible candidate for a change in background radiation at specific observation angles. In combination with the previous point about the wire grid, this could explain the origin of these anomalous points. Therefore, recurring suspect points (*i.e.*for the 1.5mm grating, the 40 and 130° angles) were excluded from the bunch reconstruction analysis that follows.

9.5.4 KK Reconstruction of the Longitudinal Bunch Profile

A KK reconstruction of the longitudinal bunch profile was carried out on the data shown in Figure 9.7, after removing the points at 40 and 130° (as per Section 9.5.3). The reconstruction comes with the caveat that the data were only from the 1.5mm grating, detecting first order SP radiation. Therefore, the reconstruction is based on a narrow range of wavelengths and is not as accurate as one from multiple gratings. The results of Chapter 3 suggest that the reconstruction is not expected to show any fine structure, since it is based on a relatively long period grating, resembling instead an asymmetric Gaussian.

The reconstruction is shown in Figure 9.10. Contrary to the above expectation the reconstructed profile appears more complicated than an asymmetric Gaussian and has indications of sub-structure. Despite inaccuracies in the reconstruction, due to only using data from one grating, the FWHM of the bunch is $4.1^{+0.7}_{-0.6}$ps. Although the profile is not a Gaussian, temporarily treating it as one gives $\sigma \approx 1.7$ps. This value can be compared to the results from LOLA.

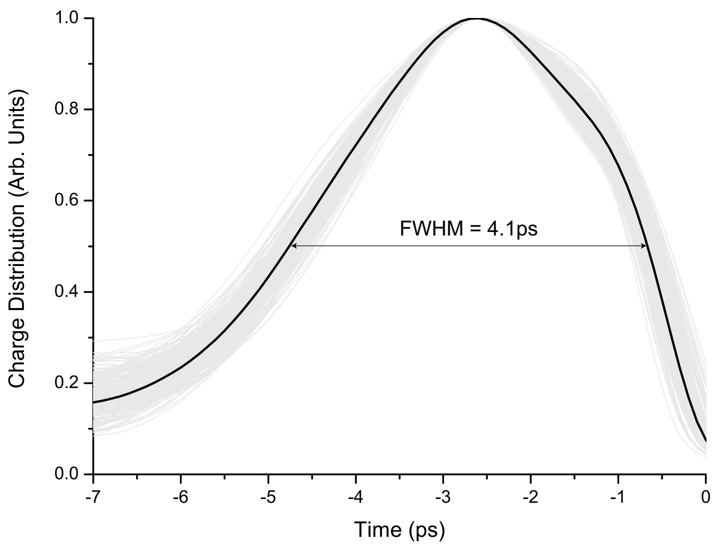

Figure 9.10: Kramers-Krönig reconstruction of data from the 1.5mm grating (see Figure 9.7) and a possible combination of three Gaussians that could give rise to this profile.

9.6 The Transverse Deflecting Cavity, LOLA

LOLA is a transverse deflecting RF structure that streaks a bunch, converting its longitudinal profile to a transverse one. The bunch can then be observed using conventional techniques for determining the transverse profile, such as imaging it with a camera on an OTR screen. The technique was proposed by Loew, Larsen & Altenmuller in 1965 [1], from whom it derives the name LOLA, and it was first built at SLAC in 1968. Its original purpose was to separate secondary particles with the same momentum but different mass, and more recently it has been used as a transverse deflector to streak bunches with potentially fs resolution [17, 26]. Hence, LOLA is a well documented technique that is perfect to compare with SP.

A direct comparison between LOLA and SP was not possible, however, since the former was not situated in ESA but at the end of the linac before the A-line bend to ESA. The bunch charge distribution was then simulated around the A-line bend to give the distribution in ESA. The results from the LOLA measurements have already been published [49], however, the procedure followed to derive them is briefly described in this chapter.

The transverse cavity of LOLA was phased so that the centre of the bunch was at the zero crossing of the RF — *i.e.* the bunch was rotated about its centre, but the remaining particles received a transverse kick proportional to their longitudinal position in the bunch. As the bunch travelled around the A-line bend, into ESA, it emitted synchrotron radiation. This was captured on a CCD camera known as a Synchrotron Light Monitor, or SLM. The width of the synchrotron stripe was proportional to the energy spread of particles in the bunch. This was recorded for three cases: i) LOLA on, ii) LOLA off, and iii) LOLA π out of phase, where the tail of the bunch was kicked upwards instead of the head. The height of the bunch on the SLM screen was a combination of the longitudinal and transverse components of the unkicked bunch, and the longitudinal distribution was recovered using these three SLM images. The analysis of the LOLA data was carried out in the following steps.

9.6.1 Calibration of the SLM Images and Determination of σ_{yz}

Each SLM image was stored as a 33×84 matrix of pixels, recording intensity. Before beginning, background noise and clusters that were far away from the beam were removed. This was done by applying a cut of 30 to each pixel data, then scaling all of the data up by a factor of 200. All negative pixels were set to zero, and the remaining numbers were rounded up to the nearest integer. Figure 9.11 shows the resulting SLM image, in pixels, for a) a streaked bunch with LOLA on, b) a bunch with LOLA off, and c) a streaked bunch with LOLA π out of phase.

Following this, the calibration from pixels on the SLM image to mm was determined. This was obtained from the SLM image file, which contained information on; i) the total number of digitized points horizontally and vertically, n_h and n_v, and ii) the number of pixels/mm if every pixel had been sampled, N_h, N_v. Thus, the calibration from pixels to mm is N_h/n_h horizontally, and N_v/n_v vertically.

The height of the image on the screen, in terms of its position in mm, gives the height of the streaked bunch, σ_{yz}, which is a combination of longitudinal and transverse length and the tilt of the bunch. This is determined by calculating the standard deviation of the image height, then dividing through by N_v/n_v.

9.6.2 Reconstruction of the Energy-z Correlation at the End of the Linac

The transverse height and bunch tilt's influence was removed from σ_{yz} before the actual bunch length, σ_{linac} was found. This was performed using a MATLAB script by Paul Emma [50], which took three values of σ_{yz} — one for each case; LOLA on, LOLA off and LOLA π out of phase — amongst other beam parameters and returned σ_{linac}. The SLM image from the previous step was then reconstructed, removing the transverse influence. Each horizontal pixel,

a)

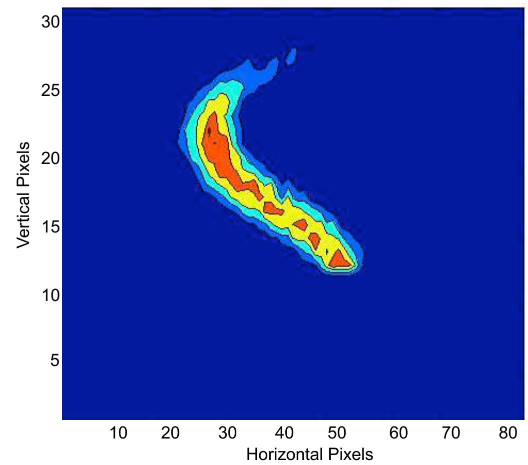

b)

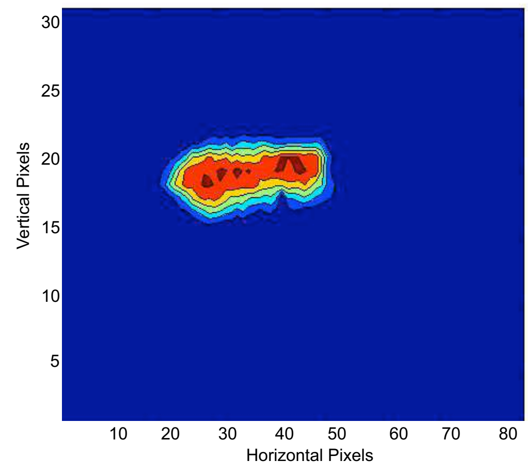

c)

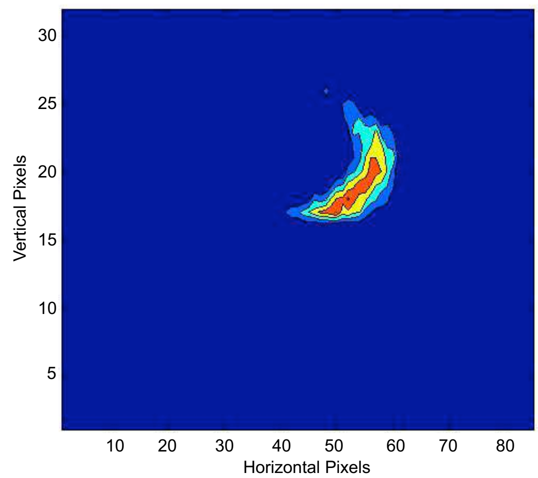

Figure 9.11: Synchrotron radiation emitted as the bunch travelled around the A-line bend was imaged on a Synchrotron Light Monitor (SLM) when a) LOLA was used, b) LOLA was not used, and c) when LOLA was used π out of phase.

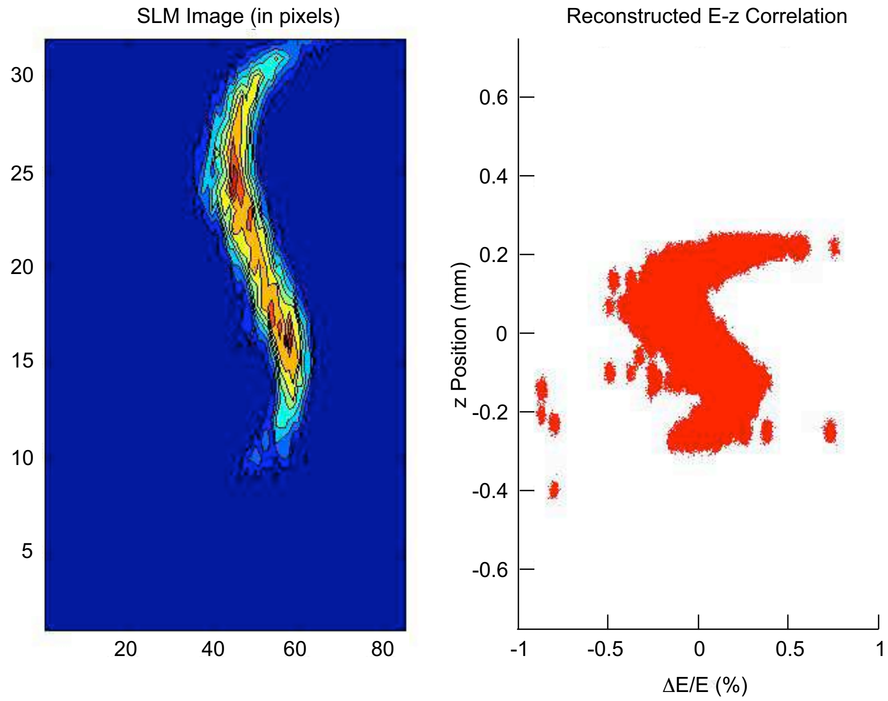

Figure 9.12: The SLM image produced by a kicked bunch and the real distribution before the A-line.

x, determined the energy spread of the bunch,

$$\frac{\Delta E}{E} = x \frac{N_h}{n_h} \frac{1}{M} \frac{1}{E_B},$$

where M is the calibration factor to convert from mm on the SLM image to MeV ($M = 1.5 \times 10^{-2}$ [50]), and E_B is the beam energy ($E_B = 28.5 \times 10^3$MeV). Then each vertical pixel, y, was converted into longitudinal position, z, by

$$z = y \frac{\sigma_{\text{linac}}}{\sigma_{yz}}.$$

Figure 9.12 shows the original SLM image and the reconstructed energy-z correlation after performing this step.

9.6.3 Calculation of the Bunch Length in ESA

After the energy-z correlation was calculated in the previous step, each particle in the bunch was passed through a transfer matrix to model the energy-z correlation in ESA. The transfer

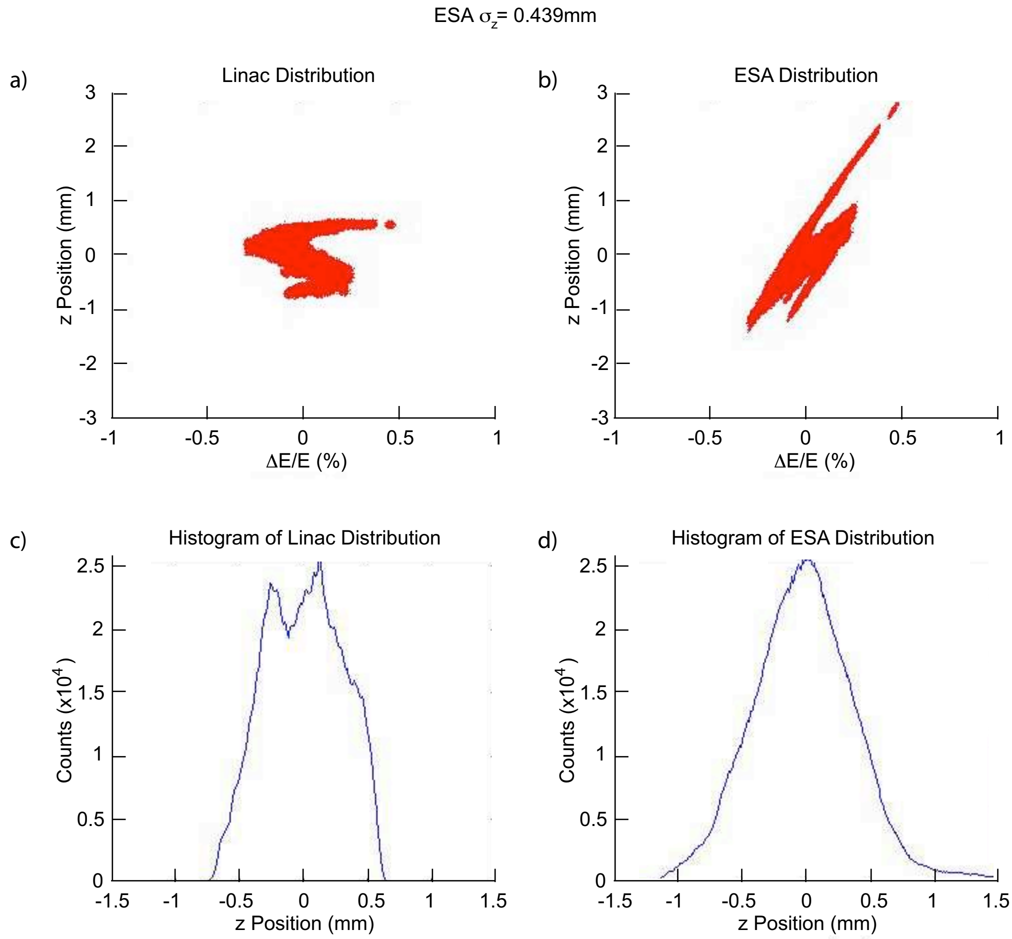

Figure 9.13: Phase space plot of a bunch a) before, and b) after travelling around the A-line bend. The projection onto the z (time) axis is shown in c) and d) respectively.

matrix is [49]

$$\begin{pmatrix} z_2 \\ \frac{\Delta E_2}{E_2} \end{pmatrix} = \begin{pmatrix} 1 & R_{56} \\ 0 & 1 \end{pmatrix} \begin{pmatrix} z_1 \\ \frac{\Delta E_1}{E_1} \end{pmatrix}, \tag{9.3}$$

where the subscript 1 represents particles in the distribution at the end of the linac (as previously determined), 2 represents the distribution in ESA, and the longitudinal dispersion is given by $R_{56} = 0.465$m [50]. Figure 9.13 shows the effect on one bunch as it passed around the A-line bend into ESA. Once this was modelled in ESA, the standard deviation of the height of the image (Figure 9.13a) gave the bunch length, σ. Figure 9.13d also shows the phase-space projection onto the z (time) axis. This projection provides some information on the bunch length. Its FWHM is $\sim$ 1mm, which is equivalent to $\sim$ 3.3ps. This is not inconsitent with the FWHM obtained in Section 9.5.4.

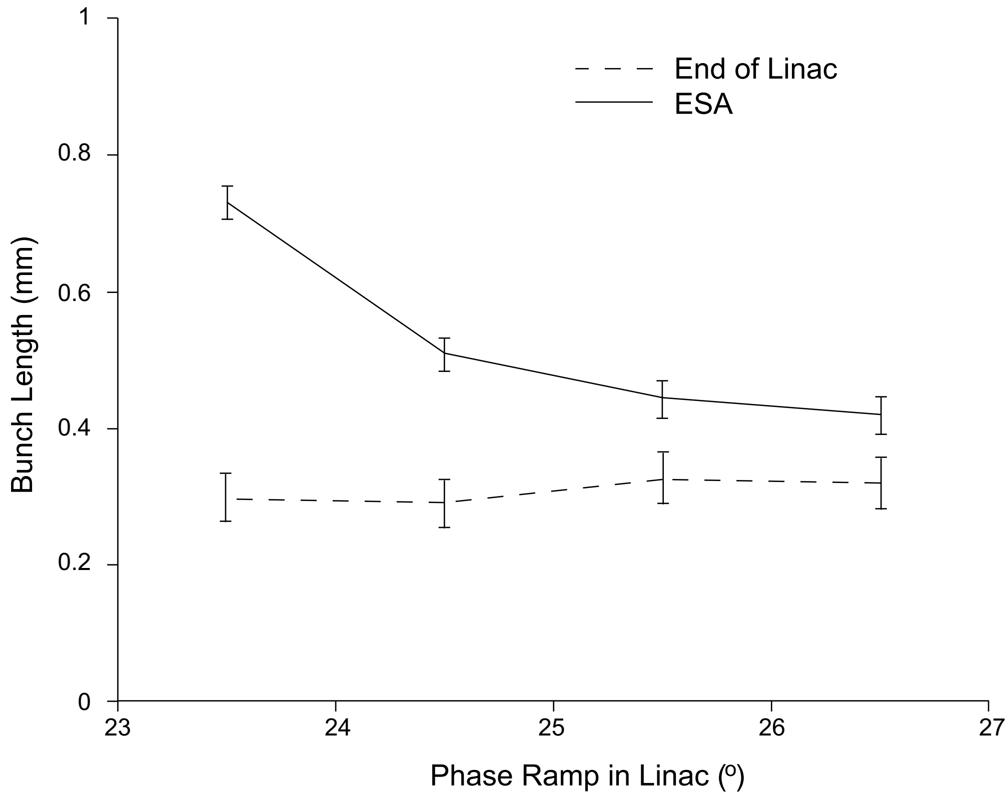

Figure 9.14: The measured σ_{linac} of the SLAC beam before the A-line (dashed), and the predicted σ of the bunch in ESA (solid) for increasing linac phase ramp(*i.e.*increasing RF cavity phase) and, hence, decreasing bunch length [49].

The energy spread of the SLAC beam can be tuned to allow for a range of bunch lengths. Therefore, different bunch lengths were analysed using LOLA following these steps, and the bunch lengths before and after the A-line bend were found. These are shown in Figure 9.14. LOLA measured bunch lengths of ~ 0.3mm before ESA, corresponding to bunch lengths in the range $0.4 - 0.7$mm in ESA. This is equivalent to $\sigma = 1.3 - 2.3$ps.

9.7 Summary

This chapter describes the first ever SP experiment in the multi-GeV regime. This was carried out at SLAC in March 2007. Coherent SP radiation was detected, providing strong support for the surface current model described in Section 2.2.3. Unfortunately, due to the time separation between measurements, the bunch reconstruction was inadequate as data from multiple gratings could not be combined. Even so, Kramers-Krönig was applied to a single measurement from the 1.5mm grating. This gave a profile that can be described by a combination of 3 Gaussians. The FWHM of the profile was 5.4ps.

Several LOLA measurements were also performed at a similar time to the SP measurements. However, LOLA was positioned at the end of the linac (not in ESA), hence the bunch was simulated in ESA after being measured at the end of the linac. After taking measurements with varying bunch lengths, this procedure returned bunch lengths, in ESA, with values of σ of between 1.3 to 2.3ps.

The approximate σ value of the SP-determined profile was $\simeq$ 1.7ps. Therefore, the SP bunch length measurement coincides with the limits found by LOLA. This provides support for coherent SP as a technique to determine the longitudinal bunch profile, and the improvements made in the following experiment take the technique further.

Chapter 10

SLAC — July 2007

The previous experiment at SLAC verified that SP radiation was observable at high energy, yet did not provide sufficient information to reliably reconstruct the longitudinal bunch profile. The measurements suggested that the SLAC bunch profile is not Gaussian, with a FWHM of 4.1ps. This would correspond to $\sigma \approx 1.7$ps if the reconstructed profile was treated as a Gaussian, and was consistent with measurements carried out with LOLA at a similar time but in a different location.

The experiment was repeated in July 2007, after some changes to the experimental apparatus to speed up data acquisition. The primary goal was to confirm that coherent SP radiation is a viable method of determining the longitudinal bunch profile of highly relativistic beams.

10.1 Experimental Additions and Data Processing

The apparatus was essentially the same as that described in Chapter 9. However, a significant improvement was made to it prior to beginning this experiment. The largest obstacle faced during the previous (March) experiment at SLAC was the time separation between different measurements. This meant that data that ideally belong together — *i.e.*a complete set of measurements from all three gratings — were separated by many hours. During this time there was concern over potential beam drift, bunch length changes, and changes in the bunch charge. As a result, data could only be analysed in isolation and not in combination with other grating measurements. This was entirely due to changing filters by hand and the length of time taken to gain access to the beamline.

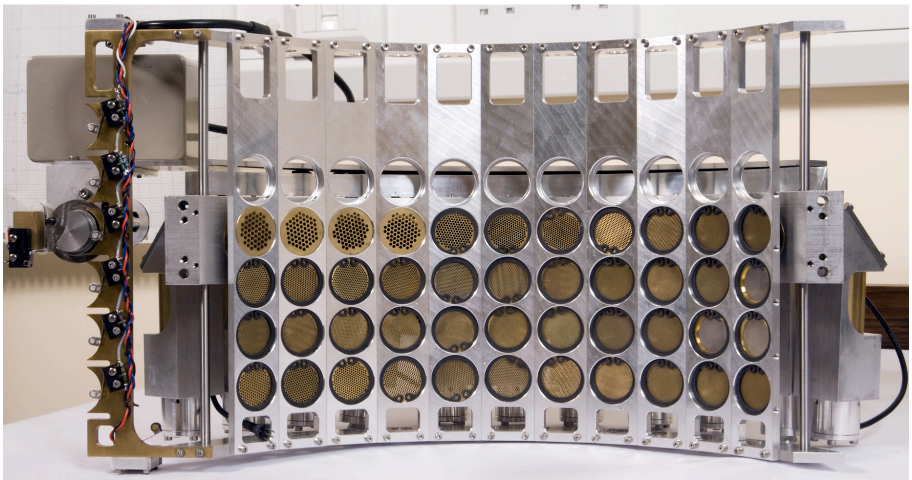

Figure 10.1: The filter changing mechanism used at SLAC in July 2007. From top to bottom the filters correspond to: an aluminium 'screen', no filters, 1.5mm first order, 1.5mm second order, 0.5mm first order, and 1mm first order radiation.

The solution to this problem was the installation of a mechanism, that held filters for all gratings and all potentially observable orders of SP radiation, that could be operated remotely. The filter changing mechanism also had provision for blocking the entrance to the optical system in order to determine the amount of irreducible background radiation. This has already been described in Chapter 4, but for convenience Figure 4.7 is repeated here in Figure 10.1, which shows the filter changing mechanism and its six filter positions. From top to bottom these are:

- A section of solid aluminium plate, sufficient to block far infrared radiation.
- An empty slot for the study of unfiltered radiation.
- WAP filters for radiation from the 1.5mm grating, 1st order.
- WAP filters for radiation from the 1.5mm grating, 2nd order.
- WAP filters for radiation from the 0.5mm grating, 1st order (also suitable for the 1mm grating, 2nd order and 1.5mm grating, 3rd order).
- WAP filters for radiation from the 1mm grating, 1st order.

Each row of filters could be quickly moved into position in front of the entrance to the optical system, according to the grating in use at the time. It was operated via a remote control that was separate from the DAQ system as the filter changing mechanism was a late addition to the experiment.

A small change to the DAQ software allowed this experiment to collect data at 10Hz, compared to the previous 1Hz, which decreases the statistical error for these measurements. Data were taken over a period of ~ 1 minute, collecting ~ 600 bunches, which were were then processed according to the procedure laid out in Sections 9.3.1 − 9.3.2. However, there were two modifications to this procedure that are described below.

The first modification to the analysis procedure became necessary upon examining measurements of the irreducible background after returning from SLAC. A small signal was observed with the blank, even when the optical system was blocked by the aluminium plate; this was more prominent in the forwards direction than the backward direction. A slightly higher signal (with the optical system blocked) was also observed with the 1.5mm grating under the same conditions. Unfortunately, no measurements exist for the 0.5mm and 1mm gratings under these conditions and so it was not possible to determine if more radiation would be seen from these gratings as well.

It was observed that the signal was higher when a grating was used than when the blank was in place. However, the mechanism by which the radiation passed through the blocked entrance of the optical system is not known. Potentially, the radiation 'leaks' through the small cracks in the filter changing mechanism where the aluminium plates join, hence the correction associated with this radiation is referred to as a 'leakage' correction. As this leaked radiation is present when the aluminium screen is used, it must also be assumed to be present when filters are used — again, leaking between any gaps in the filter changing mechanism. In this case, it is a small source of unfiltered radiation that must be subtracted from the SP signal.

As measurements only exist for the blank and 1.5mm grating, the leakage correction derived for this grating was also assumed to be applicable to the 0.5 and 1mm gratings. However, this may be an overestimate of the leaked signal for these gratings, if the radiation is dependent upon the grating period. Let L_B represent the average leaked radiation from the blank through the aluminium section of the filter changing mechanism, and L_G be the average from the 1.5mm grating under the same conditions. Then, the average leaked SP signal, or leakage correction L, is given by

$$L = L_G - L_B.$$

This was then subtracted from the observed SP radiation prior to applying further corrections. Therefore, Equation 9.2 for the data sets given here becomes

$$S_U = (R_G - R_B) - L, \tag{10.1}$$

where L is given in Table 10.1 for each observation angle.

Observation Angle (°)	Leakage Correction ($\times 10^{-10}$J)
40	3.9
50	2.6
60	1.6
70	2.3
80	3.3
90	3.3
100	2.1
110	2.9
120	1.6
130	1.8
140	2.0

Table 10.1: Correction factors due to leakage through, or around, the filter changing mechanism.

The second modification to the procedure of Sections 9.3.1 – 9.3.2 concerns the WAP filters used during this experiment. In order to supply four complete sets, each observation angle did not necessarily have a filter corresponding to the optimum transmission for the expected SP wavelength. The transmission factors of the filters used in this experiment are given in 10.2. All necessary correction factors that were applied to the data are given in Table 10.3.

All measurements reported in this chapter were made with the beam $\sim$ 3mm away from the grating.

10.2 Analysis

The analysis carried out in Chapter 9 verified that SP radiation is observable in the multi-GeV regime. Hence, the analysis in this chapter focuses mainly on the use of SP radiation as a diagnostic tool to recover the longitudinal bunch profile. There are some points of theoretical interest, nevertheless, which could not be explored fully in the previous chapter due to lack of data.

The data presented in this chapter were analysed in the same way as that of Chapter 9, except that the addition of the filter changing mechanism meant that data from multiple gratings were combined. The points previously identified as suspect in Section 9.5.3 (the 40° and 130° observation angles from the 1.5mm grating) are still present in this data set. Similar points are also observable from the 1mm grating (120° and 140°), and occasionally from the 0.5mm grating (120°). These points were also excluded from further analysis.

Observation Angle	0.5mm Grating		1mm Grating		1.5mm Grating ($n = 1$)		1.5mm Grating ($n = 2$)	
	λ(mm)	T	λ(mm)	T	λ(mm)	T	λ(mm)	T
40	0.12	1.0	0.23	0.75±0.04	0.35	0.34±0.02	0.18	1.0
50	0.18	1.0	0.36	0.36±0.02	0.53	0.5±0.03	0.27	0.57±0.03
60	0.25	0.55±0.03	0.50	0.41±0.02	0.75	0.90±0.05	0.38	0.91±0.05
70	0.33	0.34±0.02	0.66	0.87±0.04	0.99	0.92±0.05	0.49	0.39±0.02
80	0.41	0.39±0.02	0.83	0.79±0.04	1.24	0.97±0.05	0.62	0.94±0.05
90	0.50	0.41±0.02	1.00	0.8±0.04	1.50	0.8±0.04	0.75	0.9±0.05
100	0.59	0.42±0.02	1.17	0.86±0.04	1.76	0.54±0.03	0.88	0.89±0.05
110	0.67	0.31±0.02	1.34	0.88±0.04	2.01	0.72±0.04	1.01	0.79±0.05
120	0.75	0.79±0.04	1.50	0.80±0.04	2.25	0.75±0.04	1.13	0.94±0.05
130	0.821	0.68±0.03	1.64	0.43±0.02	2.46	0.66±0.03	1.23	0.89±0.05
140	0.88	0.50±0.03	1.77	0.53±0.03	2.65	0.78±0.04	1.32	0.98±0.05

Table 10.2: Transmission through the WAP filters used for each measured SP wavelength. Filters for radiation arising from the 0.5mm grating, $n = 1$, are also suitable for radiation arising from the 1mm grating, $n = 2$, and 1.5mm grating, $n = 3$, where n is the order of radiation.

Observation Angle:	40°	50°	60°	70°	80°	90°	100°	110°	120°	130°	140°
Convert ADC Counts to Joules	see Equation 9.1										
Leakage Through Filter Mechanism	see Table 10.1										
Quartz Absorption	see Table 8.1										
Quartz Reflection	see Table 9.1										
Wire Grid	0.5 ± 0.05										
Black Polyethylene	0.90 ± 0.05										
Filter Transmission	see Table 10.2										
90° Bend in Optical System	0.80 ± 0.05										
Diffraction	see Table 8.5										
Obstructed View	0.674	1.0									0.431
Pyroelectric Detector Relative Response	see Table 9.3										

Table 10.3: Complete list of all corrections that were applied to data from this experimental run.

10.2.1 Confirmation of SP Radiation

A useful check of the properties of SP radiation, that could not be explored in the previous experiment, was its dependence on the distance between the grating and the beam. All models (assuming an infinitely wide grating) predict that the energy emitted per unit solid angle is given by,

$$\left(\frac{dI}{d\Omega}\right)_1 \propto \exp\left[-\frac{2x_0}{\lambda_e}\right],$$

which has an exponential dependence on x_0, the height of the beam above the grating, and the evanescent wavelength, λ_e (Equation 2.15). Therefore, one would expect the signal to decrease exponentially as the distance between the beam and grating is increased. Figure 10.2 shows the effect on the measured SP signal at 90° from the 1 and 1.5mm gratings, after corrections have been applied, at increasing beam-grating distance.

For both gratings, the fit has the form $y = A_1 \exp\left(\frac{-x}{t_1}\right) + y_0$. Comparing this to Equation 2.14 reveals that t_1 is proportional to the evanescent wavelength, λ_e, *i.e.* $t_1 = \lambda_e/2$. Therefore, simplifying Equation 2.15 for high γ, $\beta \approx 1$ and $\theta = 90°$ gives

$$\begin{aligned} t_1 = \frac{\lambda_e}{2} &= \frac{1}{2}\frac{\lambda}{2\pi}\frac{\beta\gamma}{\sqrt{1+\beta^2\gamma^2\sin^2\theta\sin^2\phi}} \\ \therefore t_1 &\simeq \frac{\lambda}{4\pi}\frac{1}{\sin\phi}. \end{aligned}$$

The optical system collects radiation with $\phi \leq \pm 5°$, and the expected differential energy output for SP radiation follows the curve described by Figure 10.3. The average differential energy output over this range of ϕ is $\sim 7\times10^{-5}$J/sr/cm of grating length, which is emitted at $\phi \simeq 2.5°$. This yields $t_1 \simeq 1.9$mm for the 1mm grating, and $t_1 \simeq 2.8$mm for the 1.5mm grating. These values can be compared to the values obtained from the fits of Figure 10.2, where $t_1 = 1.99\pm0.93$ and $t_1 = 2.13\pm0.74$ respectively. For the case of the 1mm grating, the agreement between theory and experiment is satisfactory, whereas for the 1.5mm grating it is rather poor. However, in view of the large experimental uncertainties in this measurement, this is probably acceptable.

10.2.2 Observations of Bunch Profile Changes

Section 9.5.2 commented on the possibility that changes to the bunch profile were detectable in real time. Similar changes were detected during this experiment, again only from data taken using a grating. Two of these instances are shown in Figure 10.4, in the highlighted areas.

a)

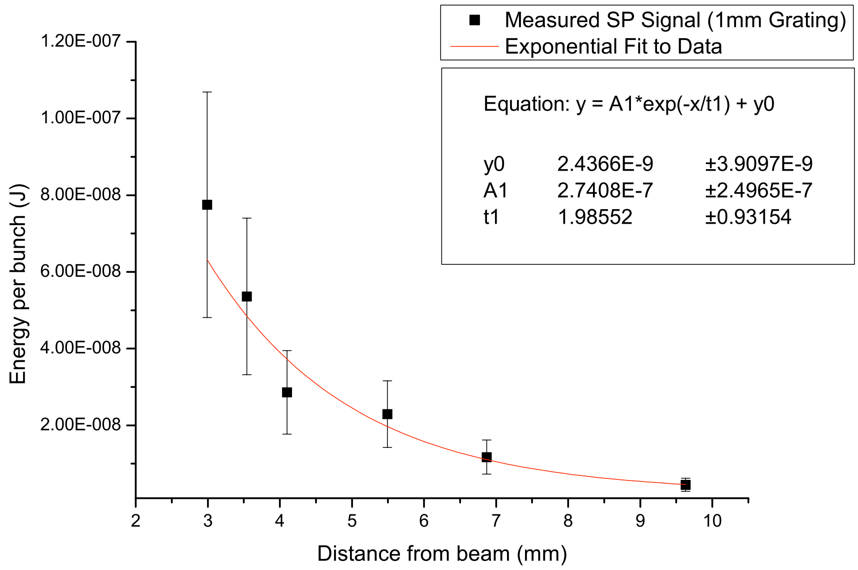

b)

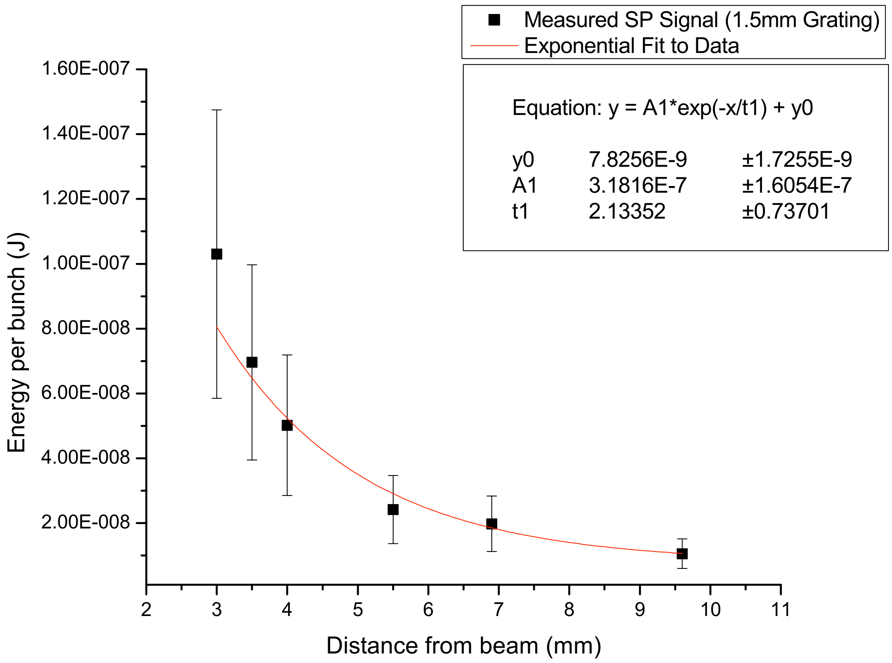

Figure 10.2: The measured energy per bunch decreases exponentially with increasing distance between the beam and a) the 1mm grating, b) the 1.5mm grating.

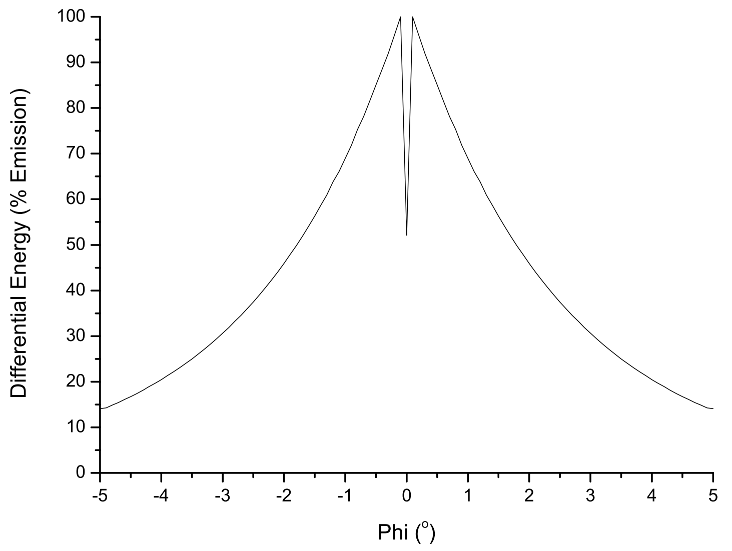

Figure 10.3: Calculated differential energy output at 90° from the 1.5mm grating at increasing values of azimuthal angle ϕ.

The first instance shows a sudden change in the spectral distribution. After $\sim$ 100 bunches the signal at 90° remains constant, whereas it decreases at 80° and increases at 100°. After another $\sim$ 70 bunches, the signal levels return to their pre-change positions, albeit slightly higher. This could indicate a change to yet another bunch profile or a return to the initial one.

The second instance demonstrates a smooth change of profile over a period of several hundred bunches. In both cases, the signal detected at the remaining observation angles stay approximately constant, with only the $80 - 100°$ signals changing. As these angles are most sensitive to changes in profile, it is highly indicative that the change in signal is due to a change in profile.

It is unlikely that these changes were due to a detector malfunction. The same detectors were used throughout both this and the March experiment, but these fluctuations were only observed during measurements taken with a grating, and never with a blank. As each measurement with a grating also had a corresponding measurement with the blank, it is unlikely that a persistent detector malfunction would not be observed in both types of data. It is also unlikely that a persistent detector malfunction would occur as infrequently, or malfunction for only several seconds at a time before returning to normal operation. Further to this, all detectors were calibrated after the SLAC experiments were completed (see Chapter 6) and were found to be operating as expected.

a)

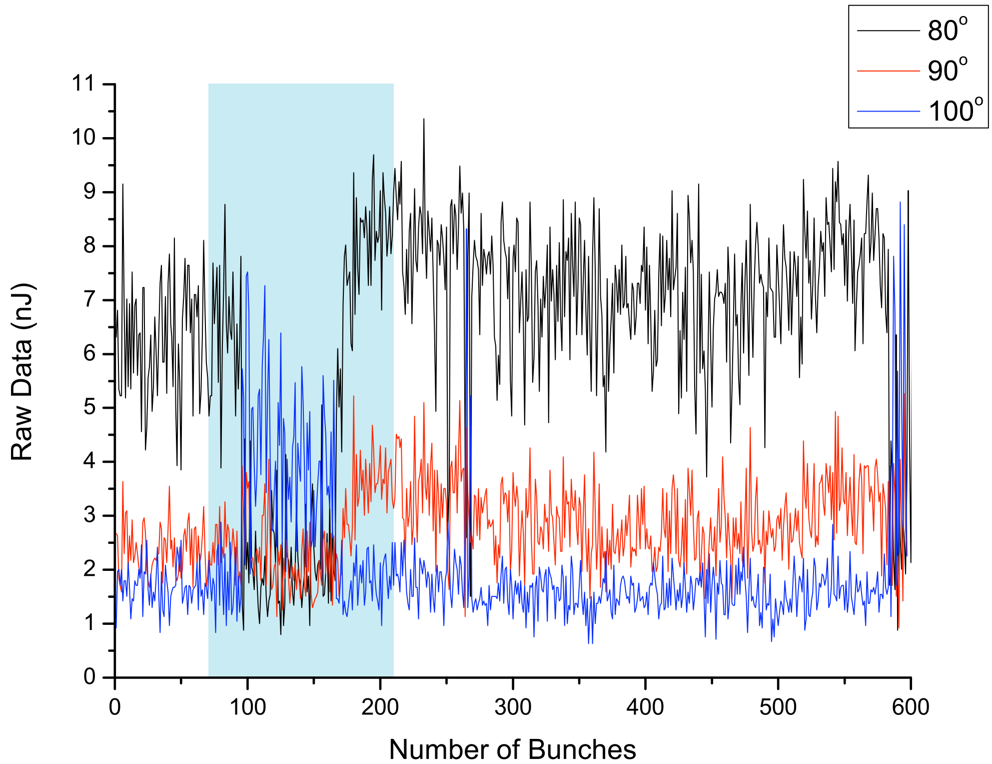

b)

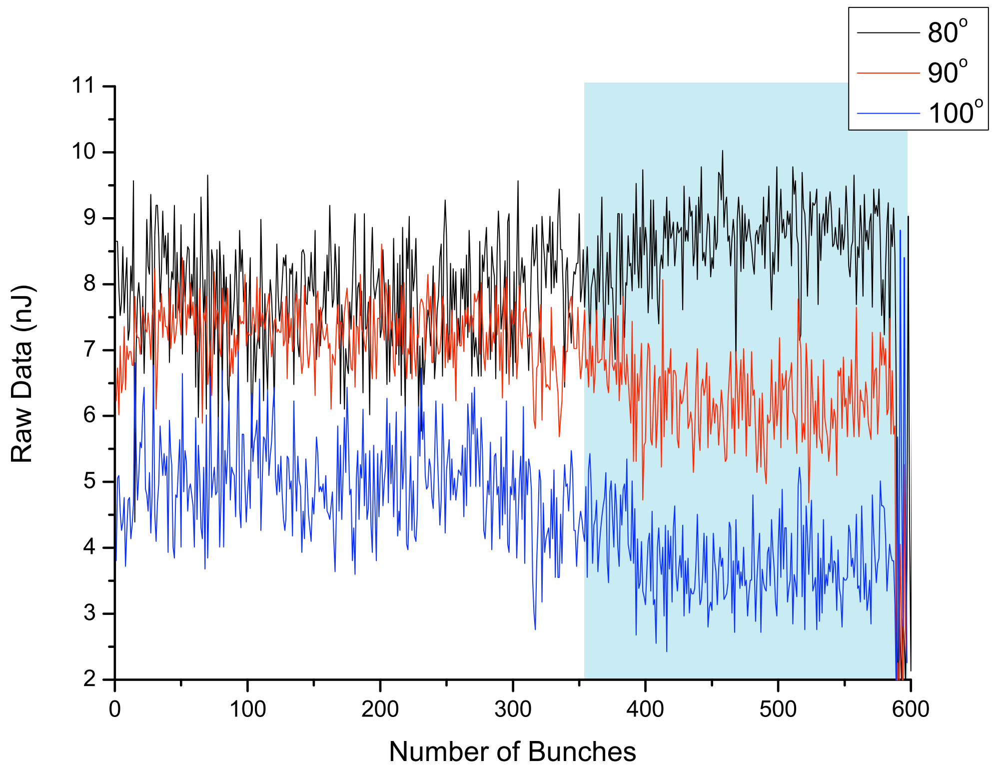

Figure 10.4: Observed changes in the bunch profile (highlighted area).

10.2.3 Kramers-Krönig Reconstructions of 'Short' Profiles

All collected data sets that covered a short period of time and possessed no variation in the observed signal levels were analysed using KK. A selection of these reconstructed profiles is presented in this chapter. The KK reconstruction of the longitudinal bunch profile obtained in Chapter 9 determined a bunch with a FWHM of 4.1ps and a potentially long overall approximate bunch length. Recalling the results of Section 3.2.5, this is at the limit of reliable reconstruction for the set of gratings that were used. Therefore, closer examination of the retrieved bunch profiles was necessary.

Reconstructing the bunch profile using KK relies on information about the bunch charge over the time the measurements were taken. This was measured $\sim$ 20m upstream of the SP experiment using a toroid. Figure 10.5 gives the toroid readings for the duration of the experiment, which vary between 1×10^{10} and 1.6×10^{10} electrons per bunch. For the measurements reported in this chapter the bunch charge varied between 1.2×10^{10} and 1.4×10^{10} electrons. As well as providing information for the KK reconstruction, comparing the bunch charge data with the measured SP energy distribution can reveal further information about the bunch itself. For example, for the same bunch charge, the lower the measured SP energy the longer the bunch.

There were no independent bunch profile measurements located in ESA. However, there was a 100GHz diode whose signal gave an indication of the bunch length. This diode was situated at a ceramic gap, and was sensitive to radiation with a wavelength of $\sim$ 3mm (100GHz). The process is similar to a simple SP experiment that detects only a single wavelength. As the bunch becomes shorter, the emitted radiation becomes progressively coherent and hence has higher energy than the radiation emitted from longer bunches. Therefore, the higher the diode reading, the shorter the bunch. This gives some basis for comparison with the reconstructed bunch profiles detected using coherent SP radiation. The output of the diode is given in Figure 10.6. The diode's output varied over the course of the experiment, and comparing data from times with low output to those with high output should show a similar increase, or decrease, in bunch length at those times, assuming that the bunch charge is constant.

Three measured spectral distributions are shown in Figures 10.7a – 10.9. A comparison of these figures provides an interesting insight into the length of the bunches that gave rise to these distributions. The measured spectral energy distributions are approximately monotonic, rising quickly towards full coherence where they then saturate. Recall that the shorter the bunch, the more coherent (and hence higher in energy) the emitted radiation. The measured energy

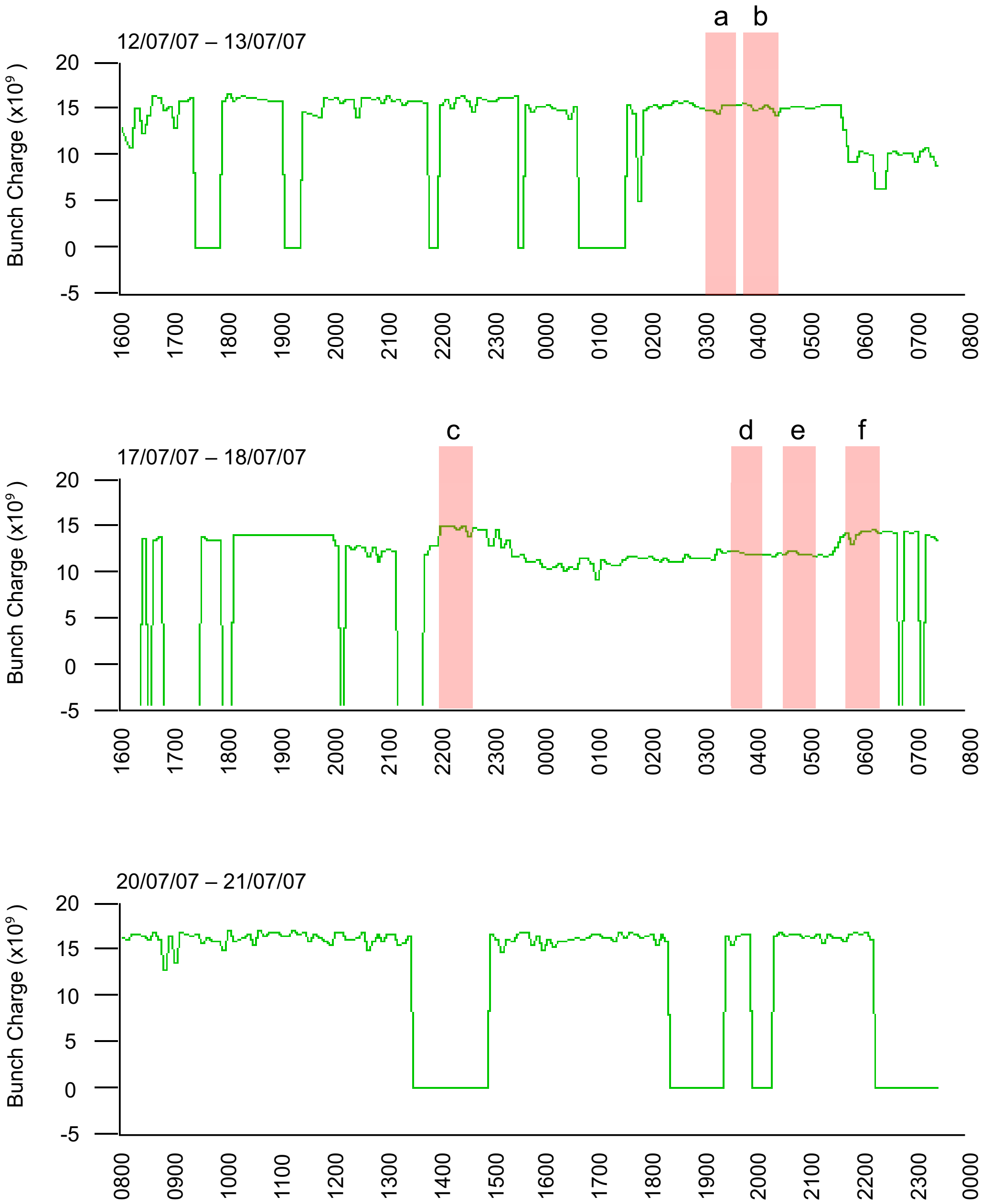

Figure 10.5: Bunch charge data for the duration of the experiment [87]. The letters correspond to the following Figures: a) 10.10, b) 10.7, c), 10.11, d) 10.8, e) 10.9, and f) 10.12.

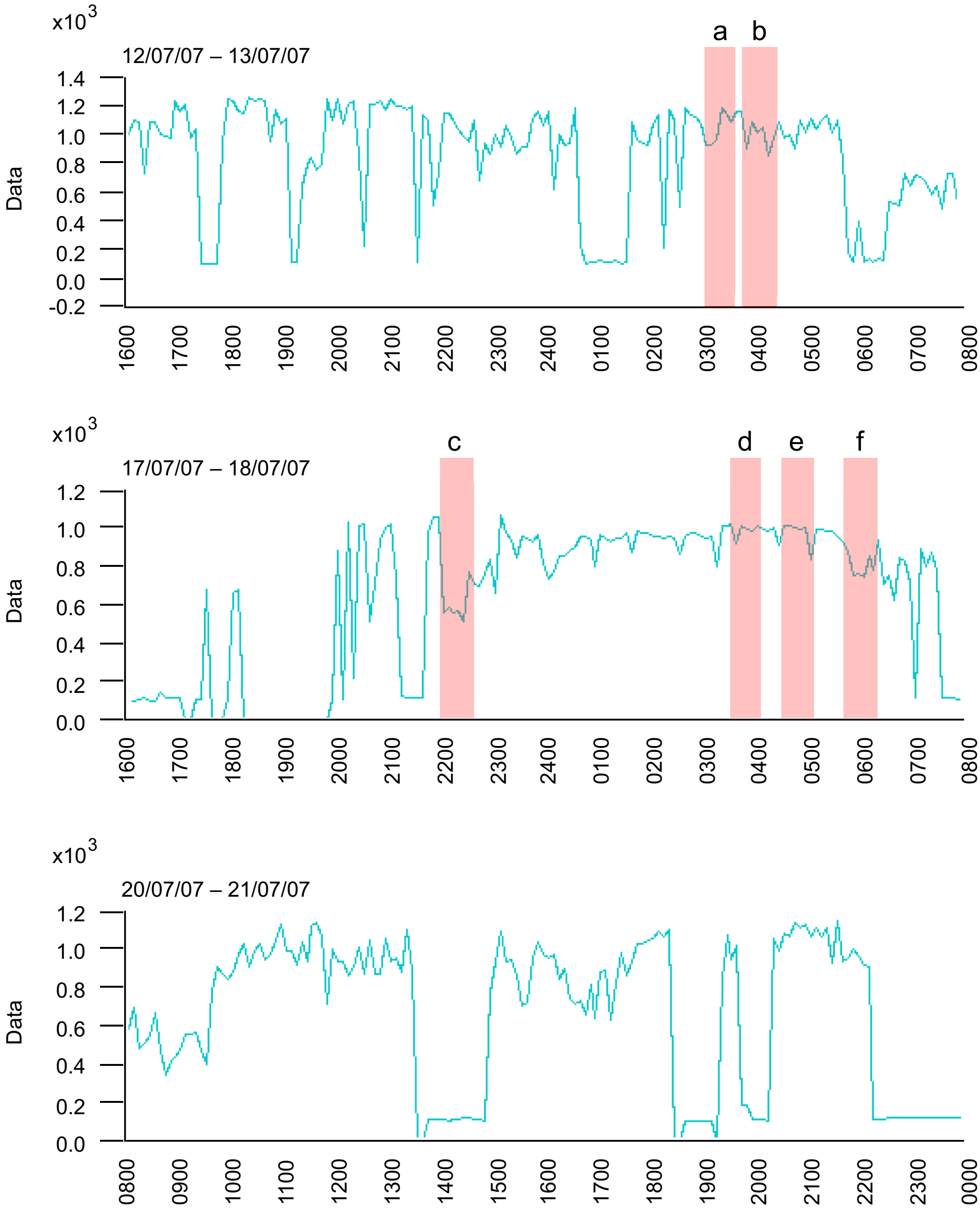

Figure 10.6: 100GHz diode data for the duration of the experiment [87]. The higher its output, the shorter the bunch. The letters correspond to the following Figures: a) 10.10, b) 10.7, c), 10.11, d) 10.8, e) 10.9, and f) 10.12.

a)

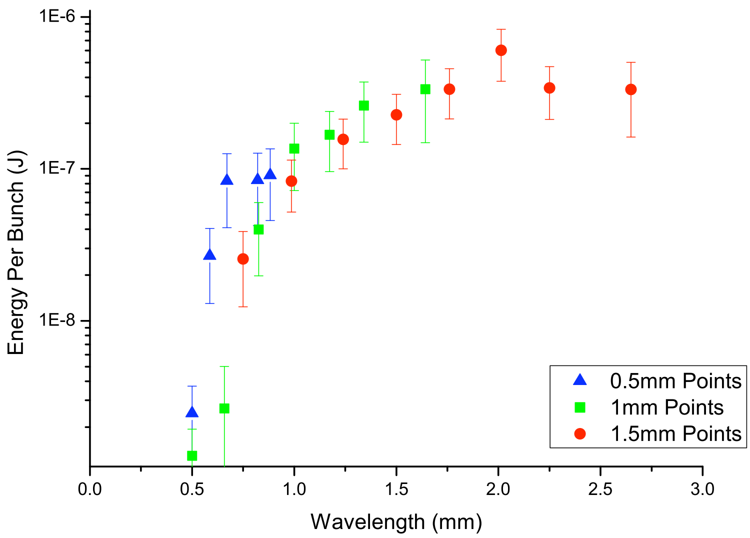

b)

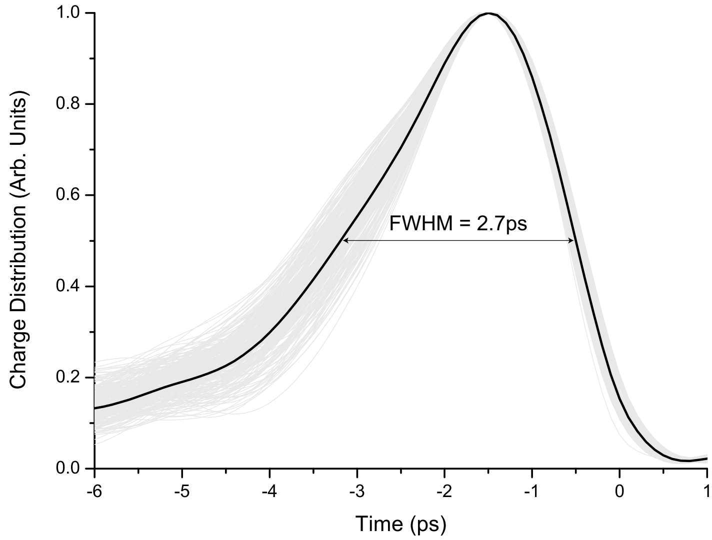

Figure 10.7: Data from 13/07/07, 03:46 – 04:20, a) SP radiation detected from three gratings (0.5, 1.0 and 1.5mm), with $N_e = 1.4 \times 10^{10}$, b) the Kramers-Krönig reconstruction of the longitudinal bunch profile.

a)

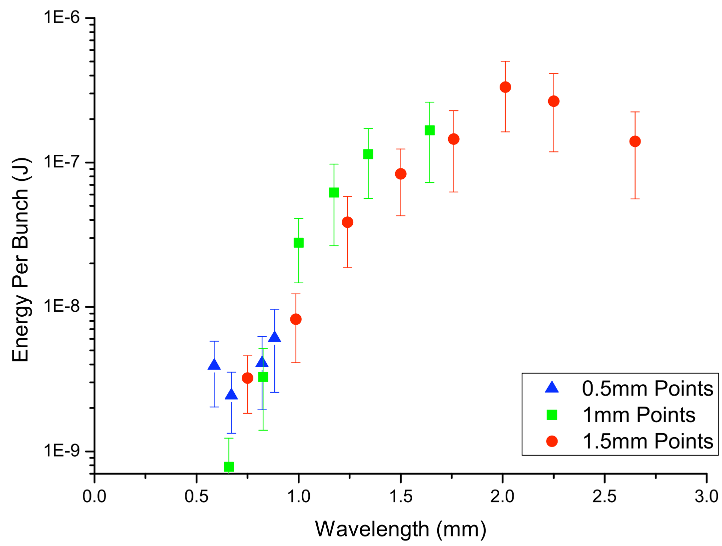

b)

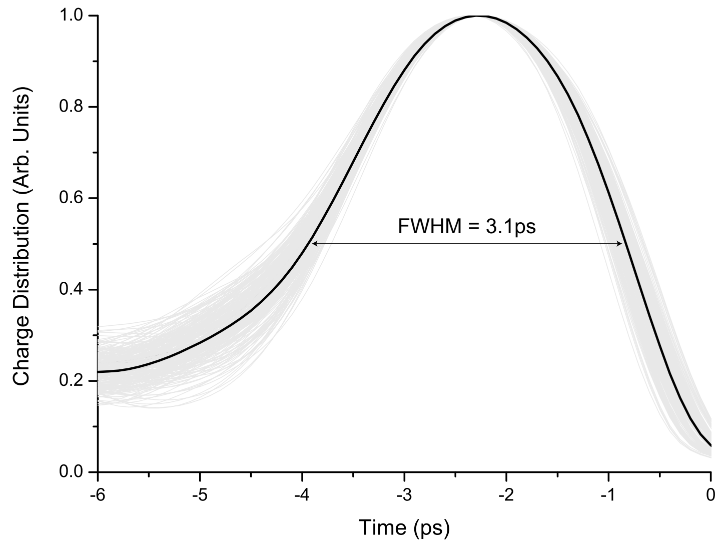

Figure 10.8: Data from 18/07/07, 02:43 – 03:48, a) SP radiation detected from three gratings (0.5, 1.0 and 1.5mm), with $N_e = 1.2 \times 10^{10}$, b) the Kramers-Krönig reconstruction of the longitudinal bunch profile.

a)

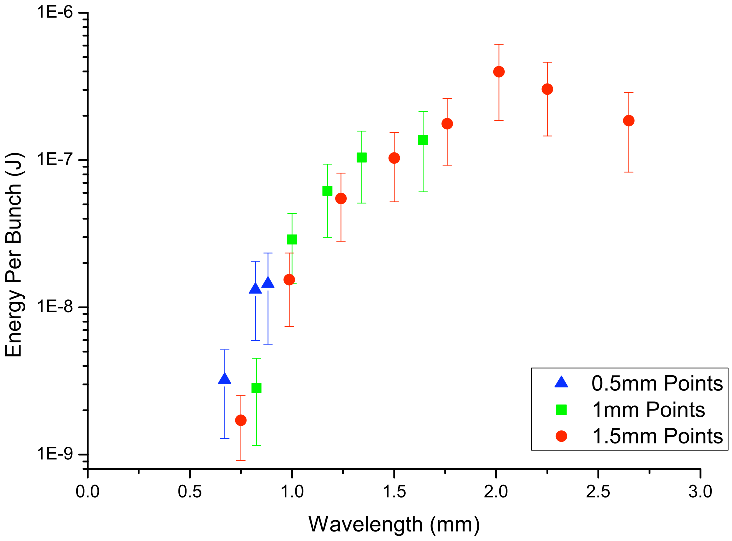

b)

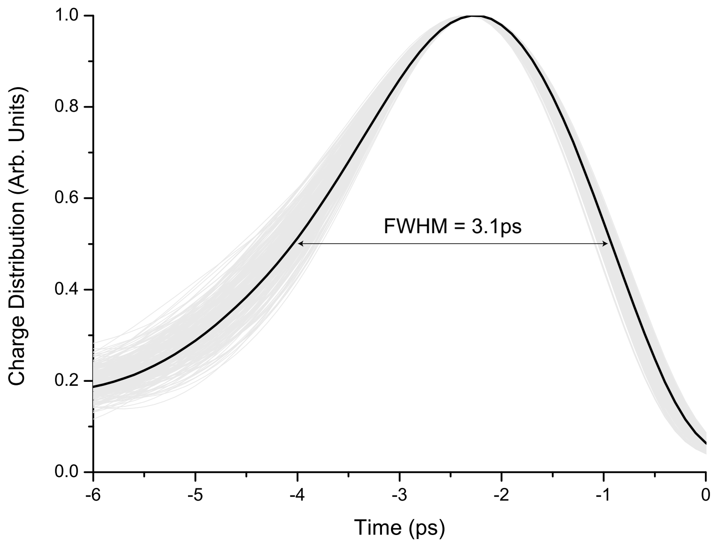

Figure 10.9: Data from 18/07/07, 04:38 – 05:05, a) SP radiation detected from three gratings (0.5, 1.0 and 1.5mm), with $N_e = 1.2 \times 10^{10}$, b) the Kramers-Krönig reconstruction of the longitudinal bunch profile.

distribution of Figure 10.7a rises and saturates more quickly than those of 10.8a and 10.9a. Hence the latter two bunch lengths may be longer overall.

This is supported by the KK reconstructions shown in Figures 10.7b – 10.9b. Consider the KK reconstruction shown in Figure 10.7b. This reconstruction tends to zero faster than other profiles presented in this chapter. However, it also appears to be a shorter bunch, with a FWHM of $2.7^{+0.6}_{-0.6}$ps. The reconstructions shown in Figures 10.8b and 10.9b are longer (FWHM = $3.1^{+0.6}_{-0.5}$ and $3.1^{+0.6}_{-0.4}$ps respectively), and do not tend to zero as quickly. All the reconstructions do not tend to zero in the negative time direction. This suggests that they are missing adequate long wavelength data. With hindsight, the gratings used at SLAC were unable to provide sufficient long wavelength information because their periods were too short compared to the bunch length. Therefore, this lack of long wavelength information is a common feature of all the KK analyses presented here. The 100GHz diode readings also support the conclusions regarding the relative lengths of these bunches. This recorded a value of 1100 during the time Figure 10.7a was taken over, and 1000 during the time Figures 10.8a and 10.9a taken over.

The majority of bunch profiles are similar in appearance and length to those presented here. In these cases the KK reconstruction is good, and gives a reasonably accurate estimate of the bunch length. The FWHM of the bunch varies between 2.7 – 3.2ps. These profiles are always asymmetric in appearance and can be described by a combination of 3 (or more) Gaussians.

10.2.4 Kramers-Krönig Reconstructions of 'Longer' Profiles

Although the majority of the bunches observed at SLAC using SP radiation had a relatively simple profile, there were several examples of more complicated profiles. A selection of these profiles is presented in this section. For example, the spectral energy distribution shown in Figure 10.10a was taken approximately 15 minutes before that of Figure 10.7a, and hence the bunches might have been assumed to be similar. However, the distribution shown in Figure 10.10a is more uneven than that of Figure 10.7a. This suggests that the bunch profile is not the same, and is instead more complicated. Further examples of non-monotonic spectral energy distributions are shown in Figures 10.11a and 10.12a, where it is much more pronounced.

The data presented in Figures 10.11a and 10.12a were taken on the same day as Figure 10.9a (18/07/07) under different beam conditions. In both cases, the 100GHz diode recorded a much lower signal, indicating that these bunches are longer than that of Figure 10.9a. This can be seen by examining the rate at which the measured energies rise towards coherence. At first they appear to rise at approximately the same rate as Figure 10.9a, but the distribution does not

a)

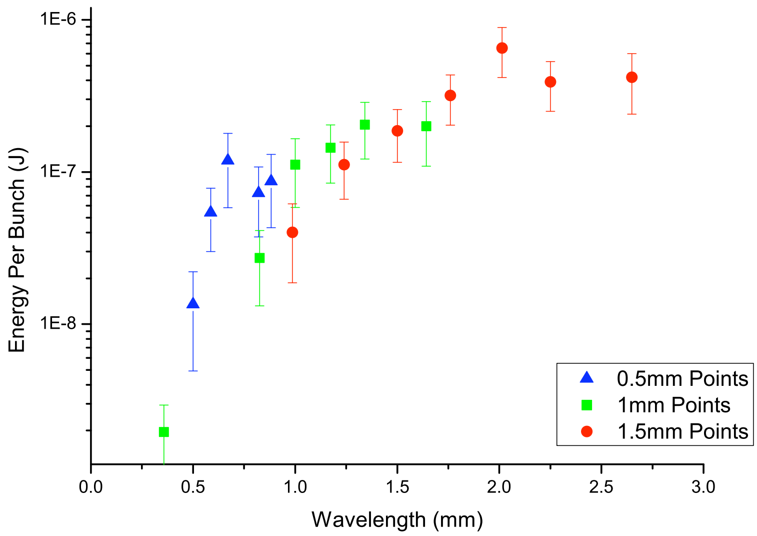

b)

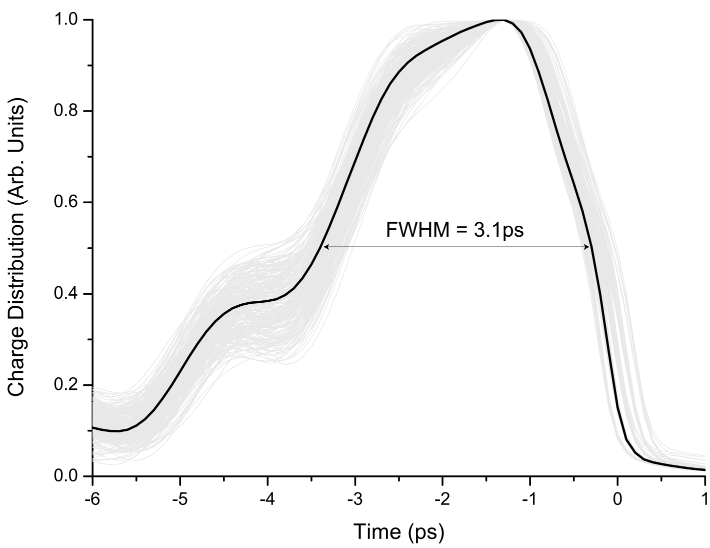

Figure 10.10: Data from 17/07/07, 22:06 – 22:44, a) SP radiation detected from three gratings (0.5, 1.0 and 1.5mm), with $N_e = 1.4 \times 10^{10}$, b) the Kramers-Krönig reconstruction of the longitudinal bunch profile.

reach saturation. Instead, the energy levels rise, fall, and then rise again. This suggests that the bunch profile is more complicated as its spectral energy distribution is more complex.

The bunch charge is also higher for these data sets, and consequently further conclusions can be drawn. For the same bunch length, an increase in bunch charge results in an increase in the output energy. However, the overall energy levels of Figures 10.11 and 10.12 are lower than Figure 10.9, despite the increased bunch charge. This also implies that they are longer bunches.

These suggestions are supported by the KK reconstructions presented in Figures 10.10b – 10.12b. Data sets that appear to have a more complicated bunch structure, judging by the shape of the measured spectral energy distribution, typically have a more complicated KK reconstruction. As the gratings used during this experiment were not ideal for the the apparent bunch lengths, as shown by the need for more long wavelength data, complicated KK profiles are more prone to error and require further consideration. The three reconstructed profiles shown in this section are typical examples of these complicated structures.

In the case of Figure 10.10b, the reconstructed profile tends closer to zero in the negative time direction than other reconstructions. This was also the case for Figure 10.7, which was measured a short time later. This suggests that although long wavelength information is missing, the gratings used were not as unsuitable as for other bunches — *i.e.*that the bunch was slightly shorter. In this case the reconstruction shows clear signs of bunch sub-structure; the bunch has a FWHM of $3.1^{+1.1}_{-0.5}$ps.

The KK reconstruction of Figure 10.11 is very poor, although a leading peak with a FWHM of $2.4^{+0.7}_{-0.4}$ps was identified. There is, apparently, a second peak (FWHM = $2.1^{+0.4}_{-0.8}$ps), but the fact that the reconstruction of it is some distance from the matching peak at $t = 0$ suggests that the later peak may be an artifact introduced by the KK analysis due a severe lack of long wavelength information. If the second peak is not an artifact, then the bunch is much longer than any others measured at SLAC. This is supported by the overall low measured spectral energies and the very low 100GHz diode reading (~ 600).

Figure 10.12b would also appear to show a relatively long bunch with substantial trailing structure. If this KK reconstruction is accurate, it would indicate a bunch with a FWHM of $5.7^{+1.1}_{-2.9}$ps. However, KK can show spurious structure when the bunch form factor has nearby zeros (Section 3.2.1), for example, a multi-Gaussian profile whose dominant peak is not the leading peak. An example of this was presented in Section 3.2.5, which is repeated for clarity in Figure 10.13. This shows the KK reconstruction of a simulated multi-Gaussian profile whose dominant peak is not the leading peak. In this case, the reconstruction underestimates the

a)

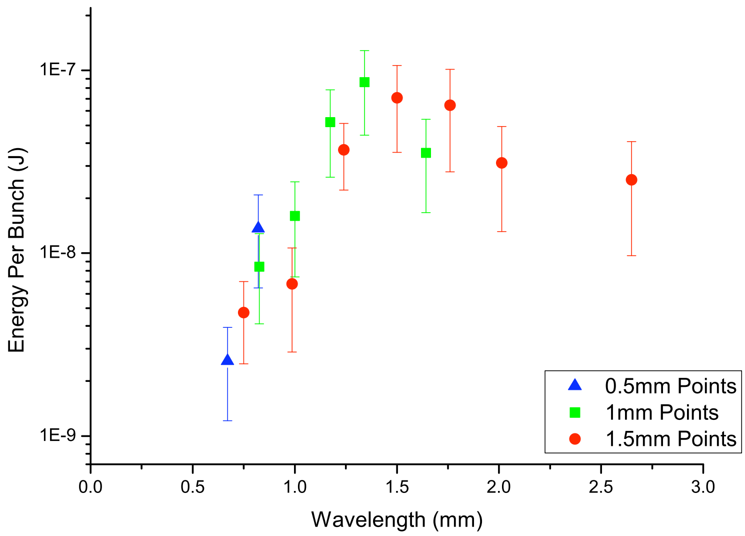

b)

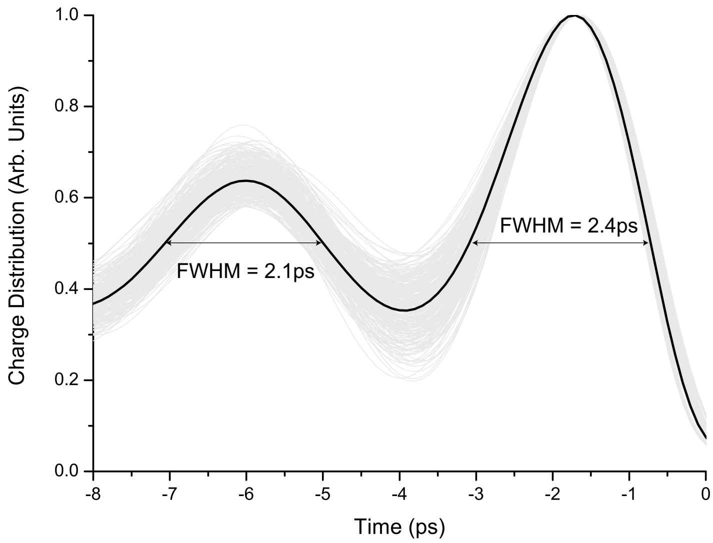

Figure 10.11: Data from 17/07/07, 22:06 – 22:44, a) SP radiation detected from three gratings (0.5, 1.0 and 1.5mm), with $N_e = 1.4 \times 10^{10}$, b) the Kramers-Krönig reconstruction of the longitudinal bunch profile.

a)

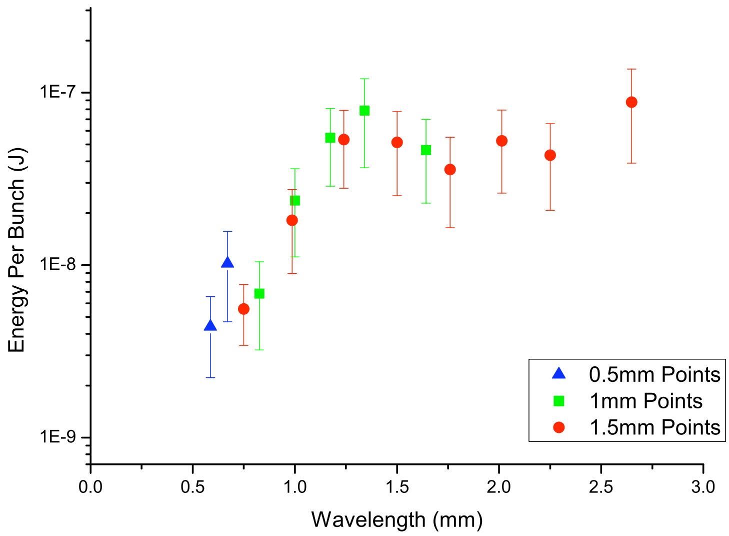

b)

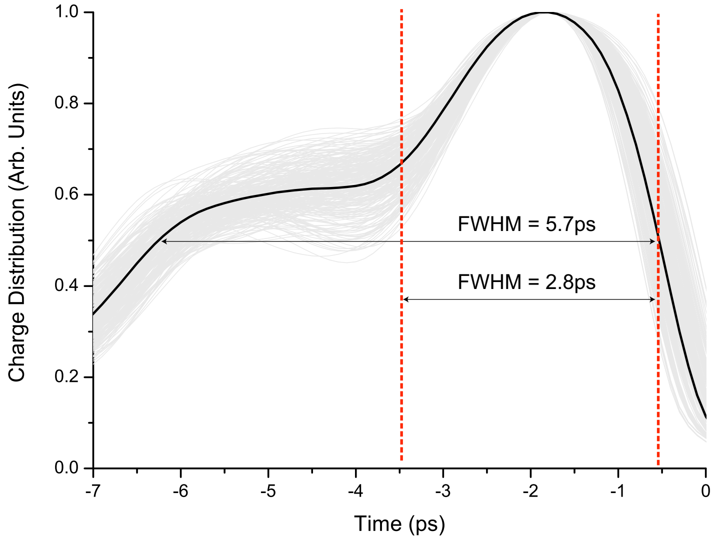

Figure 10.12: Data from 18/07/07, 05:45 – 06:16. a) SP radiation detected from three gratings (0.5, 1.0 and 1.5mm), with $N_e = 1.3 \times 10^{10}$, b) the Kramers-Krönig reconstruction of the longitudinal bunch profile with two possible FWHMs.

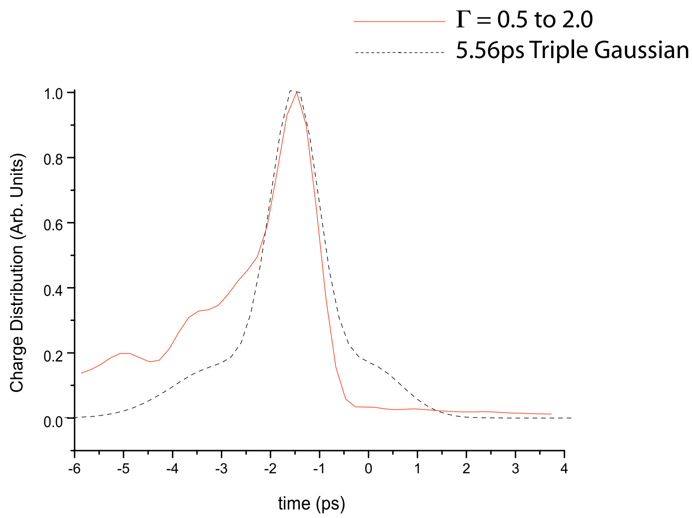

Figure 10.13: KK reconstruction of a simulated triple Gaussian with a predominant middle peak an overall approximate length of $\sim$ 6ps (from Figure 3.7, Γ =0 .5 to 2).

start of the bunch, and adds non-existent structure to the bunch. Ultimately, the reconstructed profile overestimates the overall approximate bunch length by a significant amount. However, the dominant peak (minus any preceding structure) is identified reliably, and its FWHM is typically a reasonable estimate of the actual dominant peak. Therefore, it is probable that this bunch had a non-leading dominant peak with a FWHM of $\sim$ 2.8ps but, beyond that, the KK reconstruction of the bunch profile cannot provide any firmer statements.

10.3 Summary

Coherent SP radiation has been used to determine the bunch length and longitudinal bunch profile of the 28.5GeV beam at SLAC. The major change to the experimental setup was the addition of a filter changing mechanism that allowed filters to be changed remotely and quickly. As a result of this, data were acquired much faster, which in turn improved the reliability of the reconstructed bunch profiles. The changes to the apparatus, and their effect on the various correction factors that must be applied to the data is discussed in Section 10.1.

Section 10.2 examines the collected data in more detail. A variety of bunch profiles, reconstructed using the Kramers-Krönig technique, were observed at SLAC. Some of these are given in Section 10.2.3, and are correlated with the measurements from a 100GHz diode in ESA. The reconstructed bunch lengths were consistent with the diode readings. A typical FWHM of $\sim$ 3ps was found — consistent with the March LOLA measurements. The most common bunch profile had a prominent leading peak with a longer trailing edge, and can be described by a superposition of 3 (or more) Gaussians. The quality of some reconstructions suggests that bunches were also present that were too long for the gratings used in this experiment. In this case, the dominant peak was reconstructed with a reliable FWHM, but there could be significant errors in the overall shape of the bunch. In general, the largest problem that affected all reconstructed profiles at SLAC was a lack of adequate long wavelength data. Further refinement of the reconstructed profiles might have been achieved by measurements of shorter wavelengths. However, this was not possible during this experiment as the pyroelectric detectors were relatively insensitive to these short wavelengths.

Chapter 11

Summary and Future Work

This thesis describes the measurement of the length and time profile of ps-long electron bunches using coherent Smith-Purcell (SP) radiation. Colliding beams are subject to forces known collectively as 'beam-beam effects', which partly depend on the longitudinal (time) profile of the bunch. Beam-beam effects can have a large impact on the luminosity of an accelerator, and hence on its efficiency. Therefore, the longitudinal profile is an important parameter for future high energy accelerators, such as the ILC.

Older techniques were unable to resolve ps-long bunch lengths *and*profiles, nor could they satisfy the demands of a high-energy (TeV) accelerator, *i.e.*diagnostics that do not interfere with the beam. In this respect, several new techniques are currently in development. Coherent SP radiation is a promising, non-invasive technique that has been investigated in this thesis.

SP radiation is generated when a bunch passes over a periodic, metallic grating. Radiation is emitted over a large angular spread and the SP wavelength detected depends on the angle of observation. If the emitted wavelength is equal to, or shorter than, the bunch length, radiation is emitted coherently and the emitted spectral energy distribution depends on the longitudinal profile of the bunch. Therefore, the bunch profile can be recovered — for example, using a Kramers-Krönig (KK) analysis — after measuring the spectral energy distribution of the coherent radiation.

Several theories exist that describe the generation of SP radiation. Two of these theories are considered in more detail in this thesis: SP as the result of the diffraction of evanescent waves [69, 74], and SP as the result of induced surface currents [9]. These theories conflict regarding the emission of SP radiation at high energy. The evanescent wave theory predicts that the energy of the emitted SP radiation should decrease with increasing beam energy. However, the surface current model predicts that the emitted energy should increase. Therefore, the two main goals of this thesis were: (a) To demonstrate that SP radiation is produced in the multi-GeV regime, and (b) to show that it is a suitable diagnostic tool for the determination of the time profile of ps-long bunches in future high energy accelerators such as the ILC.

11.1 Overview of the Experimental Results

This thesis reports on four experiments. The first experiment, at FELIX in November 2005, was carried out at an energy of 45MeV and was an intermediate step towards the highly relativistic regime [15]. Several experimental components were prototyped during this experiment *(e.g.*the pyroelectric detectors, WAP filters and Winston cones). Data from this experiment were re-analysed in this thesis as, at the time of publication of [15], several correction factors were previously unknown or inaccurate. The new analysis concluded that the FELIX bunch had a FWHM of $3.9^{+0.6}_{-0.6}$ps. However, further short and long wavelength data were required to more accurately reconstruct the bunch profile, which appeared to be similar to an asymmetric Gaussian.

The first ever SP experiment in the multi-GeV regime was carried out at End Station A (ESA), SLAC in March 2007 at an energy of 28.5GeV. Data from this experiment were limited by the rate of data acquisition and a full analysis of the SLAC bunch length and profile was not possible. Even so, sufficient data were collected to confirm that SP radiation was generated in this energy regime, in broad agreement with the predictions of the 'surface current' theoretical description. Evidence was also found of real time changes of the bunch profile during data acquisition. This was the most likely explanation for the changes in signal magnitude at certain wavelengths, *i.e.*to changes in the spectral distribution of the emitted SP radiation. This showed that SP radiation was sensitive to bunch changes on a short time scale.

The experimental setup was improved for the July 2007 experiment at SLAC, allowing analysis to proceed beyond the confirmation of SP radiation. A KK analysis was carried out on all suitable data sets to recover their longitudinal bunch profiles. The majority of reconstructed profiles were similar in appearance, with a large leading peak and long trailing edge. All of the measured profiles were asymmetric and, more significantly, none were Gaussian. The FWHM of the bunches observed at SLAC varied between 2.7 – 3.2ps.

Significant effort was involved in the application of the Kramers-Krönig technique to SP radiation. Investigations showed that, *given sufficient wavelength information*, a KK analysis returns a reliable measure of the bunch length and profile. When there is insufficient wavelength information, the returned overall bunch length and FWHM is still a reasonable approximation, and the main features of the profile are still identifiable. With hindsight, the grating periods used experimentally did not provide sufficient information to fully exploit this analysis technique. Thus, profiles at SLAC fell into two broad categories: 'Short' profiles that were reasonably well reconstructed by KK, and 'longer' profiles that lacked sufficient long wavelength information.

For comparison, measurements were also carried out with LOLA at SLAC in March 2007 [49]. These measurements were carried out at a different time and location to the March SP experiment. LOLA determined that the bunch length in ESA varied between $\sigma = 1.3 - 2.3$ps. This is consistent with the bunch lengths measured using coherent SP radiation ($\sigma \approx 1.2 - 1.4$ps).

A fourth set of experiments were carried out at the Rutherford Appleton Laboratory (RAL) [64]. These consisted of a number of measurements of the various correction factors required for the above analyses. The calibration of the pyroelectric detectors formed a significant part of these measurements, and was complicated by the scarcity of far-infrared sources. Other measurements carried out at this time involved the characterisation of the Winston cones, and measurements of the power transmission efficiency of the WAP filters and other components. Both the cones and the filters were designed specifically for these experiments and were found to perform as expected.

11.2 Main Conclusions

As previously stated, the accuracy of the KK reconstruction depends crucially on the supplied wavelength range. The larger the range of wavelengths available, and the more data points collected, the less reliant the KK analysis becomes on the extrapolation and interpolation of the data. Therefore, SP radiation has two large advantages over other approaches: i) Wavelengths can be selected by careful choice of the grating period, and ii) the wavelength range can be expanded by including additional gratings. With hindsight, this was not fully exploited during the experiments detailed in this thesis. Although the grating periods used were suitable for detecting SP radiation, they were not optimal for reconstructing the bunch profile and the reconstructions consistently lacked long wavelength information (*i.e.*from a longer period grating). Hence, relatively long (overall) bunch profiles were not reconstructed well.

The experimental uncertainty in the SP measurements was large. There were a number of contributors to the uncertainty, but the largest was due to the difficulty in deriving accurate calibrations for the detectors in the far-infrared part of the spectrum. Sources in this wavelength region were limited, especially at wavelengths < 1mm.

Although pyroelectric detectors have a number of advantages — they work at room temperature and are small and inexpensive — these are offset by their insensitivity to short wavelengths. Short wavelength SP radiation proved difficult to detect throughout these experiments, even though (theoretically) it should have been detected. Detection of higher orders of SP radiation was also limited by the insensitivity of the detectors. These wavelengths, if detected, would have further expanded the available wavelength region for the KK analysis.

Finally, this experiment was not single-shot. Measurements with different gratings (and blank) were separated in time, and therefore SP radiation could only provide an indication of the average bunch profile over this period of time. This may introduce further inaccuracies in the recovered profiles. However, SP radiation is inherently capable of single-shot operation and this issue could be addressed by appropriate modifications to the experimental setup.

11.3 Future Work

This thesis described three proof-of-principle experiments, designed to demonstrate the capabilities of an SP-based longitudinal bunch profile diagnostic for ps-long bunches. Although the experiments did not fully exploit the SP process, they showed that it could return a reliable measure of the bunch length, and identify the majority of structure in the bunch profile. If the SP process were fully exploited, it would be a very promising diagnostic tool for future accelerators such as the ILC.

The SLAC experiments demonstrated that SP radiation was generated in the multi-GeV regime, in broad agreement with the surface current model. The surface current model is therefore the closest theoretical approximation to the physical process. Hence, it can be used to predict the behaviour of coherent SP radiation in a number of interesting future applications.

- There is no theoretical obstacle to SP radiation being generated in the TeV regime. This approach to determining the longitudinal bunch profile should work equally as well (or better) in the ultra-high energy regime as it did at SLAC, especially if its features are fully exploited.

- In addition to using coherent SP radiation to determine the longitudinal profile of ps-long bunches in the TeV regime, calculations show no barriers to extending this technique to even shorter (*e.g.*several fs-long) bunches. This is an unexplored area for SP, but if shown to work would make it a very exciting tool compared to other methods that cannot yet reach these limits. Bunch profile diagnostics are highly desirable in this region for future laser-plasma accelerators. Such short bunches would require working in a different wavelength region, the mid-infrared, and would require a complete redesign of the gratings, filters, and detectors. However, many aspects of the experiment would also become easier, *i.e.* filters and detectors for this wavelength region are more readily available.

- The surface current model, as applied to a grating of infinite width, can predict the degree of polarisation of the emitted SP radiation. At high energy it is 100% polarised at $\phi = 0$ in the $x - z$ plane and unpolarised at all other azimuthal angles. Therefore, for a practical experiment that accepts a narrow range of azimuthal angles around $\phi = 0$, the radiation is partly polarised. This could be exploited by replacing WAP filters with polarisers.

The application of coherent SP as a working diagnostic tool in the picosecond regime would require a number of modifications. These are based on the experience derived from this work: First, the measurable wavelength range should be expanded as far as possible by carefully choosing the grating periods relative to the expected bunch lengths. This would require multiple gratings, which would increase the number of available data points. Secondly, the experiment should be adapted to single-shot operation. This could proceed by distributing a number of gratings along the vacuum chamber, each with their own associated detection systems. Finally, alternative far-infrared detectors should be investigated. The pyroelectric detectors used throughout this thesis were operating at the limit of their capability. Other detectors (*e.g.*cryogenic) will be more sensitive to the emitted radiation. The wavelength region detected during an SP experiment is also of significant interest in astronomy, where much lower energy far-infrared signals are investigated. Therefore, there may be many parallels between astronomy and the detection of coherent SP radiation that could be exploited in a future experiment.

Appendix A: Polarisation of SP Radiation

The polarisation of SP radiation is an interesting topic. However, it should be noted that it was not investigated experimentally in this thesis. Therefore what follows is based on simulations using the surface current model (Section 2.2.3) for a grating of *infinite* width. The polarisation of SP radiation arises from the grating factor R^2, which is discussed in more detail in [10]. The degree of polarisation of SP radiation at FELIX and SLAC is calculated here, and the average value in the $x - z$ plane is found.

The degree of polarisation partially depends on the beam energy, or γ. Hence, the simulated polarisation in the $x - z$ plane, for $\theta = 90°$, is shown in Figure 1 for $\gamma \approx 81$ and $\gamma \approx 55773$, which represent the beams at FELIX and SLAC respectively. The radiation is 100% polarised at $\phi = 0$, as reported in [15]. At low beam energy the polarisation in this plane decreases slowly to 50% with increasing azimuthal angle, ϕ. However, at high energy the radiation is effectively unpolarised for all $\phi \neq 0$.

The *average*polarisation in the $x-z$ plane depends on the range of azimuthal angles collected by the optical system and the (theoretical) differential energy output over these angles. The optical system collects all angles within $-5° \leq \phi \leq 5°$. Figure 2 shows the calculated differential energy output, per solid angle per unit grating length, over this range at $\theta = 90°$. At high energy this distribution becomes much more compact, with the maximum emitted energy occurring closer to $\phi = 0$ than at low energy.

The emitted differential energy, as a proportion of the maximum emitted energy, is used as a weighting function to calculate the average polarisation. At FELIX the average polarisation, as collected by the optical system, is 58.9% in the $x - z$ plane. At SLAC, this decreases to 50.6%.

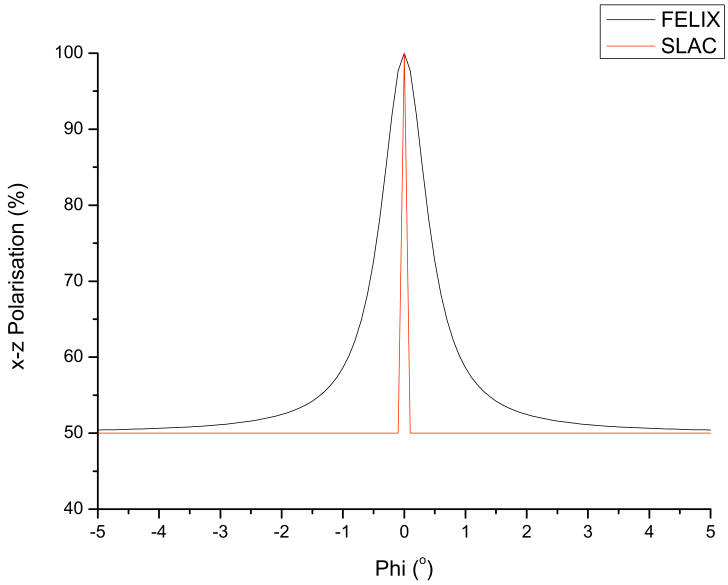

Figure 1: The degree of polarisation of SP radiation in the $x - z$ plane at $\theta = 90°$ for FELIX ($\gamma \approx 81$) and SLAC ($\gamma \approx 55773$).

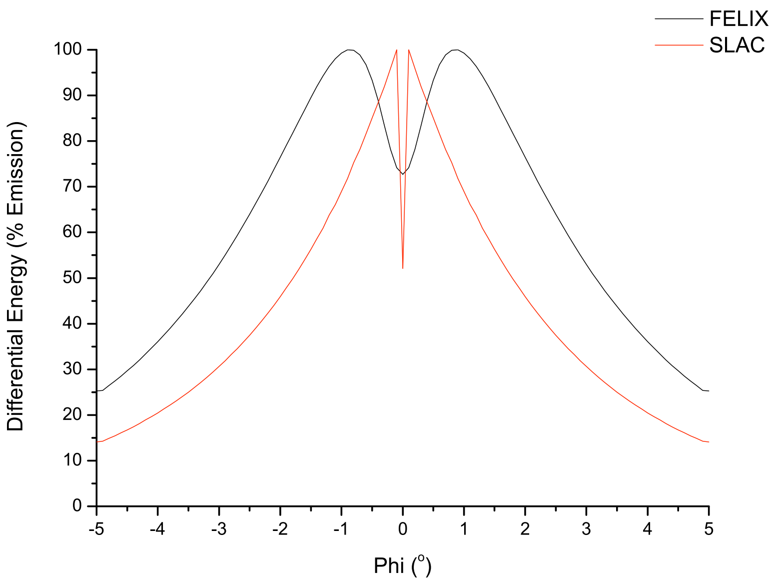

Figure 2: Differential energy output over ϕ at $\theta = 90°$ for FELIX ($\gamma \approx 81$) and SLAC ($\gamma \approx 55773$).

Bibliography

[1] O. H. Altenmueller, R. R. Larsen and G. A. Loew, *Investigations of Traveling-Wave Separators for the Stanford Two-Mile Linear Accelerator*, The Review of Scientific Instruments, Vol. **35**, No. **4**, p. 238 – 442 (1964)

[2] C. Amsler et al. (Particle Data Group), *The Review of Particle Physics*, Physics Letters B667, 1 (2008)

[3] R. W. Astheimer and F. Schwartz, *Thermal Imaging using Pyroelectric Detectors*, Applied Optics, Vol. **7** No. **9**, p. 1687 – 1695 (1968)

[4] M. Bassetti *et al.*, *Properties and Possible Use of Beam-Beam Synchrotron Radiation*, IEEE Trans. Nucl. Science, Vol. **30**, p. 2182 – 2184 (1983)

[5] G. Bonvicini, J. Welch, *Large Angle Beamstrahlung as a Beam-Beam Monitoring Tool*, NIM **A**, Vol. **419**, p. 223 – 232 (1997)

[6] M. Born and E. Wolf, *Principles of Optics: Electromagnetic Theory of Propagation, Interference and Diffraction of Light,* Cambridge University Press (1999)

[7] M. Bozzi, L. Perregrini, J. Weinzierl and C. Winnewisser, *Design, Fabrication and Measurement of Frequency-Selective Surfaces*, Society of Photo-Optical Instrumentation Engineers, Vol. **39** No. **8**, p.2263 – 2269 (2000)

[8] J. H. Brownell *et al.*, *The Angular Distribution of the Power Produced by Smith-Purcell Radiation*, J. Phys. **D**: Appl. Phys., Vol. **30,** p. 2478 – 2481 (1997)

[9] J. Brownell, J. Walsh, G. Doucas, *Spontaneous Smith-Purcell Radiation Described Through Induced Surface Currents*, Physical Review **E**, Vol. **57**, No. **1**, p. 1075 – 1080(1998)

[10] J. Brownell, G. Doucas, *Role of the Grating Profile in Smith-Purcell Radiation at High Energies*, Phys. Rev. Special Topics – Accelerators and Beams, Vol. **8**, 091301 (2005)

[11] E. Castro-Camus *et al.*, *Polarisation-Sensitive Terahertz Detection by Multicontact Photoconductive Receivers*, Applied Physics Letters, Vol. **86**, 254102 (2005)

[12] C. C. Chen, *Transmission of Microwaves Through Perforated Flat Plates of Finite Thickness*, IEEE Trans. Microwave Theory Tech., Vol **21**, p. 1 – 5 (1973)

[13] J. Cooper, *A Fast Response Pyroelectric Thermal Detector*, J. Sci. Intrum., Vol. **39**, p. 467 – 472 (1962)

[14] J. Donohue, J. Gardelle, *Simulation of Smith-Purcell Radiation using a Particle-In-Cell Code,* Phys. Rev. Special Topics – Accelerators and Beams, Vol. **8**, 060702 (2005)

[15] G. Doucas *et al.*, *Longitudinal Electron Bunch Profile Diagnostics at 45MeV using Coherent Smith-Purcell Radiation*, Phys. Rev. Special Topics: Accelerators and Beams, Vol. **9**, 092801 2006

[16] ELTEC Model 400 Pyroelectric Detector Specification Sheet: http://www.silverlight.ch/eltec/

[17] L. Fröhlich, O. Grimm, *et al., Longitudinal Bunch Shape Diagnostics with Coherent Radiation and a Transverse Deflecting Cavity at TTF2*, **SLAC-PUB-11387**

[18] V. L. Ginzburg, I. M. Frank, *Radiation of a Uniformly Moving Electron due to its Transition from One Medium into Another,* Journal of Physics, USSR, Vol. **9**, p. 353 (1945)

[19] M. J. E. Golay, *Theoretical Consideration in Heat and Infrared Detection, with Particular Reference to the Pneumatic Detector*, The Review of Scientific Instruments, Vol. **18**, No. **5**, p. 347 – 356 (1947)

[20] A. Gover, P. Dvorkis and U. Elisha, *Angular Radiation Pattern of Smith-Purcell Radiation*, Optical Society of America B, Vol. **1**, No. **5**, p. 723 – 728 (1984)

[21] O. Grimm, P. Schmüser, *Principles of Longitudinal Beam Diagnostics with Coherent Radiation*, TESLA Report, 2006

[22] O. Haeberlé, P. Rullhusen, J. M. Salomé, *Calculations of Smith-Purcell Radiation Generated by Electrons of 1—100MeV*, Phys. Rev. **E**, Vol. **49**, No. **4**, p. 3340 – 3352 (1994)

[23] P. G. Huggard *et al.*, *Far-infrared Bandpass Filters from Perforated Metal Screens*, Applied Optics, Vol. **33**, No. **1**, p. 39 – 41 (1994)

[24] P. G. Huggard *et al.*, *1.55μm Photomixer Sources for mm-wave Heterodyne Detection and Frequency Conversion with Schottkey Diodes*, Digest of the LEOS Summer Topical Meetings (2005)

[25] P. Huggard, Private communications.

[26] M. Hüning, A. Bolzmann, H. Schlarb *et al.*, *Observation of Femtosecond Bunch Length Using a Transverse Deflecting Structure*, **SLAC-PUB-11482**

[27] *International Linear Collider Reference Design Report*, ILC Global Design Effort and World Wide Study, Vol. **2** and **3** (2007)

[28] The International Linear Collider Homepage: http://www.linearcollider.org

[29] K Ishiguro, T. Tako, *The Smith-Purcell effect as a Source of Infrared Light*, Journal of Modern Optics, Vol. **8**, p. 25 – 31 (1961)

[30] J. D. Jackson, *Classical Electrodynamics*, 3rd. Edition, Wiley Press

[31] S. P. Jamison *et al.*, *Femtosecond Resolution Bunch Profile Measurements*, EPAC 2006

[32] D. V. Karlovets, A. P. Potylitsyn, *Comparison of Smith-Purcell Radiation Models and Criteria for their Verification*, Phys. Rev. Special Topics: Accelerators and Beams, Vol. **9**, 080701 (2006)

[33] A. S. Kesar, M. Hess, S. E. Korbly, R. J. Temkin, *Time and Frequency Domain Models for Smith-Purcell Radiation from a Two-Dimensional Charge Moving Above a Finite Length Grating*, Physical Review **E**, Vol. **71**, No. **1**, 016501 (2005)

[34] M. F. Kimmitt, *Far-Infrared Techniques*, Applied Physics Series, Pion Ltd. (1970)

[35] M. F. Kimmit, private communications.

[36] C. Kittel, *Introduction to Solid State Physics*, John Wiley & Sons, New York, 3rd Edition, Chap. 8 (1966)

[37] S. Korbly, A. Kesar, R. Temkin, J. Brownell, *Measurement of Subpicosecond Bunch Lengths using Coherent Smith-Purcell Radiation,* Phys. Rev. Special Topics – Accelerators and Beams, Vol. **9**, 022802 (2006)

[38] G. Kube *et al.*, *Observation of Optical Smith-Purcell Radiation at an Electron Beam Energy of 855MeV*, Phys. Rev. **E**, Vol. **65**, 056501 (2002)

[39] R. Lai, A. J. Sievers, *Determination of a Charged Particle Bunch Shape from the Coherent Far Infrared Spectrum*, Phys. Rev. **E**, Vol. **50**, No. **5**, R3342 (1994)

[40] R. Lai, U. Happek and A. J. Sievers, *Measurement of the Longitudinal Asymmetry of a Charged Particle Bunch from the Coherent Synchrotron or Transition Radiation Spectrum*, Phys. Rev. **E**, Vol. **50**, No. **6**, R4294 (1994)

[41] R. Lai and A. J. Sievers, *Phase Problem Associated with the Determination of the Longitudinal Shape of a Charged Particle Bunch from its Coherent Far-IR Spectrum*, Phys. Rev. **E**, Vol. **52**, No. **4**, 4576 (1995)

[42] R. Lai and A. J. Sievers, *Determination of Bunch Asymmetry from Coherent Radiation in the Frequency Domain*, Micro Bunches Workshop Vol. **367**, p. 312, AIP Press, Woodbury (1996)

[43] R. Lai, A. J. Sievers, *On Using the Coherent Far IR Radiation Produced by a Charged-Particle Bunch to Determine its Shape: I Analysis*, NIM **A**. Vol. **397**, R3342 (1997)

[44] E. V. Loewenstein, D. R. Smith and R. L. Morgan, *Optical Constants of Far Infrared Materials. 2: Crystalline Solids*, Applied Optics, Vol. **12**, No. 2, p. 398 – 406 (1973)

[45] J. H. Ludlow *et al., Infrared Radiation Detection by the Pyroelectric Effect*, J. Sci. Instrum., Vol. **44**, p. 694 – 696 (1967)

[46] D. H. Martin and J. Lesurf, *Submillimetre-Wave Optics*, Infrared Physics, Vol. **18**, p. 405 – 412 (1978)

[47] R. J. Y. McLeod and M. L. Baart, *Geometry and Interpolation of Curves and Surfaces*, Cambridge University Press (1998)

[48] Microtech Instruments, Golay Cell Specification Sheet: http://www.mtinstruments.com/

[49] S. Molloy, P. Emma *et al.*, *Picosecond Bunch Length and Energy-Z Correlation Measurements at SLAC's A-Line and End Station A*, PAC 2007

[50] S. Molloy, Private communications.

[51] J. Nodvick, S. Saxon, *Suppression of Coherent Radiation by Electrons in a Synchrotron*, Phys. Rev., Vol. **96**, p. 180 – 184 (1954)

[52] M. L. Oldfield *et al.*, *Measurements of the Sideband Conversation Gain Ratio of a Millimeter-Wave Heterodyne Sub-Harmonic Mixer Using a Fourier Transform Spectrometer*,International Journal of Infrared and Millimeter Waves, Vol. **18**, p. 01547 – 1563 (1997)

[53] R. Palmer, *The Interdependence of Parameters for TeV Linear Colliders*, **SLAC-PUB-4295** (1987)

[54] C. Perry, private communications.

[55] A. Rabi and R. Winston, *Ideal Concentrators for Finite Sources and Restricted Exit Angles*, Applied Optics, Vol. 15, p. 2880 – 2883(1976)

[56] R. D. Rawcliffe and C. M. Randall, *Metal Mesh Interference Filters for the Far Infrared*, Applied Optics, Vol. **6** No. **8**, p. 1356 (1967)

[57] Lord Rayleigh, Proc. Roy. Soc. (London) **A 79** p. 399 (1907)

[58] K. F. Renk and L. Genzel, *Interference Filters and Fabry-Perot Interferometers for the Far Infrared*, Applied Optics, Vol. **1** No. **5**, p. 643 (1962)

[59] G. M. Ressler and K. D. Möller, *Far Infrared Bandpass Filters and Measurements on a Reciprocal Grid,* Applied Optics, Vol. **6** No. **5**, p. 893 (1967)

[60] W. W. Salisbury, J. Opt. Soc. Am. 52, p. 1315 (1962)

[61] Y. Shibata *et al.*, *Coherent Smith-Purcell Radiation in the Millimeter-Wave Region from a Short-Bunch Beam of Relativistic Electrons*, Phys. Rev. **E**, Vol. **57**, p. 1061 – 1074 (1998)

[62] SLAC Test Facility Users Website

[63] S. J. Smith and E. M. Purcell, *Visible Light from Localised Surface Charges Moving Across a Grating*, Phys. Rev. **E**, Vol. **4**, p. 1069 (1953)

[64] The Space Science and Technology Group, Rutherford Appleton Laboratory: http://www.mmt.rl.ac.uk/

[65] Thomas Keating Absolute Power Meter Manual:
http://www.terahertz.co.uk/images/tki/pmeter/tkpowermetermanual.pdf

[66] The THz-TDS Group, Clarendon Laboratory, University of Oxford: http://www-thz.physics.ox.ac.uk/

[67] J. S. Toll, *Causality and the Dispersion Relation: Logical Foundations*, Phys Rev. Vol. **104,** p. 1760 (1956)

[68] P. Tomaselli *et al.*, *Far-Infrared Bandpass Filters from Cross-Shaped Grids*, Applied Optics, Vol. **20**, p. 1361 – 1366 (1981)

[69] G. Toraldo di Francia, *On the Theory of some Cherenkovian Effects*, Nuvo Cimento, Vol. **16**, p. 61 (1960)

[70] R. Ulrich, *Far-Infrared Properties of Metallic Mesh and its Complementary Structure*, Infrared Physics, Vol. **7**, p. 37 – 50 (1967)

[71] R. Ulrich, *Interference Filters for the Far Infrared*, Applied Optics, Vol. **7**, No. **10**, p.1987 – 1996 (1968)

[72] J. Urata *et al.*, *Superradient Smith-Purcell Emission*, Phys. Rev. Letters, Vol. **80**, p. 516 – 519 (1998)

[73] P. M. van den Berg, *Smith-Purcell Radiation from a Line Charge Moving Parallel to a Reflection Grating*, Journal of the Optical Society of America, Vol. **63**, No. **6**, p. 689 (1973)

[74] P. M. van den Berg, *Smith-Purcell Radiation from a Point Charge Moving Parallel to a Reflection Grating*, Journal of the Optical Society of America, Vol. **63**, No. **12**, p. 1588 (1973)

[75] L. van der Meer, Private communications.

[76] J. C. Vardaxoglou, *Frequency Selective Surfaces*, John Wiley and Sons (1997)

[77] T. Watanabe *et al.*, *Overall Comparison of Subpicosecond Electron Beam Diagnostics by the Polychromator, the Interferometer and the Femtosecond Streak Camera*, NIM **A** Vol. **482**, p. 315 – 317 (2002)

[78] L. Wartski, S. Roland *et al., Interference Phenomenon in Optical Transition Radiation and its Application to Particle Beam Diagnostics and Multiple-Scattering Measurements,* Journal of Applied Physics, Vol. **46**, No. **8**, p. 3644 – 3653 (1975)

[79] W. T. Welford and R. Winston, *The Optics of Nonimaging Concentrators: Light & Solar Energy*, New York: Academic Press (1978)

[80] C. P. Welsch *et al.*, *Longitudinal Beam Profile Measurements at CTF3 using a Streak Camera*, JINST **1** P09002 (2006)

[81] C. Winnewisser *et al.*, *Transmission Characteristics of Dichroic Filters Measured by THz Time-Domain Spectroscopy,* Applied Physics **A**, Vol. **66**, p. 593 – 598 (1998)

[82] C. Winnewisser *et al.*, *Transmission Features of Frequency-Selective Components in the Far-Infrared Determined by Terahertz Time-Domain Spectroscopy*, Applied Optics, Vol. **38**, p. 3961 – 3967 (1999)

[83] C. Winnewisser *et al.*, *Characterisation and Application of Dichroic Filters in the 0.1—3THz Region,* IEEE Transactions on Microwave Theory and Techniques, Vol. **48**, p. 744 – 749(2000)

[84] R. Winston, J. Minano, P. Benitez, *Nonimaging Optics*, Elsevier Academic Press (2005)

[85] J. Wolberg, *Data Analysis Using the Method of Least Squares*, Springer-Verlag Berlin and Heidelberg GmbH & Co. (2005)

[86] K. J. Woods *et al.*, *Forward Directed Smith-Purcell Radiation from Relativistic Electrons*, Phys. Rev. Letters, Vol. **74** No. **19**, p. 3808 – 3811 (1995)

[87] M. Woods, Private communications.

[88] K. Yokoya, P. Chen, *Beam-Beam Phenomena in Linear Colliders*, US-CERN Particle Accelerator School Lecture (1990)

[89] W. Zhu *et al.*, *Pyroelectric Detection of Submicrosecond Laser Pulses between 230 and* $520\mu m$*,* Applied Optics, Vol. **28**, p. 3647 – 3651 (1989)